University of Ljubljana
Faculty for Mathematics and Physics

Gregor Kramberger

Signal development in irradiated silicon detectors

Doctoral Thesis

Supervisor: Doc. Dr. Vladimir Cindro
Co-Supervisor: Prof. Dr. Marko Mikuž

Ljubljana, 2001

Abstract

This work provides a detailed study of signal formation in silicon detectors, with the emphasis on detectors with high concentration of irradiation induced defects in the lattice. These defects give rise to deep energy levels in the band gap. As a consequence, the current induced by charge motion in silicon detectors is significantly altered.

Within the framework of the study a new experimental method, *Charge correction method*, based on transient current technique (TCT) was proposed for determination of effective electron and hole trapping times in irradiated silicon detectors. Effective carrier trapping times were determined in numerous silicon pad detectors irradiated with neutrons, pions and protons. Studied detectors were fabricated on oxygenated and non-oxygenated silicon wafers with different bulk resistivities. Measured effective carrier trapping times were found to be inversely proportional to fluence and increase with temperature. No dependence on silicon resistivity and oxygen concentration was observed. In terms of charge trapping charged hadrons seem to be more damaging than neutrons. An increase of hole trapping and a decrease of electron trapping was revealed during annealing.

The formation of induced current depends strongly on electric field which is determined by effective dopant concentration. The latter was checked for non-uniformity during the reverse annealing. In high resistivity neutron irradiated detectors no significant deviations from uniform effective doping concentration was observed. The increase of effective dopant concentration with fluence becomes the most important limiting factor for successful operation of heavily irradiated detectors. A significant reduction of effective dopant concentration was achieved by continuous illumination of n^+ detector side with red light. In that way enhanced hole concentration in detector bulk is established causing changes in deep levels' contribution to the space charge. At given temperature and bias voltage illumination intensity can be fine tuned to reach optimal point of operation where effective dopant concentration is zero. In this way heavily irradiated detectors thicker than usual 300 μm can be fully efficient. An attempt was also made to determine the dominant electron and hole trap levels and their generation rates by combining the results of effective dopant concentration measurements in the presence of enhanced carrier concentration and measurements of effective carrier trapping times.

The observation of signals from ^{90}Sr source in the $p^+ - n - n^+$ micro-strip detectors connected to SCT32A read-out chip showed that voltage much higher than full depletion voltage is needed for high charge collection efficiency. This was checked throughout the beneficial and reverse annealing. The most probable signal decreased with time as expected from the measurements of the effective trapping times.

A detailed simulation was employed aiming to predict the influence of effective trapping times on induced charge. The electronic processing of the induced current was also taken into account thus enabling the simulation of strip detectors connected to read-out chip. A good agreement between measured and simulated data was found. A number of other results were obtained, among which the most interesting ones are: prediction of ballistic deficit importance, comparison of strip detectors

with p^+ and n^+ strips, detector thickness optimization and prediction of induced charge appearance on neighboring strips.

Finally, appearance of bistable damage upon applying the bias to an irradiated detector was confirmed by TCT measurements. The results are in agreement with those previously measured with the C/V technique.

Keywords:
silicon strip detectors, charge collection efficiency, effective trapping times, continuous carrier injection, detector simulation, bistable damage, TCT, LHC, ATLAS

PACS:
85.30.De; Semiconductor-device characterization, design, and modeling
85.30.Kk; Junction diodes
29.40.Wk; Solid-state detectors
29.40.Gx; Tracking and position-sensitive detectors

Contents

1

Introduction

As the collider experiments in high energy physics go towards higher energies use of silicon detectors becomes inevitable. Their superior spatial resolution, short signal formation times and good energy resolution make them ideal for tracking ionizing particles. Besides the ability to accurately measure momenta of energetic charged particles from bending of their trajectories in magnetic field their most important feature is the capability of distinguishing secondary from primary vertices. A secondary vertex arises from the decay of a short-lived particle created in the primary interaction of the colliding beam particles.

Physics interest in the future will be largely directed to the observation of short lived particles. For example the particles containing charm, bottom and top quarks as well as tau leptons have lifetimes of around 1 ps. Even at velocity close to the speed of light they can travel only a few millimeters before decaying. Silicon detectors are usually positioned a few cm to a few tens centimeters away from the interaction point. It turns out that the spatial resolution of silicon detectors needs to be of the order of a few tens microns to unambiguously isolate secondary or even the tertiary vertices. Modern techniques of semiconductor processing allow production of complex structures on a micron scale which are needed to reach the desired spatial resolution.

In the pursuit of questions about the validity of the Standard Model and possible discovery of new physics the Large Hadron Collider (LHC) [LHCDR] will be put into operation in 2006 at the European Laboratory for Particle Physics (CERN) (Fig. 1.1). It will provide proton-proton interactions at 14 TeV with high luminosity (10^{33} cm^{-2} s^{-1} during low and 10^{34} cm^{-2} s^{-1} during high luminosity running) needed to observe rarely produced particles. Among them is Higgs bozon, hypothesized to endow matter with mass. The ability to search for the Higgs bozon over a wide mass range is used as the prime criterion in designing the detectors. However there are also other interesting processes (supersymmetry, B-physics) that will be accessible at LHC and also determine the basic design features of the detector. A typical LHC detector [ATLTP, CMSTP] should have, besides the already mentioned tracking and vertexing system, a high resolution electromagnetic calorimeter, a hadron calorimeter and stand-alone precision muon momentum measurements.

This work was done in the framework of the ATLAS collaboration, which is building

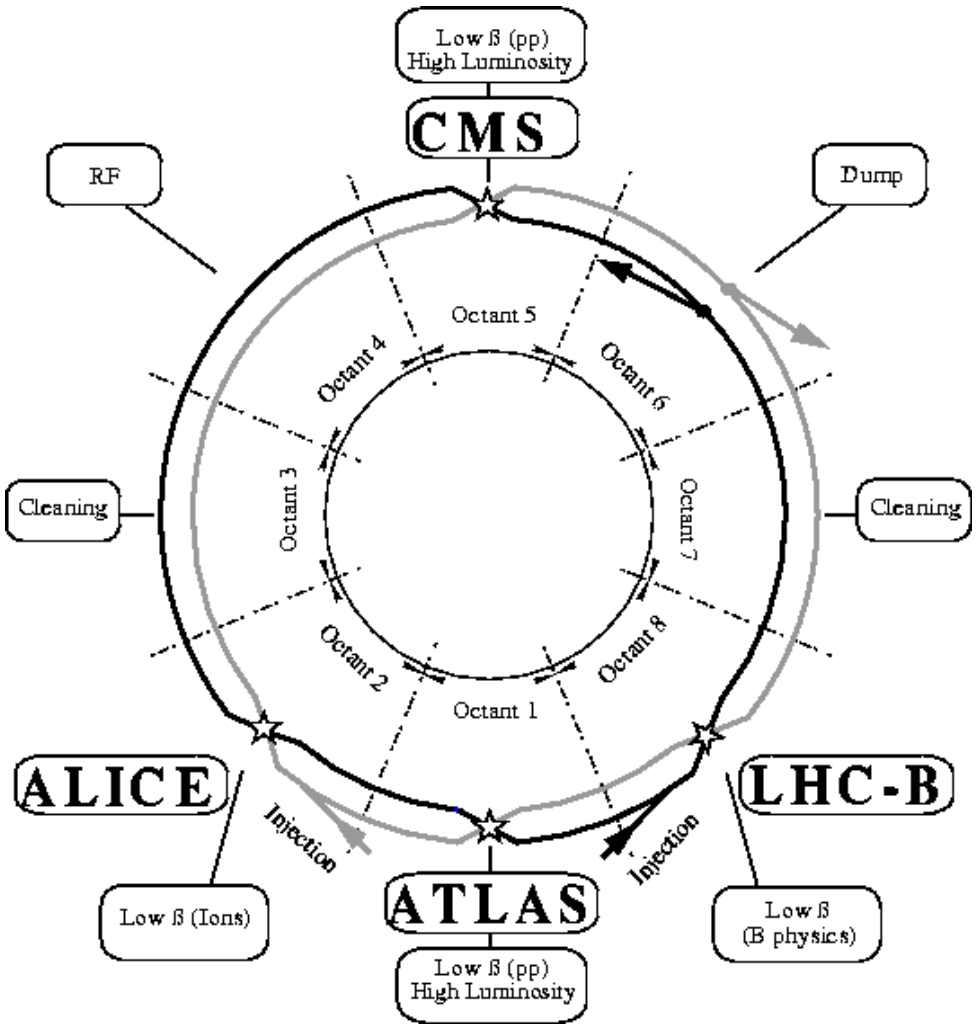

Figure 1.1 : Schematic layout of the LHC.

one of the large experiments at LHC. The overall design of the detector is given in [ATLTP] (see Fig. 1.2) and will not be discussed here. However, a brief description of the inner detector [ATLID] aimed for tracking will be given.

A superconducting solenoid is contained within a cylinder of 6.8 m length and 1.15 m radius supplying a magnetic field of 2 T. The inner detector provides pattern recognition, momentum and vertex measurements and electron identification. It consists of three parts (Fig. 1.3). The outer part of the tracking volume contains the Transition Radiation Tracker (TRT), consisting of straw-tube tracking detectors with transition radiation detection capability. The middle part (SCT - Semi-Conductor Tracker) consists of high-resolution single sided $p^+ - n - n^+$ silicon strip detectors. 768 strips are implanted on a 280-300 μm thick silicon layer at a distance of 80 μm (4 inch process $\rightarrow\approx 6\times 6$ cm^2). Two of such elements are bonded together giving an overall active area of around 12 cm times

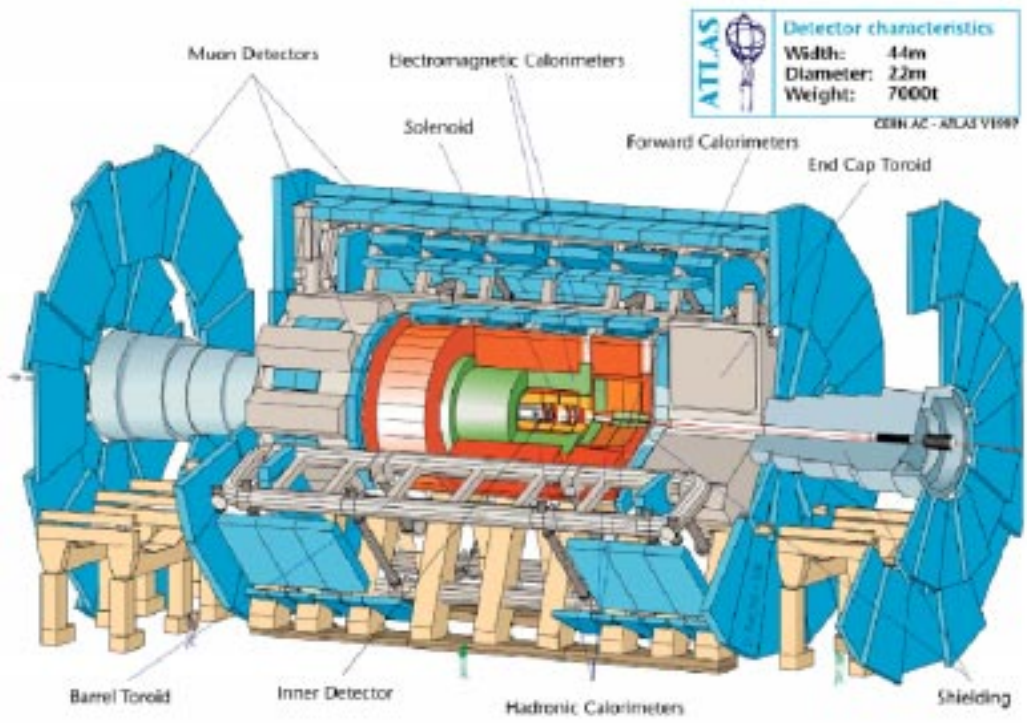

Figure 1.2 : Schematic layout of the ATLAS detector.

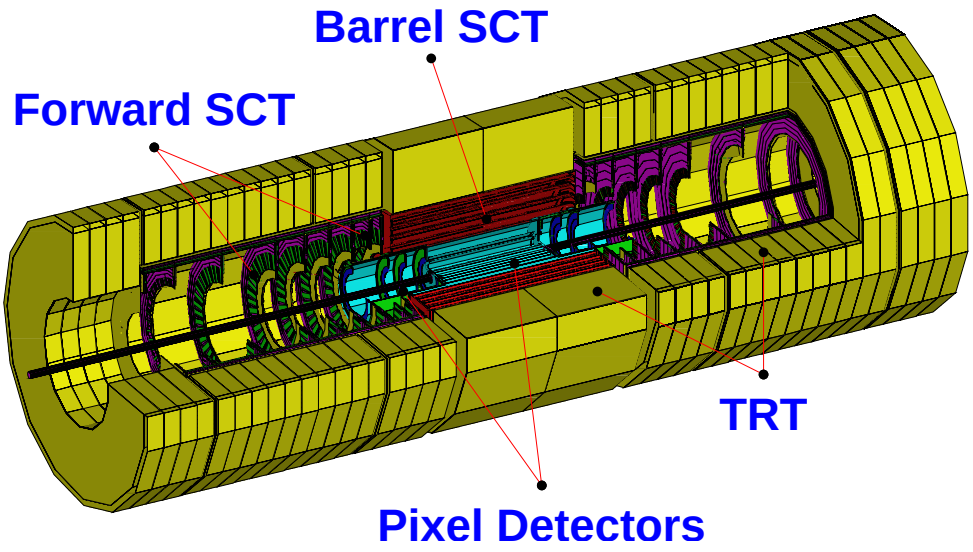

Figure 1.3 : Schematic layout of the ATLAS Inner detector (ID).

6 cm. Since strips provide only information on the coordinate perpendicular to them two detectors are glued back-to-back under a small stereo-angle of 40 mrad thus providing the second coordinate. Such structure together with read-out electronics results in a module.

All together 4088 modules [ATLID] will be arranged in four concentric cylinders around the beam axis (Barrel SCT) and nine disks on each side (Forward SCT). Disks, used to cover the forward directions, are perpendicular to the beam axis. The Semi-Conductor Tracker covers radii from 30 to 52 cm and extends up to 2.7 m along the beam pipe.

Even finer subdivision is needed to avoid ambiguities due to several simultaneous hits of the same position sensitive element. Therefore the innermost part of the inner detector consists of pixel detectors, where the silicon layer is subdivided into small pixels of size 50μm times 400 μm. The two-dimensional segmentation gives unambiguous space points. Pixel detectors are arranged in three barrels at radii of 4, 11 and 14 cm, and four disks between radii of 11 and 20 cm on each side.

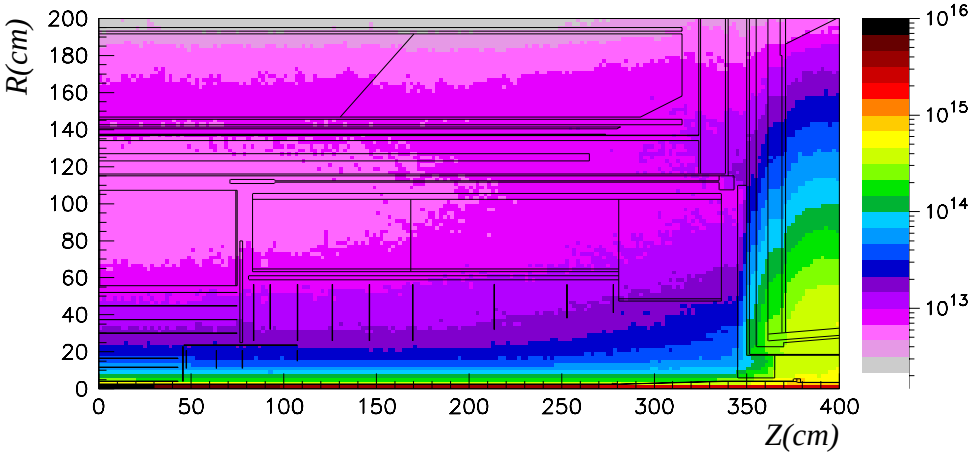

Figure 1.4 : Flux in inner detector cavity in units of 1 MeV equivalent neutrons per cm^2 per year [ATLID].

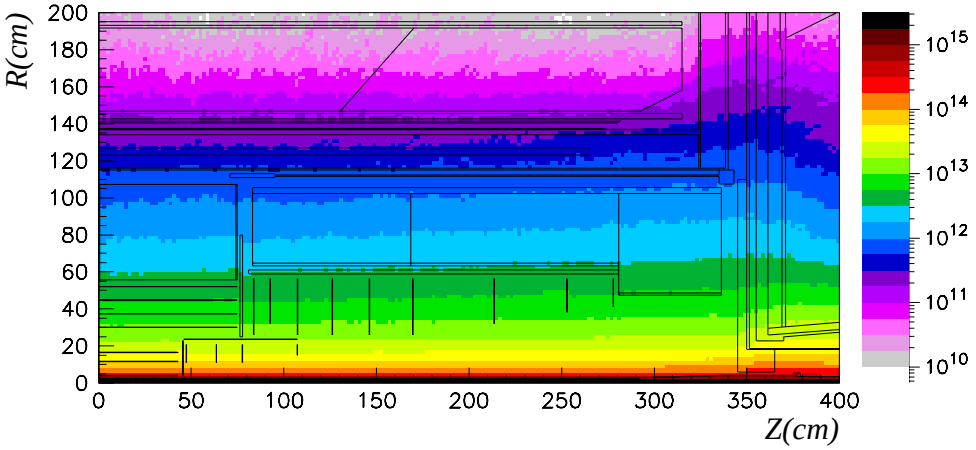

Figure 1.5 : Flux of charged hadrons in the inner detector cavity per cm^2 per year [ATLID].

High luminosity and high interaction energy at the LHC will result in extremely high

interaction rates. At maximum luminosity about 30 primary interactions will occur in every bunch crossing (each 25 ns) producing several hundred secondary particles. This will result in significant radiation damage of the inner detector, especially of the layers at small radii. Results of simulation of particle fluxes and estimated consequent damage of silicon are presented in [ATLID] and [Tay93] . Radiation doses at SCT radii are calculated to be around $1.5 \cdot 10^{13}$ equivalent 1 MeV neutrons per cm^2 per year and 4 kGy/year[1] (Fig. 1.4, 1.5). Up to an order of magnitude higher doses are expected for the innermost layers of pixel detectors.

A careful study of radiation damage of silicon detectors is thus necessary to enable a proper design and operation scenario that will provide operation of the semiconductor tracker over 10 years of data-taking. A considerable effort of many groups has been already directed to this field.

Radiation damage can be divided in damage of silicon bulk and in surface damage. The latter is related with the accumulated fixed positive charge in oxide [Gos99, Bec00]. As a consequence the conductivity of the surface is increased thus giving rise to the surface currents. An important effect is also an increase of the interstrip capacitance, which reflects itself in higher noise. Fortunately, the surface damage seems to be manageable. It depends on detector design and manufacturing, which have been studied and understood.

In the recent years extensive studies has been made to understand bulk damage [ROSE3, Lin00]. A lot of results were taken into account in detector design and operational parameters. The irradiation particle knocks off the silicon atom which can knock off more atoms thus locally destroying the lattice's periodic structure. A dislocated atom is called an interstitial atom, whereas the empty lattice site is called vacancy. Interstitials and vacancies form defect complexes which can establish energy levels (traps) in the band gap. These complexes can contain impurity atoms e.g. carbon and oxygen.

The bulk damage influences detector operation in three main ways:

- At operation temperatures of LHC detectors the n type silicon bulk undergoes type inversion and becomes effectively p type under bias. Further irradiation increases the effective negative dopant concentration and by that the operation voltage.

- The increase of the leakage current results in increased noise and contributes to higher power consumption and therefore heat.

- The silicon detector becomes less efficient. A part of the drifting charge is trapped and thus does not contribute to the signal.

Macroscopic consequences of increased negative space charge and leakage current were studied in great detail. Oxygen rich material was found to be more radiation hard for charged hadrons in terms of effective dopant concentration [ROSE3], while the leakage current exhibits universal behavior in all materials [MollT]. However, few studies were made to predict and quantify charge trapping and signal formation.

[1]Numbers given are the typical values. Maximal values are estimated to $2 \cdot 10^{13}$ cm^{-2}/year of 1 MeV neutrons equivalent and 10 kGy/year [ATLID].

The purpose of this work is to look into radiation induced effects on the charged particle signal. It covers both silicon microstrip detectors connected to the LHC type read-out electronics as well as the simple pad detectors investigated with the transient current technique. Different particles, pions, protons and neutrons were used in order to investigate the damage of charged and neutral hadrons. These measurements served as input for simulation aiming to predict and understand the detector operation as well as to optimize the operational parameters.

In the next chapter the basics of the detector operation along with theory of signal formation are presented. A simple microscopic view of the defects and their influence on detector performance, as currently understood, is described next. In the third part a summary of irradiation facilities and experimental techniques is given. After that results of measurements using transient current technique are presented. They are followed by the chapter dealing with the measurements of charge collection in silicon microstrip detectors. In the sixth part the results of preceding two chapters are used as input to the simulation of silicon pad and microstrip detectors. The bistable damage observation with transient current technique is discussed after that. Finally, the Slovene summary is given after conclusions.

2

Operation of position sensitive silicon Detectors

2.1 Principles of operation

A silicon position-sensitive detector is an array of diodes fabricated on a silicon wafer. When reverse biased, it is operating like an ionization chamber. Ionizing particles passing through silicon generate electron-hole pairs along their path. The number of pairs is proportional to the particle's energy loss. The creation of an electron-hole pair in silicon requires a mean energy of 3.6 eV with the average energy loss in silicon of about 390 eV/μm for a minimum-ionizing particle. This gives rise to 108 μm pairs per μm.

The low electron-hole pair creation energy and fast charge collection times (drift velocities $v_{dr_{e,h}}$ of order of 10^7 cm/s) make them the ideal choice for tracking in a high interaction rate environment. For a typical detector thickness of about $D = 300$ μm, on average $\overline{Q}_{mip} = 3.25 \cdot 10^4$ electron-hole pairs are obtained, a signal detectable with low-noise electronics.

The general equation

$$np = n_i^2 = N_C\, N_V e^{-\frac{E_g}{k_B T}} \tag{2.1}$$

gives in the intrinsic case ($n = p = n_i$) the density of free carriers in pure silicon in thermal equilibrium. Here n and p are concentrations of free electrons and holes. N_C and N_V are effective densities of states in the conduction and valence band, respectively, given by

$$N_{C,V} = 2\left(\frac{2\pi m^*_{e,h} k_B T}{h^2}\right)^{\frac{3}{2}} \quad . \tag{2.2}$$

E_g=1.12 eV is the band gap at room temperature [2], k_B the Boltzmann constant, h the Planck constant, T the temperature and $m^*_{e,h}$ are the effective masses of electrons and holes (see Appendix F). At room temperature $N_{C,V}$ is around 10^{19} cm^{-3} and n_i around 10^{10} cm^{-3}. The resistivity of the silicon bulk is given by [PoSCD]

$$\rho = \frac{1}{e_0\ (\mu_{lf_e}\ n + \mu_{lf_h}\ p)} \quad , \tag{2.3}$$

[2] The band gap depends on temperature as $E_g(T) = 1.170$ eV $- 4.73 \cdot 10^{-4} \frac{\text{eV}}{\text{K}}\ T^2/(T + 636\ \text{K})$ [Thu75].

where $\mu_{lf_e} = 1430$ cm^2/Vs and $\mu_{lf_h} = 460$ cm^2/Vs are the mobilities of electrons and holes in the low electric field, while e_0 is the unit charge. A 300 μm thick intrinsic silicon with a surface of 1 cm^2 has the resistance of 10 kΩ, which results in current around mA at applied voltage U of few ten volts. The fluctuations of this current are large compared to the current of few tens of nA expected ($\frac{\overline{Q}_{mip}\,\mu_{lf}\,U}{D^2}$) from the drift of the charge generated by a minimum ionizing particle.

In a reversely biased diode, on the other hand, free carriers are swept out by the electric field leaving a space charge region (SCR) depleted of free carriers and by that of much higher resistance [3]. Thus to obtain an acceptable signal/noise ratio the active volume has to be depleted.

2.1.1 $p-n$ junction

The number of free electrons and holes in silicon can be changed significantly by doping it with donors or acceptors. In general replacing some of the Si atoms in the lattice with donors or acceptors results in energy levels close to the valence or conduction band edges, the so-called shallow levels. Shallow donors are usually atoms that have in addition to the four electrons, needed for the covalent bond, one electron they can donate to the conduction band. In that case the remaining donor atom becomes positively charged. Acceptors have one electron missing to form bonding to all neighbors. So to complete the missing bond they accept an electron from the valence band, leaving a hole there. An electron capture thus changes the acceptor state from neutral to negatively charged.

If only donor levels close to the conduction band and acceptor levels close to the valence band are considered (shallow levels), energies needed for those transitions are comparable to k_BT at room temperature and almost all dopants are ionized. Thus at high enough excess concentration of dopants of certain type, the number of electrons in the conduction band equals the number of donors or the number of holes in the valence band equals the number of acceptors. The relation $n_i^2 = n\,p$ still holds as in pure silicon, while $n = p = n_i$ is no longer valid. If the concentration of donors N_D exceeds the concentration of acceptors N_A (i.e. $n > p$) the material is called n-type with electrons as majority carriers. If vice versa $N_A > N_D$ ($p > n$) the material is called p-type and majority carriers are holes. Standard doping elements are phosphorus and boron as a donor and an acceptor, respectively, with energy levels $\Delta E_C(P)$=0.044 eV [4] and $\Delta E_V(B)$=0.046 eV [5].

When the dopant concentration changes from a surplus of acceptors N_A on the p-side to a surplus of donors N_D on the n-side the p-n junction is obtained (Fig. 2.1). The gradient of electron and hole densities results in a diffusive migration of majority carriers across the junction, where they recombine. Charge migration leaves the p region with a net negative charge and the n region with a net positive charge due to unneutralized,

[3] In fact a small but permanent carrier generation due to emission and capture processes still remains in the SCR region as will be described later.

[4] Energy gap from the phosphorus energy level to the bottom of the conduction band.

[5] Energy gap from the top of the valence band to the boron level.

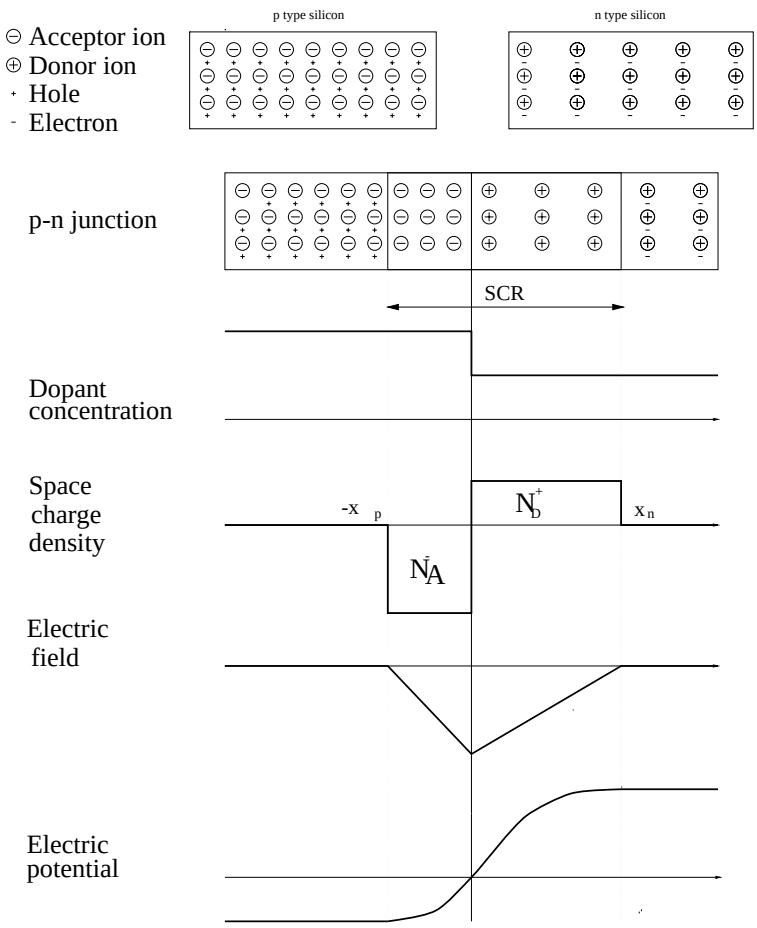

Figure 2.1 : The p-n junction: dopant concentration, space charge density, electric field strength and electric potential.

acceptor and donor ions. They form the space charge (SCR) or the depletion region. The immobile ions in the space charge region cause the electric field opposing the migration and thus an equilibrium is obtained in the system.

The electric properties of the junction can be calculated from the Poisson equation

$$-\frac{d^2V}{dx^2} = \frac{\rho_e(x)}{\epsilon_{Si}\epsilon_0} \ . \tag{2.4}$$

Assuming an abrupt junction and absence of free carriers in the depleted region

$$\rho_e(x) = \begin{cases} e_0\, N_D \ , & x_n > x > 0 \\ -e_0\, N_A \ , & -x_p < x < 0 \end{cases} \tag{2.5}$$

one obtains solutions for the electric field and electric potential as shown in Fig. 2.1. The potential difference over the SCR with no external bias applied is called the built-in

potential V_{bi}

$$V_{bi} = \frac{e_0}{2\epsilon_{Si}\epsilon_0}(N_D x_n^2 + N_A x_p^2) \ . \tag{2.6}$$

From the condition of electrical neutrality of the system it follows that the total positive and negative charge in the SCR have to be equal. It gives

$$N_A \, x_p \ = \ N_D \, x_n \, , \tag{2.7}$$

showing that the depth of depleted region $x_{n,p}$ (see Fig. 2.1) on each side of the junction is inversely proportional to the doping concentration.

For tracking detectors doping of one side (usually the p side) is much higher than of the other ($N_A \gg N_D$). In that case the depth of the depleted region on the p^+ [6] side is small compared to the depth on the weakly doped n side and the full depth of the depleted region w can be approximated with the depth on the weakly doped side ($w \approx x_n$). In that case one obtains

$$w = \sqrt{\frac{2\epsilon_{Si}\epsilon_0 V_{bi}}{e_0 \, N_D}}. \tag{2.8}$$

Using [PoSCD]

$$V_{bi} = \frac{1}{e_0}\left[E_g - k_B T \ln(\frac{N_C \, N_V}{N_D \, N_A})\right] \tag{2.9}$$

one obtains V_{bi} of about 0.5-1 V. The width of the depletion layer of an unbiased junction for detector bulk made of n-type silicon with $N_D < 10^{12}$ cm^{-3} can be estimated to a few 10 μm.

Influence of External Voltage

The $e - h$ pairs created in the depletion region by a traversing particle are separated by the electric field, collected and read out. The minority carriers created in the neutral, non-depleted region recombine with majority carriers and are not detected unless they enter the depleted region by diffusion [7].

Increasing the depth of the space charge region thus increases the collected signal. This can be achieved by applying an external voltage U with the same polarity as the built in potential. In that case V_{bi} in Eq. 2.8 is replaced by $V_{bi}+U$. Since usually $U \gg V_{bi}$, V_{bi} can be omitted and one obtains

$$w(U) \ = \sqrt{\frac{2\epsilon_{Si}\epsilon_0}{e_0 \, N_D} \, U} \ . \tag{2.10}$$

[6] Plus over p denotes high doping concentration, typically more than 10^{18} cm^{-3}.

[7] Hole recombination time in n-type silicon of few kΩ resistivity is around few hundreds of μs.

The voltage necessary to deplete the full thickness of the detector (D), called the full depletion voltage (V_{FD}), is given by

$$V_{FD} = \frac{e_0 N_D D^2}{2\epsilon_{Si}\epsilon_0}. \tag{2.11}$$

It can be seen that V_{FD} depends quadratically on detector thickness. For a typical 300 μm thick detector, a useful numerical relation can be used: $V_{FD} = 6.95 \cdot 10^{-11}\,\mathrm{Vcm}^3 \cdot N_D$.

Silicon material that is usually used for the low doped n side of silicon tracking detectors, is obtained by donor compensation[8]. This means that donor and acceptor concentrations are of the same order of magnitude, and N_D has to be replaced by the difference of the ionized donor and acceptor concentrations, hereafter referred as the effective doping concentration N_{eff}

$$N_D \to N_{eff} = |N_D - N_A| \ . \tag{2.12}$$

The Eqs. 2.10 and 2.11 are also valid in the presence of deep levels with N_D replaced by N_{eff}.

The effective dopant concentration N_{eff} is very often related to the ohmic resistivity of the silicon material. This can however lead to a confusion in case of substantial concentration of deep donor or acceptor levels. For silicon with only fully ionized shallow dopants, the following relation holds $n(p) \approx N_{eff}$ with $p(n) \ll n(p)$ and Eq. 2.3 can be simplified to

$$\rho = \frac{1}{e_0 \mu_{e(,h)} N_{eff}} \ , \tag{2.13}$$

which relates the ohmic resistivity of the material with the effective dopant concentration in the fully depleted region. This relation is valid only in absence of deep levels.

Capacitance of the $p-n$ junction

The capacitance of a depletion layer at a given voltage can be defined as

$$C(U_0) = \frac{dQ}{dU}|_{U=U_0} \ . \tag{2.14}$$

In the case of abrupt junction it is given by

$$C(U) = \frac{\epsilon_{Si}\epsilon_0 S}{w} = \sqrt{\frac{\epsilon_{Si}\epsilon_0 e_0 N_{eff}}{2U}} S \tag{2.15}$$

where $Q = e_0 N_{eff} S w$ (S is the sample area) was used together with Eq. 2.10. It shows that for N_{eff} constant over the detector thickness, the graph of $1/C^2(U)$ versus U is a straight line for reverse voltages below the full depletion voltage

$$\frac{d(1/C^2(U))}{dU} = \frac{2}{e_0 \epsilon_{Si}\epsilon_0 N_{eff} S^2} \ , \tag{2.16}$$

[8]Neutron transmutation doping is usually used to obtain high resistivity n-type material [PoSCD, Pei92].

and a constant value for higher voltages. The position of the kink determines V_{FD} and the slope determines N_{eff}.

2.1.2 Structured detectors - Position sensitive

As mentioned a position sensitive detector is in principle an array of $p-n$ junctions produced on a wafer using the the planar technology proposed in 1980 by Kemmer [Kem80, Kem84][9]. Usually the p^+ implant is segmented. The segmentation of the p^+ side determines how the position is read-out[10].

Silicon strip detectors

Silicon micro-strip detectors are produced by division of the p^+ side into strips usually few tens to few hundreds μm apart (Fig 2.2). The segmented side is usually covered by few μm layer of SiO_2 and sometimes also by Si_3N_4. The oxide and nitride layers protect the wafer during fabrication and later the detector itself. Aluminum strips allowing good ohmic contact with electronics can be placed directly on the p^+ strips (DC coupled detectors) or on a thin (> 200 nm) oxide or nitride layer. In the latter case the p^+ strips are capacitively connected to the electronics (AC coupled detectors). The latter solution is more expensive, due to additional steps in production, however high leakage currents are prevented to flow through the electronics. While the strip potential is defined by electronics' in the case of DC coupled detectors, the implant strips need to be grounded separately for the AC coupled detectors. This is done via resistors (from few 10 kΩ to a few 100 MΩ) made from polycrystalinic silicon or via a FET structure (see Appendix A). The latter bias scheme was found to be radiation intolerant and is therefore not used for operation of highly irradiated detectors [Azz96, Ham98]. In this study only polysilicon-biased detectors were used. Silicon microstrip detectors usually have a guard ring (or a more complex structure of guard rings) at the edges which acts as a sink for the surface currents from the edge of the detector.

The rear side (called also back side) of the detector has a layer of n^+ silicon to enable the ohmic contact with aluminated back side. The segmentation of the n^+ layer into strips under some angle with respect to strips on the p^+ side can be used for the second coordinate determination. The surface is in this case also pasivated with oxide. Accumulation of positive charge in the oxide requires additional structures to isolate the strips on the n^+ side. Otherwise the accomulation layer forms a conductive channel between strips and effectively short-cut them. Therefore a strip of p^+ silicon (p-stop) is inserted between two n^+ strips [Kem88, Hol89] or the so called p-spray layer of low doped p type silicon is used [Rih96] [11]. Manufacturing process, however, requires more steps which increase the cost of such detectors to a costs comparable to a production of two single sided detectors

[9] Brief explanation of the production steps can be also found in [SchuT, Pei92].

[10] In some devices, however inappropriate for the use at LHC, a coordinate can also be determined from the drift time of generated electron-hole pairs.

[11] Special field plates over the oxide can also be used to repel electrons [Hol89].

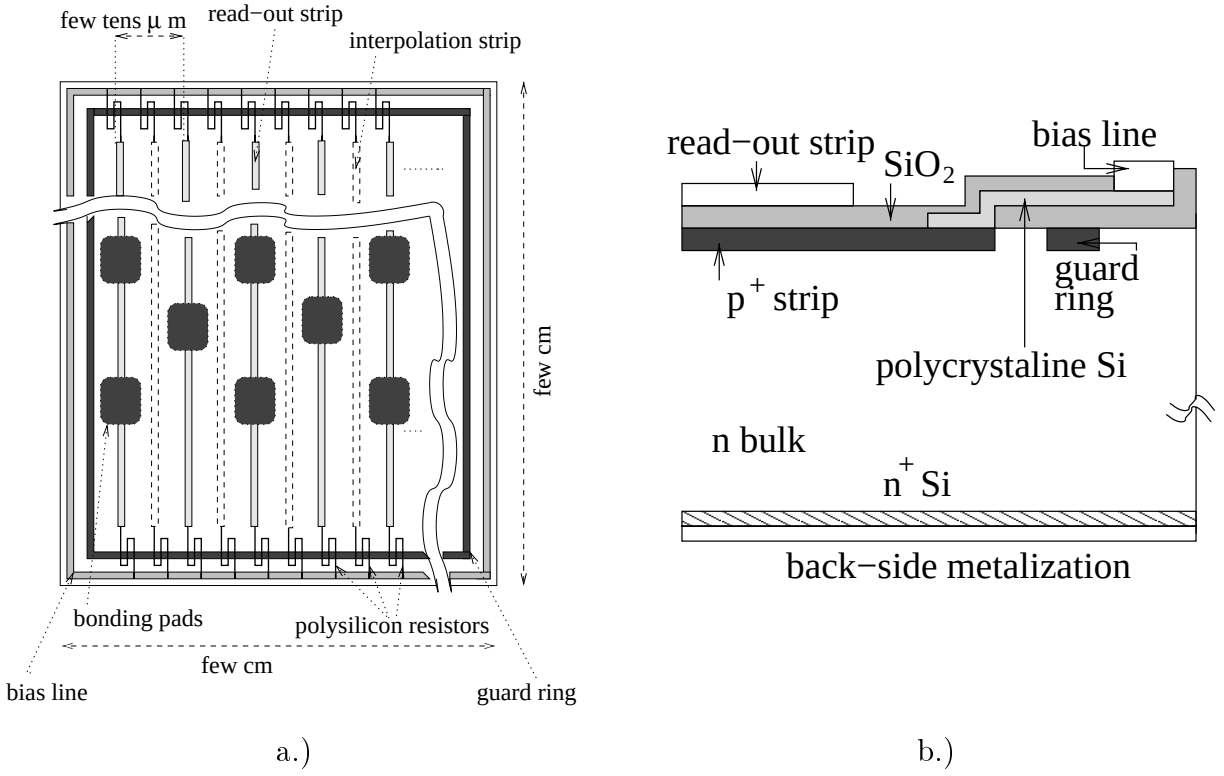

Figure 2.2 : Schematic a.) top view and b.) side view of a polysilicon biased strip detector.

glued back-to-back. Another problem with double sided detectors is the operation of the electronics at a high electric potential.

Silicon pixel detector

If the p^+ side is segmented in the pixels, coordinates of the hit are unambiguously determined by the pixel position. The size of pixels usually ranges from few tens μm $\times$ few tens μm to a few mm $\times$ few mm. The number of pixels and by that the number of read-out channels increases linearly with the active area of detector, while for the silicon strip detector the number of channels increases with the square root of the active detector area. The result is high cost of pixel detectors and electronics. Particularly expensive is connection of detectors to the electronics [12], especially when pixel dimensions are small. The use of pixel detectors, however, becomes inevitable if the detector is hit many times in one read-out cycle. The use strip detectors is in that case impossible due to ambiguities in determination of hit positions. As a results of that and also because of high resolution pixel detectors they are most often used very close to the interaction point.

[12]Most often a bump bonding technique is used.

2.1.3 Silicon pad detectors

A silicon pad detector is a simple planar diode (Fig. 2.3). Typical dimensions of around

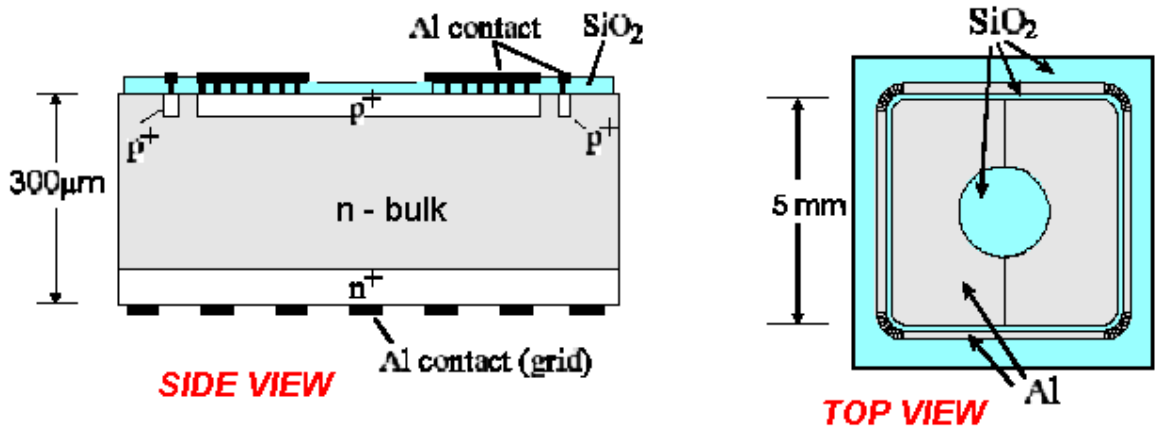

Figure 2.3 : Schematic view of a diode used in the study.

1 cm^2, simple geometry, availability and low cost of the diodes make them very suitable for studies of radiation damage. Therefore the bulk of the measurements in this work was done using diodes - pad detectors. Diodes are usually DC coupled with one or two guard rings. The pad detectors used in this thesis were designed for TCT measurements (see Section 4.3). Therefore a hole ($\phi = 2$ mm) in the metalization on the p^+ side of the diode was used for light injection, while on the n^+ side a mesh metalization was provided for the same purpose.

Although a silicon pad detector can be considered as a pixel detector with only one pixel, in general the operation of a multi-electrode pixel detector and a single electrode pad-detector are different (see section 2.2 for explanation). If, however, pixel dimensions are large (pixel size $\gg$ detector thickness) each pixel can be considered as a planar diode in terms of operation.

2.2 Signal formation in silicon detectors

The drift of mobile charges created in the electric field by a traversing ionizing particle induces a current pulse on the attached electrodes if they are connected to low impedance. The calculation of the induced current formation is in general far from trivial, particularly in a multi electrode system with electrodes connected to arbitrary impedances.

The derivation of the induced current is based on the Reciprocity theorem (see Appendix B) of the induced charge. This theorem defines the relation of potential and charges on a multi-electrode system for two states before and after one or more potentials and charges are changed

$$\sum_{electrodes} \dot{Q_n} V_n = \sum_{electrodes} Q_n \dot{V_n} \quad , \tag{2.17}$$

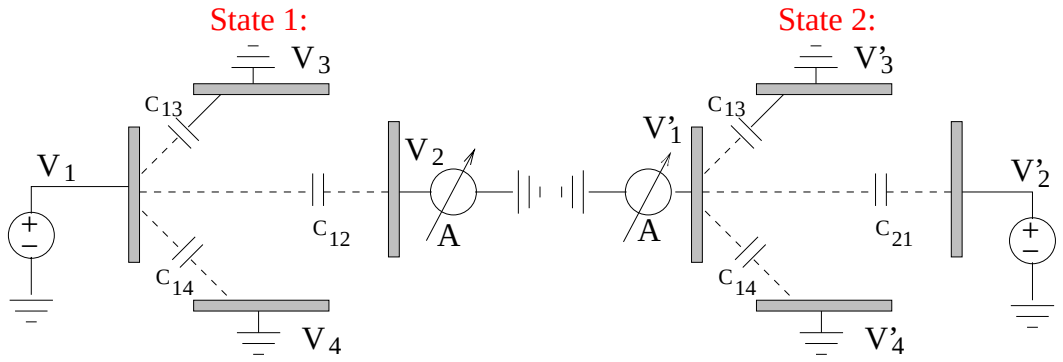

a.)

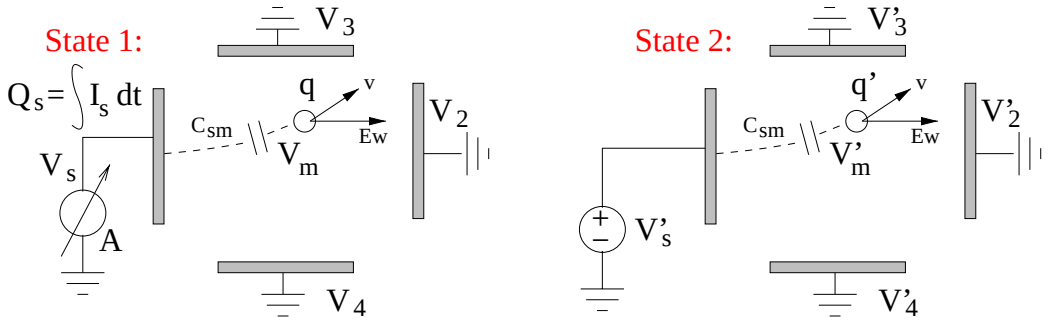

b.)

Figure 2.4 : a.) An example of application of the reciprocity theorem used to show that electrostatic coupling is independent of the direction of charge displacement $C_{12} = C_{21}$. b.) The states considered in the derivation of induced current due to motion of the charge q. The ground sign denotes the low impedance connection (amplifier).

where V_n, Q_n denote the potential of the electrode and its charge before, and $\grave{V}_n, \grave{Q}_n$ after the change of state.

Lets imagine only two electrodes in the system, with all others at fixed potential $V_n = \grave{V}_n = 0$, and consider two states (Fig. 2.4a):

- in the first state an external voltage V_1 is applied to the first electrode and the charge Q_2 is induced on the second electrode: $Q_1\,,\ V_1 \neq 0, \quad , \quad Q_2\,,\ V_2 = 0$

- in the second state an external voltage $\grave{V}_2$ is applied to the second electrode and the charge $\grave{Q}_1$ is induced on the first electrode: $\grave{Q}_1\,,\ \grave{V}_1 = 0 \quad , \quad \grave{Q}_2\,,\ \grave{V}_2 \neq 0$

If follows from Eq. 2.17 that

$$V_1 \grave{Q}_1 = \grave{V}_1 Q_2 \quad \Longrightarrow \quad C_{12} = C_{21} = \left(\frac{Q_2}{V_1}\right)_{V_{2,3,4}=0} = \left(\frac{Q_1'}{V_2'}\right)_{V_{1,3,4}=0} \quad . \tag{2.18}$$

The reciprocity theorem in this case describes the simple fact that the mutual capacitance C_{nk} between any two electrodes n, k is independent of the direction in which it is measured.

A drifting charge q can also be seen as a small electrode at point m (see Fig. 2.4b). In the actual state of concern in operation of a detector, with all the electrodes except the fictitious electrode m connected to low impedance $V_{n\neq m} = 0$, the charge q induces charge on sensing electrode Q_s which is at fixed $V_s = 0$.

Relation (Eq. 2.17) can be applied between the actual state and another, electrostatically also possible state, where the electrode potential $\grave{V}_s \neq 0$ results in the potential $\grave{V}_m$ at the charge's location and no charge ($\grave{q}_m = 0$) is present there, thus

$$\begin{aligned} q\grave{V}_m + Q_s\grave{V}_s &= \grave{q}V_m + \grave{Q}_s V_s \\ Q_s\grave{V}_s + q\,\grave{V}_m &= 0 \quad . \end{aligned} \tag{2.19}$$

The induced current I_s flowing in the sensing electrode is then calculated as

$$I_s = \frac{dQ_s}{dt} = -\frac{d(q\,\frac{\grave{V}_m}{\grave{V}_s})}{dt} \quad , \quad \frac{\grave{V}_m}{\grave{V}_s} = U_w \tag{2.20}$$

$$I_s = -\,q\frac{dU_w}{dt} = -q\,\frac{dU_w}{dt}\frac{d\vec{r}}{d\vec{r}} = -\,q\,\frac{dU_w}{d\vec{r}}\frac{d\vec{r}}{dt} \tag{2.21}$$

$$I_s = -\;q\;\nabla U_w \cdot \vec{v}_{dr} \quad , \tag{2.22}$$

where $d\vec{r}$ is the direction of the drift in the electric field (see Fig. 2.4) and $\vec{v}_{dr}$ the drift velocity of the charge q in the electric field. As the charge q moves it sees different U_w with time.

The gradient of the weighting potential $-\nabla U_w$ which it required for evaluation of Eq. 2.22 and is commonly called the weighting field $\vec{E}_w$, is a measure of electrostatic coupling between point m and the sensing electrode s. U_w is obtained by solving the Laplace equation with the boundary conditions following from its definition:

- $U_w = \grave{V}_m/\grave{V}_s = 1$: at the surface of the sensing electrode (electrodes m and s are connected).
- $U_w = \grave{V}_m/\grave{V}_s = 0$: at the surface of any other electrode n connected to low impedance (electrodes m and n are connected).

Since the weighting field is a measure of electrostatic coupling, it is calculated as if there were a vacuum between electrodes. Dielectric properties of the material between electrodes or even the presence of fixed space charge, as in the case of the reversely biased $p-n$ junction, do not enter in the calculation. It can be concluded that the weighting

field depends only on geometry of the electrodes. It is, in general, quite different from the real electric field.

If all electrodes of the detector are connected to low impedance, the induced current flowing in the sense electrode is usually written [13] in the form

$$I_s(t) \;=\; q\,\vec{E}_w(\vec{r}(t))\,\vec{v}_{dr}(\vec{r}(t)) \quad , \tag{2.23}$$

where $\vec{r}(t)$ denotes the drifting charge trajectory. The later is a solution of the equation of motion in the electric field $\vec{E}(\vec{r})$

$$\frac{d\vec{r}}{dt} \;=\; \mu\,\vec{E}(\vec{r}) \quad . \tag{2.24}$$

The mobility μ depends on the electric field strength, temperature and effective doping concentration. Its parameterization is given in Appendix C and will be extensively used in simulation of silicon detector operation.

2.2.1 Trapping of the drifting charge

The drifting charge q is composed of N elementary charges e_0, either electrons or holes. A part of carriers can be trapped during the drift. At this point it is not important how these traps appear in the silicon nor with what defects in the lattice they are related. Once the carrier gets trapped its drift velocity drops to zero, hence according to Eq. 2.23 it does not contribute to the induced current anymore. In this way trapping can be regarded as a loss of drifting carriers.

The probability of a charge carrier to find a trap centre and get trapped is proportional to its traversed path length. The number of trapped carriers after traveling a distance dl is

$$dN \;=\; -\,N\,\frac{1}{\lambda_{eff_{e,h}}}\,dl \quad , \tag{2.25}$$

where $\lambda_{eff_{e,h}}$ represents the effective carrier trapping distance.

If the carrier thermal velocity is much larger than its drift velocity (Fig. 2.5) the effective trapping distance can be expressed with effective carrier (electrons, holes) trapping time $\tau_{eff_{e,h}}$ as

$$v_{th_{e,h}} \gg v_{dr_{e,h}} \quad \Longrightarrow \quad dl \;=\; v_{th_{e,h}}\,dt \tag{2.26}$$

$$dN \;=\; -\,N\,\frac{1}{\tau_{eff_{e,h}}}\,dt \quad \text{with} \quad \tau_{eff_{e,h}} \;=\; \frac{\lambda_{eff_{e,h}}}{v_{th_{e,h}}}. \tag{2.27}$$

[13] The relation is also known as Ramo's theorem [Ram39]. The weighting field is sometimes referred to as Ramo's field.

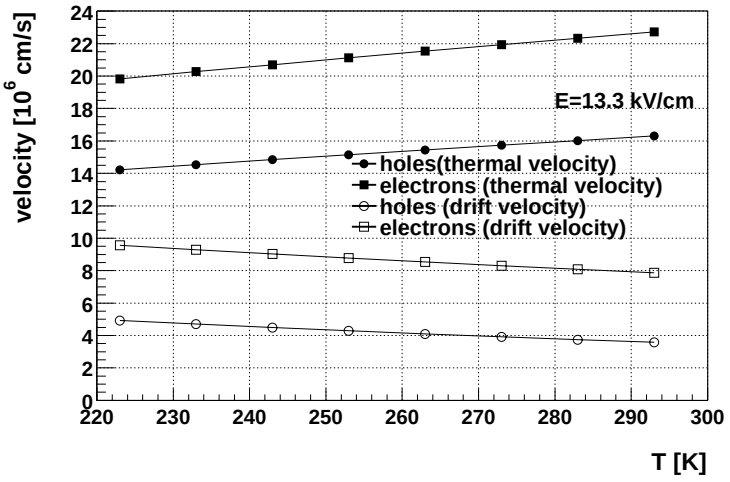

Figure 2.5 : Comparison of thermal and drift velocity in electric field $E = 13.3$ kV/cm (500 V over 300 μm) at different temperatures. The difference between v_{dr} and v_{th} is larger in weaker electric field. The values of thermal velocities and mobility dependence on electric field can be found in Appendixes F,C.

The solution of the Eq. 2.27 is an exponential decrease of the drifting carriers with time[14]

$$N(t) \;=\; N(0)\,\exp(\frac{-t}{\tau_{eff_{e,h}}}) \quad . \tag{2.28}$$

The trapped charge is eventually released and continues drifting in the electric field. If the measurement time is longer than emission times (see Appendix I) charge trapping does not influence the collected charge i.e. the integral of the induced current. Otherwise the trapped charge is lost for the measurement.

2.2.2 Example of signal formation in silicon pad detectors

The induced current resulting from the drift of a point charge in a silicon pad detector can be calculated analytically. Since the diode has only two parallel electrodes with typical lateral dimensions much larger than the detector thickness the weighting field calculation is a one dimensional problem. A constant weighting field $E_w = -1/D$ is obtained. The induced current due to drift of electrons and holes is thus given by

$$I_{e,h}(t) \;=\; -\frac{e_0\,N(t)}{D}\,v_{dr_{e,h}}(t) \quad . \tag{2.29}$$

Solution of Eq. 2.24 requires the knowledge of electric field profile in the detector. The

[14] If $v_{th_{e,h}} \approx v_{dr_{e,h}}$ the effective trapping time depends on the drift velocity, hence on the electric field. In that case $N(l) \;=\; N(l=0)\,\exp(\frac{-l_{e,h}}{\lambda_{eff_{e,h}}})$, with the traveled distance $l_{e,h} = \int |\vec{v}_{dr,e,h} + \vec{v}_{th,e,h}|dt$.

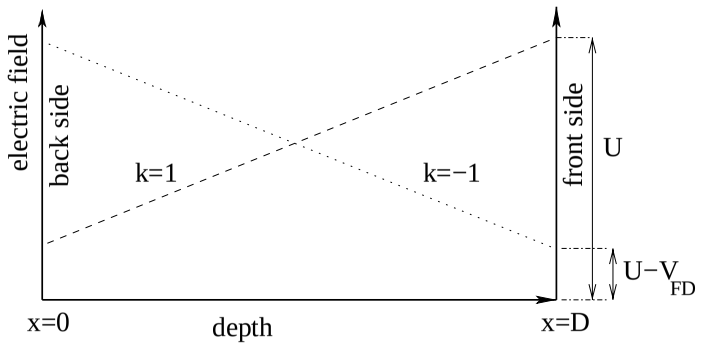

Figure 2.6 : Electric field in a silicon pad detector as assumed for the derivation of the current induced by a point charge drift.

electric field in an overdepleted detector ($U > V_{FD}$) can in most cases be assumed as linear (see Fig. 2.6)

$$E(x) = \frac{1}{D}\,(U - k\,(1 - \frac{2\,x}{D})\,V_{FD}) \quad , \quad U > V_{FD} \quad , \tag{2.30}$$

where k is the sign of the space charge in the depleted region. In the approximation of constant mobility $\mu_{0_{e,h}}$, an analytical solution of is possible. The Eq. 2.24 can be rewritten as

$$\frac{d\,x_{e,h}(t)}{dt} = \mp\mu_{0_{e,h}}\,E(x) \quad . \tag{2.31}$$

Using Eq. 2.30 in Eq. 2.31 the solution of the equation of motion is given by

$$x_{e,h}(t) = \frac{k\,U - V_{FD}}{2\,V_{FD}}\,D\left[\exp(\frac{\mp\,k\,t}{\tau_{e,h}}) - 1\right] + x_0\,\exp(\frac{\mp k\,t}{\tau_{e,h}}) \tag{2.32}$$

$$\tau_{e,h} = \frac{D^2}{2\,V_{FD}\,\mu_{0_{e,h}}} = \frac{\varepsilon\,\varepsilon_0}{e_0\,\mu_{0_{e,h}}\,|N_{eff}|} \quad , \tag{2.33}$$

where x_0 is the starting point of the drift and $\tau_{e,h}$ the transient time of electrons and holes. The drift velocity is then

$$v_{dr_{e,h}}(t) = \mu_{0_{e,h}}\left[\frac{U - k\,V_{FD}}{D} + \frac{2\,k\,x_0\,V_{FD}}{D^2}\right]\,\exp(\frac{\mp\,k\,t}{\tau_{e,h}}) = \mu_{0_{e,h}}\,E(x_0)\,\exp(\frac{\mp\,k\,t}{\tau_{e,h}}) \quad . \tag{2.34}$$

The induced current following from Eqs. 2.28,2.29 and 2.34 can then be calculated as

$$I_{e,h}(t) = \frac{e_0\,N(t=0)}{D}\,\mu_{0_{e,h}}\,E(x_0)\,\exp\left[\frac{\mp\,k\,t}{\tau_{e,h}} - \frac{t}{\tau_{eff_{e,h}}}\right] \quad . \tag{2.35}$$

The constant mobility $\mu_{0_{e,h}}$ should be evaluated at the average electric field in the detector $\mu_{0_{e,h}} = \mu_{e,h}(U/D)$. A linear parameterization of mobility $\mu_{e,h} = \mu_{0_{e,h}} (1 - aE)$ also leads to solvable Eq. 2.31 (see Appendix G), however the precise mobility parameterization is much more complex, therefore a numerical calculation is needed for higher accuracy. Another advantage of the numerical approach is the ability to account for deviations from linear field.

In the case of silicon strip detectors only a numerical solution of Eq. 2.23 is possible. The chapter describing the silicon detector simulation will deal with the induced current in strip detectors and also with the numerical solution of Eq. 2.29 for silicon pad detectors.

2.2.3 Floating Electrodes

The Eq. 2.23 is applicable for pixel and strip detectors if all pixels and strips are connected to read-out electronics with low input impedance. Silicon strip detectors often have every second or even third strip read out [Eng81, Kot85]. The strips between neighboring read-out strips are called interpolation strips. These are capacitively coupled to the read-out strips and hence the electronics.

To describe signal evolution in devices with interpolation strips (or pixels) Eq. 2.23 should be modified. Besides the sum over virtual electrode at the position of the moving charge and the sensing electrode the sum in Eq. 2.17 runs also over all electrodes in the system that are not at fixed potential.

In that way the reciprocity theorem can be applied for the actual state and a set of $n+1$ (n is the number of floating electrodes) electrostatically possible states. A system of equations analogous to Eq. 2.19 can be written in matrix form. The induced current on any electrode can be written in the same form as Eq. 2.22 with weighting field depending also on weighting fields of other electrodes. The weighting field is also time dependent since the current impulse on any electrode reflects as a voltage step on floating electrodes. A derivation of the above mentioned equations can be found in [Gat82].

The resulting weighting field $\vec{E}_{wk}^{\,`}$ of the read-out electrode k in the detector with floating electrodes is given by

$$\vec{E}_{wk}^{\,`}(t) = -\delta(t)\,\vec{E}_{wk} - \sum_{i \neq k} N_{k,i}(t)\vec{E}_{wi} \quad , \tag{2.36}$$

where $\vec{E}_{wk}$ is a weighting field calculated with weighting potential of all electrodes set to 0 except the electrode k and $N_{k,i}(t)$ is the voltage response of electrode i (V_i) to a unit voltage pulse applied at electrode k (V_k). If all electrodes are grounded, all $N_{k,i}$ are zero and Eq. 2.36 reduces to Eq. 2.23. $N_{k,i}$ is different from zero only for floating electrodes i, which are usually connected to the defined potential via a high (several MΩ) resistance. Assuming that inter-electrode resistance is also of the same order of magnitude, in the equivalent circuit they can both be set to infinite, thus only the inter-electrode capacitances are considered. The result of this assumption is a prompt response on the electrode i to the voltage step signal on electrode k with equal signal shapes at both electrodes and different signal amplitudes.

Operationally the weighting field $\vec{E}_{wk}(t)$ for the electrode k which is grounded (connected to a low impedance amplifier) is obtained by calculating the responses at electrodes i to the unit voltage (delta) pulse at the electrode k.

According to the reciprocity theorem $N_{k,i}$ is equal to the fraction of charge induced on electrode k if the charge q_i is placed on the floating electrode i. From here it follows

$$V_i(t) = \frac{q_k}{q_i} V_k \, \delta(t) \quad \Longrightarrow \quad N_{k,i}(t) \; = \; \frac{q_k}{q_i} \, \delta(t) \quad . \tag{2.37}$$

The sum of all fractions $\sum_k \frac{q_k}{q_i}$ must equal 1 [15] to be in agreement with the charge conservation law. The induced current of the read-out electrode k is thus given by

$$I_k(t) \; = q\vec{E}_{wk}\vec{v}(t) + \; q \sum_{i \neq k} N_{k,i}\vec{E}_{wi} \, \vec{v}(t) \tag{2.38}$$

In order to calculate the induced current the coefficients $N_{k,i}$ need to be calculated.

2.2.4 Calculation of charge sharing in silicon strip detectors

In silicon strip detectors the charge fraction q_k/q_i depends on the detector thickness, distance between strips, their width and the number of interpolation strips. In the model used for the calculation [Kot85] strips are replaced with thin parallel wires at the same fixed potential. If the strip width and pitch are small compared to the detector thickness the accuracy of calculated $\frac{q_k}{q_i}$ increases fast with number of wires. The electrostatic calculation is based on assumption that the charge collection time (~ 10 ns) and integration time of the amplifier (≤ 100 ns) are short compared to time constant of charge flow from the interpolation strip. The input capacitance of the charge sensitive preamplifier (~ 100 pF) is required to be much larger than the inter-strip capacitance (~ 1 pF).

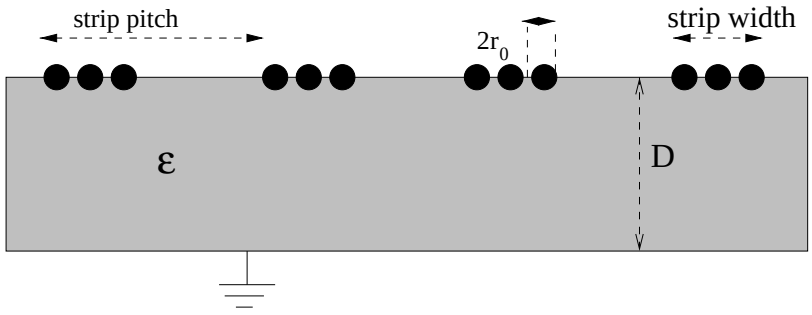

Figure 2.7 : Schematic picture of the detector in the calculation of charge sharing. Every strip is replaced by group of equidistant wires with radius r_0.

[15] The back plane is considered an electrode.

The geometry of the system is shown in Fig. 2.7. Every strip is replaced with n wires of radius r_0, uniformly distributed over the strip width. If the backplane is grounded, a charge Q_j on wire j induces a potential on wire l

$$\Phi_{lj} = \frac{Q_j}{2\pi\varepsilon_o\varepsilon_r} \ln[\frac{r_{lj}}{\sqrt{r_{lj}^2 + 4\,D^2}}] = C_{lj}^{-1}\, Q_j, \quad l \neq j \tag{2.39}$$

$$\Phi_{ll} = \frac{Q_l}{2\pi\varepsilon_o\varepsilon_r} \ln[\frac{r_0}{2D}] = C_{ll}^{-1}\, Q_l \quad , \tag{2.40}$$

where r_{lj} is the distance between wires l and j. The dielectric constant ε_r is calculated as $\varepsilon_r = \frac{1}{2}(\varepsilon_{Si}+1)$, since the wire borders to air and silicon. The calculation of charge transfer from interpolation strips to read out strips is obtained by solving the set of equations

$$V_l = \sum_j \Phi_{lj} = \sum_j (C_{lj})^{-1}\, Q_j = V_s, \quad l \in s \tag{2.41}$$

$$\sum_{j\in s} Q_j = Q_s \tag{2.42}$$

Eq. 2.41 determines the potential on wire l as the sum of contributions from all wires. The coefficients $(C_{lj})^{-1}$ are calculated from Eq. 2.39 and Eq. 2.40. The total charge induced on the strip s is the sum of charges on the wires replacing the strip (Eq. 2.42).

The boundary conditions are given as

- $Q_i = q_i$ for the interpolation strip, collecting the charge
- $Q_j = 0$ for all other interpolation strips
- $V_k = 0$ for the wires replacing read-out strips

The unknown parameters are the charges induced on read-out strips and the potentials of the interpolation strips. The $N_{k,i}$ is determined as ratio of the charge induced on the read-out strips (Q_k) and the charge on the interpolation strip (q_i).

There are two free parameters in the calculation: the number of wires n replacing the strip and the radius of those wires r_0. It turns out that a sufficient convergence is reached if $n > 5$. The results between $n = 25$ and $n = 5$ differ by $< 2\%$. The best agreement with measurements [ZontM] is obtained if the radius of wires is such that wires touch each other i.e. the distance between wires is equal to $2r_0$. The difference between the measurements and calculation is in that case below 2%.

The calculation performed in this work was done using 15 read-out strips, which is sufficient. The difference in $N_{k,i}$ between the calculation using 30 and 15 strips was less than 0.01%.

2.3 Electronic processing of the signal

2.3.1 Read-out scheme

The current induced by drifting charge is usually integrated and amplified with a charge sensitive preamplifier and shaped later on. The schematic picture of a charge sensitive

preamplifier and shaping circuit is shown in Fig. 2.8. The role of pulse shaping is to minimize the measurement error with respect to noise, and at high counting rates to minimize the effects of pulse overlap or pileup. Typically several tens of such channels are integrated into a read-out chip.

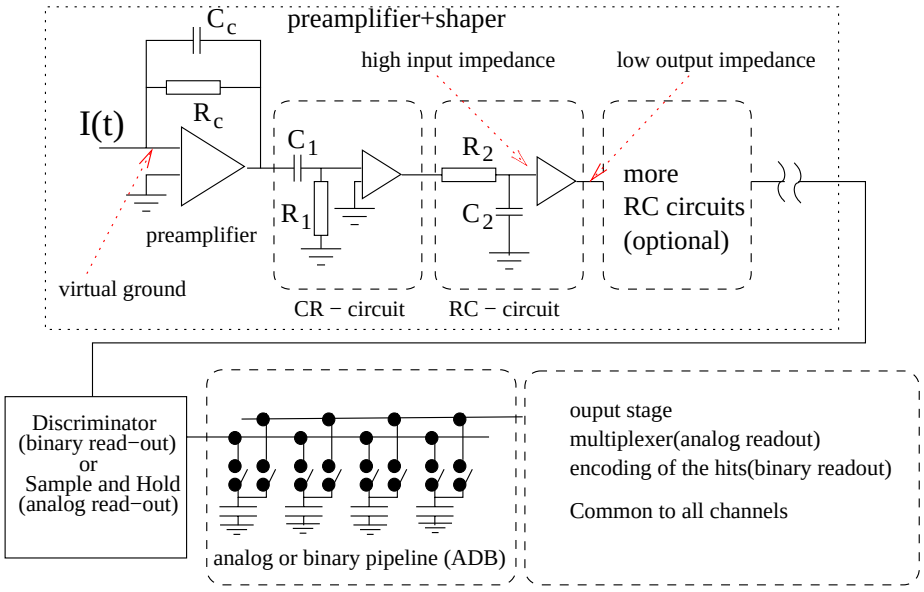

Figure 2.8 : Schematic picture of one channel of a typical LHC silicon detector read-out chip.

In most cases the signals are shaped using an CR shaper differentiating the signal followed by a series of RC integrators. A CR circuit is a bandwidth limiting circuit at low frequencies, while a RC circuit is limiting at high frequencies. To calculate the voltage signal at the output of the preamplifier and shaping circuit transfer functions of each component have to be known.

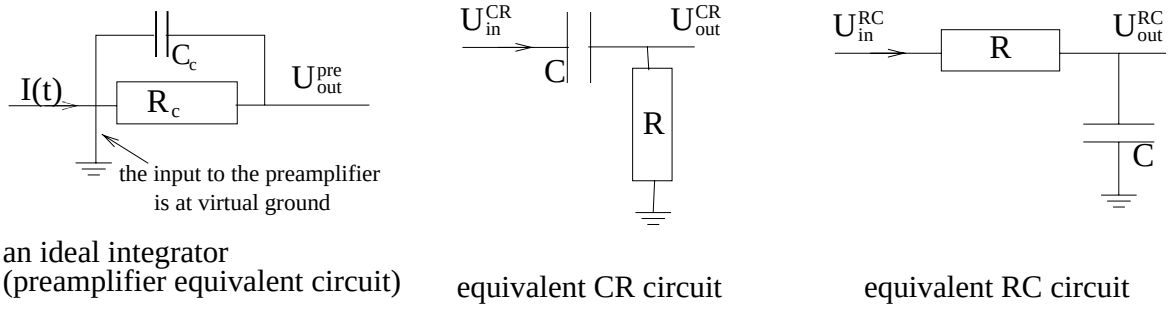

Figure 2.9 : Equivalent circuits for preamplifier (amplification is omitted) , differentiator (CR) and integrator (RC).

Preamplifier

An ideal preamplifier is considered as a current integrator. Its equivalent circuit is shown in Fig. 2.9. The response - voltage at the output stage of the preamplifier can be calculated from

$$I(t) = C_c \frac{dU_{out}^{pre}}{dt} + \frac{U_{out}^{pre}}{R_c} \tag{2.43}$$

$$\frac{I(t)}{C_c} = \frac{dU_{out}^{pre}}{dt} + \frac{U_{out}^{pre}}{\tau_{pre}} \quad , \quad \tau_{pre} = R_c\, C_c \tag{2.44}$$

with a solution

$$U_{out}^{pre}(t) = \frac{1}{C_c}\, e^{\frac{-t}{\tau_{pre}}} \int_{-\infty}^{t} I(t^{'}) e^{\frac{t^{'}}{\tau_{pre}}} dt^{'} \quad , \tag{2.45}$$

CR-circuit (differentiation)

The equivalent circuit is shown in Fig. 2.9. The transfer function can be derived from

$$U_{in} = \frac{Q}{C} + U_{out}^{CR} \tag{2.46}$$

Differentiating both sides

$$\frac{dU_{in}}{dt} = \frac{1}{C}\frac{dQ}{dt} + \frac{dU_{out}^{CR}}{dt} \quad , \quad \frac{dQ}{dt} = I = \frac{U_{out}^{CR}}{R} \tag{2.47}$$

$$\frac{dU_{in}}{dt} = \frac{1}{\tau_{CR}} U_{out}^{CR} + \frac{dU_{out}^{CR}}{dt} \quad , \quad \tau_{CR} = C\ R \tag{2.48}$$

The solution of the differential equation 2.48 can be calculated as

$$U_{out}^{CR}(t) = U_{in}(t) - \frac{1}{\tau_{CR}}\, e^{\frac{-t}{\tau_{CR}}} \int_{-\infty}^{t} U_{in}(t^{'}) e^{\frac{t^{'}}{\tau_{CR}}} dt^{'} \tag{2.49}$$

RC-circuit (integration)

A equivalent circuit is shown in Fig. 2.9. The transfer function can be derived in the same way as for an CR circuit from

$$U_{in} = I\, R + U_{out}^{RC} \tag{2.50}$$

Substituting

$$I = \frac{dQ}{dt} = C \frac{dU_{out}^{RC}}{dt} \tag{2.51}$$

one gets

$$U_{in} = \tau_{RC} \frac{dU_{out}^{RC}}{dt} + U_{out}^{RC} \quad , \quad \tau_{RC} = R\, C \quad . \tag{2.52}$$

Eq. 2.52 has the solution

$$U_{out}^{RC}(t) = \frac{1}{\tau_{RC}} e^{\frac{-t}{\tau_{RC}}} \int_{-\infty}^{t} U_{in}(t') e^{\frac{t'}{\tau_{RC}}} dt' \quad , \tag{2.53}$$

The voltage output from each circuit serves as an input to the next one. An example of the preamplifier and CR-RC^n shaping circuit response (Fig. 2.8) to an instant current pulse ($Q_{in}\delta(t)$) is shown in Fig. 2.10a. The amplitude of the integrated and shaped pulse U_{out} is proportional to the induced charge. The zero-to-peak time is usually denoted with τ_p (peaking time)[16].

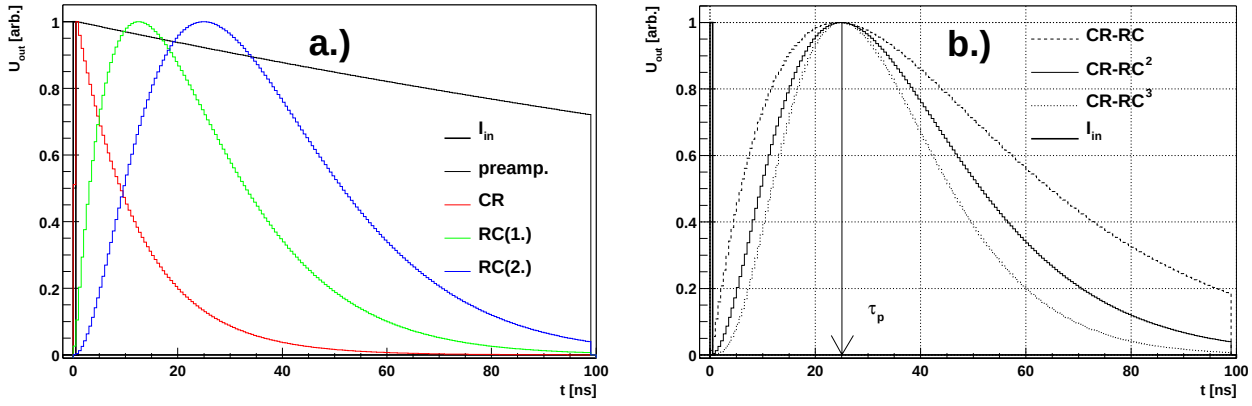

Figure 2.10 : a.) The response of the front end electronics to the instant current pulse at different stages and b.) the response of the front end electronics with different shaping circuits and the same peaking time τ_p. In both a.) and b.) $C_c = 1$ pF and $R_c = 1$ MΩ. All responses are normalized to 1. Capacitors in CR and RC circuits in b.) have the same capacitance (1 pF) and different resistors R=25kΩ/n, where n denotes the number of RC integrations.

2.3.2 Problem of Sampling at LHC experiments

At LHC experiments the silicon detectors will not trigger the experiment at the first level [ATLTP, CMSTP]. The output voltage from the front-end U_{out} will be sampled with the bunch crossing frequency (40MHz). The sampled values will be stored in an pipeline (Fig.2.8)[17] of a length around 2μs. In this time the trigger decision will be taken and the read-out cycle will start. The delay between particle traversing the detector and the trigger decision is fixed hence the trigger signal is uniquely related to the time of the particle arrival. If the trigger signal does not arrive in the the time determined with the length of the pipeline the cells will be overwritten with new values. Such a read-out scheme is often called analog read-out.

The ATLAS experiment decided to put a discriminator after the preamplifier and shaper circuit and store only the binary information whereas the strip was hit or not

[16] The shape of the output voltage signal after injecting an instant current pulse in the preamplifier is in general for a CR-RC^n shaping circuit given by $U_{out}(t) = (\frac{nt}{\tau_p})^n \exp(-\frac{nt}{\tau_p})$.

[17] Pipeline is an array of capacitor-cells.

(binary read-out). The drawback of this method, compared to the analog, is worse resolution at a given read-out pitch and no possibility for off-line processing (common mode rejection, optimizing the cuts etc.). On the other hand manipulation with logical signals is easier, far less subjected to interferences and most of all cheaper.

One of the main requirements for the LHC electronics is a good time resolution. Each cell in the pipeline should be unambiguously related to a certain bunch-crossing. In addition, the electronics must be capable of resolving two hits 50 ns (2 BCT) apart. These requirements constrain the peaking time of shaping circuits to few tens of ns, preventing the tail of the signal extending in the following cells from being recognized as a hit.

Another solution was proposed to overcome this difficulty. It allows peaking times longer than BCT. Upon the arrival of the trigger more cells are read out and the signal is deconvoluted from them in order to find the right bunch-crossing from which the ionizing particle originates. The detailed description of the method can be found in [Gad92, Bin93, Bre94].

There are two LHC design read-out chips using this deconvolution technique, APV [Hal95, Mes00] and Felix [Roe96], while the SCT chip [Ang97] has a peaking time of τ_p =BCT and does not need a deconvolution circuit. The APV will be used by the CMS experiment, the Felix was a prototype chip for the ATLAS experiment and SCT is the analog version of the ATLAS binary chip ABCD [Dab99]. They share the same front-end, but different pipelines and control logic. In the measurements presented in this work, microstrip detectors were read out using the SCT chip.

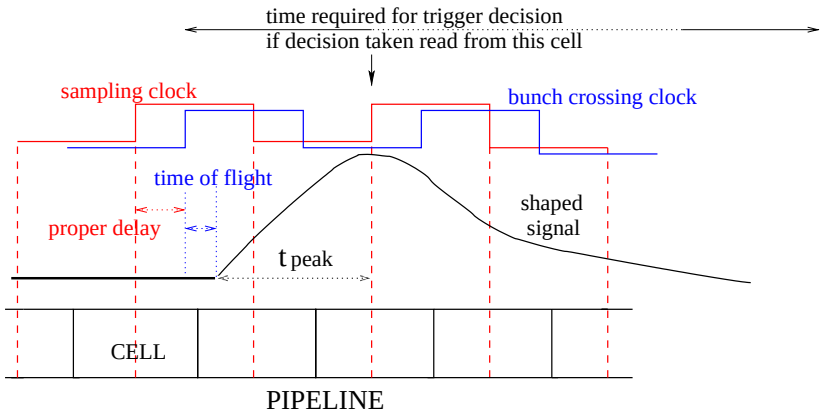

Figure 2.11 : Schematic view of sampling the signal into the pipeline. If the delay between particle arrival and sampling clock is not properly set the stored amplitude is smaller than the maximal amplitude.

The sampling of the front-end output in the pipeline plays an important role in the detection of the signal. In order to detect the maximal signal, the output from the front-end should be sampled at peak. The sampling clock of the chip and the bunch crossing clock therefore have to be synchronized and adequately delayed with respect to each other (Fig. 2.11). The delay depends on the distance between detector and the collision point

(time of flight) and also on the shape of the induced current. While the detector position is fixed, the induced current shape changes with applied voltage, ionizing particle hit position and the spatial distribution of energy loss. This results in different time needed for the signal to reach maximum t_{peak} for each individual event. In principle it is possible to read the signal for each event at t_{peak}, however in practical operation a proper fixed sampling time maximizing the CCE should be chosen for each detector. Such time will be hereafter called the best sampling time τ_{best}.

2.3.3 Ballistic deficit

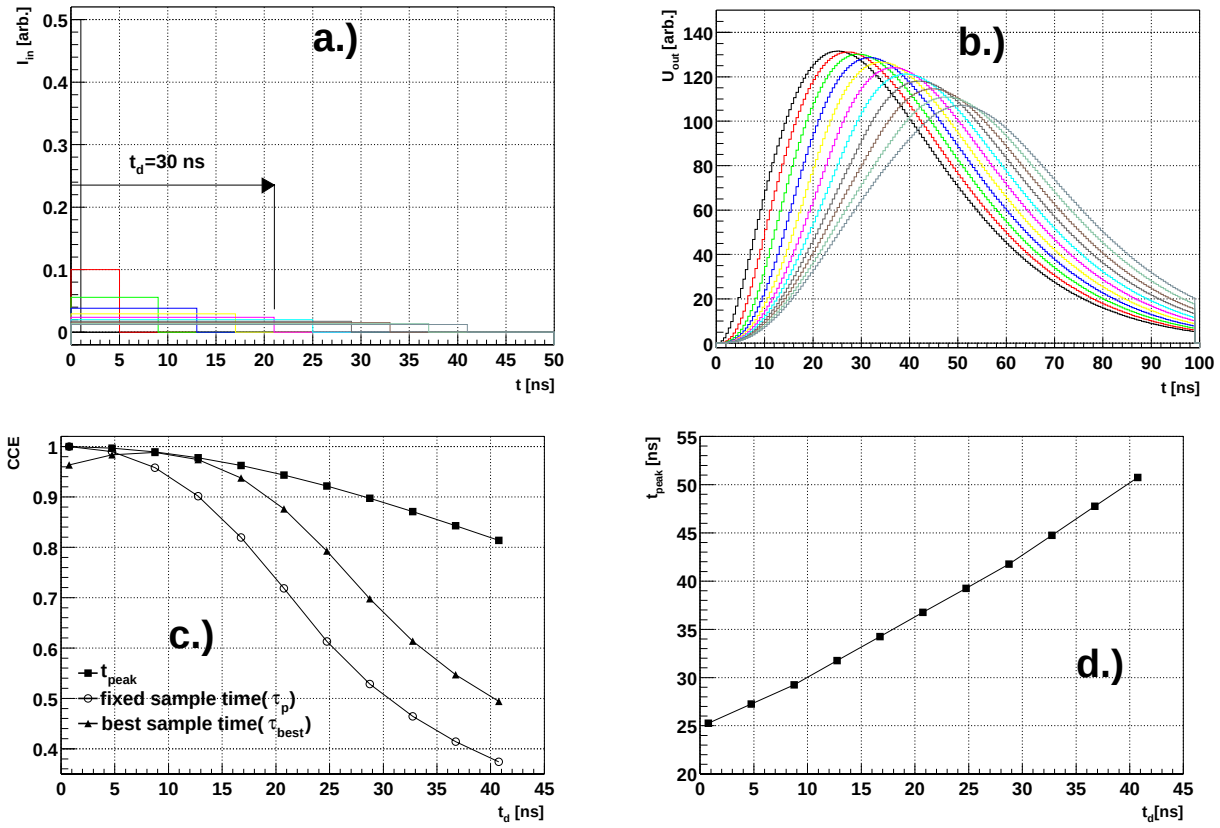

Figure 2.12 : a.) Injected current shapes and b.) the resulting output U_{out} from the preamplifier and shaper circuit (CR-RC^2, $\tau_p = 25$ ns). The reduction of the measured charge (normalized to 1) for the signal sampled at peak and at nominal peaking time τ_p is shown in c.) and shift of the peak time in d.).

The problem of the induced current extending over the time comparable with the nominal peaking time and the corresponding loss of the measured charge is known as ballistic deficit. An example of ballistic deficit can be seen in Fig. 2.12a,b. The injected constant current of different duration ($t_d = (1+4\,n)$ ns) and same integral (charge) results in different $U_{out}(t)$. Two effects can be clearly seen. The amplitude of the output voltage

signal (Fig. 2.12c) decreases for current pulses of longer duration t_d and the time t_{peak} is shifting to longer times (Fig. 2.12d). Even at current duration times shorter than τ_p the amplitude of the output signal is reduced compared to the instant current pulse.

If the distribution of the induced current pulse duration due to ionizing particle passage would have a peak at 10 ns the best sampling time would be around $\tau_{best} = 35$ ns. In case of broad tails [18] of the distribution sampling at τ_{best} would result in a few percent loss of the measured charge for instant pulses and also a few percent loss for pulses with duration up to τ_p.

Shapes of induced current like in Fig. 2.12a would be obtained for ionizing particles in a silicon pad detector in the absence of effective space charge (silicon material of very high resistivity) and trapping of drifting charge. The study of the induced current pulse shapes in irradiated and non-irradiated silicon detectors and their processing will be studied in more detail in the chapter describing results of detector simulation.

2.3.4 Noise

The noise and its dependence on irradiation is not the topic of this work. However, it can affect signal detection and therefore some basic considerations should be given.

For example, if charge is induced on more strips, it can happen that the signal induced on some of them is comparable with noise. The signal from these strips can be attributed to noise and ignored in the measurement of total signal. This problem appears for large incident angles of minimum ionizing particles with respect to the detector surface and is more expressed in irradiated detectors, where the noise is higher compared to non-irradiated ones.

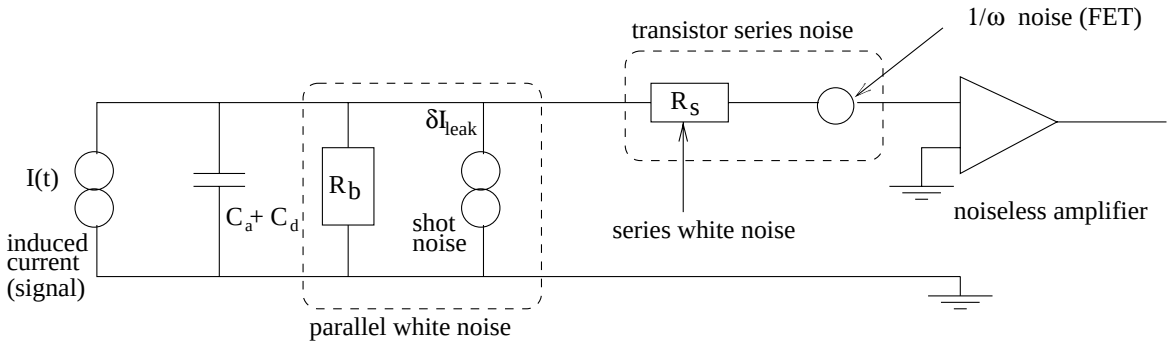

Figure 2.13 : Basic noise sources in the detector amplifier circuit. The parallel frequency dependent noise coming from frequency dependent resistors is negligible and therefore not shown.

In the noise analysis the equivalent circuit shown in Fig. 2.13 is used. Regarding to connection of the noise source with the preamplifier the noise is split into serial and parallel noise.

[18] This effect is more pronounced for the photons generating a point-like charge.

The input stage of a preamplifier is usually a bipolar, JFET or MOS transistor. Such devices are called charge-controlled devices in which the current through the device is controlled by the amount of charge in the conducting channel of the device. The induced charge on the input electrode changes the charge in the conducting channel and by that the current and its integral-amplified charge.

The series white noise of an amplifier given in equivalent noise charge (ENC) can be written in the form [Rad88]

$$ENC_s = \sqrt{\frac{4\,k_B\,T R_s}{\tau_p}(C_a + C_d)^2} = \alpha + \gamma C_d \tag{2.54}$$

where C_a (100 pF) is the capacitance of the transistor electrode and R_s [19] the equivalent resistance in series with the input electrode. In that way the preamplifier is described as a noise-less preamplifier in series with a resistor which is the source of thermal noise. The origin of the series noise is the shot noise from emitter into the base in bipolar transistors and thermal noise modulating the conducting channel width in field-effect transistors [20]. The parameterization is usually given as a constant part (α) dependent only on read-out chip parameters and a term γ that gets multiplied by the detector (input) capacitance C_d. Typical values for α used at LHC experiments are in the range of $\alpha = 600 - 800$ electrons while $\gamma = 25 - 40$ electrons/pF.

The parallel white noise has two major contributions: the shot noise due to detector leakage current and thermal noise on the bias resistor. The contributions from leakage current shot noise ENC_I for a CR-RC circuit and thermal noise from a bias resistor ENC_{R_b} are calculated as

$$ENC_I = \frac{e}{e_\circ}\sqrt{\frac{e_\circ\, I\, \tau_p}{4}} \tag{2.55}$$

$$ENC_{R_b} = \frac{e}{e_\circ}\sqrt{\frac{k_B\, T\, \tau_p}{2\, R_b}} \quad . \tag{2.56}$$

Both parallel noise contributions are un-correlated and therefore summed in squares

$$ENC_p = \sqrt{ENC_I^2 + ENC_{R_b}^2} \quad . \tag{2.57}$$

The parallel and series noise are also not correlated thus the total noise is given by

$$ENC^2 = ENC_p^2 + ENC_s^2 \quad . \tag{2.58}$$

Opposite to the behavior of the series noise which increases with decreasing τ_p the parallel noise increases with τ_p. This results in relatively high series noise of the LHC electronics and only small contributions from the shot and bias resistor noise.

[19] For bipolar transistors $R_s = r_{bb'} + t_e/(2C_a)$ and for field-effect transistors $R_s = 2t_e/3C_a$. The time needed for carriers to travel through the conducting channel is denoted with t_e and the resistance between the base contact and active region of the base with r_{bb}.

[20] Besides the white noise the $1/\omega$ noise arises from fluctuations in the gate-channel interface which modulate the conducting channel in MOS devices. The reason is in frequency dependent charge trapping-detrapping processes in SiO_2. The contribution is typically of few tens electrons.

3

Radiation damage in silicon detectors

3.1 Radiation Induced Defects

The damage caused by irradiation can be divided into surface and bulk damage.

Due to the interest of electronic industry, the surface damage is better understood and can be controlled to a certain extent by proper design and manufacturing process. Surface damage mainly manifests is charge accumulation in the oxide and subsequent electrical breakdown. Charge accumulation at the silicon-oxide interface also significantly decreases the inter-strip resistance of microstrip detectors.

Bulk damage is a consequence of formation of deep levels in the band gap by irradiation. A lot of studies were done in the past in order to: characterize deep level defects, determine their evolution with time, find the influence of fluence, irradiation particle and silicon material on the defect formation. These studies are far from complete.

The first part of this chapter will focus on defect generation mechanism, comparison of irradiations with different particles, known defects and time evolution of the defects. The influence of deep level defects on operation of silicon detectors will be shown in the second part.

3.1.1 Defect Generation

The energy loss of an incoming particle by interaction with matter can be divided into ionizing and non-ionizing energy loss (NIEL). Due to fast recombination of charge carriers the ionizing energy loss does not lead to bulk damage. NIEL contains displacements of lattice atoms and nuclear reactions.

The introduction rate of defects, resulting from nuclear reactions, is more than two orders of magnitude lower compared to introduction rates of defects originating from displaced silicon atoms and thus negligible [ZontT, SchuT].

An incoming particle with mass m can transfer a significant part of its energy E to the silicon atom (m_{Si}). The maximal transferred energy E_{max} follows from non-relativistic

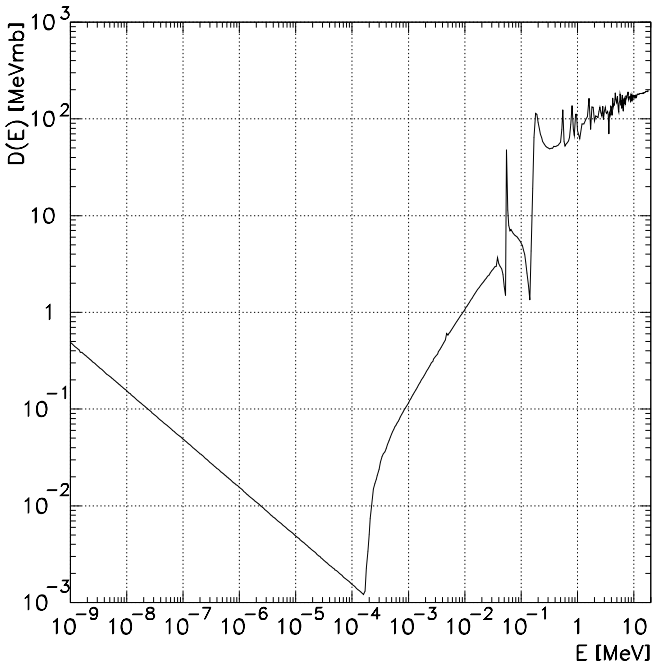

Figure 3.1 : The neutron damage function for silicon according to Ougouag [Oug90].

collision kinematics

$$\frac{E_{max}}{E} = \frac{4\,m\,m_{\mathrm{Si}}}{(m + m_{\mathrm{Si}})^2} \quad . \tag{3.1}$$

For example as much as 13% of the incoming neutron energy can be transferred to the Si atom. Bulk damage occurs when the transfer of kinetic energy is sufficient to displace a silicon atom from its lattice site (Primary Knocked off Atom - PKA). Around 25 eV of recoil energy is required [Kin59]. The displaced atom may come to rest in a interstitial position (I), leaving a vacancy (V) at its original location. If the kinetic energy of the recoiling atom is sufficient it can displace further Si atoms, creating a cluster of displacements. Most of the resulting vacancies and interstitials recombine while others diffuse away and eventually create stable defects.

3.1.2 Comparing Radiation Damage Measurements

Only non-ionizing energy loss (NIEL) is to be taken into account when bulk damage caused by different particles or particles of different energies is compared. According to this "NIEL hypothesis" the radiation damage of the bulk depends on the non-ionizing energy loss only. This has been experimentally demonstrated for protons, neutrons and pions [ROSE1, Chi95, WunsT, FeicT, Bat95, Aar95]. Lately, however, it has been shown that this hypothesis is violated if oxygenated silicon materials are used. The significant

difference in $|N_{eff}|$ increase with irradiation between charged hadrons and neutrons at equal NIEL was observed. The measurements of effective trapping probability presented in this work will also reveal a NIEL hypothesis violation. However, leakage current increase scales with NIEL [MollT] and therefore the NIEL calculation still serves as the reference for normalization of fluences of different particles or particles of different energies.

According to the "NIEL hypothesis" any displacement damage induced change in the material properties scales with the amount of energy imparted in displacing collisions, irrespective of the spatial distribution of the introduced displacement defects in a PKA cascade and irrespective of the various annealing sequences taking place after the initial damage. The displacement damage cross section, measured in MeVmb, is given by the so called damage function $D(E)$ [Laz87]. It measures the average value of kinetic energy released to the crystal by an incoming particle of energy E.The total displacement-damage energy per unit volume deposited in the silicon crystal can be written as

$$\rho_{dis} \;=\; \frac{8}{a^3}\, t_{irr} \int_0^\infty \frac{d\phi(E)}{dE}\, D(E) dE \quad , \tag{3.2}$$

where t_{irr} denotes the irradiation time, $\phi(E)$ the flux of incoming particles and $a = 0.543$ nm the linear dimension of the cubic unit cell of the crystal resulting in $\frac{8}{a^3}$ for the space density of the target nuclei.

The damage caused by different particles is usually compared to the damage caused by neutrons. Since the damage function depends on neutron energy (Fig. 3.1), the NIEL of 1 MeV neutrons is taken as the reference point. The standard value of 1 MeV neutrons NIEL is 95 MeVmb [D1MeV]. Irradiation with particles A with a spectral distribution $\frac{d\phi_A}{dE}$ and cut-offs E_{min} and E_{max} would cause the same damage as 1 MeV neutrons if

$$\rho_{dis} \;=\; \frac{8}{a^3}\, t_{irr} \int_{E_{min}}^{E_{max}} \frac{d\phi_A(E)}{dE}\, D_A(E) dE = \frac{8}{a^3}\, \Phi_{\rm eq} D_n(1\ {\rm MeV}) \quad , \tag{3.3}$$

where $\Phi_{\rm eq}$ denotes the equivalent integrated flux (fluence) of 1 MeV neutrons which would have caused the same damage as the fluence

$$\Phi = t_{irr} \int_{E_{min}}^{E_{max}} \frac{d\phi_A}{dE}(E)\, dE \tag{3.4}$$

of particles actually applied. It is possible to define the hardness factor κ_A as

$$\kappa_A = \frac{1}{D_n(1\ {\rm MeV})} \cdot \frac{\int_{E_{min}}^{E_{max}} D_A(E)\, \frac{d\phi_A}{dE}(E)\, dE}{\int_{E_{min}}^{E_{max}} \frac{d\phi_A}{dE}(E)\, dE}. \tag{3.5}$$

It follows from here that

$$\Phi_{\rm eq} \;=\; \kappa_A\, \Phi_A \ . \tag{3.6}$$

Primary Vacancies	Primary Interstitials	Replaced impurities
Group A		
$V + P \rightarrow VP$	$I + VP \rightarrow P$	$C_i + C_s \rightarrow C_i$-$C_s$
$V + O \rightarrow V\,O$	$I + VO \rightarrow O$	$C_i + O_i \rightarrow C_i$-$O_i$
$V + VO \rightarrow V_2O$	$I + V_2 \rightarrow V$	$C_i + P_s \rightarrow C_i$-$P_s$
$V + C_i \rightarrow C_s$	$I + C_s \rightarrow C_i$	
$V + V_2O \rightarrow V_3O$	$I + V_2O \rightarrow VO$	
$V_2 + V \rightarrow V_3$	$I + C_iO \rightarrow C_iOI$	
	$I + C_iOI \rightarrow C_iOI$	
	$I + C_iC_s \rightarrow C_iC_sI$	
	$I + C_iC_sI \rightarrow C_iC_sII$	
Group B		
$V + V \rightarrow V_2$	$I + V \rightarrow Si$	
$V_2 + V \rightarrow V_3$		

Table 3.1 : Survey of possible defect reactions. Group A reactions are caused by diffusion of interstitials and vacancies throughout the crystal. Most frequent reactions during a primary cascade are gathered in group B. Indexes $_i$ and $_s$ stand for interstitial and substitutional.

3.1.3 Types of Defects

After the interaction of the traversing particle with the lattice an interstitial-vacancy pair (Frenkel pair) or a cluster can be produced, depending on the energy transferred to the primary atom. Though physical properties of clusters are not determined yet, theoretical models have been proposed [CluMo]. In the first phase the disordered region consists of many interstitials and vacancies. Most of the vacancies and interstitials recombine, some vacancies may interact to form stable divacancies or higher vacancy complexes while the rest diffuses away. Those can react with other radiation induced defects, forming defect complexes, or react with impurity atoms such as carbon, oxygen and phosphorus, those being among the most common impurities in silicon. When only a Frenkel pair is created only reactions with existing defects are possible. Thus reactions of the defects can be divided into two groups. In the group A are reactions of vacancies and interstitials diffusing throughout the crystal. The most frequent reactions within the clusters, where the defect density is high, belong to the group B. Possible reactions of both groups are listed in Table 3.1 and the most relevant defect configurations are shown schematically in Fig. 3.2.

3.1.4 Time Evolution Of Defects

Concentration of defects generated directly by irradiation is proportional to the equivalent fluence. The defects can be divided into three groups regarding their time development after the creation:

- defects stable in time

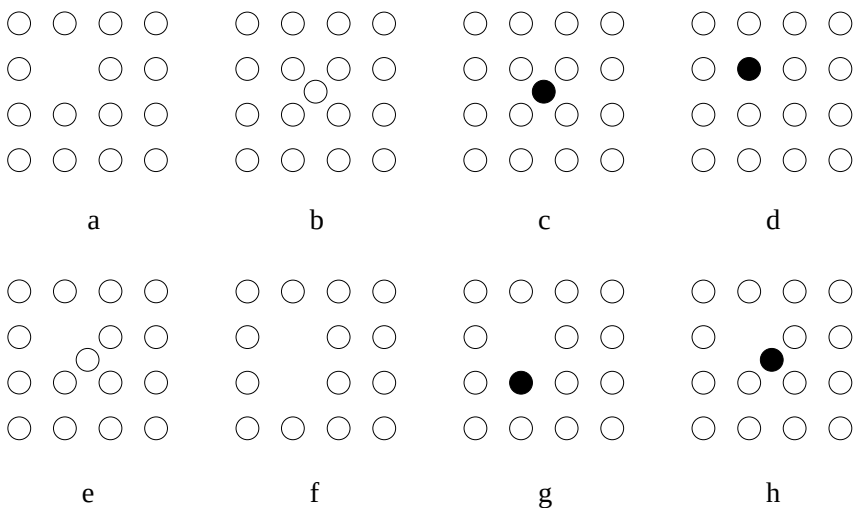

Figure 3.2 : Various possible defect configurations. Simple defects are: a.) vacancy V, b.) interstitial silicon atom I, c.) interstitial impurity atom, d.) substitutional impurity atom (e.g. phosphorus as donor). Examples of defect complexes are: e.) close pair I-V, f.) divacancy V-V, g.) substitutional impurity atom and vacancy (e.g. VP complex), h.) interstitial impurity atom and vacancy (e.g. VO complex)

- defects decaying into new defects (dissociation)
- defects reacting with other defects thus forming new defects

In case of the dissociation $X \rightarrow Y$ the reaction can be described as a first order process

$$-\frac{dN_Y}{dt} = \frac{dN_X}{dt} = -k_1^Y N_X \ , \tag{3.7}$$

with the solution

$$N_X(t) = N_X^0 e^{-k_1^Y t} = N_X^0 e^{-t/\tau_1^Y} \quad , \quad \tau_1^Y = \frac{1}{k_1^Y} \tag{3.8}$$

$$N_Y(t) = N_X^0 (1 - e^{-k_1^Y t}) = N_X^0 (1 - e^{-t/\tau_1^Y}) \ . \tag{3.9}$$

When the new complex is formed by reaction of two defects $X_A + X_B \rightarrow Y$, it can be described by

$$-\frac{dN_Y}{dt} = \frac{dN_{X_A}}{dt} = \frac{dN_{X_B}}{dt} = -k_2^Y N_{X_A} N_{X_B} \ , \tag{3.10}$$

with the solution ($N_{X_A}^0 > N_{X_B}^0$)

$$N_Y(t) = N_{X_B}^0 \frac{1 - e^{-k_2^Y t (N_{X_A}^0 - N_{X_B}^0)}}{1 - (N_{X_B}^0 / N_{X_A}^0) e^{-k_2^Y t (N_{X_A}^0 - N_{X_B}^0)}} \ . \tag{3.11}$$

In the case of two defects with similar initial concentrations $N^0_{X_A} = N^0_{X_B}$ or a reaction between defects of the same type one obtains

$$N_X(t) = \frac{N^0_X}{1 + N^0_X k^Y_2 t} = \frac{N^0_X}{1 + t/\tau^Y_2} \quad , \quad \tau^Y_2 = \frac{1}{k^Y_2 N^0_X} \tag{3.12}$$

$$N_Y(t) = N^0_X - N_X(t) = N^0_X(1 - \frac{1}{1 + N^0_X k^Y_2 t}) = N^0_X(1 - \frac{1}{1 + t/\tau^Y_2}) \ . \tag{3.13}$$

describing a second order process. If, however, concentration of one type of interacting defects is much larger than the concentration of the other ($N^0_{X_A} \gg N^0_{X_B}$) the dynamics of the process can again be described by the first order equation with $k^Y_1 = k^Y_2 N^0_{X_A}$.

In the equations, N^0_X is the initial concentration of defect X, which is proportional to the fluence, and k^Y_1 and k^Y_2 are the reaction constants for the first and second order processes. From equations 3.7 and 3.10 it can be seen that in the first order reaction, the reaction rate depends linearly on defect concentration while in the second order case the dependence is quadratic.

Since the energy needed for breaking up the defect (dissociation) or forming a new defect is supplied by the lattice vibrations the reaction constant is strongly temperature dependent. The lattice atom vibration energy is governed by the Maxwell-Boltzmann distribution. The probability of sufficient energy transfer from lattice vibration to the defect is therefore exponential with temperature. As a consequence

$$k^Y_{1,2} \propto \exp(-\frac{E_a}{k_B T}) \quad \Longrightarrow \quad \frac{\tau^Y_{1,2}(T_0)}{\tau^Y_{1,2}(T_1)} = \frac{k^Y_{1,2}(T_1)}{k^Y_{1,2}(T_0)} = \exp\big[\frac{E_a}{k_B}(\frac{1}{T_0} - \frac{1}{T_1})\big] \tag{3.14}$$

where E_a is the activation energy for defect dissociation or reaction.

At a given time after the irradiation concentration N_t of a general defect formed either directly by irradiation or by primary defect decay or reactions will be given by

$$N_t \ = \ g_t \, \Phi_{\rm eq} \, f_t \quad , \tag{3.15}$$

where g_t is the creation amplitude and $f_t \in [0, 1]$ describes the evolution of the defect with time. For the defects constant in time $f_t = 1$. In the case of defect evolution being described by a first order processes, f_t is an exponential and depends on time only (see Eqs. 3.8, 3.9). If the evolution of defect is described by a second order process, f_t is a function of both time and fluence (see Eq. 3.11).

3.2 Effects of deep level defects in silicon

In non-irradiated silicon the density of deep level defects is far below the density of shallow dopants which determine to a large part the electrical behavior of silicon. In these situation the deep level defects can be considered as a disturbance to the semiconductor which properties remain basically intact. The concentration of the deep level defects can

exceed the concentration of shallow dopant density in an irradiated silicon. The result is a drastic change of silicon properties.

Each defect can have several charge states. In the simplest case, like for shallow dopants, a donor can assume two charge states, neutral with the electron loosely bound to the donor site and positively ionized. The acceptor may be neutral or negatively ionized. A general type of defect is much more complex. It may be a complex structure of missing silicon atoms in the lattice and impurity atoms, capable of switching between several chemical binding structures and by that between the charge states. Changing from one state to another may be accomplished by thermal excitation. If this involves a change of the charge state of the defect, it is accompanied by emission or capture of an electron or hole.

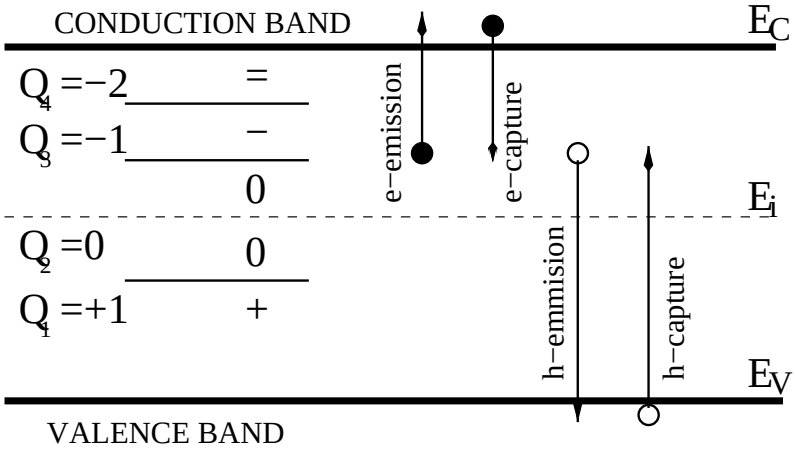

Figure 3.3 : A schematic view of carrier capture and emission processes for a defect with multiple charge states. A simple defect has only one energy level and two charge states.

As will be shown later the emission and capture processes are related to each other so that a (non-degenerate) defect is characterized by the following properties:

- k energy levels $E_{t,k}$ describing the energy involved in changing the charge state.
- $k+1$ charge states $Q_{t,l}(l = 0, k)$ of the defect, ordered from most positive to most negative
- k electron capture cross sections σ_{t,l_e}
- k hole capture cross sections σ_{t,l_h}

In the most common case simple donors and acceptors, which have only one energy level and two charge states, are completely characterized by their energy level and two cross sections.

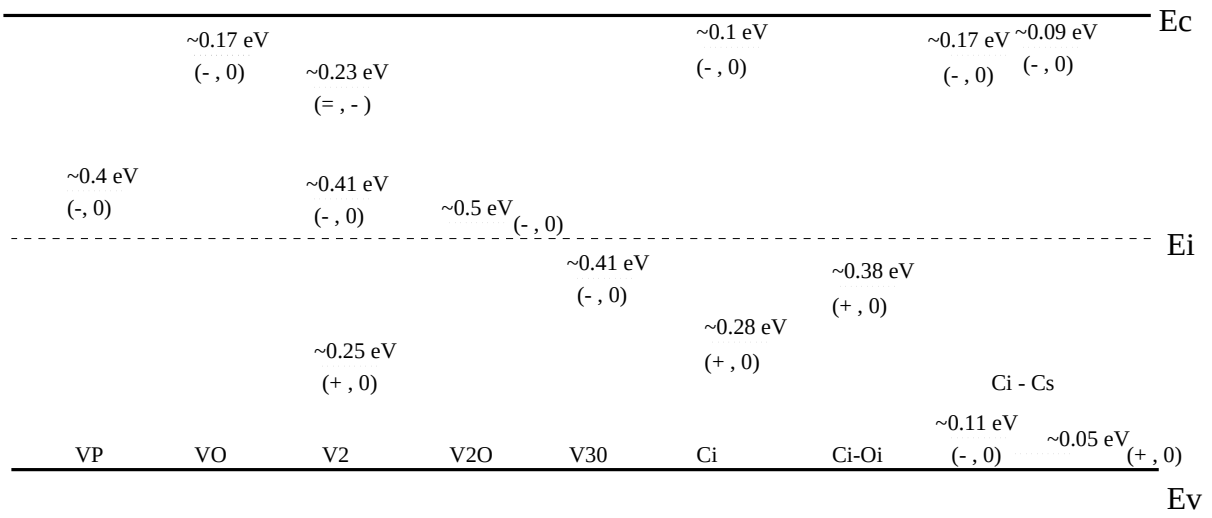

Figure 3.4 : Energy levels of some vacancy and carbon related defects. The defect charge states are shown in brackets, e.g. minus and neutral (-,0). Above the dotted line the energy of the trap is written; in the lower half ΔE_V and in the upper half ΔE_C. Sign = denotes the doubly charged state. In the figure, data from [SchuT] were used.

3.2.1 Defects in thermal equilibrium

It thermal equilibrium the electron occupation probability of a state and therefore also of simple defect states is described by the Fermi function

$$F(E) \;=\; \frac{1}{1+\exp\left(\frac{E-E_F}{k_B\,T}\right)} \quad , \tag{3.16}$$

where E_F is the Fermi level, E the defect energy level. An occupied simple donor is neutral while an occupied simple acceptor is negatively charged. In the following the short hand notation

$$\chi(E) = \exp(\frac{E-E_i}{k_B\,T}) \tag{3.17}$$

will be used, with E_i the Fermi level for the intrinsic silicon ($p = n = n_i$) derived from the charge neutrality condition

$$E_i \;=\; \frac{E_V+E_C}{2} \;+\; \frac{1}{2}\,k_B\,T\ln(\frac{N_V}{N_C}) \quad , \tag{3.18}$$

where the bottom of the conduction band is denoted with E_C, the top of the valence band with E_V and the density of states in conduction and valence band with N_C and N_V.

Electron and hole concentration in any silicon material are thus given as

$$n = N_C \exp(-\frac{E_C - E_F}{k_B T}) = n_i \exp(\frac{E_F - E_i}{k_B T}) = n_i \chi_F \tag{3.19}$$

$$p = N_V \exp(-\frac{E_F - E_V}{k_B T}) = n_i \exp(\frac{E_i - E_F}{k_B T}) = \frac{n_i}{\chi_F} \quad . \tag{3.20}$$

The Fermi level is found from the requirement of overall charge neutrality

$$\sum_{\text{donors}} N_t^j \left[1 - F(E_t^j)\right] - \sum_{\text{acceptors}} N_t^j F(E_t^j) + N_D - N_A - n + p = 0 \quad , \tag{3.21}$$

where the N_t denotes the concentration of deep defects. Also the complete ionization of shallow dopants is assumed.

Although the thermal equilibrium occupation probabilities are completely described by Fermi function, this is the result of a continuous change of the charge state of individual defects. Thermal equilibrium thus allows us to find the relations between the capture and emission processes.

Considering a single defect level in thermal equilibrium the rate of electron capture has to be equal to the rate of electron emission. An analog relation holds for holes (see Fig. 3.3). This follows from the requirements that the average occupation probability of defects does not change and there is no net flow of electrons between the valence and conduction bands. With the introduction of the capture coefficients

$$c_n = v_{th_e} \sigma_{t_e} \quad , \quad c_p = v_{th_h} \sigma_{t_h} \quad , \tag{3.22}$$

for the product of thermal velocity and capture cross section and the emission probabilities ϵ_n and ϵ_p one gets:

$$n\, c_n\, N_t\, (1 - F(E_t)) = N_t\, F(E_t)\, \epsilon_n \tag{3.23}$$

$$p\, c_p\, N_t\, F(E_t) = N_t\, (1 - F(E_t)) \epsilon_p \tag{3.24}$$

$$F(E_t) = \frac{1}{1 + \exp(\frac{E_t - E_F}{k_B T})} = \frac{1}{1 + \frac{\chi_t}{\chi_F}} \quad , \tag{3.25}$$

from which the electron capture (also called recombination) and emission (also called generation) probabilities of a simple defect are obtained as

$$\frac{1}{\tau_c^n} = n\, c_n \quad , \quad \frac{1}{\tau_c^p} = p\, c_p \tag{3.26}$$

$$\epsilon_n = \frac{1}{\tau_\epsilon^n} = n\, c_n \exp(\frac{E_t - E_F}{k_B T}) = n_i\, c_n \exp(\frac{E_t - E_i}{k_B T}) = n_i\, c_n\, \chi_t \tag{3.27}$$

$$\epsilon_p = \frac{1}{\tau_\epsilon^p} = p\, c_p \exp(\frac{E_F - E_t}{k_B T}) = n_i\, c_p \exp(\frac{E_i - E_t}{k_B T}) = n_i\, c_p\, / \chi_t \quad . \tag{3.28}$$

τ_c^n is the mean time it takes until an unoccupied defect changes its charge state by electron capture, τ_c^p, τ_ϵ^n, and τ_ϵ^p are defined in an analogous way. These relations (Eqs. 3.26, 3.27, 3.28) are also valid in non-equilibrium situations. As emission probabilities are related to capture cross sections, simple defects will be fully described by the energy level E_t and electron and hole capture cross sections.

3.2.2 Defects in the fully depleted space charge region

First consider the situation under the approximation that the space charge region is completely depleted of charge carriers. This is a good assumption for a reversely biased detector with low leakage current. Thus the capture processes can be neglected. Occupation probability of a defect and its carrier generation rate are determined by considering emission processes only. Capture cross-sections appear indirectly with the use of the relation between emission and capture processes (Eqs. 3.27, 3.28) derived in thermal equilibrium.

The average occupation probability of a defect $P_t(E_t)$ is determined by the requirement of equal electron G_n and hole G_p generation rates:

$$G_n \;=\; N_t\, P_t\, \epsilon_n \;=\; N_t\,(1-P_t)\,\epsilon_p \;=\; G_p \quad , \tag{3.29}$$

$$P_t \;=\; \frac{1}{1+\frac{c_n}{c_p}\chi_t^2} \quad , \quad 1-P_t \;=\; \frac{1}{1+\frac{c_p}{c_n}\chi_t^{-2}} \quad . \tag{3.30}$$

It is reasonable to assume that the capture coefficients for electrons and holes are of the same order of magnitude. With this assumption defects with energy levels more than few times $k_B\,T$ above the intrinsic level E_i are expected to be in the unoccupied (more positive) state and those below E_i in the occupied (more negative state). The intrinsic level qualitatively play a similar role in the space charge region as the Fermi level did in the thermal equilibrium case.

In the space charge region the role of the simple deep defects can be described in the following way

- donors above E_i are positively charged, acceptors below E_i are negatively charged
- donors below E_i and acceptors above E_i are neutral
- there exists a transition region extending a few times $k_B\,T$ around E_i

3.2.3 Defects in a general stationary situation

In some cases the assumption of a space charge region fully depleted of free carriers is not valid. Such cases are

- continuous carrier injection (e.g. by light illumination)
- transition region between neutral semiconductor and fully depleted space charge region
- high leakage currents .

The excess generation rate is defined as the difference between generation rate G and recombination rate R with excess generation rate $U \;=\; G-R$ defined separately for

electrons and holes

$$\frac{U_n}{N_t} = P_t\,\epsilon_n - (1 - P_t)\,c_n\,n = c_n\left[P_t\,n_i\,\chi_t - (1 - P_t)\,n\right] \tag{3.31}$$

$$\frac{U_p}{N_t} = (1 - P_t)\,\epsilon_p - P_t\,c_p\,p = c_p\left[(1 - P_t)\,n_i/\chi_t - P_t\,p\right] \quad . \tag{3.32}$$

In a stationary state the defect occupation probability has to be constant. Therefore the excess generation rates for electrons and holes have to be equal, $U = U_n = U_p$. From here the defect occupation probability can be derived as

$$P_t = \left[\frac{c_p\,p + c_n\,n_i\,\chi_t}{c_n\,n + c_p\,n_i/\chi_t} + 1\right]^{-1} \quad . \tag{3.33}$$

The excess generation rate $U = G - R$ is given by

$$U = G - R = \zeta_t(n_i^2 - p\,n) \tag{3.34}$$

$$\zeta_t = N_t\,\frac{c_n\,c_p}{c_n\,n + c_p\,n_i/\chi_t + c_p\,p + c_n\,n_i\,\chi_t} \tag{3.35}$$

The generalization of Eq. 3.35 for many defects is done by summing ζ_t over the defects. In principle p and n are spatially dependent and by that also ζ_t.

3.3 Consequences of deep levels to detector operation

Deep levels influence detector operation in three ways:

- N_{eff} increases with irradiation
- leakage current increases with irradiation
- irradiation creates trapping centres, where drifting charge can be trapped.

3.3.1 Change in N_{eff}

Deep levels contribute to the effective space charge. The space charge density of a single defect type is given by

$$\begin{aligned} Q_t &= e_0\,N_t\,(1 - P_t) \quad \text{for donors} \\ Q_t &= -\,e_0\,N_t\,P_t \quad \text{for acceptors.} \end{aligned} \tag{3.36}$$

Irradiation of silicon produces many different defects. The sum of Q_t/e_0 over all defects gives the effective dopant concentration N_{eff} as

$$N_{eff} = \sum_{donors} N_t\,(1 - P_t) - \sum_{acceptors} N_t\,P_t + N_D - N_A \quad . \tag{3.37}$$

Combining Eq. 3.37 and Eq. 3.15 one gets

$$N_{eff}(\Phi_{\rm eq}, t, T) = \Phi_{\rm eq} \left[\sum_{donors} g_t \, f_t(t) \, (1 - P_t(T)) - \sum_{acceptors} g_t \, f_t(t) \, P_t(T) \right] + \\ + N_D(\Phi_{\rm eq}) - N_A(\Phi_{\rm eq}) \quad . \tag{3.38}$$

The irradiation of silicon produces more electrically active primary acceptors than donors that are electrically active [21]. If n-type silicon is irradiated $|N_{eff}|$ decreases initially with fluence up to the inversion point where $N_{eff} \approx 0$. At this point, silicon bulk undergoes type inversion from n-type to p-type (negative space charge) under reverse bias. After that, $|N_{eff}|$ increases with fluence and by that also V_{FD}.

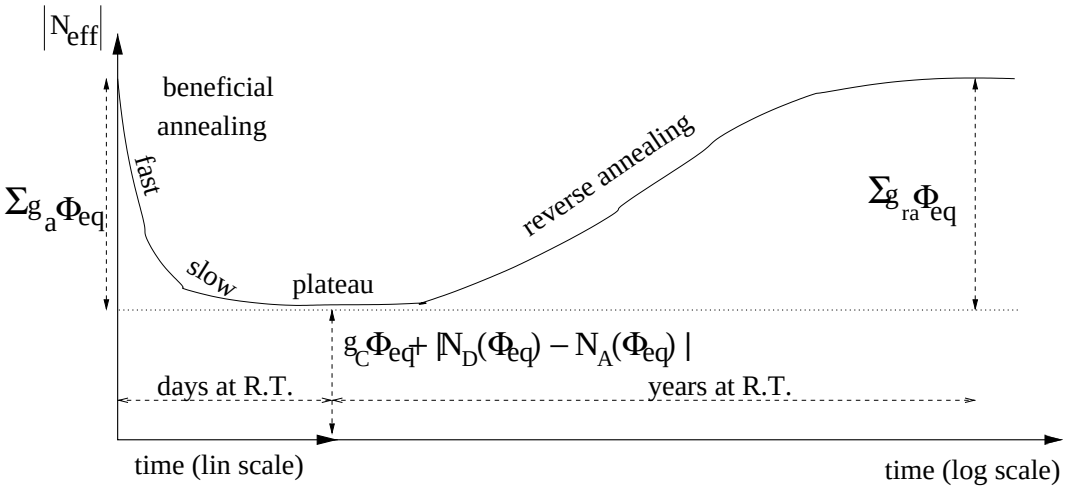

Figure 3.5 : Schematic plot of time development of N_{eff} for inverted silicon material. All three phases are shown with introduction rates for the relevant defects. Note that reverse annealing is shown in logarithmic time scale.

Measurements of N_{eff} time development after irradiation (Fig. 3.5) show that in the beginning the electrically active defects decay into non-active (annealing). After around 10 days at room temperature the concentration of electrically active defects starts rising again due to electrically non-active defects turning into electrically active ones (reverse annealing). The initial slope of N_{eff} rise due to reverse annealing is found to scale linearly with fluence indicating that reverse annealing is a first order process [Mik99, MollT].

Since only first order processes determine the time evolution of N_{eff}, it can be param-

[21] Besides introduction of new defects, irradiation may also influence the concentration of initial dopants. The fluence dependence of the initial shallow dopants is not clear yet. Different proposals are presented in Appendix D.

eterized as [22]

$$\begin{aligned}\Delta N_{eff}(t) &= N_{eff,0} - N_{eff}(t) \\ \frac{\Delta N_{eff}(t)}{\Phi_{\rm eq}} &= g_c + \sum_{annealing} g_a\, e^{-t/\tau_a} + \sum_{rev.annealing} g_{ra}\,(1 - e^{-t/\tau_{ra}}) + \\ &\quad + \frac{(N_D(0) - N_D(\Phi_{\rm eq})) - (N_A(0) - N_A(\Phi_{\rm eq}))}{\Phi_{\rm eq}} \quad ,\end{aligned} \tag{3.39}$$

where $N_{eff,0}$ is the effective doping concentration before irradiation, g_c is the generation rate for defects constant in time, g_a the generation rate of defects that anneal with time constants τ_a and g_{ra} generation rate of defects responsible for the reverse annealing with time constants τ_{ra} [23]. The time constants τ_a and τ_{ra} depend exponentially on temperature according to Eq. 3.14. Usually the parameterization with a single annealing and reverse annealing defect gives already a good fit to measured data at room temperature, starting a few hours after irradiation. A survey of parameters is given in Appendix D.

The temperature dependence of N_{eff} is hidden in $P_t(T)$. N_{eff} is usually extracted from capacitance measurements (C/V technique), where the determination of N_{eff} depends on both the measurement frequency and temperature. Using this method at 10kHz, a few percent lower $|N_{eff}|$ was observed [KolaD, Chi00] at -20°C as compared to 20°C.

3.3.2 Change in leakage current

Bulk current through the depleted region comes from two main contributions: diffusion of charge carriers from the non-depleted region (diffusion current) and generation of carriers in the depleted region (generation current). The generation current represents the dominant contribution to the leakage current in highly irradiated and even in most of the non-irradiated silicon detectors [PoSCD].

The generation current depends on the pair generation rate and generation volume. According to the Eq. 3.29 the charge generation accomplished by alternate emission of electrons and holes in the space charge region can be calculated as

$$\begin{aligned} G \;&=\; G_n \;=\; G_p \;=\; N_t\,\frac{c_n\,c_p}{c_n\chi_t + c_p/\chi_t}\,n_i \;= \\ &=\; N_t\,P_t\,c_n\,n_i\,\chi_t \;=\; g_t\,\Phi_{\rm eq}\,f_t\,P_t\,\chi_t\,v_{th_e}\sigma_{t_e}\,n_i \end{aligned} \tag{3.41}$$

[22] Similar parameterization which is widely used is described in Appendix D and is called "Hamburg model" [MollT].

[23]

$$\begin{aligned} g_a &= g_t\,P_t && \text{annealing amplitude of acceptor or reverse annealing amplitude of donor} \\ g_{ra} &= g_t\,(1 - P_t) && \text{reverse annealing amplitude of acceptor or annealing amplitude of donor} \\ g_c &= \sum_{const.\ don.} g_t\,(1 - P_t) - \sum_{const.\ acc.} g_t\,P_t \end{aligned} \tag{3.40}$$

Since only the difference between electrically active donors and acceptors determines the effective space charge, the concentration of defects N_t can be much higher than N_{eff}.

The generated electron-hole pairs are immediately separated by the electric field, thus giving rise to the current

$$I_{SCR} = e_0\, w\, S \sum_{defects} G = e_0\, w\, S\, \Phi_{\rm eq} \sum_t g_t\, f_t\, P_t\, \chi_t\, v_{th_e} \sigma_{t_e}\, n_i \quad . \tag{3.42}$$

Since $w(U) \propto \sqrt{U}$ also the bulk generation current is proportional to $\sqrt{U}$ as long as the diode is not fully depleted (I/V measurement). The electron-hole generation rate on defects and their contribution to the generation current is maximal if the energy level of defects and intrinsic level are equal $E_t = E_i$ ($\exp(-|E_t - E_i|/k_B\, T)$).

Leakage current increases linearly with fluence, as it is evident from Eq. 3.42. In order to compare different measurements the leakage current damage constant α is introduced by normalizing the increase [24] of the leakage current after irradiation to the volume ($V = w\, S$) and fluence

$$\frac{\Delta I_{SCR}}{V\, \Phi_{\rm eq}} = \alpha(t, T) \quad . \tag{3.43}$$

Only the contribution of defects constant in time ($f_t = 1$) and annealing ($f_t = \exp(-\frac{t}{\tau_t})$) defects has been observed in the leakage current, while no reverse annealing was ever found. The measurements were therefore fitted with an ansatz [Lem94, WunsT, SchuT, FeicT]

$$\alpha(t) = \alpha_c + \sum_i \alpha_i e^{-t/\tau_i^{\alpha}} \quad . \tag{3.44}$$

where α_c represents the contribution of defects constant in time, α_i contributions of decaying defects, τ_i their decay times and t time after irradiation.

However recent results [ZontT, MollT] show also a long term annealing component, that follows an effective logarithmic time dependence, described by an ansatz (see Appendix D)

$$\alpha(t) = \alpha_1\, \exp(-\frac{t}{\tau_\alpha}) + \alpha_0 - \alpha_2 \ln(\frac{t}{t_{norm}}) \; . \tag{3.45}$$

The temperature dependence of the leakage current comes from all terms in Eq. 3.41 except N_t. Only the traps with E_t around E_i need to be considered, capture cross-sections are taken as independent of temperature and $v_{th} \propto \sqrt{T}$. Thus one obtains a simple relation

$$I_{SCR} \propto T^2\, \exp(-\frac{E_g}{2\, k_B\, T}) \quad . \tag{3.46}$$

Measurements of reverse current dependence on temperature in irradiated detectors show that the levels somewhat away from the mid-gap contribute significantly. In addition, cross-sections exhibit power law dependence on temperature. The result is an effective behavior of I_{SCR} as with an E_g of 1.2 eV [MollT] in Eq. 3.46 instead of the nominal 1.12 eV.

[24] Leakage currents densities before irradiations are around few hundreds nA/cm^3. The increase after irradiation is usually so large that ΔI_{SCR} can be replaced by the current after irradiation.

3.3.3 Trapping of the drifting charge

The levels in the band gap act as traps for the drifting charge. Each level can trap both electrons and holes and by that the defect changes its charge state. For example a simple donor can trap holes if it is occupied and electrons if it is empty. The analogue holds for an acceptor. Since in the SCR both acceptors and donors above the intrinsic level are predominantly empty they mainly trap electrons (electron traps). In the same way acceptors and donors below the intrinsic level mainly trap holes (hole traps).

For the calculation of carrier trapping probabilities a similar consideration as in Eq. 3.26 is used with the concentration of defects replacing the concentration of free carriers. The trapping probability is here defined as:

$$\frac{1}{\tau^t_{tr_e}} = c_n\,(1 - P_t)\,N_t \quad \text{electrons} \tag{3.47}$$

$$\frac{1}{\tau^t_{tr_h}} = c_p\,P_t\,N_t \quad \text{holes.} \tag{3.48}$$

The trapping time $\tau^t_{tr_{e,h}}$ represents the mean time that a free carrier spends in the space charge region before it is trapped by trap t. To get the effective trapping probability $1/\tau_{eff_{e,h}}$ for electrons and holes one has to sum over the trapping probabilities of all defects

$$\frac{1}{\tau_{eff_{e,h}}} = \sum_t \frac{1}{\tau^t_{tr_{e,h}}} = \sum_t N_t\,(1 - P^{e,h}_t)\,\sigma_{t_{e,h}}\,v_{th_{e,h}} \quad , \tag{3.49}$$

where $P^e_t = P_t$ and $P^h_t = 1 - P_t$. Using the relation 3.15, Eq. 3.49 can be rewritten as [25]

$$\frac{1}{\tau_{eff_{e,h}}} = \Phi_{\text{eq}} \sum_t g_t\,f_t\,(1 - P^{e,h}_t)\,\sigma_{t_{e,h}}\,v_{th_{e,h}} \quad . \tag{3.50}$$

If the traps are constant in time or created with a first order process, f_t does not depend on fluence. Hence, the effective trapping probability at a given temperature and time after irradiation can be parameterized as

$$\frac{1}{\tau_{eff_{e,h}}} = \beta_{e,h}(t,T)\,\Phi_{\text{eq}} \quad . \tag{3.51}$$

As will be shown later, the measurements performed in this thesis confirm this assumption. Analogous to leakage current damage constant α, $\beta_{e,h}$ can be called the effective electron or hole trapping damage constant.

[25] In Eq. 3.50 it is assumed that all deep levels are formed by irradiation and there is almost no trapping centres in the silicon before that.

4

Experimental techniques

4.1 Irradiation Facilities

Three different sources of hadrons were used for irradiation of silicon detectors. While silicon strip detectors were irradiated with neutrons only, all three sources were used for irradiation of silicon pad detectors. The use of different irradiation particles was necessary to check the validity of the "NIEL hypothesis" for effective trapping times.

4.1.1 Neutron irradiation facility

The reactor research centre of the Jožef Stefan Institute is located in Podgorica near Ljubljana. It is the site of a nuclear reactor of the TRIGA type, constructed to provide neutrons for experimental purposes. It can be run with a large span in operating power (few W to 250 kW), enabling irradiations with various neutron fluxes at the same irradiation site.

The main part of the reactor is its core, consisting of fuel and control rods. It is surrounded by a graphite reflector and placed into a reactor vessel filled with water, all within a thick concrete shield. The vertical channels occupying a fuel rod position give access to the irradiation site located at the edge of the core or even at its centre. The space available for samples in these channels is limited to samples with less than 1.3 cm in diameter and shorter than 12 cm. The vertical channel F19 (Fig. 4.1) was used for the irradiations. It provided:

- Neutron spectrum with a significant portion of fast neutrons (above 0.1 MeV). The proximity of the core provides high neutron fluxes with a relatively high portion of fast neutrons. About 1/3 of the flux is above 0.1 MeV [Kri98].

- High fluxes of fast neutrons that range from 10^9 up to $2 \cdot 10^{12}$ n/cm^{2}s.

Samples were irradiated in irradiation capsules which were designed satisfying additional requirements:

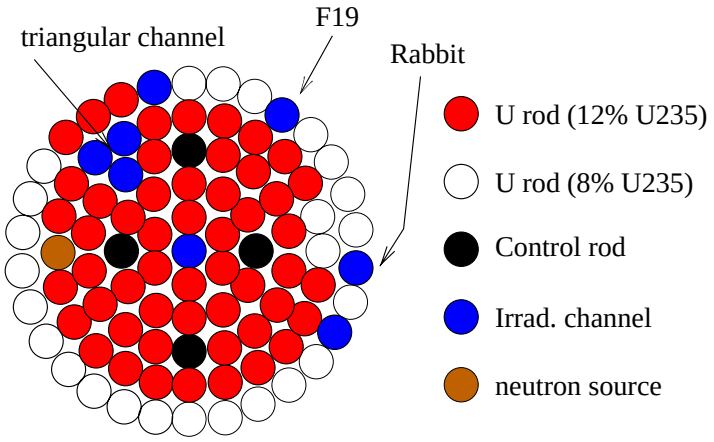

Figure 4.1 : Schematic view of the reactor core as of 23.4.2001. This was most common configuration of the core during irradiations performed in this thesis.

- irradiation of samples under bias with the possibility to perform C/V and I/V measurements during and after irradiation.
- to avoid thermal runaway of biased detectors and to ensure their stable temperature during and after the irradiation, a closed liquid cooling circuit was designed.

A more detailed description of the capsule design can be found in [ZontT].

Neutron Spectrum and Dosimetry

The neutron spectrum in the irradiation channel F19 (Fig. 4.2) was determined by simulation [MauPC] and measurement [Kri98]. The simulated spectrum was obtained using a Monte Carlo simulation, where fuel elements and rod positions were taken into account. A more detailed description of the simulation can be found in [ZontT]. Experimental measurement of the neutron spectrum was performed using the activation method [Kri98]. It exploits the activation of different materials with neutrons. The resulting spectrum together with the simulated is one shown in Fig. 4.2. From the neutron spectrum the hardness factor was calculated by using different damage functions [Oug90, Gri90]. The value $\kappa = 0.90 \pm 0.03$ relative to $\phi(E > 0.1\text{MeV})$ was obtained by [ZontT]. The homogeneity of the neutron field was determined by a separate measurement [Kri98]. At the irradiation spot in F19, the radial gradient was measured to be about 4%/cm and the vertical gradient about 1%/cm.

The neutron flux is expected to vary linearly with reactor power. The irradiations in the F19 channel were performed at different reactor power, thus varying the neutron flux. The flux determined by activation method showed that it indeed scales linearly with power with a scaling factor of $7.5 \cdot 10^9$ n/cm^{2}s/kW as can be seen in Fig. 4.3.

Since the core of the reactor was changed a few times during the irradiations of samples used in this thesis it was more appropriate to determine the equivalent 1 MeV neu-

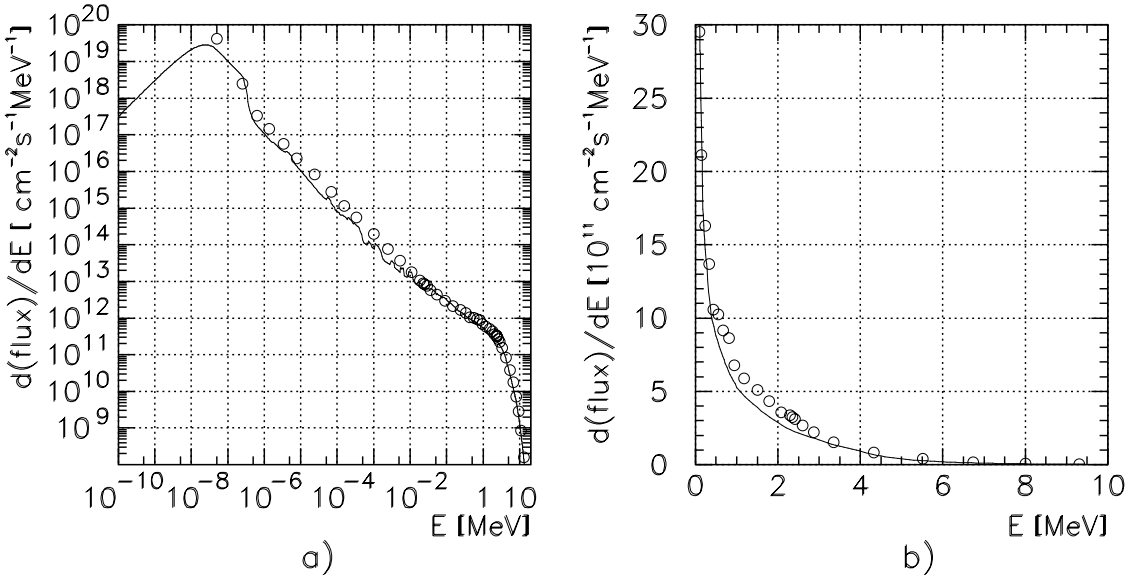

Figure 4.2 : Measured [Kri98] (full line) and simulated [MauPC] (open circles) neutron spectrum in the irradiation channel F19. In figure a) logarithmic scale is used to present the full energy range while on the linear scale in figure b) only the fast neutron spectrum can be seen.

tron flux for every change than to re-measure the spectrum and flux with activation method. The measurements exploited the universality of leakage current damage constant $\alpha(20°\mathrm{C}) = 4 \cdot 10^{17}$ A/cm after annealing for 80 min at 60°C. The dosimetry diodes [26] were used for that purpose. From the leakage current the equivalent flux of 1 MeV neutrons at a given reactor power (P_C) was determined as[27]

$$\phi_{\mathrm{eq}}(P_C) = \frac{\Delta I_{SCR}}{\alpha(20°\mathrm{C})\, t_{irr}\, S\, D} \quad . \tag{4.1}$$

From here the equivalent fluence at any reactor power (P_M) and time of irradiation was obtained as

$$\Phi_{\mathrm{eq}} = \phi_{\mathrm{eq}}(P_C) \cdot \frac{P_M}{P_C} \cdot t_{irr} \tag{4.2}$$

Often dosimetry diodes were also irradiated together with samples under study and received fluence was directly measured from Eq. 4.1. A good agreement between measured and target fluence was found. The error on fluence was estimated to 10%.

[26] The $p^+ - n - n^+$ diodes were produced by ELMA, Zelenograd, Russia. They were between 300-350 μm thick and have one guard ring.

[27] A more detailed explanation of the leakage current measurements can be found in Section 4.2.3.

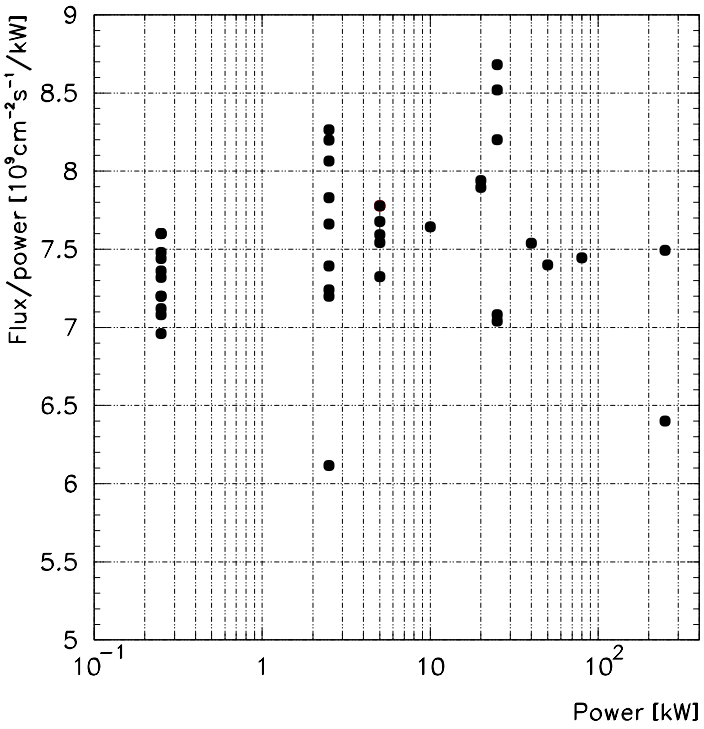

Figure 4.3 : Flux of fast neutrons (E > 0.1 MeV) divided by reactor power versus the reactor power. The constant value of this ratio confirms the validity of the assumption that the neutron flux scales linearly with the reactor power. The scattering of measurements (RMS=3%) is within the error on the flux measurements (from [ZontT]).

4.1.2 Pion irradiation facility

The pion irradiation facility is located at the Paul Scherer Institute (PSI) in Villigen, Switzerland. It is built around the 590 MeV proton cyclotron. The design of the cyclotron is based on criteria that allow operation at very high beam intensities. The accelerator has several secondary beam lines located around two targets. The πE1 beam line used for the irradiation supplies high intensity continuous pion and muon beams with momenta ranging from 10 to 500 MeV/c. The beam line has two modes of operation. It can be operated at higher fluxes, however with lower momentum resolution or at lower fluxes and higher momentum resolution. In the first case the upper energy of the beam is limited to 280 MeV/c. For the irradiation purposes high flux and lower resolution ($FWHM/E = 0.8$ %[piE1]) is more adequate, since the hardness factor in this energy range is almost constant. The energy of positive pions in irradiations performed at the PSI was chosen to be around 200 MeV.

The irradiation site (Fig. 4.4) was not equipped with a scanning xy-table, therefore the size of the samples was restricted to fit within the uniform part of the beam spot (0.7×0.7 cm^2). The placement of the samples into the beam was achieved by using a

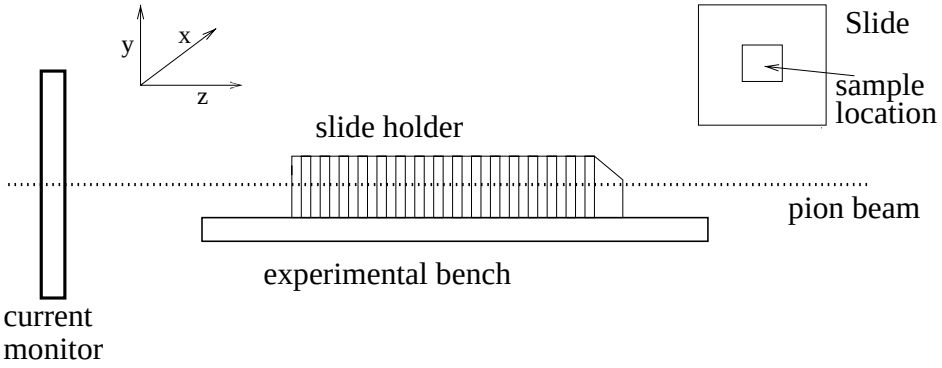

Figure 4.4 : Schematic view of irradiation site at PSI.

slide-holder aligned in the way that the beam went through the centre of the slides. The cardboard slides that fit precisely into the slide-holder had a square hole in the middle where the samples were placed.

This setup used for irradiation did not allow for biasing the samples. It was also not equipped with a temperature regulator, therefore the temperature was the same as the ambiental temperature which during irradiation varied between 23°C and 27°C. The highest fluence of $\Phi_\pi = 2 \cdot 10^{14}$ cm^{-2} was achieved in approximately one day.

Dosimetry

The dosimetry in the πE1 line was performed using Al-activation. The aluminum atom converts into sodium via the reaction ^{27}Al(π^+,2p n)Na^{24} with a well known cross section. The decay time of ^{24}Na$(\beta^-, \gamma)^{24}$Ca is around 15 hours. A NaI spectrometer was used for the determination of the ^{24}Na activity from the photon peak at $E_\gamma = 1369$ keV. The specific activity of the aluminum is proportional to the total fluence of the pions received if the activity is corrected for the time of irradiation and time before the activity measurement was taken. The systematic error of the method was estimated to be about 8% [PIrS].

The pion-induced ionization current was measured with a wire chamber, placed in front of the experimental bench. The wire chamber was connected to a counter. The ratio of the fluence determined from Al-activation and the number of counts gives the flux per count. A series of such measurements were performed to determine the flux in the center of the beam along the beam axis (see Fig. 4.5).

The homogeneity of the beam in the plane perpendicular to the beam axis was also measured (Fig. 4.6). It can be seen that the samples of 0.7×0.7 cm^2 placed in the beam centre were irradiated uniformly.

The hardness factor κ_{π^+} was estimated using the leakage current damage constant measurement. The samples irradiated to certain fluences were annealed for 80 min at 60° C. The measured leakage current was then normalized to 1 MeV neutrons [MollT]. The hardness factor for pions with energy around 200 MeV was found to be 1.14 by [Fre99]

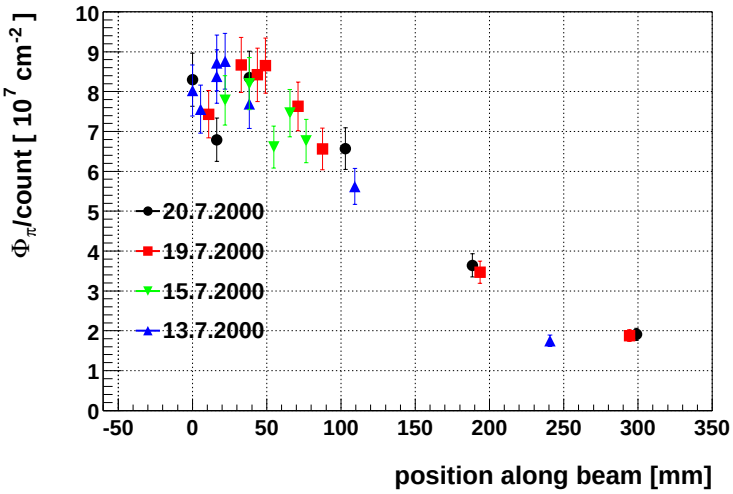

Figure 4.5 : The flux in the centre of the beam along the beam direction. The point $z = 0$ mm is in the position of slot #8 of the slide-holder.

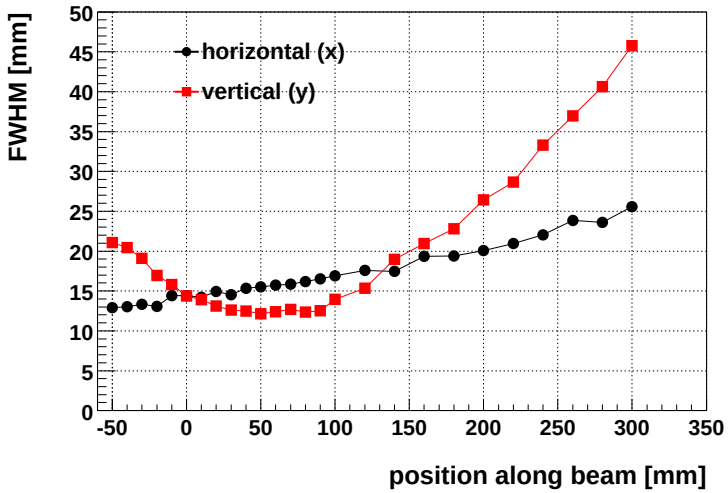

Figure 4.6 : FWHM of the beam profile in the plane perpendicular to the beam at the πE1 irradiation site. The samples were placed at the position of the peak in the flux ($z = 0 - 100$ mm).

and 1.27 by [Ruz00]. The average value of $\kappa_{\pi^+} = 1.2$ was therefore used in this thesis.

4.1.3 Proton irradiation facility

The CERN PS accelerator was used as a source of 24 GeV protons. The irradiation site was equipped with an automatic trolley system providing handling of irradiated samples outside the irradiation area. Samples were mounted in the same way as for the pion

irradiation with the slide-holder mounted on the trolley instead on the experimental bench.

A beam spot of around 2 cm in diameter was measured [PIrS]. This allowed homogeneous irradiation of samples with dimensions of 0.7×0.7 cm^2. Every 14 s, a bunch of $3-13 \cdot 10^{10}$ protons (spill) hit the detectors. A resulting flux of $2-9 \cdot 10^9$ p cm^{-2} s^{-1} could be achieved [PIrS]. The samples were irradiated without bias at ambiental temperature between 29°C and 31°C. The highest fluence of $\Phi_{p^+} = 3.2 \cdot 10^{14}$ cm^{-2} was reached within 18 hours.

Dosimetry

The fluence determination in the proton irradiations was done in the same way as in pion irradiations using the Al-activation. The same spectrometer as for pion irradiation was used to measure the aluminum activity.

The hardness factor for 24 GeV protons used in equivalent fluence calculation was determined from the leakage current damage constant. Its value is 0.62 [Lin00].

Equivalent fluences were checked with leakage current damage constant measurements. If the procedure proposed by [MollT] and explained in section 4.1.1 is used $\alpha(20°\text{C}) = 4 \cdot 10^{-17}$ A/cm should be obtained. As can be seen in Fig. 4.7 the measured leakage current damage constants agree within the error with $\alpha(20°\text{C}) = 4 \cdot 10^{-17}$ A/cm, thus cross-checking the value of the hardness factor and fluence determined from aluminum foil activation.

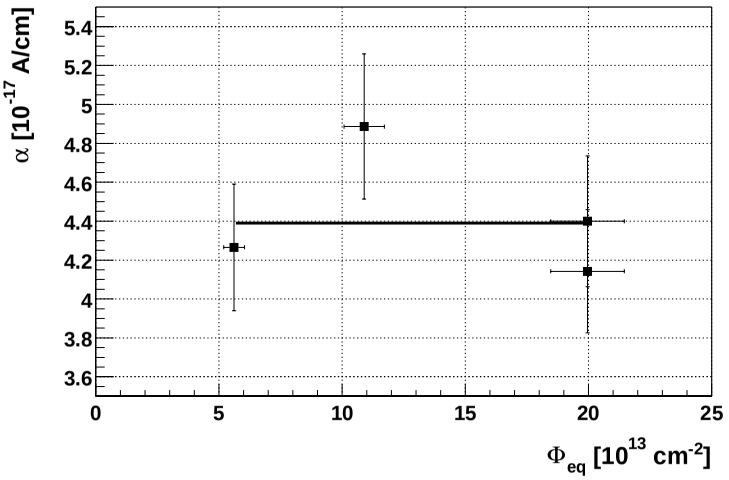

Figure 4.7 : The leakage current damage constant α measured at 20°C after 80 minutes annealing at 60°C.

4.2 C/V-I/V Measurements

The measurement of capacitance as a function of applied bias voltage is a basic tool for determination of the effective dopant concentration and full depletion voltage. The

dependence of leakage current on voltage is used to determine the detector break-down voltage and the leakage current damage constant.

4.2.1 C/V and I/V measurement setup

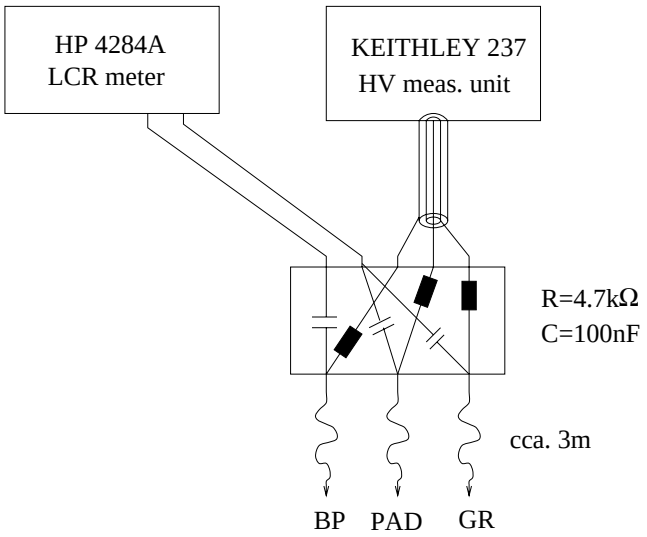

Figure 4.8 : Measurement setup for C/V and I/V measurements: BP, PAD and GR are connections to sample back plane, pad (strips) and guard ring, respectively.

A schematic view of the measurement setup is shown in Fig. 4.8. Its main components were a LCR meter (HP 4284A), a precise current meter and a high voltage source (KEITHLEY 237) [28]. A Yokogawa UT15 temperature controller connected to a Pt-100 sensor placed close to the sample was used to measure the sample temperature. All units were controlled and read out by a personal computer, where some on-line data analysis was also performed.

To shield the LCR meter from high DC biasing voltages, decoupling capacitors were used as shown in figure 4.8. The influence of changes in the impedance of the voltage source on the measurements was reduced by use of decoupling resistors (Fig. 4.8).

Most of the measurements were performed at fixed temperature ranging from -10°C to 25°C. When stored, samples were kept at stable temperature. For samples biased during storage, Wentzel high voltage power supplies were used. Annealing and reverse annealing were accelerated by heating in an oven stabilized to 60°C, stable to about ±1°C. The temperature history during heating was measured by a Pt-100 sensor, placed close to the sample and connected to a Yokogawa controller. The temperature was read from the controller by computer and stored to a file. The measured temperature history was used to correct the heating time for temperature variations (Eq. 3.14).

[28] It can supply up to 1100 V with a current limit of 1 mA in the highest voltage range.

4.2.2 C/V measurements

Capacitance is determined from the complex impedance. It is calculated from the measured amplitude and phase shift of the current signal in response to an AC measuring voltage with user selected frequency. The AC voltage amplitude can be set from 5 mV to 2 V. High measurement voltages give the advantage of better signal to noise ratio. They are however a significant disturbance at bias voltages of a few volts. Typically amplitudes around 10 mV were used.

The LCR meter provides means to transform the measured complex impedance to different physical parameters according to a selected model. Since a partially biased diode can be roughly described by an equivalent circuit presented in Fig. 4.9, an adequate RC model should be selected. Neither the parallel nor the serial RC model offered by LCR meter correspond to the equivalent circuit of the partially depleted diode. But it turns out that N_{eff} can be correctly determined even when using an inappropriate model [29].

The depleted region of a detector can be approximated by a capacitor as the dynamic resistivity of depleted bulk $R_{db} = dU/dI$ is high ($2\,\pi\,\nu\,C_{db} \gg 1/R_{db}$). On the other hand the undepleted bulk can be considered as a resistor ($2\,\pi\,\nu\,C_{ub} \ll 1/R_{ub} \quad , \quad \nu \lessapprox 30$ kHz). At lower voltages the bulk can be thus described as a capacitor and resistor what makes the serial model more appropriate. As the resistance of undepleted bulk decreases and its capacitance increases with voltage ($R_{ub} \propto (1 - \sqrt{U/V_{FD}})$, $C_{ub} \propto 1/(1 - \sqrt{U/V_{FD}})$) at voltages close to the full depletion voltage the detector bulk can be described well by a single capacitor and both serial and parallel model should give the same result. The parallel model however has the advantage that it can take into account changes in the surface current, presented by the surface resistor. They are hard to predict but can get very important close to the breakdown where the differential resistance is small. Since for determination of full depletion voltage from the C/V characteristic, one is interested in its shape close to full depletion, the parallel model suits better and was used throughout this work.

Increase of the measurement frequency reflects in a dominant contribution of capacitances in impedances of depleted and undepleted regions of an irradiated detector [30]. An equivalent circuit of an irradiated detector can thus be approximated by two serial capacitors with constant sum of capacitances. Therefore at 1 MHz the measured capacitance is almost independent of the applied voltage. The resistivity of the undepleted bulk in non-irradiated detectors, however is so low (few kΩcm) that the undepleted bulk can be always approximated by resistor for $\nu \leq 1$ MHz.

The temperature also affects capacitance measurements of irradiated detectors. Since resistance of both depleted (R_{db}) and undepleted (R_{ub}) regions is approximately proportional[31] to $e^{-E_g/2k_BT}$, decreasing the temperature by a few 10°C has the same relative effect as the above mentioned increase in frequency. The temperature does not affect

[29] A detailed analysis of the influence of each component in the model from Fig. 4.9 to the measured capacitance is disscused in [ZontT].

[30] Irradiation of silicon results in an increase of its ohmic resistivity which can become even larger than that of the intrinsic silicon.

[31] For depleted region see eq. 3.42 and for undepleted regions equations 2.1 and 2.3.

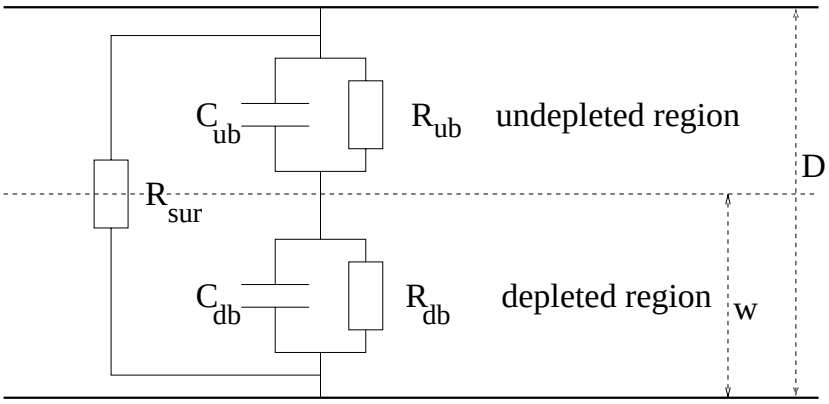

Figure 4.9 : A simple model of a partially biased diode. Both depleted region and undepleted region are modeled by a capacitor and a resistor connected in parallel. Depleted and undepleted regions are connected in series with a parallel resistor to account for the surface current.

the capacitance measurements of non-irradiated detectors as the resistivity of undepleted bulk does not significantly change with temperature [32].

The effect of decoupling capacitors and resistors was taken into account by calibration. HP4284A enables frequency dependent calibration in a large frequency range. Calibration is done at open and closed circuit and with known load[33].

The measurement of the C/V characteristic was controlled by a custom written LabView program, running on a PC. Bias voltage (DC) was raised in predefined steps and sample capacitance was measured at each step with different frequencies of measuring (AC) voltage. The leakage current and temperature were also measured at each step. Measured capacitance was converted to $1/C^2$ and plotted in dependence of the bias voltage.

The full depletion voltage was determined as the position of the kink in $1/C^2$ vs. voltage curve. The exact position of the kink was determined by the intersection of two lines, one fitted to the slope at large depletion depths and the second to the plateau at full depletion (see Fig. 4.10). The interval of fit was determined from a visual examination of the plot.

To determine the effective dopant concentration N_{eff}, a homogeneous distribution over the sample was assumed as discussed in Section 2.1.1. In such case N_{eff} can be determined from the full depletion voltage by equation

$$N_{eff} = \frac{2\varepsilon_{Si}\varepsilon_0}{e_0 D^2} V_{FD} \ . \tag{4.3}$$

[32]The carrier emitted to conduction or valence band from shallow dopants determine the resistivity. The occupation probability of shallow dopants in Eq. 2.13 is almost constant at temperatures of interest, while the dependence of mobility on temperature is relatively modest.

[33]A capacitor of 44 pF was used since this is an approximate capacitance of fully depleted 300 μm thick diodes with an area of order of 1 cm^2, used in this study.

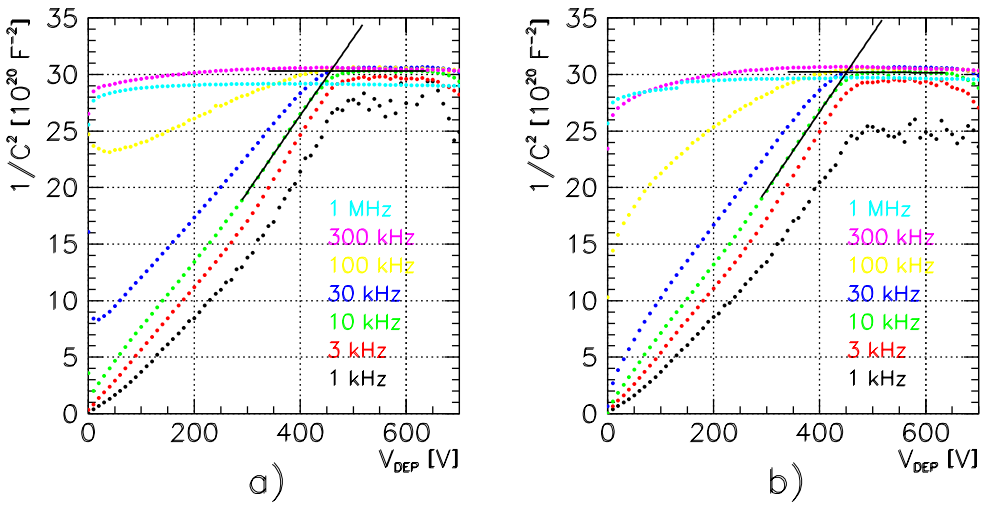

Figure 4.10 : A comparison of a $1/C^2$ vs. voltage characteristics as obtained by a a) parallel and b) serial RC model. Straight line fits to the slope at large depletion depths and to the plateau above full depletion are also shown. The intersection of the lines was used to determine the full depletion voltage. Full depletion voltages as obtained by both models agree within errors.

The conversion factor depends on the sample thickness and for 300 μm thick samples Eq. 4.3 can be written with a fixed numerical factor $N_{eff} = 1.44 \cdot 10^{10}$ V^{-1}cm$^{-3} \cdot V_{FD}$.

The main sources of systematic error in determination of the full depletion voltage come from the selection of measurement frequency and temperature. Measurements were performed at different frequencies (1 kHz, 3 kHz, 10 kHz, 30 kHz, 100 kHz, 300 kHz and 1 MHz. The frequency of 10 kHz was usually used to determine V_{FD}. 10 kHz is a compromise between a good signal to noise ratio[34], sensitivity to traps with long trapping times and applicability of the simple RC model used. Since it is also the most commonly used frequency of other groups, it also enables a comparison of measurements.

The systematic error due to the sources listed above is estimated to be below 10%. The variations of V_{FD} due to different selections of range of fits to the linear part at high depletion depths is on a percent level. That means that the largest contribution to the error on introduction rates of different defects comes from the $\sim 10\%$ systematic error of the dosimetry.

4.2.3 I/V measurements

As mentioned at each step of the C/V characteristic measurements the reverse current was also recorded. The setup allowed the separation of the bulk-generated current from

[34]Impedance of capacitor is inversely proportional to the frequency of the measurement voltage.

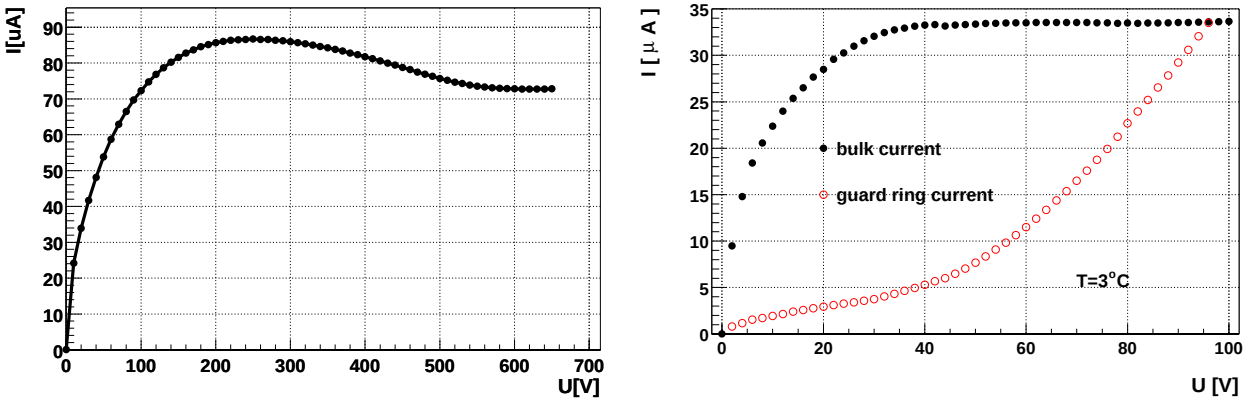

a.) b.)

Figure 4.11 : a.) I/V measurement of the diode used for determination of the proton damage factor. The diode was irradiated to $\Phi_{eq} = 2 \cdot 10^{14}$ cm^{-2}. Guard rings were kept at the same potential as the pad but their current is not included in the measurement. Measurement at $T = 24°$C was taken after 80 min annealing at 60°C. b.) I/V measurement of the strip detector B01 irradiated with neutrons to $\Phi_{eq} = 4.5 \cdot 10^{13}$ cm^{-2} after 15 h annealing at 25°C. The measurement was taken at $T = 3°$C. Both the guard ring and bulk current are shown.

the guard ring current (see Fig. 4.8). While both guard ring and the pad were connected to the same potential, only the current flowing through the pad was measured to reduce the contribution of the surface-generated current.

In some cases the specific mounting of the pad detectors into housing allowed only measurements of the current with guard rings floating. Although I/V measurements in these cases were not appropriate to study the temperature, fluence and time dependence of the leakage current damage constant α, the increase of the leakage current due to continuous light illumination of one detector side (see Section 5.4) could still be measured.

From Eqs. 2.10 and 3.42 it follows that the bulk generation current is increasing as the square root of the depletion voltage until the sample is fully depleted and the values at the plateau can be used to determine α (Eq. 3.43).

The I/V curve of an inverted $p^+ - n - n^+$ pad detectors (Fig. 4.11) however deviates from the expected $I \propto \sqrt{U}$ shape. A characteristic bump can be observed on all samples after inversion. The explanation has been proposed in [FBG]. After inversion, the depleted region starts to grow from the n side while guard rings are on the p side. For low depletion voltages, the surface current is thus not fully collected by guard rings and contributes to the current measured on the central pad.

When the sample is fully depleted guard rings are fully operational again (fig. 4.11). The leakage current at the minimum after the bump has been used as the best estimate of the bulk generation current. The uncertainty of α due to the error on leakage current determination by this method is at the level of few percent [ZontT].

4.3 TCT measurements

4.3.1 Basics of TCT measurements

The transient current technique (TCT) is based on observing the induced current pulse, arising from the drift of free carriers generated in the detector by a short laser pulse. If free carriers are generated in the active region of the detector, their drift induces a current according to Ramo's theorem (Eq. 2.23). In the case of silicon pad detectors, which were used in TCT studies presented in this work, the induced current is in general given by Eqs. 2.29 and 2.35 if the approximation of constant mobility and linear electric field is used. One can easily see that the induced current between terminals of the silicon detector follows in time the electric field distribution that is seen by the moving charge. This remains true even if the mobility is not constant, the picture is however smeared.

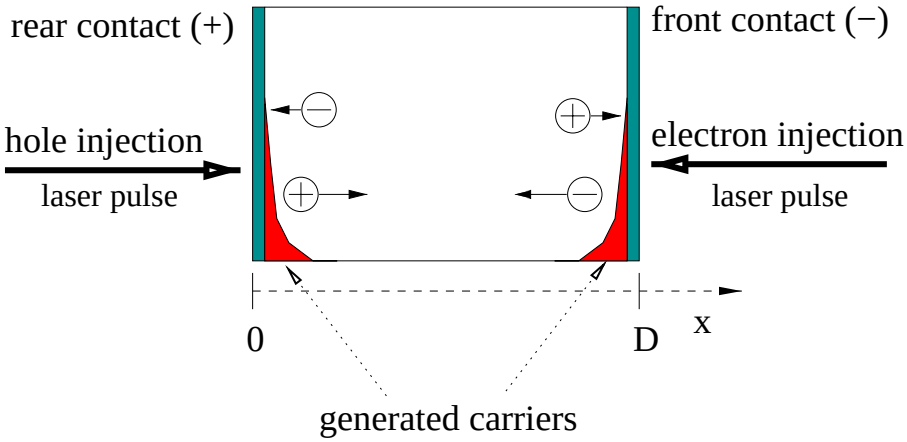

Figure 4.12 : Schematic view of TCT operation.

If N electron-hole pairs are created in the direct vicinity of the front or rear contact of the fully depleted detector (Fig. 4.12) either only electrons or holes will travel across the whole detector. The complementary carriers are collected immediately by the adjacent electrode. These two situations are therefore referred to as electron and hole injection. In reality, free carriers are not generated in the negligibly small distance from the surface but rather exhibit an exponential spatial distribution

$$n(x, t=0) = p(x, t=0) = \frac{N_{e-h}}{\alpha_{abs}\, S_i} \begin{cases} \exp\left(-\frac{(D-x)}{\alpha_{abs}}\right) & \text{electron injection} \\ \exp\left(-\frac{x}{\alpha_{abs}}\right) & \text{hole injection} \end{cases} \qquad x \in [0, D] \quad (4.4)$$

where N_{e-h} denotes the number of generated electron hole pairs, S_i the illuminated area and α_{abs} the absorption length, whose dependence on the wavelength of the laser and the temperature can be found in Appendix F. From now on the x axis of the coordinate system is supposed to originate in the back (n^+) electrode and point towards the front (p^+) electrode.

Red laser

In general the total induced current will be the sum of both $I(t) = I_h(t) + I_e(t)$. However, using the red laser with a wavelength of $\lambda = 670$ nm with penetration depth of $\alpha_{abs}(293\ \mathrm{K}) = 3.3\ \mu$m the contribution of carriers drifting to the adjacent electrode to the total induced current is negligible. An example of induced currents at different voltages after electron and hole injection is shown in Fig. 4.13.

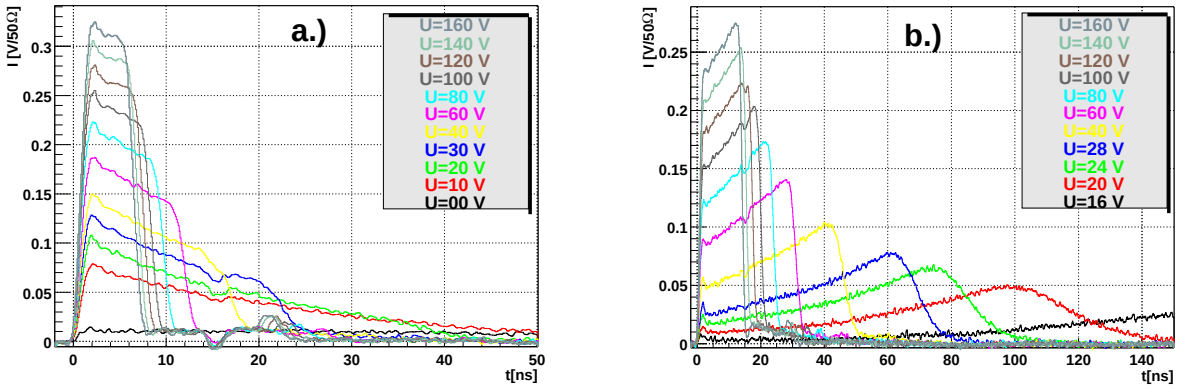

Figure 4.13 : Current pulse shapes measured at $T = 293$ K at different bias voltages after a.) electron and b.) hole injection in an non-irradiated $p^+ - n - n^+$ pad detector ($V_{FD} = 14$ V). Electrons and holes were generated by a short (1 ns) 670 nm laser pulse.

The electron drift velocity is large in the beginning of the drift and decreases towards the end of drift (Fig. 4.13a). This clearly indicates a high electric field region at the front contact and lower electric field at the back contact. On the other side, holes are generated in the low field region and their drift velocity increases during their passage through the detector. Such electric field profile is in agreement with electric field in the non-irradiated detector with an effective space charge being positive. Hence one of the main benefits of the current pulse measurement is the direct evidence of the sign of the space charge. An increased reverse bias voltage results in a higher electric field and accordingly larger induced current. At high electric field strengths the drift velocity starts to saturate. Generally the drift time of holes is around three times longer than for electrons. This is in agreement with the ratio of mobilities.

If the reverse bias is smaller than V_{FD} and the space charge is positive, electrons injected at the front contact travel towards the low field region with a reduced velocity, causing a long tail in the current to emerge. In contrast to that, holes are injected at the back and have to diffuse through the undepleted bulk region in order to reach the depleted region where they are swept by electric field. Since diffusion is a relatively slow process the peak of the induced current appears at late times.

If the space charge is negative the above picture is inverted. The induced current of electrons has qualitatively the same shape as the induced current of holes in the case of positive space charge and vice versa.

IR laser

An IR laser with $\lambda = 1060$ nm, has a penetration depth a few times larger than the detector thickness. Free carriers are generated almost uniformly along the beam as by a charged particle traversing the detector (Fig. 4.14). The total induced current is the sum of electron and hole currents. It can be calculated as,

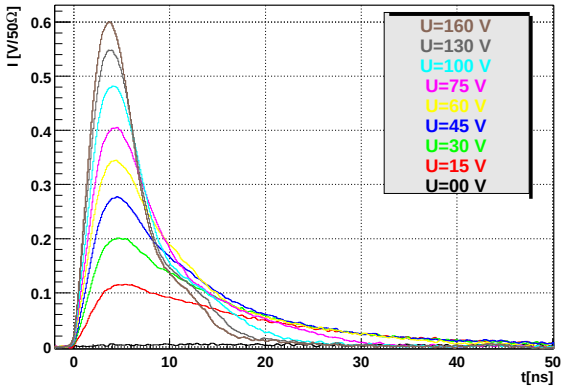

Figure 4.14 : Current pulse shapes measured at $T = 293$ K at different bias voltages after generation of free carriers in an non-irradiated $p^+ - n - n^+$ pad detector ($V_{FD} = 60$ V). Electrons and holes were generated by as short IR laser pulse.

$$I_{e,h}(t) = \int_0^D \frac{e_0\, N_{e-h}}{\alpha_{abs}\, D}\, v_{dr_{e,h}}(t, \grave{x})\, \exp(\frac{-t}{\tau_{eff_{e,h}}})\, \frac{\exp(-\grave{x}/\alpha_{abs})}{1 - \exp(-D/\alpha_{abs})}\, d\grave{x}, \qquad (4.5)$$

where $v_{dr_{e,h}}(t, \grave{x})$ is obtained from the solution of the motion equation for a point charge generated in $\grave{x}$ at $t = 0$ (see Eq. 2.34). In the initial phase of the current evolution, larger contribution to the total current comes from electrons drifting to the back contact. The tail of the signal comes from holes created close to the back contact and drifting to the front contact. The full charge collection time is determined by the drift time of holes.

4.3.2 Experimental Setup

The experimental setup (Fig. 4.15) is in principle the same as the setup from other groups [Ere95, FeicT] with a couple of differences. The core of the setup is a fast wide-band current amplifier (0.01-1GHz) connected to the detector on one side and to the digitizing osciloscope (TDS 754C) on the other side. The osciloscope is able to provide a maximum of 1 G samples per second at the analog band-width of 500 MHz. In order to decouple the voltage source and the input of the amplifier a Bias-T (Picosecond PulseLab 5532) was used. The voltage source (Keithely 2001) also served as a current meter.

Two laser diodes with a wavelength of $\lambda = 670$ nm and $\lambda = 1060$ nm were used. They were driven with six parallel advanced high-speed CMOS Schmitt inverters and controlled with the TTL signal from a pulse generator (HP 8116A), which also provided the trigger

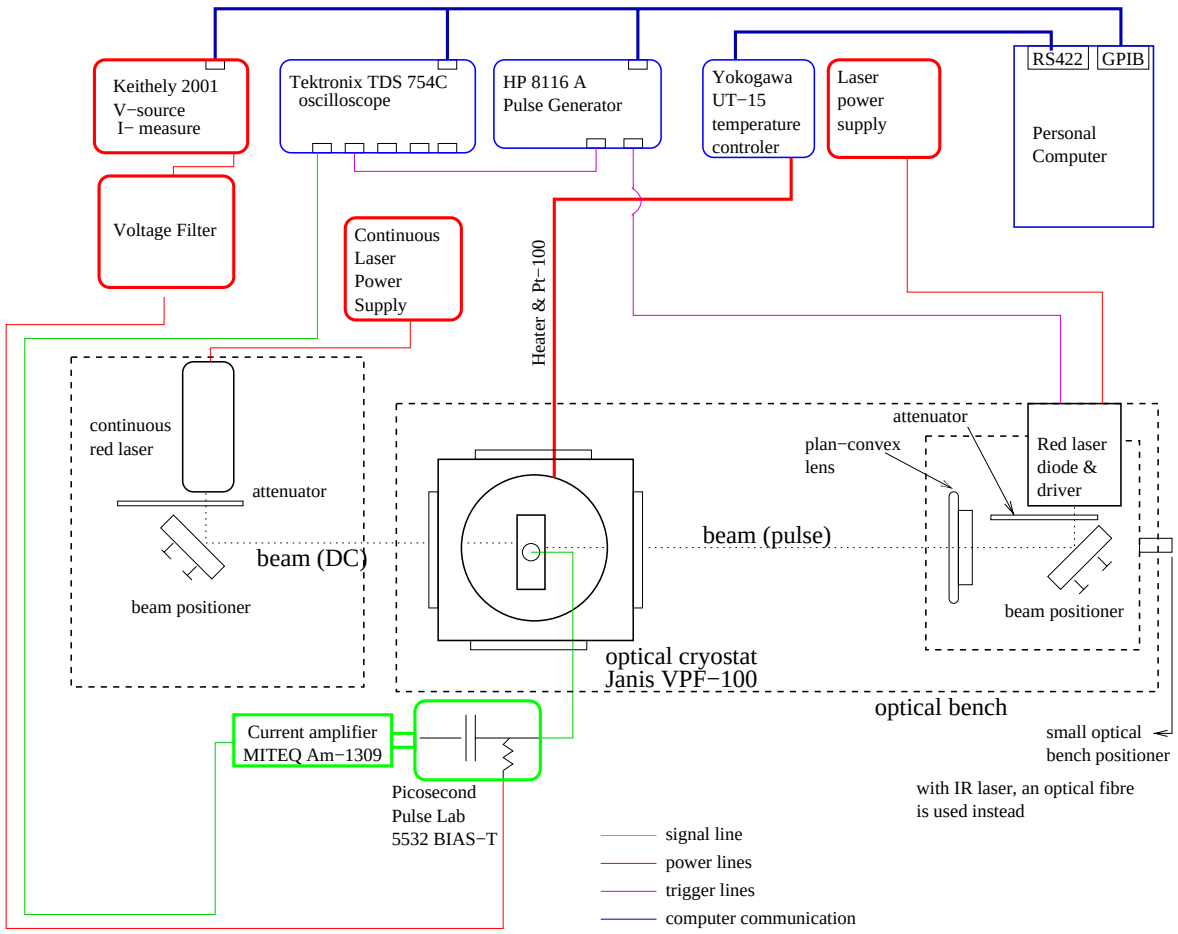

Figure 4.15 : Schematic top view of the TCT experimental setup. The Peltier cooling is not shown. The cryostat is in this case replaced by a plate with cold side facing to pulsed laser. Cooling of the warm side is provided by the air fans.

for the osciloscope. The resulting light pulse has a width of 1.4 ns FWHM as can be seen in Fig. 4.16.

The IR laser diode was coupled to a light guide with a cone of 0.3 rd at the output, while a more complex optical system was used to guide the light from the red laser diode. At the output the light was attenuated by a circular neutral density filter and focused with a $f = 100$ mm plan-convex lens. The diameter of the spot size was variable from a couple of mm to a minimum value of 100 μm.

The samples were mounted into an aluminum box to assure radio frequency shielding Fig. 4.17. For the same reason all the connections were made with semi-rigid micro-coaxial cables.

The cooling was provided either by a Peltier cooler, capable of controlling the temperature of the samples in the temperature range from $T = 273$ K to $T = 330$ K, or

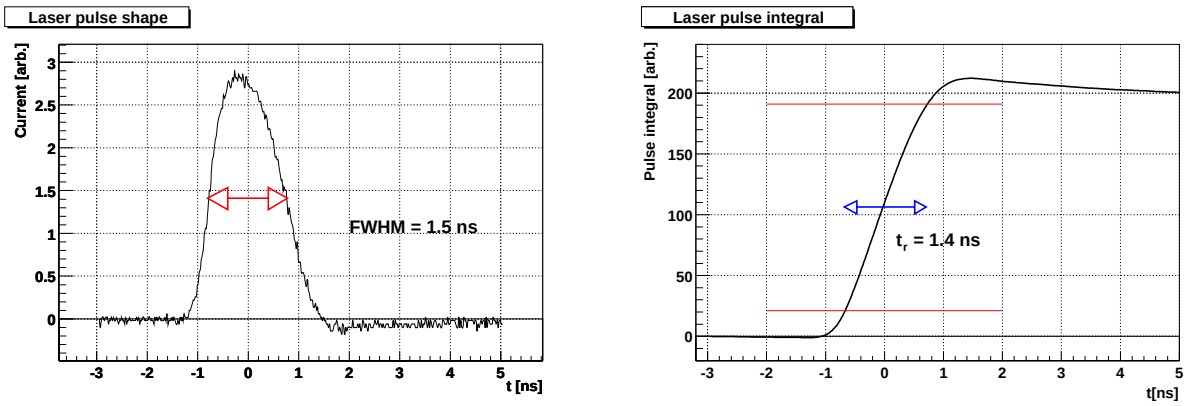

a.) b.)

Figure 4.16 : a.) Laser pulse shape as measured with a fast photo diode (rise time $\approx$ 100 ps) and recorded on the 500 Mhz osciloscope and b.) the pulse integral as a function of time.

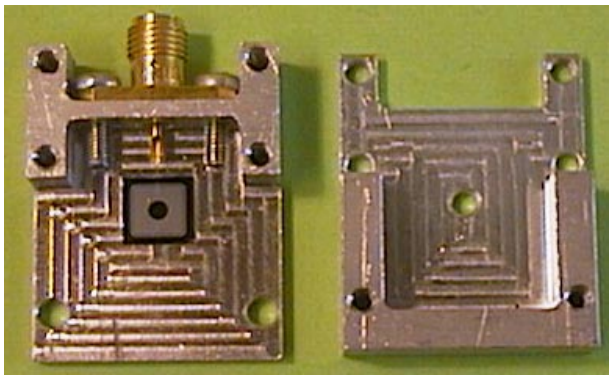

Figure 4.17 : The aluminum box providing the RF shielding. The sample can be seen on the left hand side.

by the pour-fill liquid-N_2 optical cryostat (Janis VPF-100) equipped with a heater and temperature controller (Yokogawa UT-15). The temperature was measured with a Pt-100 sensor and stabilized to 0.2K.

The choice of the optical cryostat offered a possibility of continuous illumination of both detector sides by using another red laser. In that way holes or electrons were continuously (DC) injected.

4.3.3 Data acquisition and signal deconvolution

The data acquisition was fully controlled by a computer. The data taken were stored to disk and analyzed with custom written software.

The equivalent circuit of the read-out system is shown in Fig. 4.18. Such a circuit acts like an amplifying ($A = 55$ dB) low pass filter (RC-shaper). The transfer function of

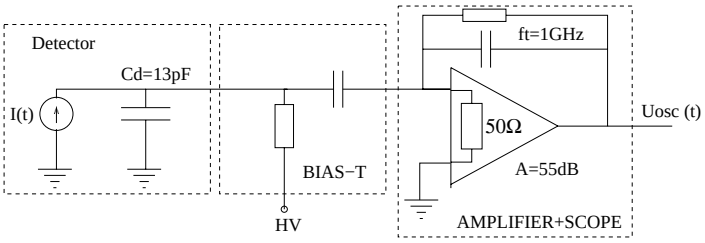

Figure 4.18 : The equivalent circuit used to extract the transfer function. The circuit acts as an amplifying RC-shaper.

the circuit ξ can be calculated in the frequency domain as:

$$\frac{1}{Z} = \frac{1}{R} + j\,\omega\,C_d \quad , \quad j = \sqrt{-1} \tag{4.6}$$

$$U_{osc}(\omega) = A\,Z\,I(\omega) = \xi(\omega) I(\omega) \tag{4.7}$$

$$\xi(\omega) = \frac{A\,R}{1 + j\,\omega\,C_d\,R} = \frac{A\,R}{1 + j\,\omega\,\tau_{TCT}} \quad , \tag{4.8}$$

where U_{osc} is the voltage measured at the osciloscope, I the induced current, C_d the detector capacitance, $R = 50\ \Omega$ the input impedance of the oscilloscope and $\tau_{TCT} = R\,C_d$. The pad detectors had dimensions of approximately 6×6 mm^2 [35], which gives $C_d = 13$ pF and $\tau_{TCT} = 650$ ps. This is a cut-off frequency of $\nu_d = 1/(2\pi\tau_{TCT}) = 244$ MHz which is much less than the cut-off frequency of the current amplifier $\nu_t = 1$ GHz. The induced current transfer function is therefore completely dominated by the detector capacitance and osciloscope impedance. The decoupling capacitor which is in series with R (BIAS-T) has a very high capacitance ($\sim 1\ \mu$F) and is transparent for induced currents and therefore neglected.

Eq. 4.7 can be written in the time domain as

$$U_{osc}(t) = \frac{A\,R}{\tau_{TCT}}\, e^{\frac{-t}{\tau_{TCT}}} \int_{-\infty}^{t} I(t') e^{\frac{t'}{\tau_{TCT}}} dt' \quad . \tag{4.9}$$

From here it follows that each pulse can be accounted for the transfer function (deconvoluted) as

$$I(t) = \frac{\tau}{R}\frac{dU_{osc}(t)}{dt} + \frac{U_{osc}(t)}{R} \quad . \tag{4.10}$$

The transfer function and the diode capacitance were verified by using a non-irradiated high resistivity diode (15 kΩcm) with $V_{FD} \approx 14$ V (see Table 5.1 , diode from wafer

[35] The active area was 5×5 mm^2. The guard ring, however, also contributes to the capacitance and has to be included in the calculation. The calculated value agrees well with measurements of non-irradiated pad detectors.

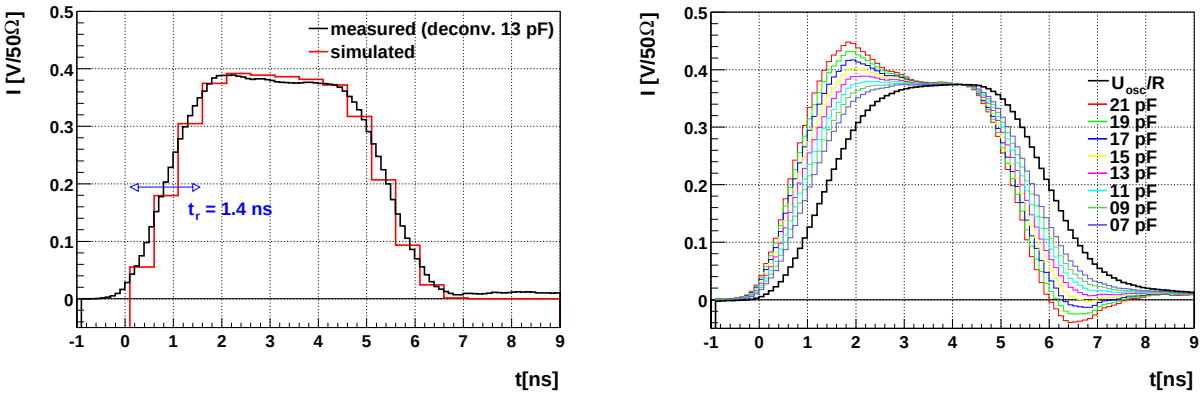

Figure 4.19 : a.) Simulated and measured (deconvoluted with $C_d = 13$pF) induced current at $U = 180$ V and $T = 293$ K. The rise time t_r of the measured induced current is in agreement with the rise time of the laser pulse (see Fig. 4.16). b.) Measured current pulses after deconvolution with different values of C_d. The non-deconvoluted current pulse is also shown (black line).

W339). The electric field in such diode at $U = 180$ V is almost linear and therefore every individual electron (in case of electron injection) induces a constant current along the whole drift. If the electron drift time is larger than the laser pulse duration, the rise of the induced current (Fig. 4.19a) coincides with the rise of the laser pulse (Fig. 4.16b).

The measured induced current deconvoluted with $C_d = 13$ pF is also in good agreement with simulation [36] (Fig. 4.19a). Variation of τ_{TCT} in Eq. 4.10 through variation of the capacitance confirms the choice of $C_d = 13$ pF as can be seen in Fig. 4.19b. At capacitances larger than 13 pF a bump in the induced current at times around rise time and undershoot at the end of the current pulse emerge. If the capacitance is lower than 13 pF the slope of the induced current after the rise gives the wrong sign of the space charge.

4.3.4 Calibration of the setup

It is important to determine the number of electron-hole pairs (N_{e-h}), created by the laser pulse. In case of electron-hole pairs concentration comparable or larger than the effective dopant concentration the electric field in SCR is screened. This influences the drift of free carriers and by that the induced current.

To determine the number of electron-hole pairs (N_{e-h}), created by the laser pulse, an energy spectrum of alpha particles, as well as the energy-loss spectrum of electrons from a ^{90}Sr source were recorded. A $p^+ - n - n^+$ pad detector manufactured by ITE on standard material with 300 μm thickness was used for this purpose. The full depletion voltage of the detector was $V_{FD} \approx 50$ V.

The intensity (number of photons) of the laser pulse was measured with light power meter. At a given repetition frequency of laser pulses ν and a measured average power $\bar{P}$

[36] The description of the simulation will be given in Chapter 7.

the number of generated electron-hole pairs N_{e-h} per pulse can be calculated as

$$N_{e-h} = \eta N_\gamma = \eta \frac{\bar{P}}{E_\gamma} = \eta \quad \frac{\bar{P}}{\nu} \quad \frac{\lambda}{1240\,\text{nm eV}} \tag{4.11}$$

where N_γ is the number of photons in the pulse, E_γ their energy and η the fraction of pulse energy used for $e-h$ pair generation. The measured induced current after electron injection at different light powers is shown in Fig. 4.20. At the repetition frequency

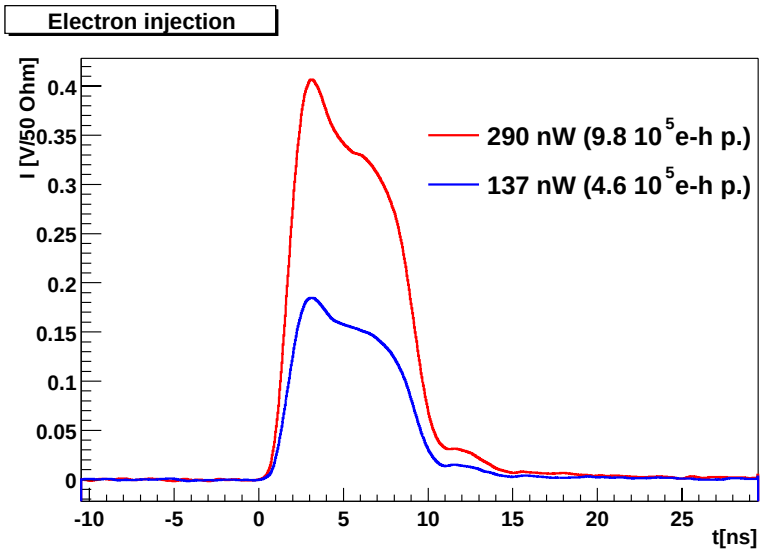

Figure 4.20 : Electron injection current shapes at $U = 100$ V for two different average powers at 500kHz. An average over 30 events is shown. The approximate number of generated electron-hole pairs per pulse N_{e-h} is given in the brackets.

$\nu = 500$ kHz and measured power $\bar{P} = 290$ nW with an assumption of $\eta = 1$ around $N_{e-h} = 9.8{\cdot}10^5$ were created. The resulting integral of the current measured on osciloscope

$$Q = A\, N_{e-h}\, e_0 = \int \frac{U_{osc}(t)}{R}\, dt \tag{4.12}$$

gives the value of $Q = 0.055$ nAs for the amplified charge. Reducing the power to $\bar{P} = 137$ nW one gets $Q = 0.025$ nAs, which confirms the linear scaling of the number of electron-hole pairs ($N_{e-h} = 4.6 \cdot 10^5$) with power.

To verify calculated N_{e-h} and to estimate η, measurements using α particles from ^{241}Am source ($E_{max} = 5.8$ MeV) were performed . The recorded spectrum is shown in Fig. 4.21a. The most probable energy loss of alpha particles corresponds to a measured charge $Q = 0.068$ nAs assuming $\eta \approx 1$. The resulting number of electron-hole pairs is approximately $N_{e-h} = 1.22 \cdot 10^6$. This corresponds to a deposited energy of 4.4 MeV. An around 20% lower detected energy can be explained by ionizing losses in the source cover, 5 mm layer of air and the SiO_2 pasivation layer.

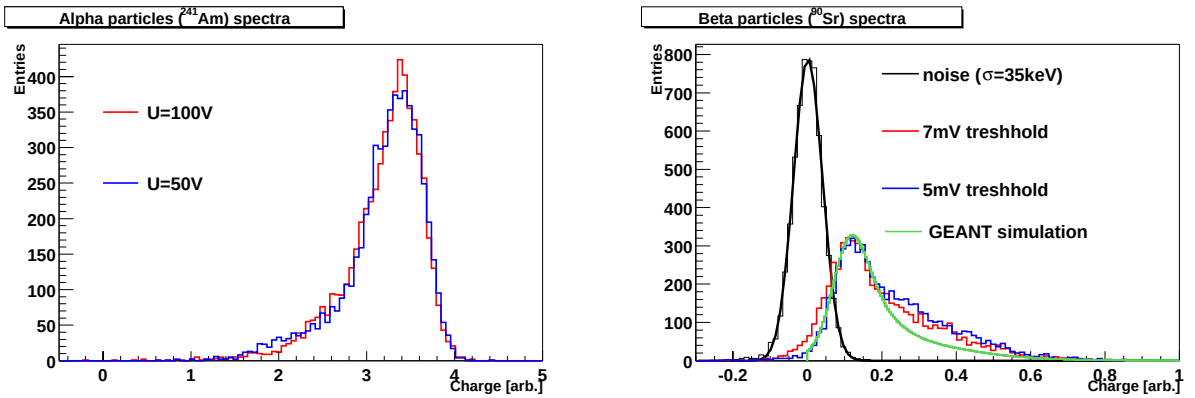

a.) b.)

Figure 4.21 : Spectrum of the α-s from ^{241}Am source after penetrating source housing, 5 mm of air and pasivation of the diode a.). Spectrum of the ^{90}Sr electrons in the silicon pad detector b.). Different trigger thresholds and noise are shown. The measured spectrum is compared with simulated one.

Both photons ($\lambda = 670$ nm) and α particles penetrate only a few microns into silicon, while electrons from the strontium source deposit their energy along the full path in the diode. The recorded spectrum is shown in Fig. 4.21b. Since a self-triggering mode[37] was used both the electrons stopped in the diode and those penetrating through it contributed to the energy loss spectrum. A GEANT simulation was used to predict the position of the peak in spectrum. It was found to be at ~ 110 keV$\equiv 31000\, e-h$ pairs. The corresponding amplified charge was $Q = 0.0024$ nAs. From the measurements with visible light and alpha particles around a 25% larger Q would be expected. The difference can be attributed to the relatively low signal to noise ratio and consequent error on the most probable energy determination, and also to uncertainty in simulation.

The calibration confirmed a much smaller density of created electron-hole pairs compared to N_{eff} when using the light of $\lambda > 670$ nm. For a typical red light beam spot of an area of 1 mm^2 and $N_{e-h} = 3 \cdot 10^5$ pairs created in depth of around 10 μm [38] one gets $N_{e-h}/V_{e-h} \approx 3 \cdot 10^{10}$ cm^{-3} $\ll N_{eff}$. In the case of hole injection where the mesh metalization of the back side was used the illumination area was even larger, hence the concentration of electron-hole pairs was lower. It can be concluded that the space charge is not significantly screened by the generated free carriers.

[37] The number of created electron-hole pairs was to small to induce current high enough to use an edge trigger. Instead, a few ns wide positive pulse of a minimum height (threshold) was required to trigger the acquisition.

[38] Due to finite duration of the pulse the electron-hole pairs created earlier already drifted away before the latter pairs are created. This assumption was done at bias voltage of 10 V. At higher voltages the depth of creation is larger than 10 μm.

5

TCT measurements with diodes

5.1 Samples

Several p^+-n-n^+ pad detectors processed on high (15 kΩcm) and low resistivity (1 kΩcm, 2 kΩcm) standard and oxygen enriched silicon wafers were irradiated. The samples were produced at ST Microelectronics and at Brookhaven National Laboratory (BNL). Their properties and treatment is listed in Table 5.1.

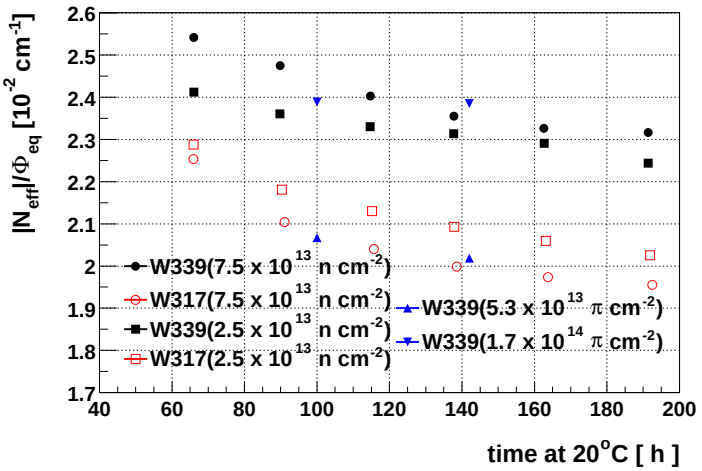

Figure 5.1 : Evolution of the effective dopant concentration after irradiation. For easier comparison N_{eff} is normalized to the fluence. The fit intervals used for determination of V_{FD} of each sample were kept fixed for all steps thus minimizing the systematic error.

During and after irradiation the diodes were kept unbiased. After the irradiation they were mounted onto an aluminum support (Fig. 4.17) using a room-temperature curing conductive glue. Then they were annealed at $T = 20°C$ to the minimum in V_{FD}. The evolution of N_{eff} during annealing was measured with the C/V method at the frequency $\nu = 10$ kHz (Fig. 5.1). The minimum values of V_{FD} are shown in Fig. 5.2. There

is a nearly perfect agreement of V_{FD} for samples fabricated on non-oxygenated high-resistivity material at equal NIEL equivalent fluences for different particles. Taking into account the negligible remaining donor concentration after irradiation this confirms the dosimetry measurements at different irradiation sites. Once reaching the minimum in V_{FD} the diodes were stored at $T = -17°C$ until the measurements were performed.

Sample	Oxygenation	Initial resistivity and V_{FD}	Fluences Φ_{eq} [10^{13} n/cm^2]
W339	no	15 kΩcm V_{FD} =10-15 V	neutrons: 0, 2.5, 5, 7.5, 10, 15, 20 pions: 5.3, 16.7 protons: 5.6 , 10.9 , 19.9
W336	no	2 kΩcm $V_{FD} \approx$ 135 V	neutrons: - pions: 5.3, 16.7 protons: 10.9 , 19.9
W333	no	1 kΩcm $V_{FD} \approx$ 295 V	neutrons: - pions: 9.5, 24 protons: 10.9 , 19.9
W317	60 h at $T = 1200°C$	15 kΩcm $V_{FD} \approx$ 20 V	neutrons: 2.5, 7.5 pions: - protons: 5.6, 19.9
W309	60 h at $T = 1200°C$	2 kΩcm $V_{FD} \approx$ 135 V	neutrons: - pions: 9.5, 24 protons: 10.9 , 19.9
W301	60 h at $T = 1200°C$	1 kΩcm $V_{FD} \approx$ 295 V	neutrons: - pions: 9.5, 24 protons: 10.9
BNL920	no	$\approx$ 1 kΩcm V_{FD} =170-210 V	neutrons: 10, 20 pions: - protons: -
BNL917	12 h at $T = 1200°C$	$\approx$ 1 kΩcm $V_{FD} \approx$ 250 V	neutrons: 10, 20 pions: - protons: -

Table 5.1 : Diode properties and irradiation fluences. Samples labeled with W were processed by ST Microelectronics on Wacker silicon wafers, while those labeled with BNL were processed on Topsil silicon. Time and temperature of diffusion oxygenation is given. The silicon crystals were cut along the $< 111 >$ plane.

5.2 Determination of effective trapping time

The dependence of effective dopant concentration and leakage current damage constant on fluence, time after irradiation and temperature was studied in the past in great detail

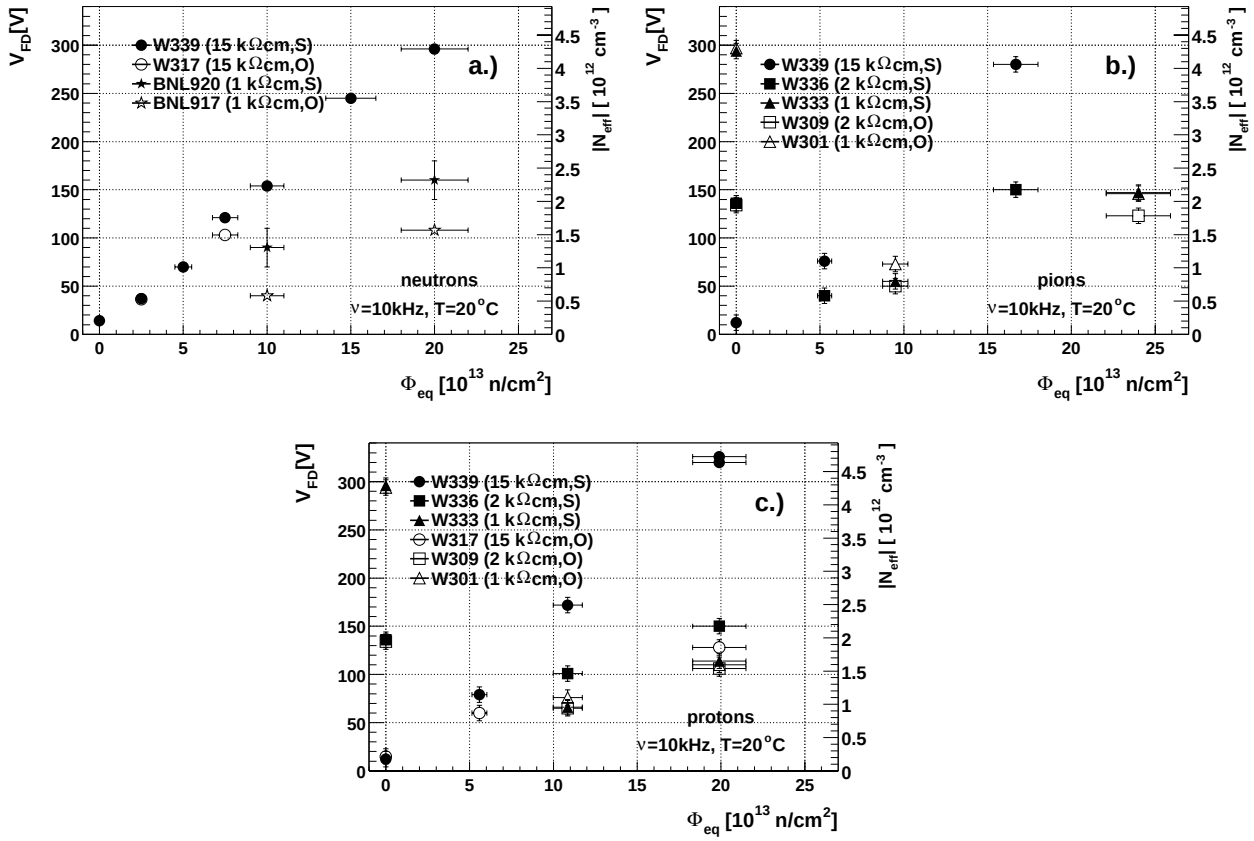

Figure 5.2 : V_{FD} as measured with the C/V method at the annealing minimum: a.) neutron, b.) pion and c.) proton irradiation. V_{FD} of the BNL920 samples has a larger uncertainty due to non-ideal C/V characteristics. The material type is given in brackets: O for oxygenated and S for standard material.

for different silicon materials and irradiation particle types. Although very important, the systematic study of effective doping concentration and leakage current can be attributed also to well established methods for their determination (C/V and I/V technique). Far less work was devoted to study of effective trapping times, mainly because of lacking a simple and reliable determination procedure. Most measurements were focused to the reduction of charge collection efficiency (see Chapter 6) which depends on the effective trapping times but also on the drift velocity.

The effective trapping times can be calculated from measured defects' cross sections and introduction rates obtained by other methods (i.e. Deep Level Transient Spectroscopy (DLTS), Thermally Stimulated Current (TSC)). The inaccuracy of cross-section measurements, sensitivity to all defects and determination of defects' introduction rates (g_t) all contribute to a very inaccurate determination of effective trapping times.

The transient current technique is an ideal tool to study effective trapping times, because of the known induced current pulse shape. In the past different methods, based on TCT, were exploited for the determination of effective trapping times.

Method proposed in [Kra93][39] requires the measurement of induced current pulse duration and its integral-charge, after electron or hole injection. The difference in collected charge between irradiated (Q_{irr}) and non-irradiated detector (Q_{nirr}) is the trapped charge. The effective trapping time is calculated from

$$
\begin{aligned}
Q_{nirr} &= \int_{t_s}^{t_e} I_{nirr}(t)\,dt = \int_{t_s}^{t_e} I_{irr}(t)\,dt \\
Q_{irr} &= \int_{t_s}^{t_e} I_{irr}(t)\exp(\frac{t-t_s}{\tau_{eff}})\,dt \approx Q_{nirr}(1-\frac{<t>}{\tau_{eff}}) \quad , \quad \tau_{eff} \gg t_c = t_e - t_s \qquad (5.1) \\
\frac{Q_{nirr}-Q_{irr}}{Q_{nirr}} &\approx \frac{t_c}{2\,\tau_{eff}} \quad \text{where} \quad <t> \approx \frac{t_c}{2}
\end{aligned}
$$

where I_{nirr} and I_{irr} are the induced currents for non-irradiated detector and irradiated detector in absence of charge trapping, while t_s and t_e denote start time and end time of the current pulse. The weakness of this method is that it can be applied at low fluences only, where $t_c \ll \tau_{eff}$. Even if higher terms are included method fails if $t_c \lesssim \tau_{eff}$. It is also difficult to inject the same amount of electrons or holes by light for different measurements.

The method proposed in [Gar00] is similar to the previous method. Instead of the simple expression (Eq. 5.1) for the reduction of charge collection efficiency, a charge transport model, including the effective trapping probability, is assumed. The effective trapping times are those giving the best agreement between measured and simulated charge collection efficiency. The electron-hole pairs were generated in microstrip detectors by the use of an IR laser.

In the reference [Ler99] the induced current pulse shapes are fitted with a complex charge transport model where besides the effective trapping times the field profile and mobility parameterization were also free parameters of the fit. They were tuned to the best agreement of measured and calculated current responses.

Assuming a linear field and approximately constant mobility in the silicon bulk, the induced current pulse shapes after electron or hole injection can be fitted with $I(t)$ from Eq. 2.35 in the transient region [FeicT]. The unknown parameters of the fit are the amplitude of the current and the effective trapping time. The required transient time constant $\tau_{e,h}$ can be determined from the full depletion voltage by using Eq. 2.33. Determination of effective trapping times is very sensitive to any deviation of the electric field profile from the linear assumption and to the value of constant mobility. A solution of Eq. 2.31 where a constant mobility is replaced by a linear approximation can also be used to obtain better fits. For a detailed discussion the reader is referred to Appendix G.

The method used for determination of the effective trapping times used in this work is a new method which was recently proposed independently by [Kra00] and [Bro00]. It is based on the correction of time-resolved current pulse shapes due to trapping. It is general enough to be valid not only for solid state particle detectors, but also for other devices such as gaseous and liquid detectors.

[39] Instead of short wavelength laser light alpha particles were used.

5.2.1 Charge correction method

The measured charge in an non-irradiated detector reaches a plateau at voltages exceeding V_{FD}, provided the current integration time is longer than the drift time of electrons and holes. This indicates that trapping is negligible before irradiation.

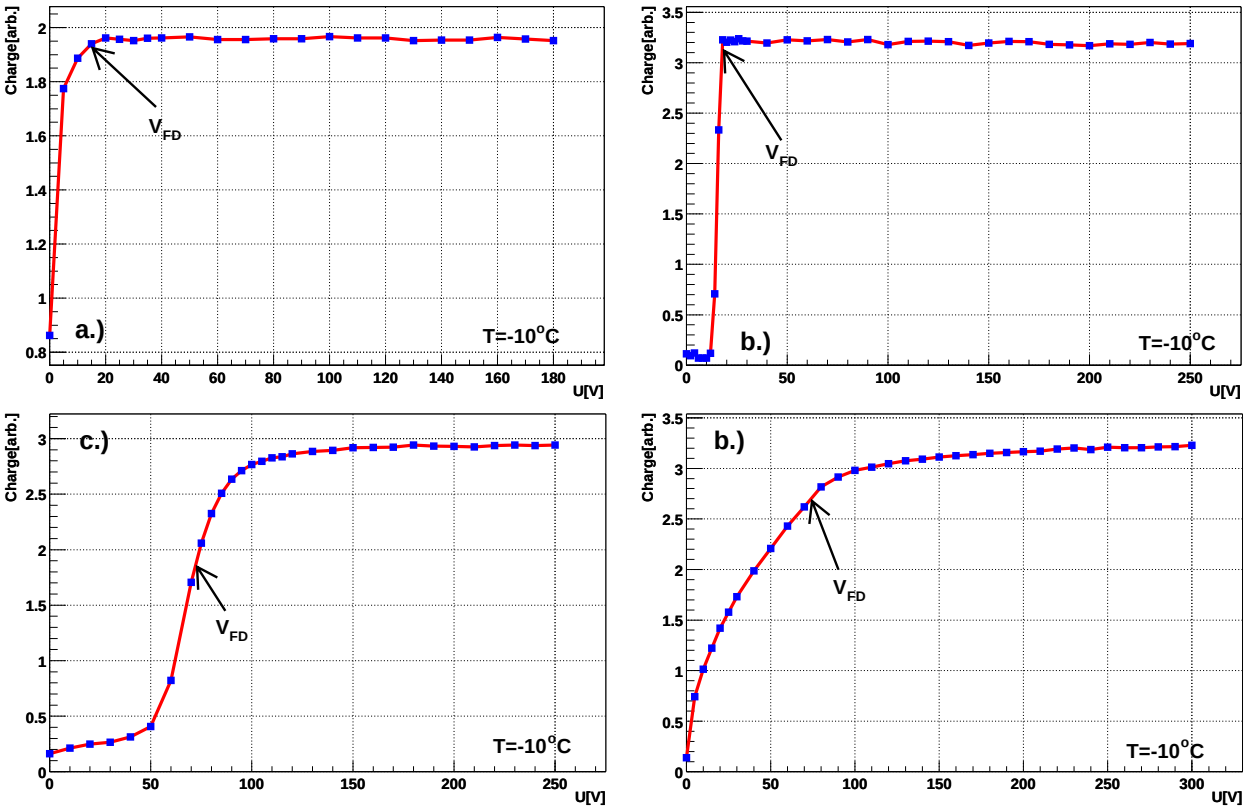

Figure 5.3 : Measured charge integrated over 60 ns after: a.) electron injection and b.) hole injection in the non-irradiated sample W339 and the same for the sample irradiated to $\Phi_{\text{eq}} = 5 \cdot 10^{13}$ n/cm^2 : c.) electron injection and d.) hole injection. For the irradiated sample the measured charge does not saturate at voltages above V_{FD}. The y-axis unit corresponds to $\approx 3 \cdot 10^5$ e-h pairs.

During the drift through an irradiated detector a part of the drifting charge is trapped at radiation-induced traps. An increase of drift velocity due to the higher field at voltages above V_{FD} reduces the drift time of the charge and by that the amount of the charge being trapped (Fig. 5.3). If the integration time of the induced current is large enough, all the trapped charge is detrapped and the collected charge (current integral) saturates at voltages above V_{FD}. At LHC, however, a short bunch crossing time (BCT=25 ns) and a large number of created particles require short shaping times of readout electronics in order to relate signals to the corresponding bunch crossing. If the detrapping times are much longer than BCT (Eqs. 3.27, 3.28), the charge once trapped is lost for the measurement [Ci00E].

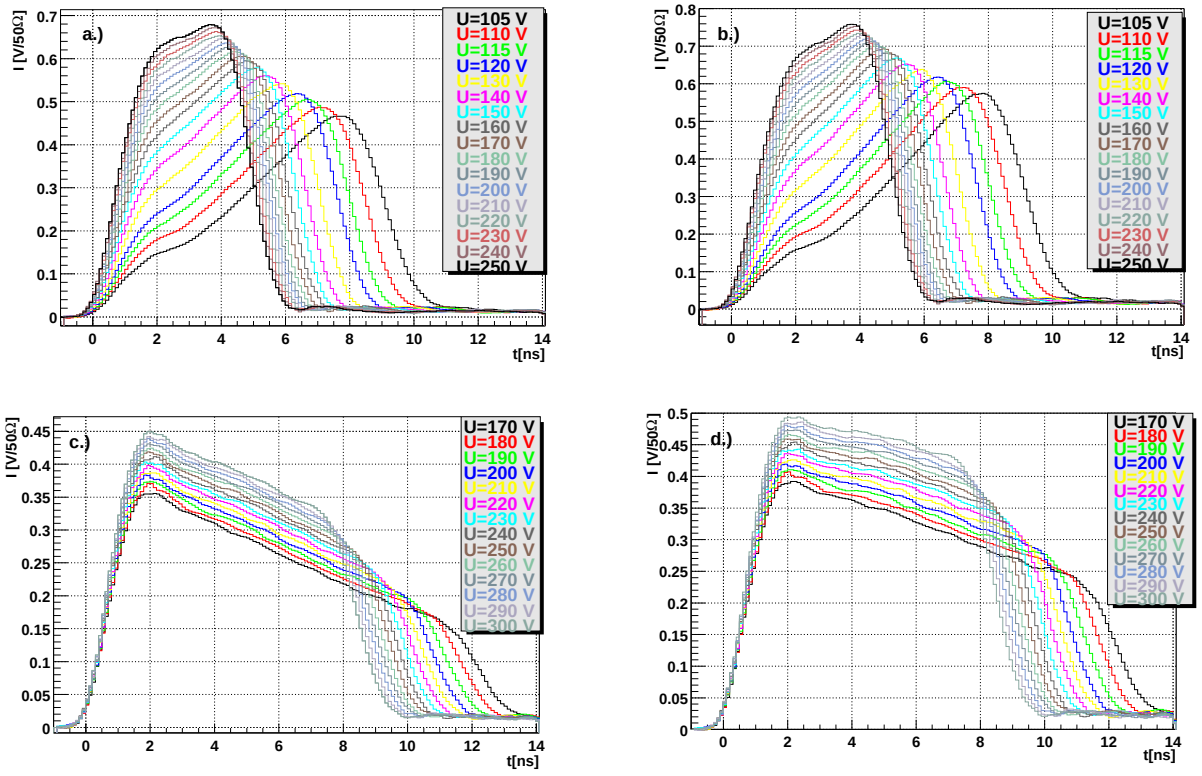

Figure 5.4 : Measured and corrected induced current shapes for the sample W339 irradiated to $\Phi_{\text{eq}} = 5 \cdot 10^{13}$ n/cm^2 and measured at $T = -10°$ C: a.) measured electron, b.) corrected electron, c.) measured hole, d.) corrected hole signals.

The induced current from an instant hole or electron injection in the diode is given by Eq. 2.29. The amount of the drifting charge decreases with time due to trapping as

$$N_{e,h}(t) = N_{e,h}(0) \exp(\frac{-t}{\tau_{eff_{e,h}}}) \quad . \tag{5.2}$$

The effective trapping time can be determined from the current integral at voltages above V_{FD}. From Eqs. 2.29 and 5.2 it can be seen that correcting the measured $I_m(t)$ with a single exponential can compensate for trapping (Fig. 5.4), provided that the laser pulse is short compared to the drift time:

$$I_c(t) \; = \; I_m(t) \; \exp(\frac{t - t_0}{\tau_{tr}}) \quad . \tag{5.3}$$

Here t_0 is the carrier injection time, in our case set to the start of the laser pulse.

If τ_{tr} in Eq. (5.3) represents the correct effective trapping time then the integral of I_c over time is equal for all voltages above V_{FD} (Fig. 5.5). At voltages below V_{FD} the correction of current shapes cannot be done with a single effective trapping time, since the occupation of traps ($P_t^{h,e}$) in the depleted region and undepleted bulk is different.

Therefore the method was applied at voltages above V_{FD} only. It is also evident that the ratio of measured and corrected charge at a given voltage represents the charge collection efficiency.

An example of extracting the effective trapping probability for electrons is shown in Fig. 5.5. If $1/\tau_{tr} > 1/\tau_{eff_{e,h}}$ the corrected charge is to high at low voltages where the charge drift is long and vice versa for $1/\tau_{tr} < 1/\tau_{eff_{e,h}}$. If $1/\tau_{tr} = 1/\tau_{eff_{e,h}}$ the corrected charge does not depend on voltage. The slope of the linear fit to the corrected charge as a function of voltage thus changes sign at $1/\tau_{tr} = 1/\tau_{eff_{e,h}}$. In Fig. 5.6 an example of

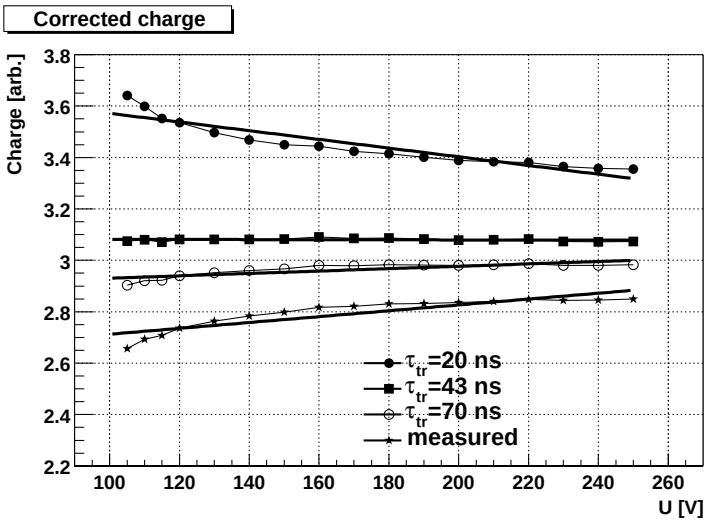

Figure 5.5 : Measured charge and charge corrected with different τ_{tr}.

finding the effective trapping probability is shown.

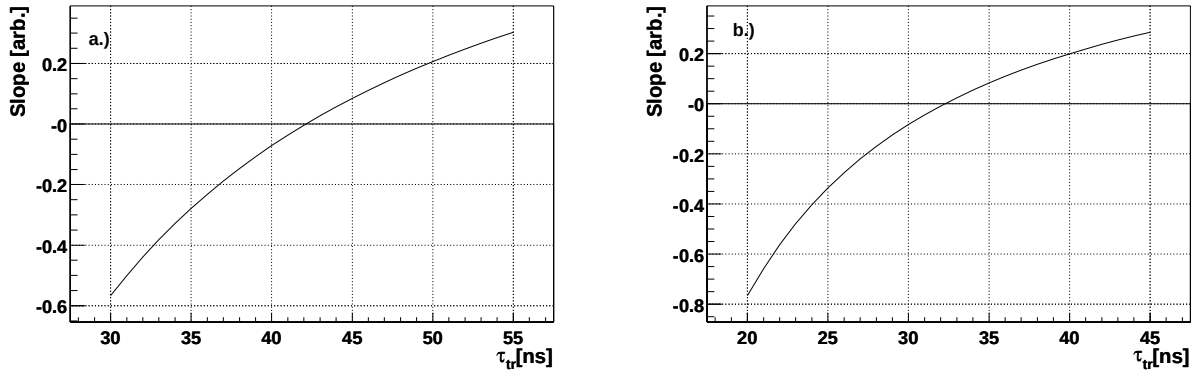

Figure 5.6 : The slope of the linear fit to the corrected charge vs. voltage as a function of τ_{tr} for the W339 sample irradiated to $\Phi_{\text{eq}} = 5 \cdot 10^{13}$ n/cm^2: a.) electrons and b.) holes. The effective trapping probability is determined from the zero intersection point.

The effective trapping time can also be determined from the corrected charge dependence on τ_{tr} at different bias voltages (see Fig. 5.7) [Bro00]. The point of intersection of

all curves gives the effective trapping time. The result is however the same.

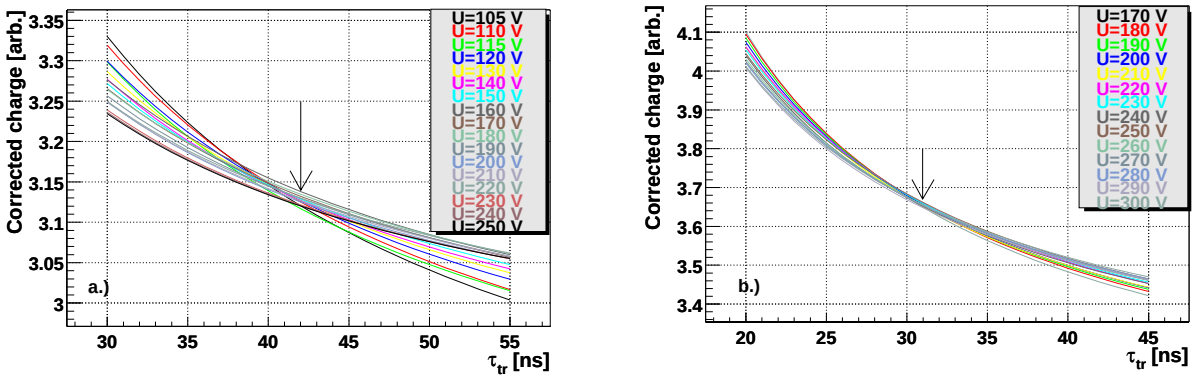

Figure 5.7 : The corrected charge dependence on τ_{tr} at different bias voltages for the W339 sample irradiated to $\Phi_{\mathrm{eq}} = 5 \cdot 10^{13}$ n/cm^2. The effective trapping probability is determined from the intersection point of the corrected charge curves at different voltages (denoted by arrow). The temperature was $T = -10^{\circ}$ C.

The uncertainty of the charge correction method comes from the variation of the slope given by the fit. The latter is related to the number of points included in the fit. The average error was estimated to 10% of the effective trapping time by changing the fit intervals on different samples. In Fig. 5.8 an example of the fit interval influence is shown. The τ_{eff} was always determined with the largest fit interval for which the duration of the induced current pulses was shorter than $t = 16$ ns [40].

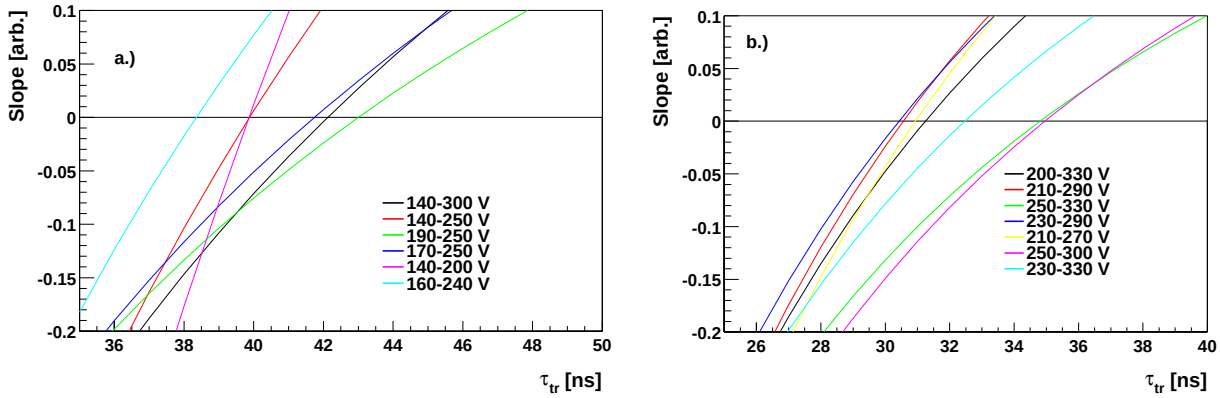

Figure 5.8 : Dependence of effective trapping time determination on the variation of the fit interval at $T = -10^{\circ}$C for the W339 sample irradiated to $\Phi_{\mathrm{eq}} = 5 \cdot 10^{13}$ n/cm^2: a.) electrons and b.) holes.

The stability of the method was tested on one diode kept at $T = -17^{\circ}$C between the measurements to prevent annealing. Therefore the effective trapping probability should be constant. This is confirmed in the Fig. 5.9. The difference in τ_{eff} between different

[40] This limit was imposed by appearance of signal reflection at latter times.

measurements is less than 10% and could be attributed to different fit intervals used. For comparison the effective trapping probability measured at different repetition rates of carrier injection is also shown. In the examined range of repetition rates (5-80 Hz) almost no effect of injection rate can be observed.

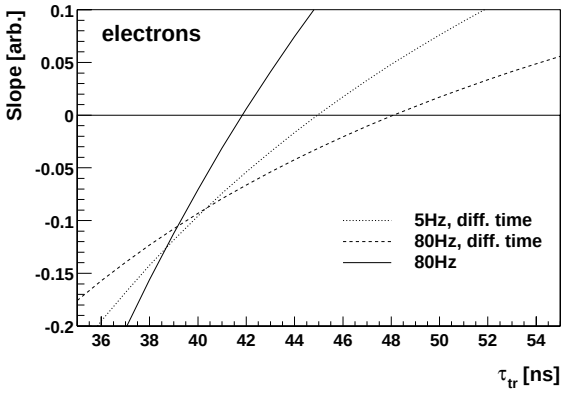

Figure 5.9 : Determination of τ_{eff} at different repetition rates of the laser pulse for the W339 sample irradiated to $\Phi_{\rm eq} = 5 \cdot 10^{13}$ n/cm^2 and measured at $T = -10^\circ$ C.

5.2.2 Material and particle dependence

The effective trapping probability for electrons and holes, measured at $T = -10^\circ$C after $\sim 6-10$ days of room temperature annealing, for different particles and silicon materials can be seen in Fig. 5.10. A clear linear dependence of the trapping probability on $\Phi_{\rm eq}$ can be observed, indicating an effective absence of trapping centres formed in second-order reactions. The resistivity of the silicon material in the range from 1 kΩcm to 15 kΩcm does not influence the effective trapping probability. There is also no difference between standard and oxygenated silicon materials, although the latter exhibits a smaller increase of negative space charge upon charged hadron irradiation [Lin00].

It appears, however, that different particle types have different $\beta_{e,h}$ (Eq. 3.51) as can be seen in Table 5.2. $\beta_{e,h}$ for charged hadrons are about 30-40% larger than those for neutrons. The effective trapping probability thus does not scale with NIEL when comparing neutrons with charged particles. As demonstrated in Section 5.1, the agreement of V_{FD} of standard material at the same equivalent fluences for different irradiations excludes a dosimetry error required to cause the observed level of $\beta_{e,h}$ dependence on particle type. A possible qualitative explanation could be that NIEL from charged hadrons produces more point defects than NIEL of neutrons which in turn creates more cluster defects. Point defects thus appear to be more efficient as trapping centres. Since oxygen acts as a vacancy sink and is observed not to influence trapping, these defects are likely to be interstitial-related.

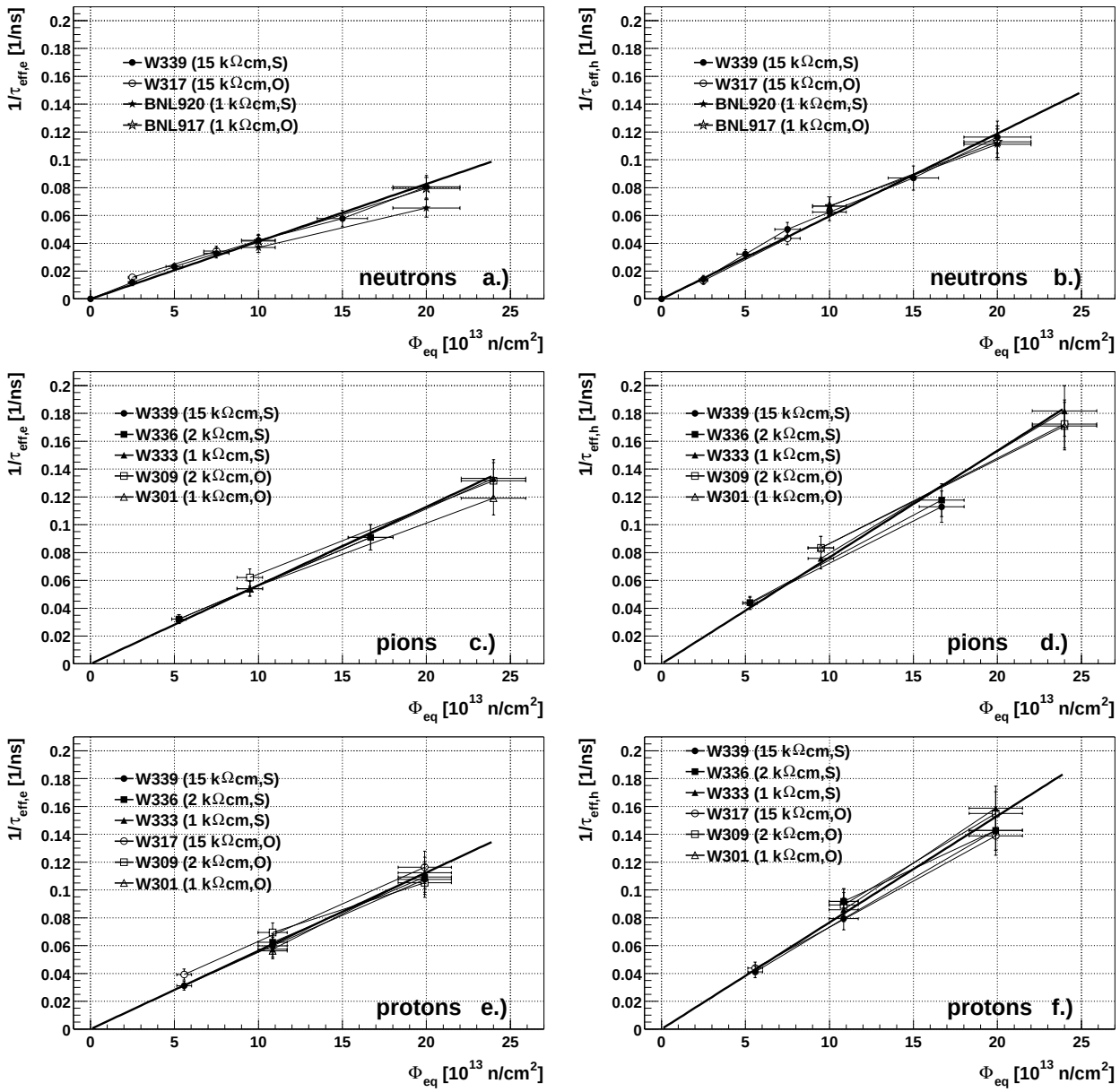

Figure 5.10 : Fluence dependence of effective trapping probability for electrons and holes for neutron, pion and proton-irradiated samples : a.)electrons (neutron irradiation), b.) holes (neutron irradiation), c.) electrons (pion irradiation) and d.) holes (pion irradiation) e.) electrons (proton irradiation) and f.) holes (proton irradiation). Measurements were taken at $T = -10°\mathrm{C}$ after $\sim 6 - 10$ days of annealing at room temperature. Resistivity and material type are given in brackets: O-oxygenated and S-standard material.

5.2.3 Temperature dependence

Three parameters in $\beta_{e,h}$ depend on temperature (see Eq. 3.50): thermal velocity of the carriers, capture cross-sections and occupation probabilities of the traps. A square-root temperature dependence is characteristic for $v_{th_{e,h}}$. The capture cross-section dependence

	β_e [10^{-16} cm^2/ns]	β_h [10^{-16} cm^2/ns]
neutrons	4.1 ± 0.1	6.0 ± 0.2
pions	5.7 ± 0.2	7.7 ± 0.2
protons	5.6 ± 0.2	7.7 ± 0.2

Table 5.2 : β for electrons and holes for different particle types at $T = -10°$C after ~ 10 days of room temperature annealing. The error quoted does not include a $\sim 10\%$ systematic error on dosimetry.

on temperature is poorly known, scaling as $\sigma(T)/\sigma(T_o) = (T/T_o)^m$ with m ranging between -2 and 2 is suggested in [Aba78, Hal96].

Let us assume that one defect dominates trapping of the drifting electrons and equivalently, there exists a dominating hole trap. The occupation probability of a trap, described by the energy level E_t, in the depleted region can be calculated by using Eq. 3.30. Temperature scaling of $\beta_{e,h}$, dominated by a single trap, can thus be written as:

$$\beta_{e,h}(T) = \frac{1}{\tau_{eff_{e,h}}\,\Phi_{\rm eq}} = \beta_{e,h}(T_o)\,\frac{1-P_t^{e,h}(T)}{1-P_t^{e,h}(T_o)}\left(\frac{T}{T_o}\right)^{m+\frac{1}{2}} \tag{5.4}$$

In order to study the dependence of effective trapping probability on temperature, measurements for all the diodes from Table 5.1 were performed in the temperature interval from 223 K to 293 K. The temperature range was constrained by practical limitations. For lower temperatures, fast drift, especially of electrons, rendered the experimental determination of τ_{eff} questionable. And at higher temperatures, the resulting reverse current was to high to be properly handled by our experimental set-up.

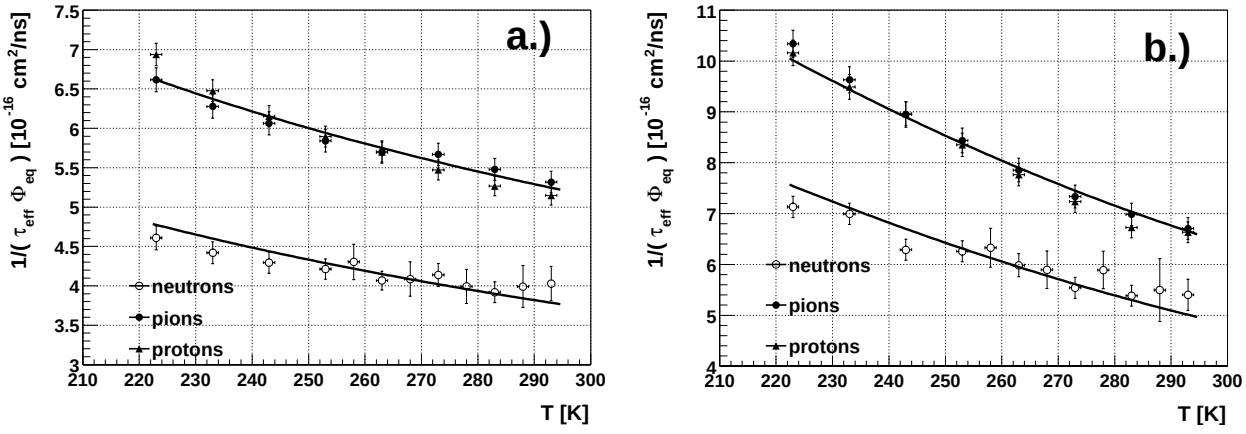

Figure 5.11 : Temperature dependence of β for: a.) electrons and b.) holes. The measured points are the average of βs for all measured samples.

The measured temperature dependence of average $\beta_{e,h}$ for all three particle types is shown in Fig. 5.11 exhibiting a 20 - 30 % decrease of trapping probability over the

temperature range covered. An examination of terms in Eq. 5.4 showed that such behavior could be caused either by a negative m in cross-section scaling, or by a near to mid-gap position of the trap, supported by an appropriate c_e/c_h ratio, or a combination of the two effects. Therefore, an extraction of separate trap parameters was considered unjustified. An effective parameterization of the form

$$\beta_{e,h}(T) = \beta_{e,h}(T_0) \cdot (\frac{T}{T_0})^{\kappa_{e,h}} \tag{5.5}$$

with $\kappa_{e,h}$ universal for all particle types yielded acceptable fits (see Fig. 5.11) to all data. Fit results are listed in Table 5.3. This could indicate, that the same two traps, albeit introduced at different rates, play the dominant role in trapping induced by neutron and charged hadron irradiation.

$\kappa_e = -0.86 \pm 0.06$	$\kappa_h = -1.52 \pm 0.07$

Table 5.3 : Parameters $\kappa_{e,h}$, determining temperature scaling of $\beta_{e,h}$, as obtained from the fit of Eq. 5.5 to measured data.

5.2.4 Annealing of effective trapping probability

With time, defects can either decay or interact with others to form new ones. The consequence of this is a change in effective trapping probability, covered by the annealing function $f_t(t)$ in Eq. 3.50. Annealing of $\beta_{e,h}$ was studied with two diodes from wafers W339 (standard, 15 kΩcm) and W317 (oxygenated, 15 kΩcm) irradiated with neutrons to 7.5 10^{13} cm^{-2}. After the diodes reached the minimum in V_{FD} at room temperature, accelerated annealing was performed in steps at 60°C. Between annealing steps TCT measurements were done at $T = 10$°C. The diodes were mounted to the same Peltier temperature regulator to ensure equal temperature history. Dependence of $\beta_{e,h}$ on annealing time is shown in Fig. 5.12. It can be seen that, for both standard and oxygenated material, β_e at 10°C decreases with time after irradiation by about 35%, while β_h increases by about 30%. An elementary model assuming the decay of the dominant electron trap into another stable one was evaluated and observed to describe the annealing data well. The same model, applied to the dominant hole trap, fits also the time dependence of β_h. The relevant fit function was

$$\beta_{e,h}(t) \; = \; \beta_{0_{e,h}} \cdot e^{-\frac{t}{\tau_{ta_{e,h}}}} \; + \; \beta_{\infty_{e,h}} \cdot (1 - e^{-\frac{t}{\tau_{ta_{e,h}}}}) \tag{5.6}$$

with $\beta_{0_{e,h}} \equiv \beta_{e,h}$ and $\beta_{\infty_{e,h}}$ the trapping rates at early and late annealing times, respectively. The results of the fits are gathered in Table 5.4. The same time development would also be obtained by assuming a trap with $\beta_s = \beta_\infty$, stable throughout the annealing, and decay or creation of a second defect with $\beta_d = \beta_0 - \beta_\infty$. Parameters for standard and oxygenated samples exhibit the same behavior within the rather large uncertainties.

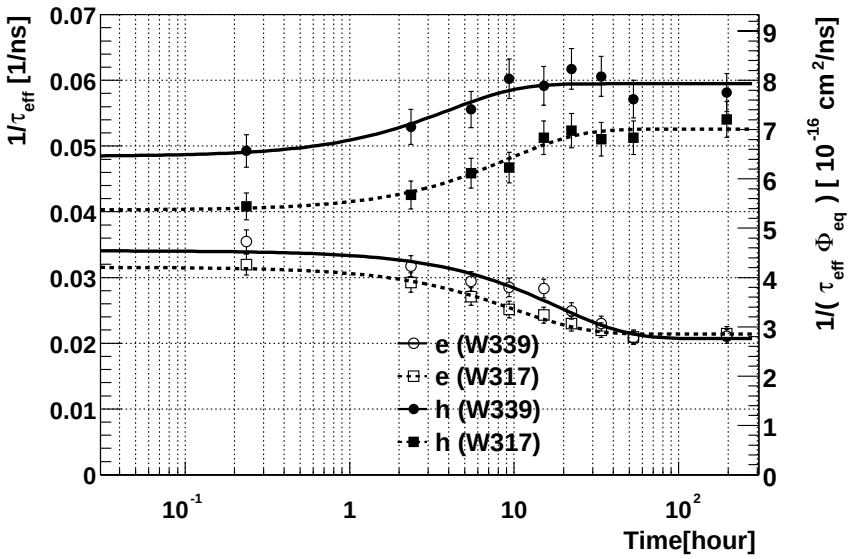

Figure 5.12 : Annealing of effective trapping probability at 60°C. Measurements were taken at $T = 10$°C.

	β_{0_e} $[10^{-16}\ \frac{\text{cm}^2}{\text{ns}}]$	β_{∞_e} $[10^{-16}\ \frac{\text{cm}^2}{\text{ns}}]$	β_{0_h} $[10^{-16}\ \frac{\text{cm}^2}{\text{ns}}]$	β_{∞_h} $[10^{-16}\ \frac{\text{cm}^2}{\text{ns}}]$	τ_{ta_e} [hour]	τ_{ta_h} [hour]
W339	4.5 ± 0.2	2.8 ± 0.1	6.5 ± 0.3	7.9 ± 0.2	19 ± 5	4.2 ± 2.3
W317	4.2 ± 0.2	2.8 ± 0.1	5.4 ± 0.3	7.0 ± 0.2	10.6 ± 3.5	9.7 ± 4.5

Table 5.4 : Amplitudes and time constants for the parameterization of β annealing.

Annealing times are of order of 10 hours at 60°C, about the same order of magnitude as characteristic times of reverse annealing. Although depending in detail on the activation energy, the effect of trapping probability annealing can thus be expected to play a rather marginal role in the lifetime of a typical LHC experiment.

	κ_e	κ_h
W339	-1.55 ± 0.24	-1.50 ± 0.24
W317	-1.58 ± 0.20	-1.50 ± 0.20

Table 5.5 : Temperature scaling parameter $\kappa_{e,h}$ as obtained from the fit of Eq. 5.5 to temperature dependence of the effective trapping probability for diodes W339 and W317 at the end of annealing.

After the last annealing step, temperature scans of both diodes were performed (Fig. 5.13). The temperature scaling parameter $\kappa_{e,h}$ (Table 5.5) of the effective trapping probability was found to be comparable with its value in the minimum of V_{FD} (Table 5.3) for holes, while for electrons its value increased nearly by a factor of two. As a consequence,

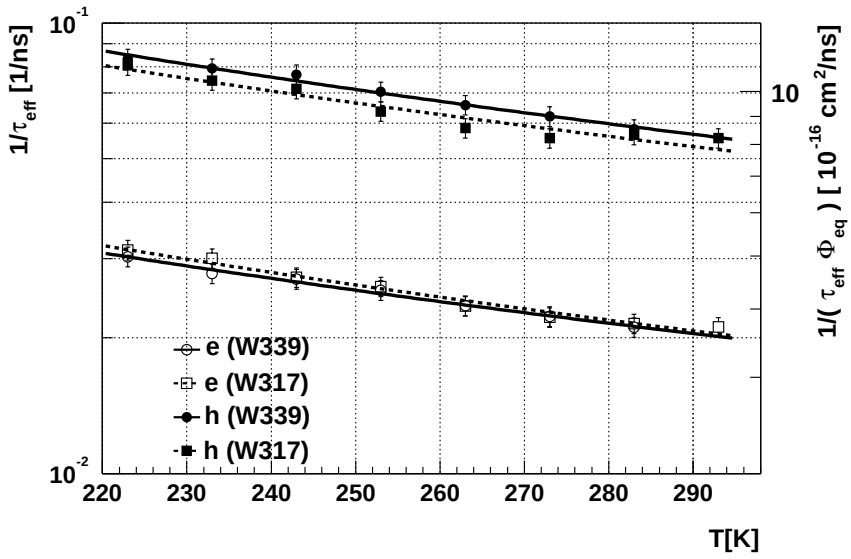

Figure 5.13 : Temperature dependence of the effective trapping probability for the W317 and W339 samples after the annealing procedure.

β_e at the end of annealing turns out larger than β_e at early annealing times, if measured at temperatures lower than -40°C.

5.3 TCT measurements of N_{eff} reverse annealing

Most of the reverse annealing measurements in the past were done using the C/V method. The voltage of full depletion can be, however, also determined from the TCT measurements.

If electrons are injected in a detector irradiated beyond the type inversion point almost no charge is observed at low voltages. The junction grows from the back side of the detector, hence electrons are injected in the low field region, which they must overcome by diffusion. Induced current integration time of 60 ns is too short for most of electrons to reach the part of the detector, where the field is high. At a given "pinch-off voltage" (V_{PO}) the undepleted region becomes so thin that 60 ns is enough for electrons to penetrate it by diffusion and the collected charge abruptly increases. Hence, V_{PO} depends on the integration time. Once the electric field is established in the whole detector ($V_{FD,TCT}$) any further increase of charge with the applied voltage is attributed to smaller amount of the charge trapped.

An example of $V_{FD,TCT}$ and V_{PO} determination is shown in Fig. 5.14a. The intersection point of two lines gives the $V_{FD,TCT}$ or V_{PO}. One can make the same considerations about the fit interval and errors as in the case of V_{FD} determination with the C/V method. A difference of 60 V between $V_{FD,TCT}$ and V_{PO} can be observed. It is not obvious if either $V_{FD,TCT}$ or V_{PO} correspond to V_{FD} as measured with the C/V method [Ere00, Ver00] (see Table 5.6).

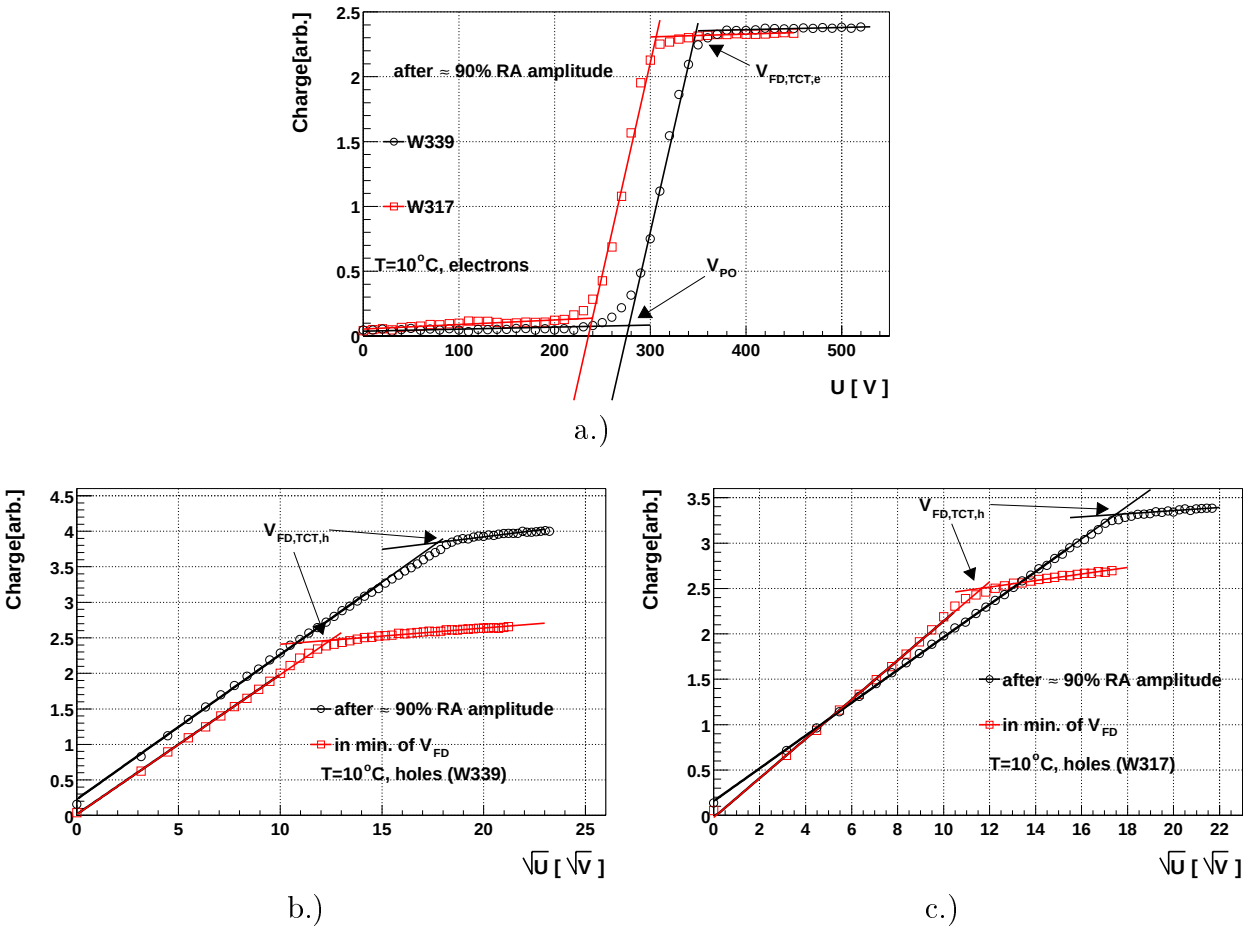

Figure 5.14 : a.) Determination of the $V_{FD,TCT}$ and V_{PO} in case of electron injection for a samples W339 and W317 irradiated with neutrons to $\Phi_{\text{eq}} = 7.5 \cdot 10^{13}$ cm^{-1} after $\approx 90\%$ of reverse annealing. Determination of the $V_{FD,TCT}$ from hole signals in the minimum of V_{FD} and after $\approx 90\%$ of reverse annealing for b.) sample W339 and c.) sample W317.

	V_{PO}	$V_{FD,TCT,e}$	$V_{FD,TCT,h}$	V_{FD}
W339	74 V	145 V	155 V	121 V
W317	65 V	125 V	133 V	103 V

Table 5.6 : The measurements of different voltages for diodes from wafers W339 and W317 irradiated with neutrons to $\Phi_{\text{eq}} = 7.5 \cdot 10^{13}$ cm^{-2} after beneficial annealing was completed. The TCT measurements were performed at $T = 10°$ C and integration time of 60 ns, while C/V measurements were done at 10 kHz and $T = 20°$ C.

Holes, on the other hand, are injected in the high field region. An increase of voltage is reflected in the increase of the depleted region width. Since only the holes drifting in the depleted part of the detector contribute to the charge integrated in the time window of 60 ns, the collected charge should increase linearly with depletion depth. Constant

effective doping concentration thus results in a $\sqrt{U}$ increase of the collected charge [41] as long the diode is not fully depleted.

The influence of trapping on the shape of the induced current vs. voltage plot is small as can be explained by the following reasoning. If the mobility is taken as constant the drift time of carriers does not change as long as the full depletion is not reached. This follows from

$$t_c = \frac{w}{v_{dr_h}} = \frac{w^2}{\mu_{0_h} U} \propto \frac{1}{\mu_{0_h}} \quad , \quad w^2 \propto U. \tag{5.7}$$

If N_{eff} is constant in the depleted region (Eq. 2.33), the voltage only changes the amplitude of the induced current proportionally to the electric field strength i.e. $\propto \sqrt{U}$, while its time evolution remains the same for all voltages bellow the full depletion voltage as can be seen in Fig. 5.15. Charge trapping therefore preserves the proportions between induced currents at different voltages and by that also the $\sqrt{U/V_{FD}}$ scaling of the induced charge on voltage.

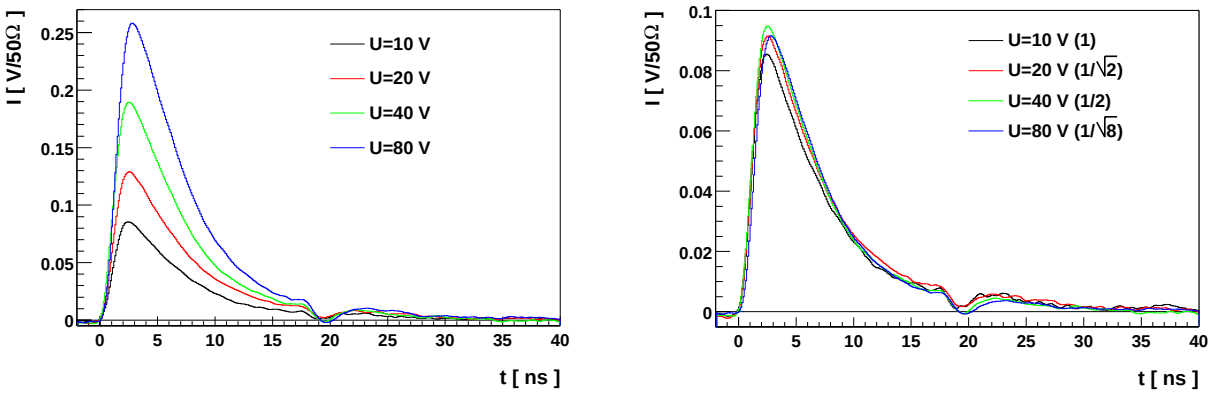

a.) b.)

Figure 5.15 : a.) Induced current after hole injection for sample W317 irradiated with neutrons to $\Phi_{\text{eq}} = 7.5 \cdot 10^{13}$ cm^{-1} ($V_{FD} = 103$ V). Measurements were performed at $T = 10°$C. b.) The induced currents from a.) are scaled with $\sqrt{10\text{ V}/U}$. The scaling factor is given in brackets.

Again at $U > V_{FD}$ the increase of collected charge is a consequence of faster drift and less charge trapped. In Figs. 5.14a,b examples of $V_{FD,TCT}$ determination are shown. Somewhat (see Table 5.6) larger values are obtained with respect to those obtained by electron injection.

A linear rise of the charge in the $\sqrt{U}$ scale confirms the assumption of almost constant effective dopant concentration in the larger part of the detector volume for high resistivity standard and high resistivity oxygenated material irradiated with neutrons.

[41] Since the undepleted bulk has a high resistance the weighting field is constant and determined by the diode thickness. On the other hand, a non-irradiated diode is equivalent to a thinner fully depleted diode of thickness equal to the depletion layer, because the electrical contact is brought to the boundary of the depletion layer by the conductive undepleted bulk. The charge is therefore constant as soon the light penetration depth is smaller than depleted region.

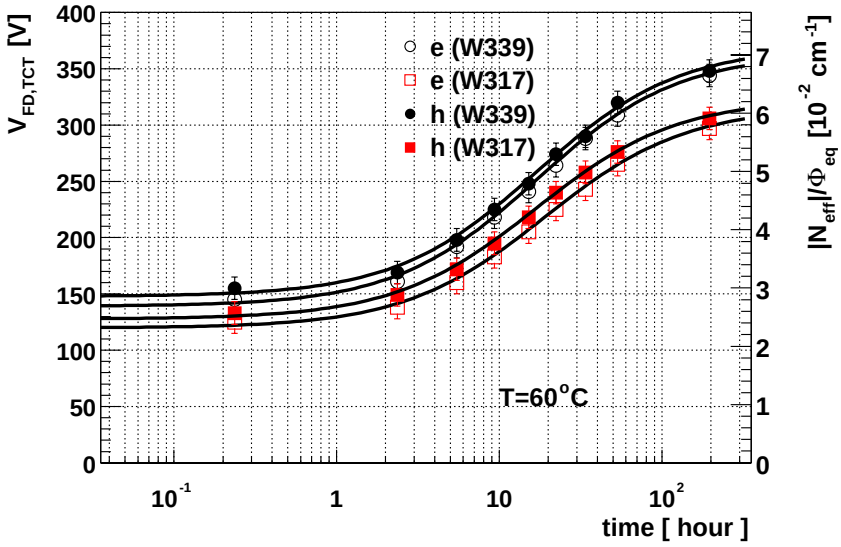

Figure 5.16 : Evolution of the $V_{FD,TCT}$ with time. Samples W339 (standard) and W317 (oxygenated), irradiated with neutrons to $\Phi_{\rm eq} = 7.5 \cdot 10^{13}$ cm^{-2}, were reverse annealed at a elevated temperature of $T = 60°$C, while measurements were performed at $T = 10°$C. The fit with ansatz of Eq. 5.8 is also shown. Note a systematic difference between $V_{FD,TCT}$ extracted in case of electron and hole injection.

The same diodes as used for the study of annealing of effective trapping times were used to determine the parameters of N_{eff} reverse annealing (Section 5.2.4). The study of reverse annealing using TCT is important for two reasons:

- If the effective dopant concentration becomes non-homogeneous during the reverse annealing the effective dopant concentration estimation from C/V method would become wrong. Using TCT, at any point in time the N_{eff} profile can be checked for non uniformity.

- It has been shown before [Fre00] that $V_{FD,TCT}$ corresponds, with some possible offset, to V_{FD}. However, the parameters of reverse annealing extracted from $V_{FD,TCT}$ measurements need to be verified also with signal measurements.

  Since different groups use either V_{PO} or $V_{FD,TCT}$ for the voltage of full depletion the evolution of their difference during reverse annealing should be established.

As can be seen in 5.14a,b N_{eff} has a uniform profile also after almost completed reverse annealing. The use of Eq. 4.3 is therefore justified at any point in time after neutron irradiation of high resistivity silicon material.

If N_{eff} had a linear profile, with a significant part of the detector bulk with positive space charge and the remaining part with negative space charge as suggested by [Ere95, Bea98, Men99] the junction would have grown from both sides. As a result a double kink would be observed in the charge versus voltage plot. However, other materials can have

more non-uniform effective doping concentration profile. The latter may also depend on irradiation particles.

The evolution of $V_{FD,TCT}$ and N_{eff} with time after irradiation is shown in Fig. 5.16. Since most of the beneficial annealing was completed before the first measurement the ansatz used for fitting to data included only reverse annealing defects and defects constant in time

$$\frac{|N_{eff}(t)|}{\Phi_{\rm eq}} = g_c + g_Y \left[1 - \frac{1}{1 + t/\tau_{ra}}\right] \tag{5.8}$$

To ease comparison with other groups a solution of the second order process [42] was used for reverse annealing evolution. A more correct approach would be to fit two exponentials, this would however, yield three more free parameters. The measured parameters are listed in Table 5.7.

	τ_{ra} [hours] (e)	τ_{ra} [hours] (h)	g_Y [cm^{-1}] (e)	g_Y [cm^{-1}] (h)
W339	17.8 ± 3.5	17.8 ± 3.5	4.3 ± 0.3	4.23 ± 0.24
W317	20 ± 4.5	17.5 ± 3.9	3.75 ± 0.3	3.75 ± 0.3

Table 5.7 : Reverse annealing amplitudes and time constants obtained from fit of Eq. 5.8 to the measured data.

The time constant and reverse annealing amplitude for W339 sample agree within the error with previous measurements [ROSE3]. Using the activation energy 1.31 eV [Lin99] in Eq. 3.14 a factor 509 is obtained to scale τ_{ra} to $T = 20°$ C. This yields time constants of around 400 days which is comparable with 480 days found in [ROSE3]. In the same reference $g_Y \approx 5$ cm^{-1} was measured (see Appendix D). Somewhat longer time constants for oxygenated samples were expected from previous measurements using the C/V method [ROSE3].

The difference $V_{FD,TCT} - V_{PO}$ was found to be approximately constant during reverse annealing (Fig. 5.17) if an integration of 60 ns is used. The reverse annealing time constant and amplitude derived from V_{PO} are thus the same as those obtained from $V_{FD,TCT}$.

5.4 Field engineering by continuous carrier injection

The operational voltage becomes the limiting factor for successful detector operation at high fluences due to the potential danger of electric breakdown and increased power consumption. This issue is particularly important for beam monitors and luminosity meters if silicon detectors are applied.

[42] In the past it was assumed that reverse annealing is a second order process where two identical electrically non active defects form a new electrically active defect complex. Such process would give an initial slope of the reverse annealing proportional to square of the fluence. Since it is seen [ZontT] to be linearly dependent on fluence the second order model was used with ${k_2}^Y \rightarrow {k_2}^Y/\Phi_{\rm eq}$. Although physically unjustified, this model gives good fits also in the late phase of reverse annealing, requiring the smallest number of free parameters.

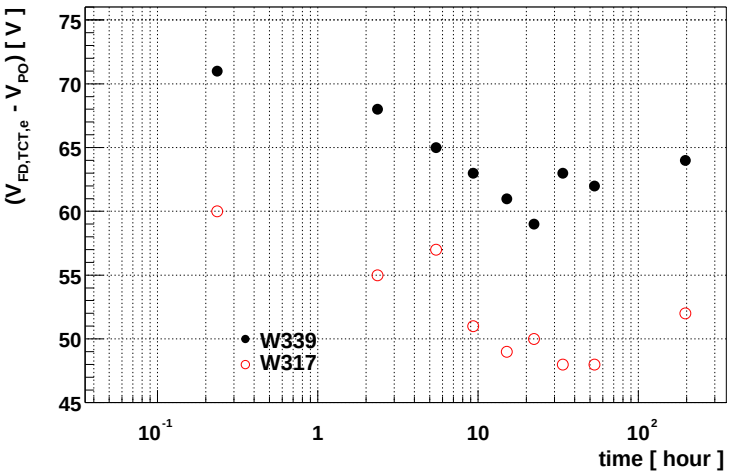

Figure 5.17 : Evolution of the $V_{FD,TCT,e} - V_{PO}$ with time. Charge was integrated in a time window of 60 ns. Note suppressed zero on y-axis.

One way to deal with the problem of high operational voltage is the operation of detectors at cryogenic temperatures, where the effective space charge is reduced. This phenomenon is called the Lazarus effect [Pal98].

Another solution is space charge manipulation with continuous injection of charge carriers. This can be achieved by continuous (DC) illumination of one detector side with light of short wavelength (< 700 nm). The enhanced electron or hole concentration in the active volume of the detector influences the occupation probability of traps that contribute to the space charge as it follows from Eqs. 3.33 and 3.36.

If holes are injected, concentration of active deep donors is increased and concentration of active deep acceptors is reduced. The analogue holds for electron injection. At temperatures above $T = 170$ K the bulk of heavily irradiated silicon detector is effectively p-type. A continuous hole injection reduces the negative space charge and by that the voltage needed to establish the electric field through the whole thickness of the detector. Such a mode of operation was proposed in [Lut96, Ere99], however it was left experimentally only partially studied [Dez99, Ve00L].

The set of diodes from W339 wafer irradiated with neutrons was used for this purpose (see Table 5.1).

5.4.1 Concentration of free carriers

Due to continuous electron or hole injection, an additional DC current flows through the detector. Once the electric field is established in the whole detector the current is constant. From the equation for current density $j = e_0\, p\, v$ it follows

$$p = \frac{\Delta I}{e_0\, S_i\, v_{dr_h}} = \frac{\Delta I}{e_0\, S_i\, \mu_h(E)\, E} \quad , \tag{5.9}$$

where ΔI is the surplus current due to continuous hole injection (Fig. 5.18) and S_i the size of illuminated area. Analogous equation holds for electrons.

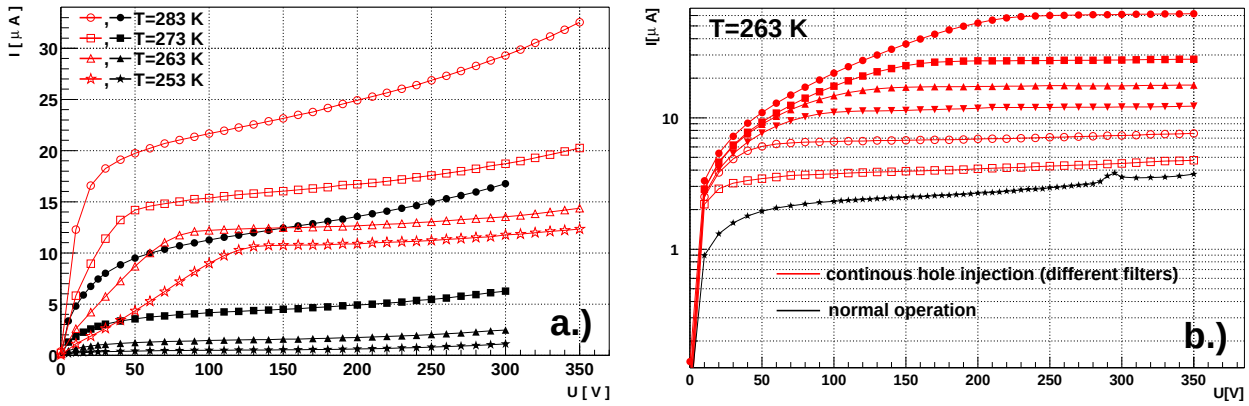

Figure 5.18 : Measured leakage current in the presence of continuous hole injection (red) and without continuous hole injection (black). a.) The sum of current due to illumination, generation current and guard ring current at different temperatures is shown for the diode irradiated to $5 \cdot 10^{13}$ n/cm^2. A constant ΔI at all temperatures is evident. b.) The increase of current upon illumination of the back of the diode irradiated to $7.5 \cdot 10^{13}$ n/cm^2 with continuous light of different intensities.

The concentration of free carriers is governed by two terms, depending on the applied voltage and on the light intensity. As the bias voltage increases the drift velocity of the carriers increases as well. In the case of a constant continuous carrier generation rate this results in a decrease of the carrier concentration in the space charge region as less time is needed for carriers to drift over the entire thickness of detector.

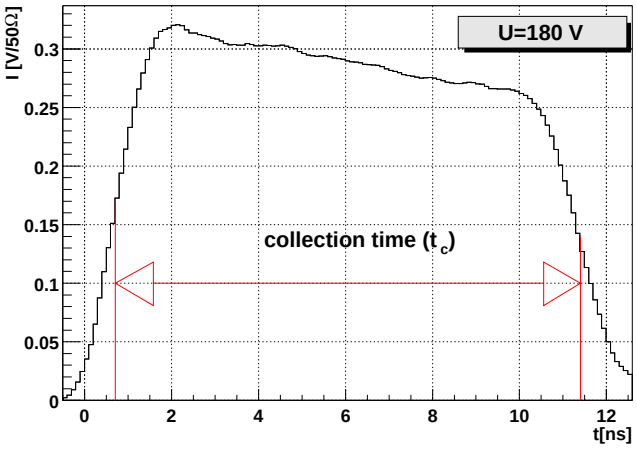

Figure 5.19 : TCT signal for holes at $T = 263$ K for a diode irradiated to $5 \cdot 10^{13}$ n/cm^2. The surplus current due to continuous illumination of the diode was $\Delta I/S = 220$ μA cm^{-2}.

The spatial dependence of free carrier concentration in Eq. 5.9 comes from spatial

dependence of the drift velocity. Whenever the effective space charge is close to zero or the voltage is well above the voltage needed to establish the electric field in the whole detector, the spatial dependence of v_{dr} can be neglected and taken as a constant. A homogeneous distribution of free carriers is adopted in further considerations.

The average drift velocity can be determined from the measurements as

$$\overline{v_{dr_{e,h}}} = \frac{D}{t_c} \quad , \tag{5.10}$$

where t_c is the collection time, defined here as the time between the induced current pulse (pulsed carrier injection) reaches 50% of its amplitude on rise and fall (see Fig. 5.19).

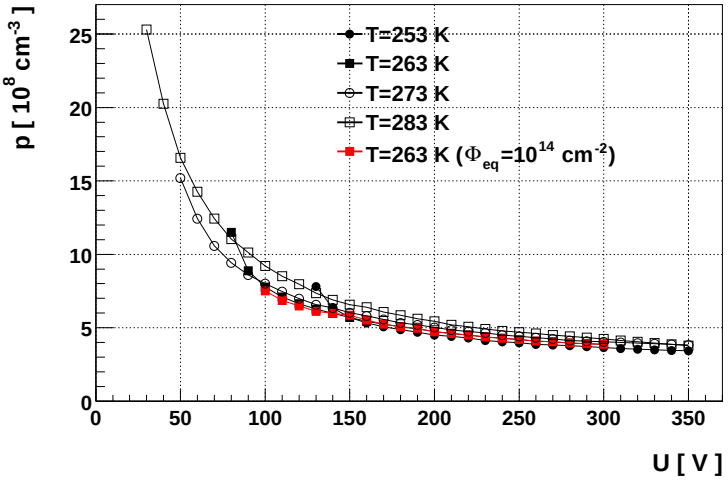

Figure 5.20 : The hole concentration as a function of applied voltage for the detector irradiated to $5{\cdot}10^{13}$ n/cm^2 at different temperatures. The additional current due to continuous illumination of the diode was $\Delta I/S = 220$ μA cm^{-2}. The same concentration at higher voltages is observed for a detector irradiated to $1 \cdot 10^{14}$ n/cm^2 at equal $\Delta I/S$.

The concentration of injected free carriers was not deduced from the light intensity measurements but evaluated from the current increase (ΔI) and the induced current pulse shape (t_c). The measured hole concentration is shown in Fig. 5.20 for the diode irradiated to $\Phi_{\rm eq} = 5 \cdot 10^{13}$ cm^{-2}. An asymptotic behavior can be seen at higher voltages as the drift velocity approaches its saturation value. Hole concentration [43] at a given continuous injection intensity was found to be independent on fluence. This indicates that carrier mobility is not changed by irradiation, as it was already shown by [LiZ95]. The same conclusion can be drawn from the measurements of drift time t_c performed for samples shown in Fig. 5.20.

As can be seen the concentration of the continuously injected holes was typically around 10^9 cm^3 which is far from sufficient to influence the effective space charge, unless they are trapped.

[43] This also holds for continuous electron injection.

5.4.2 Effect of continuous holes or electrons injection

To confirm the assumption of beneficial continuous hole injection and non-beneficial electron injection on operation of irradiated detectors, TCT signals were studied in the presence of continuous electron and hole injection. As expected continuous injection of electrons increases $V_{FD,TCT}$ [44] (see Section 5.3 for definition), while continuous hole injection decreases $V_{FD,TCT}$ (Fig. 5.21a,b). $V_{FD,TCT}$ determined from both electron signals and hole signals confirm that.

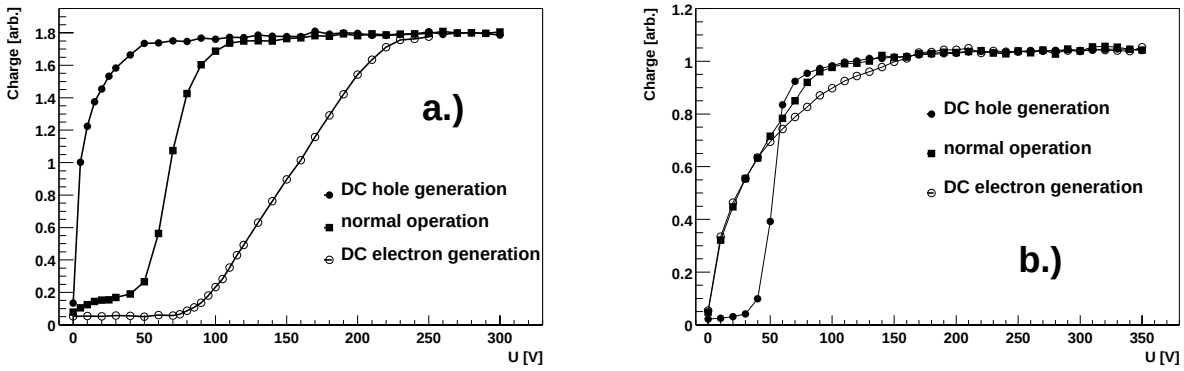

Figure 5.21 : Dependence of the collected charge on voltage at $T = 263$ K in the presence of enhanced electron and hole concentration for: a.) electrons and b.) holes. The detector irradiated to $\Phi_{\mathrm{eq}} = 5 \cdot 10^{13}$ cm^{-2} was used. Note that the concentrations of free electrons and holes were different.

It is evident that enhanced electron concentration in the bulk is not beneficial, hence the rest of the study will deal with operation of detector in the presence of enhanced hole concentration.

The absence of low field electron injection and rather a $\sqrt{U}$ dependence of collected charge in the presence of enhanced hole concentration indicates that silicon bulk is effectively of n-type. The analogous picture is obtained for hole signal. The bulk type re-inversion upon DC hole injection from effectively $p^+ - p - n^+$ to $p^+ - n - n^+$ is confirmed by the induced current shapes.

5.4.3 Space charge re-inversion

As it follows from Eq. 5.9 the concentration of free holes in the bulk can be varied with voltage and light intensity. According to Eqs. 3.33 and 3.37 the effective space charge is influenced as well. This effect can be observed in Fig. 5.22.

Induced current pulse shapes acquired in the presence of continuous hole injection show a clear change in slope as the bias voltage is increased. The diode bulk is effectively of n-type (re-inverted) at low voltages and becomes more p-type (inverted) as the

[44] In this mode of operation the detector may not be fully depleted in the way that the concentration of free carriers could not be negligible compared to N_{eff}. $V_{FD,TCT}$ here denotes the voltage needed for establishing the electric field in the entire thickness of detector.

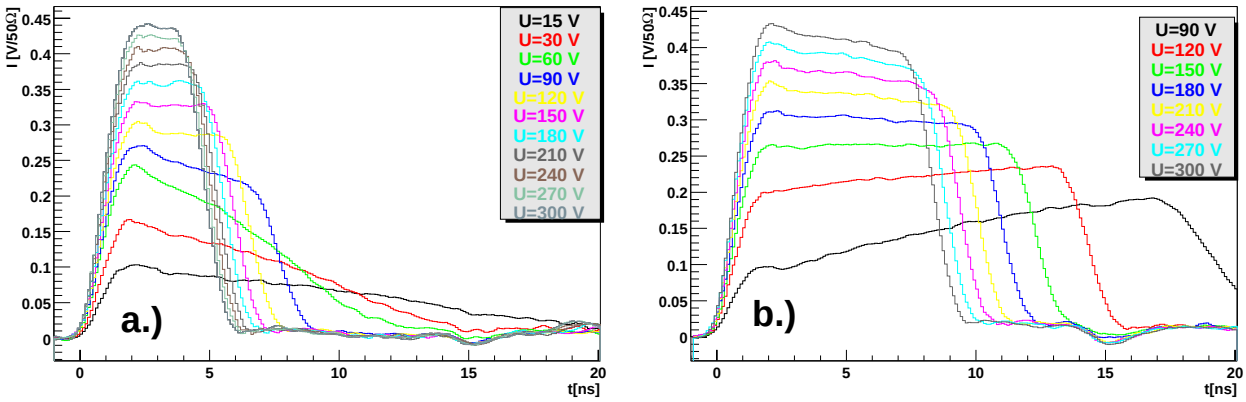

Figure 5.22 : Observation of type re-inversion in the presence of continuous hole generation ($\Delta I/S \approx 220\ \mu\mathrm{Acm}^{-2}$) in the sample irradiated to $\Phi_{\mathrm{eq}} = 5 \cdot 10^{13}\ \mathrm{cm}^{-2}$. As the voltage increases the hole concentration changes resulting in a.) electron and b.) hole signal. The measurements were performed at $T = 263$ K.

voltage increases. In this particular case the free hole concentration ranged from 0.2 to $1.4 \cdot 10^{9}\ \mathrm{cm}^{-3}$.

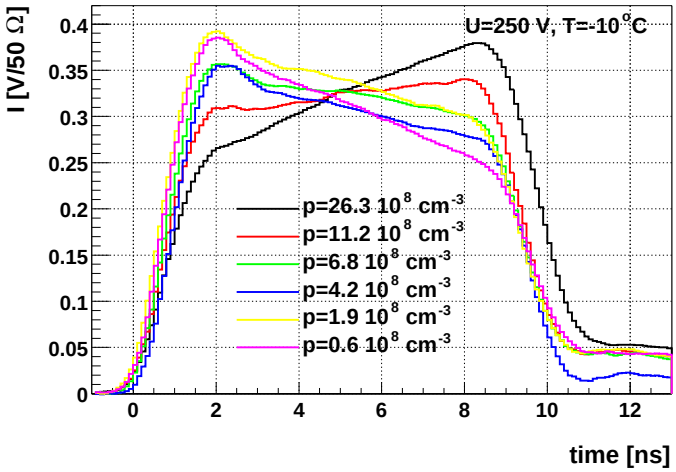

Figure 5.23 : Comparison of the hole signal shapes measured in the presence of different free hole concentrations induced by the DC illumination of the sample irradiated to $\Phi_{\mathrm{eq}} = 7.5 \cdot 10^{13}\ \mathrm{cm}^{-2}$. A clear type re-inversion can be seen.

A similar picture can be observed if the voltage is kept fixed and the hole concentration is changed by the intensity of continuous illumination. In Fig. 5.23 it can be seen that as the injection level increases, the induced current shape changes from the one characteristic for a $p^+ - p - n^+$ device to the one typically observed in $p^+ - n - n^+$ devices.

The effective space charge concentration and its sign are strongly dependent on temperature in the case of enhanced free carrier concentration. The dominant dependence comes from emission terms in Eq. 3.33 and a minor dependence from $c_{n,p}(T)$. The effect

of the temperature can be seen in Fig. 5.24. N_{eff} at a given voltage changes sign as the temperature increases.

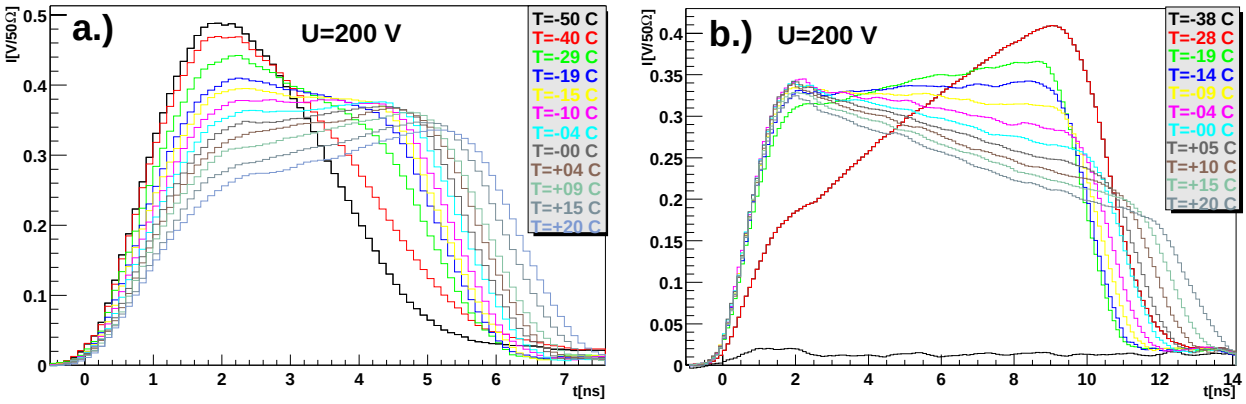

Figure 5.24 : Induced current shapes measured at different temperatures for a.) electrons and b.) holes in a detector irradiated to $5 \cdot 10^{13}$ n/cm^2. The operation voltage and continuous illumination intensity were kept fixed resulting in approximately $\Delta I/S \approx 220$ μAcm^{-2}. At $T = -38$°C the bias voltage of 200 V was not sufficient to establish electric field in the whole detector bulk. Detector is re-inverted therefore high electric field region is at the p^+ contact and low electric field region is at the n^+ contact. Consequently holes are injected in the low field region and their signal is missing.

Since now N_{eff} depends on voltage it cannot be determined from $V_{FD,TCT}$ using the Eq. 4.3. Instead, a transient time method can be used (see Section 5.4.5).

5.4.4 Effective trapping times

The charge correction method used for the determination of effective trapping times, can be applied only if the occupation probability of traps (Eq. 3.33) does not vary with the applied voltage (see Eq. 3.50). This is true in a fully depleted detector where the concentration of free carriers is negligible. In the case of continuous hole injection the concentration of free holes depends according to Eq. 5.9 on velocity and thus on the bias voltage. However, this dependence is asymptotic once the bias voltage becomes sufficiently high as can be seen in Fig. 5.20. Thus, in the region of weak dependence of free hole concentration on bias voltage, the charge correction method is applicable.

The results obtained (Fig. 5.25) for a set of W339 samples irradiated to different fluences with neutrons show that the effective trapping probability is not significantly influenced by the enhanced free hole concentration of order 10^9 cm^{-3}. There is an indication of only a slight decrease of $1/\tau_{eff_h}$ and a slight increase of $1/\tau_{eff_e}$ as compared to the normal operation of the detector.

As will be shown, in contrast to minor influence of the enhanced free hole concentration on $1/\tau_{eff_{e,h}}$, a substantial change in N_{eff} is observed (see the following section).

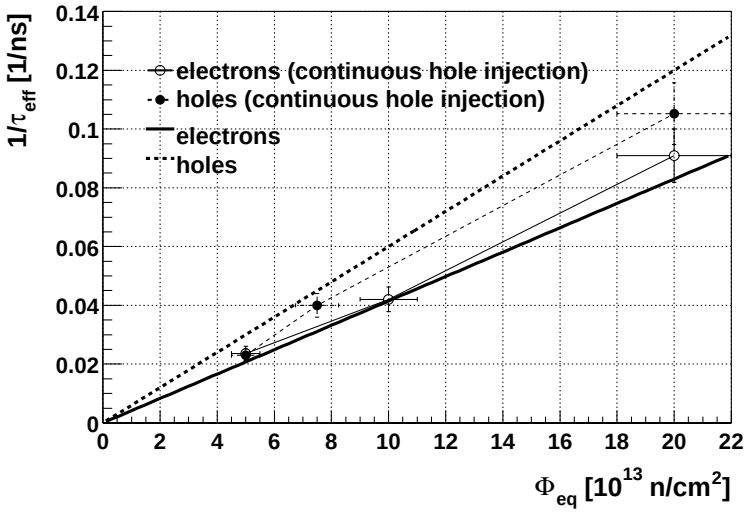

Figure 5.25 : Effective trapping probabilities in the presence of DC light illumination as a function of fluence. The measurements were performed at $T = 263$ K. The free hole concentration was around $p \sim 3.5 - 5 \cdot 10^8$ cm^{-3}. A comparison with the normal diode operation is also shown (thick lines).

5.4.5 Effective space charge concentration

Assuming a linear field in the bulk or at least in a major part of the bulk and an approximately constant drift velocity, the effective doping concentration can be determined using the Eq. 2.35, with the start point of the drift (x_0) either at the front or back of the diode. In that case the measured induced current shape exhibits an exponential behavior (Eq. 2.35):

$$I_{e,h}(t) \propto \exp\left[\frac{\mp k\, t}{\tau_{e,h}} - \frac{t}{\tau_{eff_{e,h}}}\right] \quad , \quad t < \text{drift time} \tag{5.11}$$

With known effective trapping times the transient time constant $\tau_{e,h}$ can be measured from the fit of $I_{e,h}(t)$ from Eq. 5.11 to the measured induced current. The free parameters of the fit are the induced current amplitude and the transient time constant. The relation between N_{eff} and $\tau_{e,h}$ is given by Eq. 2.33 and for this particular case:

$$\frac{1}{\tau_{e,h}} = \frac{\varepsilon\, \varepsilon_0\, U}{q\, e_0\, \overline{v_{dr_{e,h}}}\, D\, N_{eff}} = \frac{\varepsilon\, \varepsilon_0\, U\, t_c}{q\, e_0\, D^2\, N_{eff}} \quad . \tag{5.12}$$

No continuous hole injection - normal operation

If no holes are continuously injected N_{eff} of an irradiated diode does not vary with the applied voltage. This is shown in Fig. 5.26 by a measurement performed with the diode irradiated to $\Phi_{\text{eq}} = 5 \cdot 10^{13}$ n/cm^2. The measured effective dopant concentration was $N_{eff} = (1 \pm 0.1) \cdot 10^{12}$ cm^{-3}. This value is in agreement with the C/V measurement of $N_{eff} = 10^{12}$ cm^{-3}.

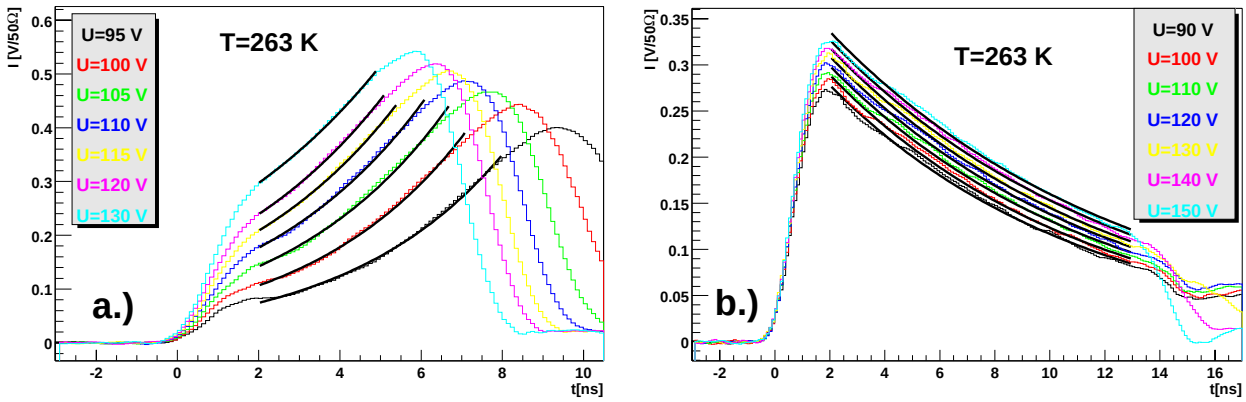

Figure 5.26 : An example of Eq. 5.11 fit to the measured induced current in case of normal operation of diode for: a.) electrons and b.) holes at $T = 263$ K. The diode was irradiated to $5 \cdot 10^{13}$ n/cm^2.

A small change of N_{eff} is expected if the operating temperature varies between 253 K and 283 K [Chi00, KolaD]. N_{eff} determined from TCT signals at different temperatures showed only a small variation comparable to the N_{eff} variation at different voltages.

The choice of the fit interval influences the estimated value of $N_{eff}(U)$. The drift of electrons at high voltages in the depleted region lasts only a few ns which is comparable with the light pulse duration. In addition the electron transient time is longer than the drift time which results in a large uncertainty in its determination. The lower limit of the fit interval was set to 2 ns which is the time of the light pulse duration, while the upper limit was set, for the same reason, 2 ns before the maximum of the current pulse.

Around three times longer drift time of holes and for the same factor smaller hole transient time constant make determination of $N_{eff}(U)$ much more reliable. The same lower limit of the fit interval was selected as for the electron injection. The upper limit of the fit interval was set to 1 ns before the steep decrease - kink - in the induced current (9.5 ns would be selected in Fig. 5.19).

An agreement of N_{eff} measured with the C/V and transient time methods confirm the applicability of the latter.

Continuous hole injection

An example of the determination of N_{eff} from electron and hole induced current shapes in the presence of enhanced free hole concentration is shown in Fig. 5.27.

A whole set of such measurements with a detector irradiated to $\Phi_{\text{eq}} = 5 \cdot 10^{13}$ n/cm^2 was acquired at temperatures ranging from 243 K to 293 K. The additional current density was kept fixed at $\Delta I/S = 220$ μA/cm^2. The resulting N_{eff} as a function of free hole concentration is shown in Fig. 5.28. The initially negative N_{eff} decreases as the concentration of holes p grows. At a certain hole concentration the diode behaves as intrinsic. This re-inversion point is a strong function of temperature. Operation of diode with $N_{eff} \approx 0$ at $T = 263$ K requires a factor of 7 smaller hole concentration p compared to the operation at $T = 283$ K. A reduction of hole concentration p at $T \leq 253$ K for

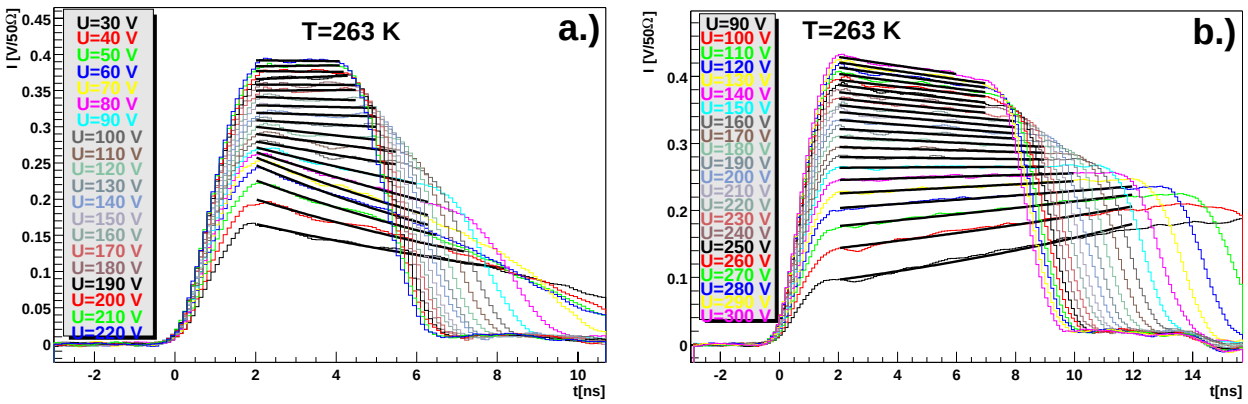

Figure 5.27 : An example of Eq. 5.11 fit to the measured induced current in the presence of enhanced free hole concentration for: a.) electrons and b.) holes at $T = 263$ K. The diode was irradiated to $5 \cdot 10^{13}$ n/cm^2.

reaching $N_{eff} \approx 0$ by a voltage increase is impossible due to drift velocity saturation. Consequently lower intensities of light are needed at lower temperatures to operate the diode at $N_{eff} \approx 0$.

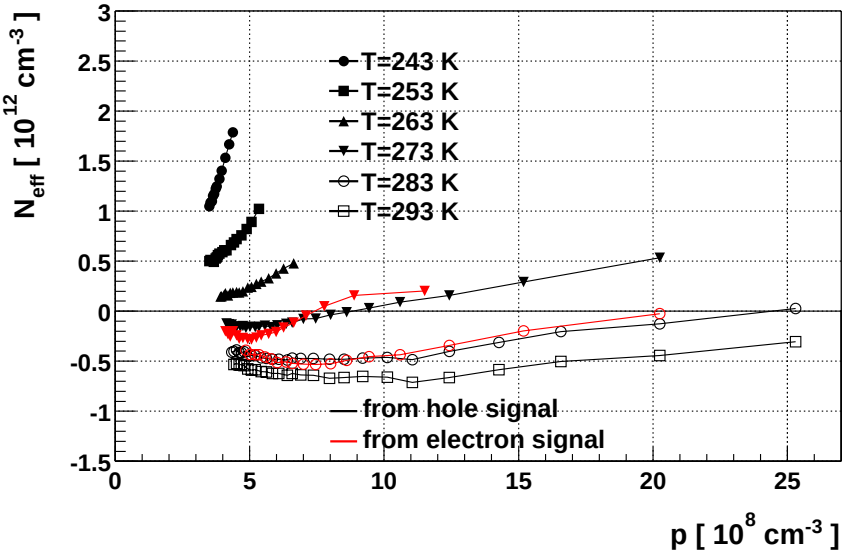

Figure 5.28 : Effective space charge dependence on hole density as calculated from Eq. 5.9. The difference in free hole concentration is caused by different bias voltages. At lower temperatures the effective space charge obtained from the electron signal is unreliable due to short electron signal and therefore uncertain fit.

To confirm this assumption TCT signals of a detector irradiated to $\Phi_{\text{eq}} = 7.5 \cdot 10^{13}$ cm^{-2} were measured using different continuous light intensities. In Fig. 5.29 the results are shown with the applied voltage fixed to 180 V.

In the presence of deep levels N_{eff} is given by Eq. 3.38. The enhanced free hole

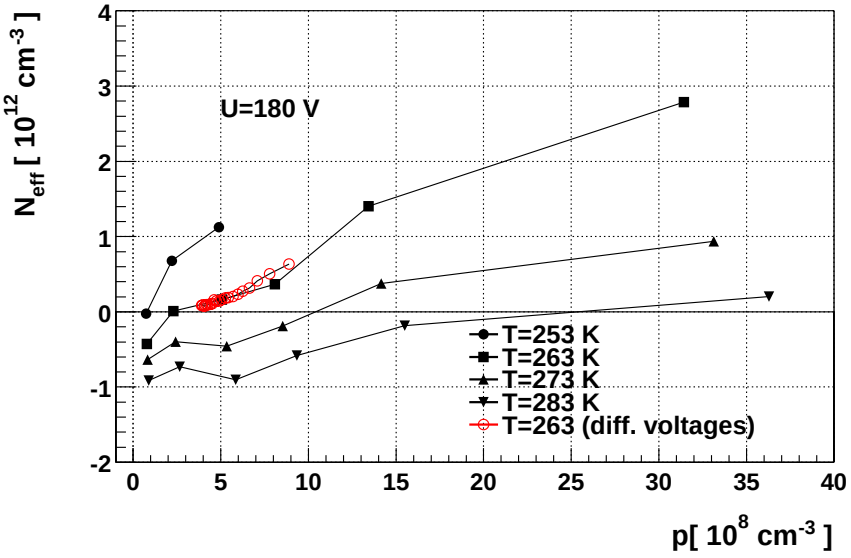

Figure 5.29 : Effective space charge concentration dependence on free hole density regulated with different continuous light intensity at $U = 180$ V. For comparison N_{eff} at different free hole concentrations controlled by applied bias is also shown (red). The diode was irradiated to $\Phi_{\text{eq}} = 7.5 \cdot 10^{13}$ cm^{-2}.

concentration affects the occupation probability of traps ($P_t(p,T)$). If the initial dopant concentration terms can be neglected, due to the nearly complete dopant removal or very low initial dopant concentration, a choice of T and p at which $N_{eff} \approx 0$ is universal for all fluences [45].

Since the free hole concentration can be regulated by the applied voltage and illumination intensity, at selected operation voltage and temperature, the light intensity can be fine tuned to reach the optimal point of operation where $N_{eff} \approx 0$. In pricinple, the operation voltage could be set as low as a few volts and still be sufficient to establish an electric field in the whole thickness of the detector. However, the trapping of drifting charge in practice requires a much higher voltage to reduce the drift time and by that the amount of charge trapped.

Another advantage of the continuous illumination operation mode is the ability to use thicker detectors. Once $N_{eff} \approx 0$ at given operation voltage, the electric field is established in the whole volume even in a very thick detector (e.g. $D = 1.5$ mm). The minimum ionizing particle signal is proportional to detector thickness, hence to some extent higher signals could be obtained.

5.4.6 Practical aspects of operation

Operation of the device with an enhanced free hole concentration in the bulk requires a careful choice of the continuous illumination intensity in order to reach the optimal point

[45] This is true at a given point in the annealing. At different times optimal p and T can be different.

of operation.

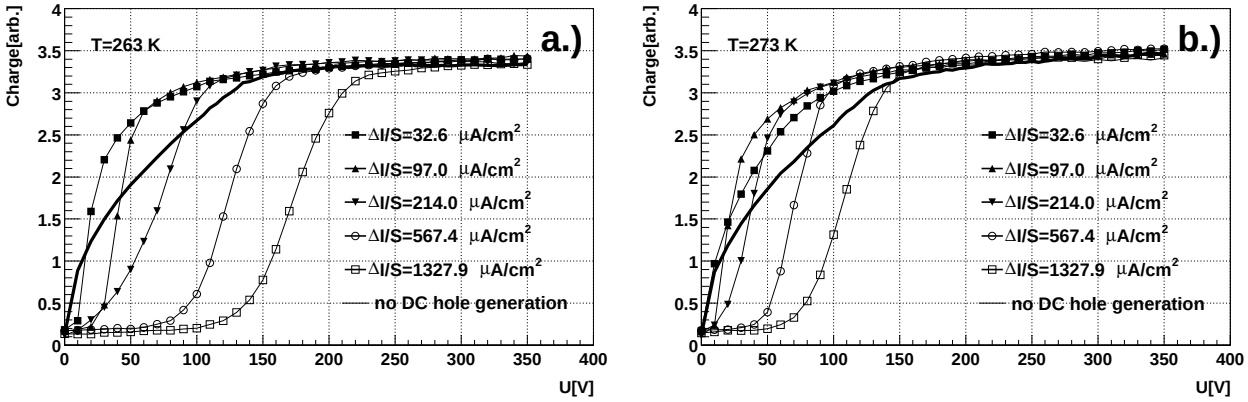

Figure 5.30 : Collected hole charge (60 ns integration time) at different additional hole current densities in the diode irradiated to $\Phi_{\rm eq} = 5 \cdot 10^{13}$ cm^{-2}: a.) measured at $T = 263$ K and b.) at $T = 273$ K. The thick line denotes the measurement without continuous hole injection $\Delta I/S = 0$.

An example of light intensity (additional hole current) selection can be seen in Fig. 5.30. The lowest additional hole current density used is the best choice if the detector is operated at $T = 263$ K, since it gives the lowest $V_{FD,TCT}$. One can notice that even this current is too high since the characteristic shape of the induced charge vs. voltage curve indicates low field injection. Around 60 V lower $V_{FD,TCT}$ was reached when compared to the diode operated in normal mode.

At $T = 273$ K the shape of the charge-voltage plots indicate that the optimal additional hole current density is between 32 μA cm^{-2} (high field injection) and 97 μA cm^{-2} (low field injection). It is evident that reaching the optimal point of operation at higher temperature requires higher additional hole current density.

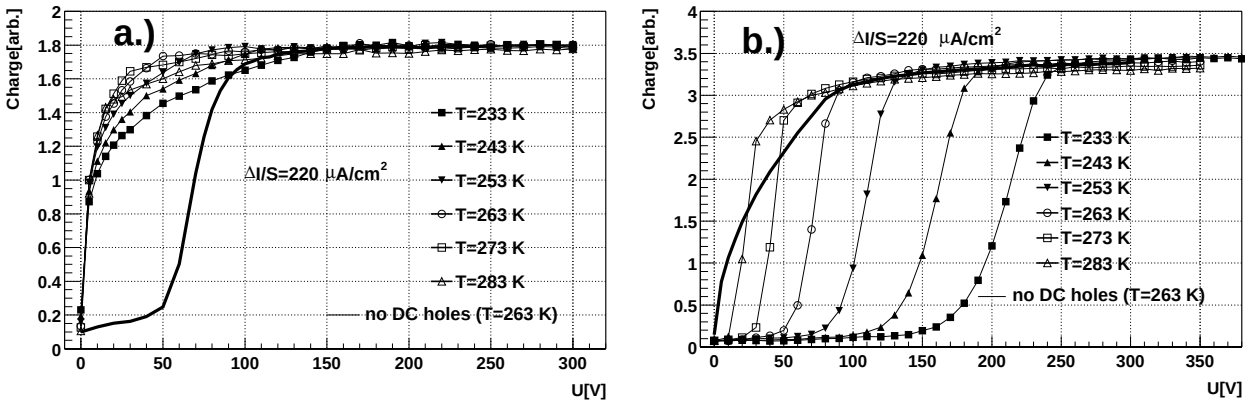

Figure 5.31 : Temperature dependence of collected a.) electron and b.) hole charge (60 ns current integration) in the sample irradiated to $\Phi_{\rm eq} = 5 \cdot 10^{13}$ cm^{-2}. The comparison with no continuous hole injection is also shown.

The same conclusions can be drawn if the additional hole current is fixed and the temperature varies (Fig. 5.31). In the investigated temperature range the additional hole

current density was too high so that electrons were always injected in the high field region and holes in the low field region. However, it can be clearly seen that as the temperature increases $V_{FD,TCT}$ is reduced.

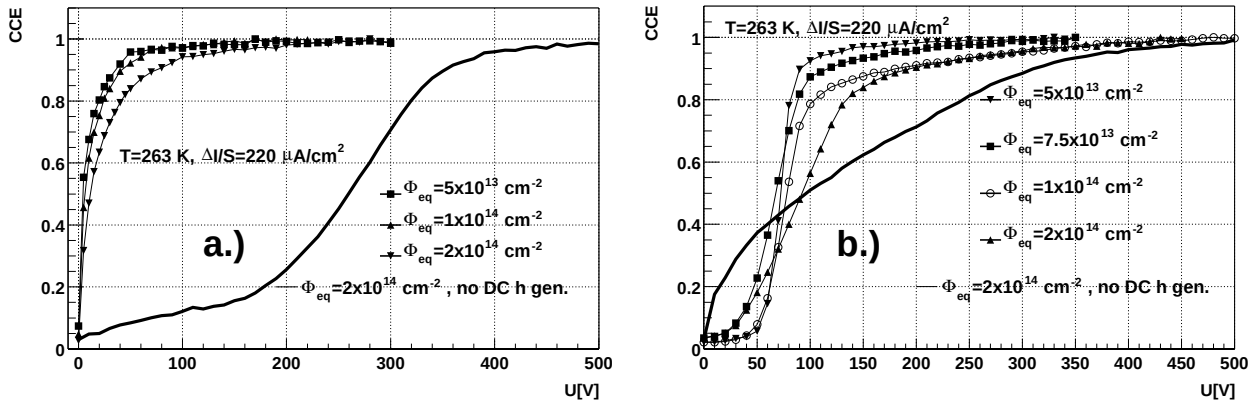

Figure 5.32 : Collected a.) electron and b.) hole charge at $T = 263$ K in samples irradiated to different fluences and operated in the presence of enhanced free hole concentration. The plots are normalized so that the maximum charge equals 1. The normal detector operation mode is represented with thick line.

If the temperature and additional hole current are close to the optimal the $V_{FD,TCT}$ is approximately constant, regardless of the fluence. Even somewhat away from the optimal point a large reduction of $V_{FD,TCT}$ can be achieved as can be seen in Fig. 5.32. A reduction of $V_{FD,TCT}$ of around 200 V at the highest fluence was achieved with DC hole injection. As the optimal operation point is approached the difference in $V_{FD,TCT}$ of around 40-50 V at $T = 263$ K between detectors irradiated to $5 \cdot 10^{13}$ cm^{-2} and $2 \cdot 10^{14}$ cm^{-2} vanishes as shown in Fig. 5.33. The minimum value of around 35 V was reached at $T = 283$ K for the given additional hole current. At higher temperatures $V_{FD,TCT}$ starts to increase again. A relatively high $V_{FD,TCT}$ at the optimal point is a consequence of charge loss at lower voltages due to the relatively short integration time (60 ns) and larger amount of trapped drifting charge.

The reduction of $V_{FD,TCT}$ has an important effect on power dissipation where it compensates the increase of the leakage current due to continuous hole injection, hence the actual power consumption at the optimal operation point is at the same level or even lower compared to normal operation (see Fig. 5.34). The calculation of the power consumption was done using the leakage current damage constant $\alpha = 4 \cdot 10^{-17}$ A cm^{-1} and generation rate $g_c = 0.02$ cm^{-1} of irradiation induced defects responsible for an increase of N_{eff} and $V_{FD,TCT}$ in the normal operation mode. At the optimal operation point at lower temperature the power dissipation is further reduced due to lower additional hole current.

If thicker detectors are used, detector operation in presence of continuous hole injection becomes even more beneficial in terms of power dissipation. The additional hole current stays at the same level as for thinner detectors while the bulk generation current increases linearly with thickness.

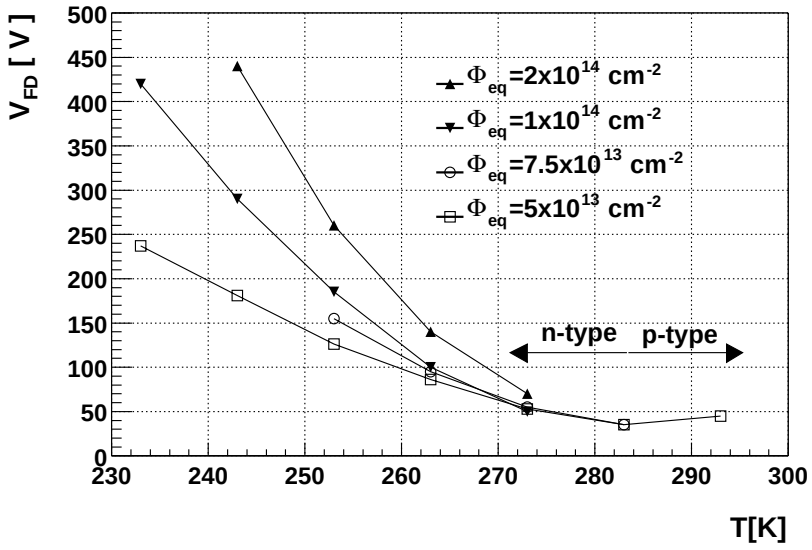

Figure 5.33 : The $V_{FD,TCT}$ dependence on temperature at different fluences. The additional hole current density was $\Delta I/S \approx 220 - 230$ μAcm^{-2}.

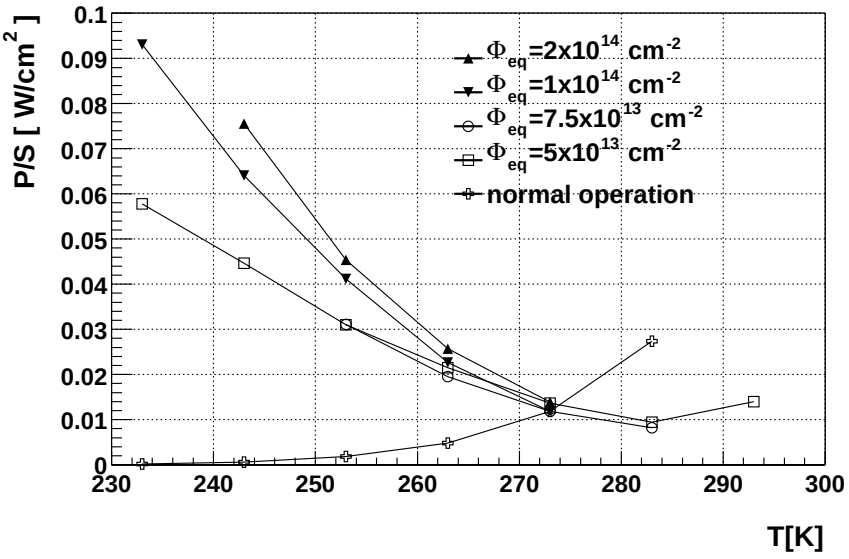

Figure 5.34 : Power dissipation dependence on temperature at different fluences and an additional hole current density of $\Delta I/S \approx 220 - 230$ μAcm^{-2}. The power consumption in normal operation mode at $\Phi_{\rm eq} = 2 \cdot 10^{14}$ cm^{-2} is also shown.

The relevant parameter for operation of silicon detectors is the signal to noise ratio. The additional current flowing through the detector increases the shot-noise.The noise can be estimated using Eq. 2.55. In the case of a silicon detector operated at $T = 263$ K, the additional current density of around $\Delta I/S \approx 25$ μAcm^{-2} is needed for the optimal

point of operation. Assuming a typical active surface of the strip $S_s = 0.03$ cm^2 (6 cm strip of ~ 50 μm pitch) and pixel $S_s = 0.0004$ cm^2 (400×100 μm^2) the resulting increase of the shot noise would be ENC$\sim$ 450 e for a strip detector and ENC$\sim$ 50 e for pixel detector both connected to fast electronics with $\tau_p = 25$ ns. Since the series noise and parallel noise are summed in squares, the shot noise for a pixel detector would contribute negligibly to the total noise.

The total noise of the strip detector in the normal operation mode is dominated by series noise. If it is considered to be around 800-900 e, the additional shot-noise contribution would result in a $\sim 20\%$ higher noise. The noise increase can, on the other hand, be compensated by a thicker detector delivering a larger signal.

5.5 Defect characterization

The combination of effective trapping time measurements and study of detector operation in presence of continuous hole injection allows some conclusions about the properties of the defects responsible for charge trapping.

Only the presence of donors in the bottom part of the band gap or close to the mid-gap can change the sign of the space charge to positive in the presence of enhanced hole concentration and is electrically neutral in a normally operated detector. If only one donor is taken as responsible for the change of space charge and all acceptor levels are considered as unoccupied (neutral), which is a very conservative assumption, the trap's introduction rate g_t [46] can be calculated by using Eqs. 3.33 and 3.36 as:

$$g_t \sim \frac{N_{eff}(p,T)}{\left[1 - P_t(p,T,E_t)\right] \Phi_{\rm eq}} \quad , \quad n \ll p \quad . \tag{5.13}$$

The capture cross-section ratio in the above equation is considered to be of order of 1. As shown in Fig. 5.29 a positive effective dopant concentration of around $2.8 \cdot 10^{12}$ is reached for a diode irradiated to $\Phi_{\rm eq} = 7.5 \cdot 10^{13}$ cm^{-2} at $p = 3.2 \cdot 10^9$ cm^{-3} and $T = 263$ K. According to Eq. 5.13 the introduction rate of the responsible defect should be at least $g_t > 0.04$ cm^{-1}. There are only two candidates found by the DLTS method: C_i and C_i-O_i complex [ROSE3, Wat99] (see Fig.3.2). g_t as a function of E_t is shown in Fig. 5.35a (magenta). Once $E_t < 0.4$ eV uncertainty of $\sigma_{t_e}/\sigma_{t_h}$ has a small effect on $g_t(E_t)$ (red). The values of $g_t(E_t < 0.4\,\text{eV})$ are around 10-100 times larger than those obtained from DLTS measurements.

The introduction rate of the dominant hole trap can be extracted also from the measurements of effective trapping times. It can be calculated from Eqs. 3.50, 3.51 as

$$g_t = \frac{\beta_h}{P_t \, v_{th_h} \, \sigma_{t_h}} \quad . \tag{5.14}$$

$g_t(E_t)$ derived from above equation

[46] In principle the product $g_t \, f_t$ should be used. Since all the measured samples had approximately the same time history g_t will be used instead of $g_t \, f_t$.

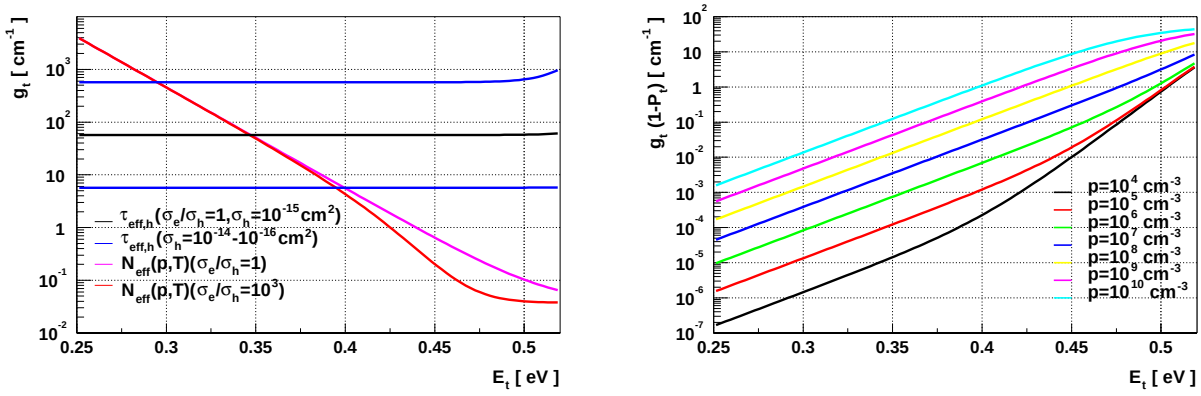

a.) b.)

Figure 5.35 : a.) Dependence of g_t as calculated from Eq. 5.13 ($N_{eff}(p,T)$) and Eq. 5.14(τ_{eff_h}) using the measured data at $T = 263$ K. The assumed values for unknown quantities are given in brackets. b.) The influence of the hole trap level to the effective dopant concentration at $T = 263$ K for different free hole densities. $\sigma_{t_e}/\sigma_{t_h} = 1$ was assumed. For easier reading σ_{t_e} is written as σ_e and σ_{t_h} as σ_h.

Assuming $\sigma_{t_h} \approx 10^{-15}$ cm^2 for the dominant hole trap, $g_t(E_t)$ derived from Eq. 5.14 is shown in the Fig. 5.35a (black). It is clear that g_t depends strongly on σ_{t_h} and does not depend on the energy level of the trap (blue).

There should be the same dominant trap responsible for the change in N_{eff} in the continuous hole injection mode of operation and for the trapping of drifting holes in the normal mode of operation. Therefore both methods (Eqs. 5.13, 5.14) should give the same g_t. This requirement can be used for determination of the trap level. The energy level of $E_{ht} = 0.35$ eV gives $g_{ht} = 58$ cm^{-1} from both methods. The trap level could be identified with C_i-O_i ($E_t = 0.36$ eV). The uncertainty of E_t is however large and comes mainly from the unknown σ_{t_h} (Fig. 5.35a, intersection of magenta and blue lines).

The trap level found explains also why almost no difference in the τ_{eff_h} was measured between operation of detector in the presence of enhanced hole concentration and operation of fully depleted detector (normal operation). Since g_t is large and $P_t \approx 1$ (see Fig. 5.35b) a small change in P_t reflects in minor change of the effective trapping time, while the change in the space charge concentration can be large[47].

Using analogous Eqs. 5.13, 5.14 for electrons the dominant electron trap can be found. A dominant deep acceptor with energy level above E_i is assumed. Deep acceptor with $E_t < E_i$ would be almost completely ionized, especially at cryogenic temperatures, and one would not be able to explain reduction of the $|N_{eff}|$ with temperature [Man00, Dav00] nor the increase of the $|N_{eff}(n,T)|$ in presence of enhanced electron concentration. The latter was determined for the diode from wafer W339 irradiated to $\Phi_{eq} = 5 \cdot 10^{13}$ cm^{-2}. $N_{eff} = -2.2 \cdot 10^{12}$ cm^{-3} was obtained at $n = 2.1 \cdot 10^8$ cm^{-3} and $T = 293$ K [48].

[47] A change of P_t for 0.1% is enough.

[48] At given illumination intensity increase of $|N_{eff}|$ was so high that N_{eff} could not be determined at $T = 263$ K.

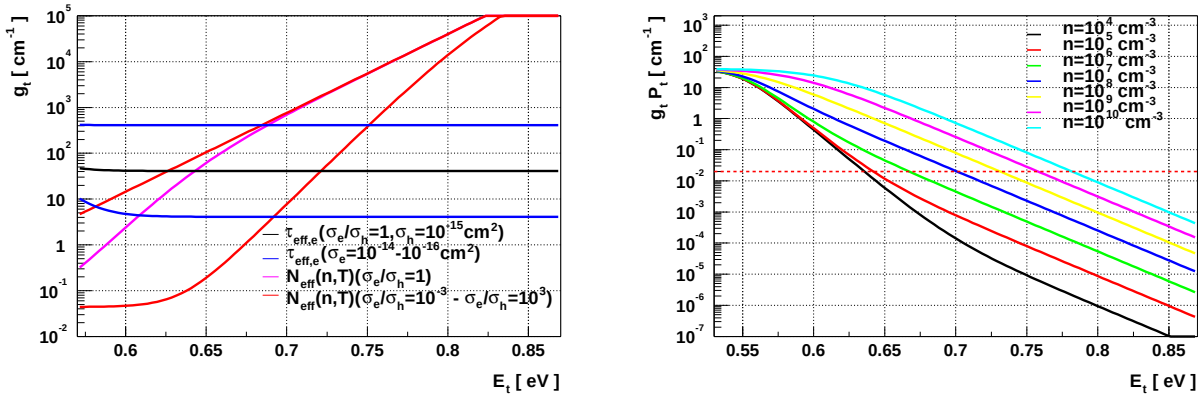

a.) b.)

Figure 5.36 : a.) Dependence of g_t on electron trap level calculated by using the measured data at $T = 293$ K. The assumed values for unknown quantities are given in brackets. b.) The influence of the electron trap position to the effective dopant concentration at $T = 263$ K for different free electron densities. $\sigma_{t_e}/\sigma_{t_h} = 1$ was assumed. The dashed red line denotes the generation rate of active deep acceptors responsible for change in N_{eff} in normal operation mode. For easier reading σ_{t_e} is written as σ_e and σ_{t_h} as σ_h.

The cross-section of both methods gives $E_{et} = 0.64$ eV and $g_{et} = 41$ cm^{-1} as can be seen in Fig. 5.36a. According to the position of the trap it could be related to multi-vacancy complexes with $E_t = 0.66$ eV [ROSE3, Wat99]. As the trap level is close to E_i, its occupancy is very sensitive to concentration of free electrons. In Fig. 5.36b the contribution of the trap to the effective dopant concentration as a function of free electron density at $T = 263$ K is shown. At low density of free electrons its contribution to the effective dopant concentration becomes comparable to the measured N_{eff} in the normally operated detector.

With the dominant electron and hole traps identified, their contribution to the effective dopant concentration $N_{eff}/\Phi_{\rm eq}$ in the case of normally operated detector ($n, p \approx 0$) can be calculated as

$$\frac{N_{eff}}{\Phi_{\rm eq}} = g_{ht}\,P_{ht} - g_{et}\,(1 - P_{et}) \quad . \tag{5.15}$$

The temperature dependence of $|N_{eff}|/\Phi_{\rm eq}$ can be seen in Fig. 5.37. The contribution of the hole trap is negligible hence the electron trap prevails. Although that calculation is in rough agreement with C/V data at 293 K, C/V measurements show a weaker temperature dependence. A possible explanation would be a temperature dependence of $\sigma_{t_e}/\sigma_{t_h}$ or a large uncertainty of measured trap levels and carrier capture cross-sections.

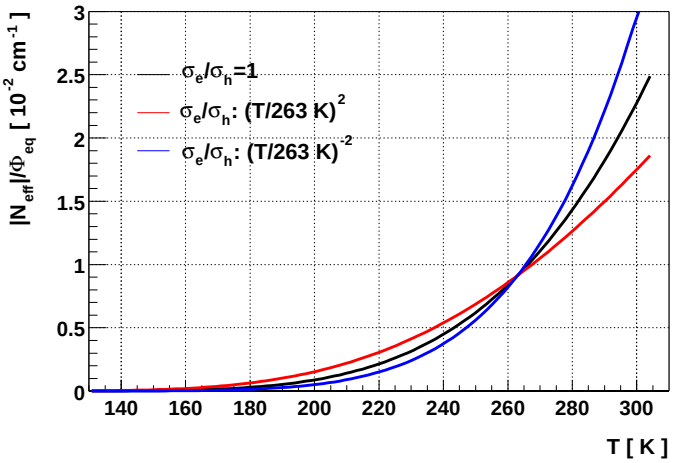

Figure 5.37 : The temperature dependence of $|N_{eff}|/\Phi_{\rm eq}$ as predicted from determination of dominant electron and hole traps. The case of different $\sigma_{t_e}/\sigma_{t_h}$ temperature dependence is also shown. For easier reading σ_{t_e} is written as σ_e and σ_{t_h} as σ_h.

6

Measurements with microstrip detectors

Measurements with irradiated silicon strip detectors are important to evaluate and predict the performance of microstrip detectors and electronics at LHC experiments. Although the diodes are more adequate for studies of effective trapping times, evolution of N_{eff} and leakage current, some properties of silicon strip detectors originating from geometry of electrodes and also from accompanying read-out electronics require also measurements with irradiated silicon detectors connected to LHC-design electronics. Electrons from a radioactive source are often used as a source of charged particles, which generate electron-hole pairs in the detector.

6.1 Detectors

Two equal, single-sided detectors of 280 μm thickness, hereafter referred as B01 and B02, with a strip pitch of 25 μm have been used for these studies. p^+ strips of 4 cm length and 10 microns width were fabricated on high-resistivity n-bulk wafer by CSEM and biased through polysilicon resistors of about 5 MΩ. A single guard ring was used as the guard structure. The read-out electronics was AC-coupled to every second p^+ strip by 10 μm wide aluminum strips. Silicon nitride (100 nm thick) on top of silicon oxide (200 nm) was used as decoupling dielectric. The detectors were mounted on a support frame. A Pt-100 sensor was contacted to the same support near the detector for temperature monitoring.

Leakage currents and V_{FD} were determined from I/V and C/V measurements. The V_{FD} of the detectors was about 60 V before irradiation, the leakage current was approximately 5 nA/cm^2 measured at V_{FD} and room temperature.

6.2 Setup

Detectors were connected to the SCT32A read-out chip [Ang97] fabricated in the radiation hard BiCMOS DMILL process [Den93]. SCT32A is a 32 channel fast analogue read-out chip with amplifier peaking time of around 25 ns. The output from the preamplifier is sampled every 25 ns into a 2.8 μs long pipeline integrated in the chip.

Only the electrons from the ^{90}Sr source that penetrated the silicon detector and a thin aluminum (~ 100 μm) foil and still left a detectable amount of energy in the scintillator were able to trigger the read-out. Those electrons were shown [KramD] to be close to minimum ionizing. A coincidence between clock pulses and signals from the photomultiplier coupled to scintillator was used to select the events sampled in the peak of the output from the preamplifier. For that purpose very narrow NIM pulses [49] (2-3 ns) were

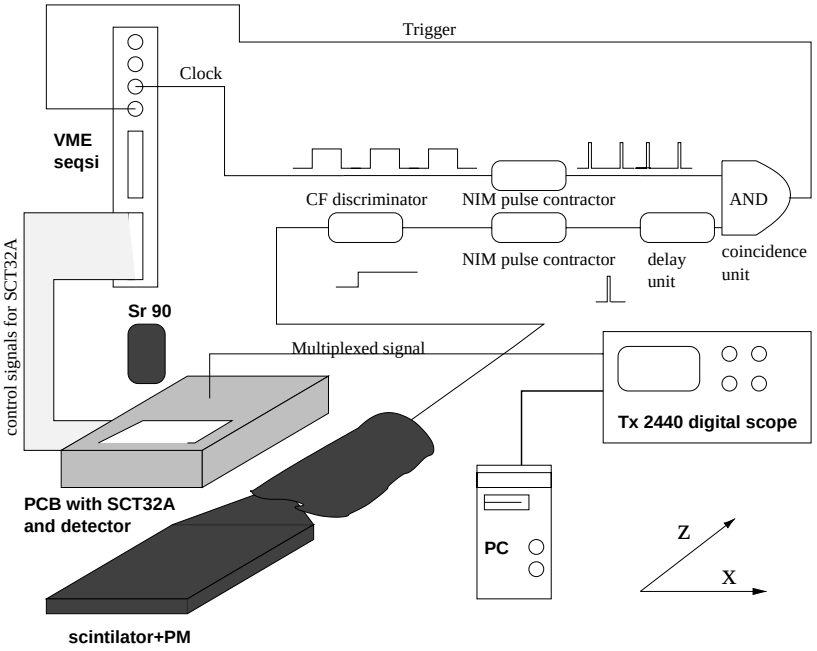

Figure 6.1 : Schematics view of a setup used for a beta source measurements. A detailed scheme can be found in Appendix E.

used (Fig. 6.1). In order to use the same chip several times, a glass fan-in between chip and detector was used. This enabled to make several bondings to the same chip.

A schematic view of the setup is shown in Fig. 6.2. The electron-source housing collimated the electrons to $\cos\theta > 0.8$ which was further reduced in x-direction by the total width of the strips connected to electronics and in z-direction by the aluminum box and scintillator position to around $\cos\theta \geq 0.95$.

A computer controlled digitizing osciloscope was used to perform analog to digital conversion of the multiplexed signal from the read-out chip. Raw data were stored to disk for analysis. The control signals needed to run the chip were provided by a VME-SEQSI unit.

The number of dead channels increased from initially none to 2 for the detector irradiated to low-fluence and to 8 after high fluence irradiation. It is possible that this

[49] The custom made circuit design can be found in Appendix E.

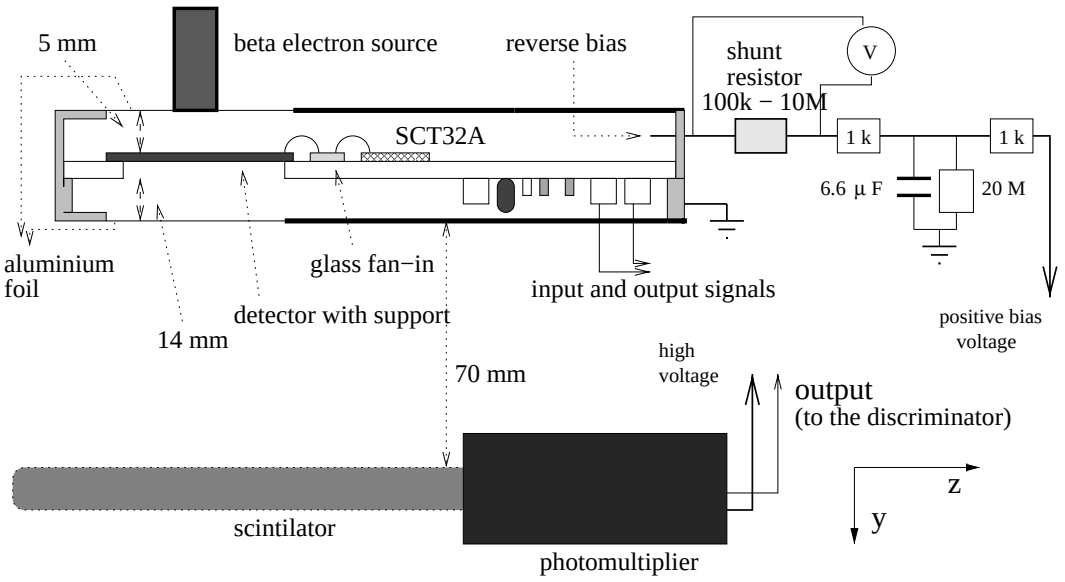

Figure 6.2 : A close look to the detector and trigger part of the setup. Resistance is given in Ω.

happened due to bonding errors, since the same glass fan-in was used for all measurements. Checking bonds under the microscope did not give clear evidence to support this explanation, since it was difficult to identify the contacts between the bonds. Therefore the dead channels were excluded from the analysis.

6.3 Irradiation

The detectors were irradiated with neutrons. During the irradiation detectors were reverse biased and cooled with water/glycol mixture flow through a small cooling block being in thermal contact with the detector support frame. B01 was irradiated to the normalized fluence of $\Phi = 4.5 \cdot 10^{13}$ n/cm^2 and B02 to $\Phi = 1.5 \cdot 10^{14}$ n/cm^2. The conditions during and after irradiation are shown in Table 6.1.

detector	normalized flux [n/cm^2 s] (time)	during: T (bias)	after: T (bias)
B01	$\phi = 2.1 \cdot 10^{12}$ (25 s)	$T \approx 5°$C (60V)	$T \approx 5°$C (200V)
B02	$\phi = 7.2 \cdot 10^{12}$ (240 s)	$T \approx 0°$C (190V)	$T \approx 0°$C (190V)

Table 6.1 : Conditions (normalized flux, temperature and bias) during and one week after the irradiation. Note that 190 V on detector B02 was not enough to fully deplete it during the storage at the reactor, while 200 V on detector B01 was sufficient already one hour after the irradiation.

The detectors were kept at the reactor one week after irradiation, since the activation

level was to high to move them to the laboratory. This was mainly due to activation of the cooling block. During this time they were biased and kept at low temperature (Table 6.1) in order to slow down the annealing process. The I/V and C/V measurements were performed during that time starting immediately after irradiation.

The setup for C/V and I/V measurements used at the reactor was similar to the one used in the laboratory. The Keithley 237 high voltage power supply and current measuring unit was replaced by a Wentzel power supply and a Keithley 617 current meter. Instead of HP4284A, a HP4243 LCR meter was used. The same decoupling scheme as shown in Fig. 4.8 was used.

The evolution of V_{FD} and leakage current after irradiation for both detectors is shown in Fig. 6.3. Immediately after irradiation full depletion voltage of almost 1000V was measured on detector B02 and $\alpha(20°\mathrm{C}) = 24 \cdot 10^{-17}$ A/cm (normalized to 20°C using Eq. 3.46) for detector B01. This is an indication of very high introduction rates for defects annealing with short time constants.

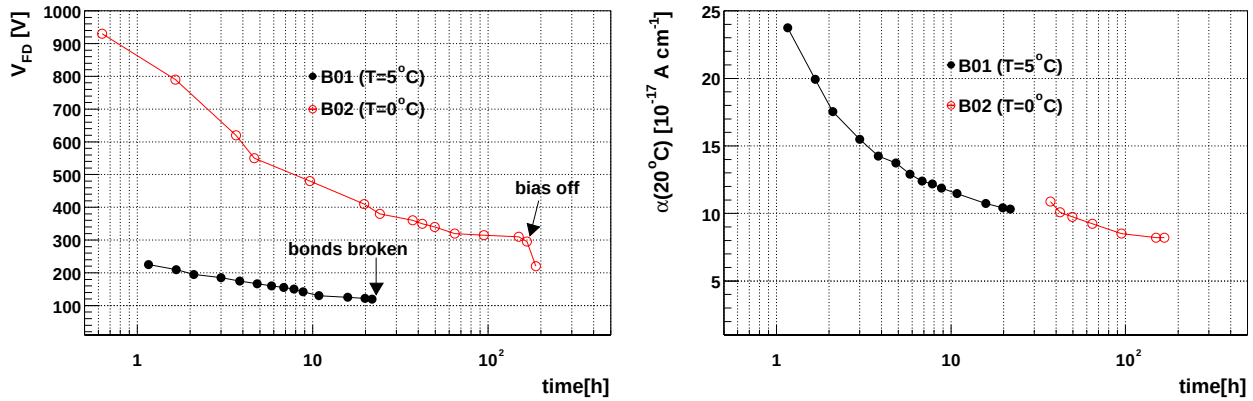

a.) b.)

Figure 6.3 : a.) The evolution of V_{FD} and b.) α for detectors B01 and B02 measured at the reactor after irradiation. The effect of bias voltage can be seen for detector B02. As the bias was switched off during the transportation of the detector to the laboratory the V_{FD} decreased. V_{FD} in the early annealing phase of detector B02 was determined from the line fit of $1/C^2(U)$ extrapolated to the geometric capacitance, due to detector break down. Once the V_{FD} was small enough the method described in Section 4.2.2 was used and also the leakage current at V_{FD} was determined. The bonds on detector B01 broke one day after the irradiation, thus no measurements were possible after that time.

When the detectors were brought to the laboratory, the bias was switched off and detectors were bonded to the electronics. All the measurements were performed in the refrigerator. In this way it was possible to perform tests at different temperatures.

6.4 Analysis of the signal measurements

Around $N = 20000$ events (coincident between scintillator trigger and clock signal) were taken at a given voltage and temperature. The extraction of the deposited charge signal and identification of the hit strips from the raw data was performed in several steps.

6.4.1 Pedestals and noise

In order to indubitably determine the signal as a consequence of a charged particle passage through the detector, the strip signal must substantially exceed the noise. It is therefore essential to determine the noise before the actual search for the signal.

- In the first loop over the N recorded events, the channel mean signal - pedestal ($\overline{P^i}$) and noise (σ_i) were calculated as

$$\overline{P^i} = \frac{1}{N}\sum_j^N {P_j}^i \quad , \quad \sigma_i^2 = \frac{1}{N}\sum_{j=1}^N ({P_j}^i - \overline{P^i})^2 = \frac{1}{N}\sum_{j=1}^N {P_j}^{i2} - \overline{P^i}^2 \quad , \tag{6.1}$$

  where ${P_j}^i$ is the raw signal (voltage level) of the i-th channel for the j-th event.

- In the second loop the pedestals and noise from the first loop were used to define strip signal ${S_j}^i = {P_j}^i - {P_j}^{cm} - \overline{P^i}$, where ${P_j}^{cm}$ denotes the common mode level calculated in two steps for each event separately as

$${P_j}^{cm} = \frac{1}{N_k}\sum_i^{N_k} {P_j}^i - \overline{P^i} \quad \text{for} \quad {P_j}^i - \overline{P^i} < 3\,\sigma_i \quad , \tag{6.2}$$

$$\sigma_j^{cm} = \frac{1}{N_k}\sum_i^{N_k} {P_j}^i - {P_j}^{cm} - \overline{P^i} \quad , \tag{6.3}$$

  where the sum runs over all strips N_k. After the first step common mode level ${P_j}^{cm}$ was calculated again in the same way as in Eq. 6.2 with an additional requirement that only channels with ${S_j}^i < 3\,\sigma_j^{cm}$ were included in the calculation of the event common mode.

  With calculated common mode level for each event the pedestals and noise were recalculated only with events satisfying ${S_j}^i < 3\,\sigma_i$

$$\overline{P^i} = \frac{1}{N}\sum_j^N {P_j}^i - {P_j}^{cm} \quad , \quad \sigma_i^2 = \frac{1}{N}\sum_{j=1}^N {S_j}^{i2} \quad \text{for} \quad {S_j}^i < 3\,\sigma_i \quad . \tag{6.4}$$

  If ${S_j}^i > 3\,\sigma_i$ the strip was considered as being hit hence excluded from pedestal and noise calculation.

- The second loop was repeated, however with pedestals and noise taken from the previous loop.

As expected the noise of each channel is gaussian (Fig. 6.4 a), however it was found that it depends on the digitization range-scale of the osciloscope. Due to large pedestal spread (Fig. 6.4 b) a scale of 200 mV/div was required to cover the signals equal up to 3 m.i.p. signal in all channels. The dynamic range (8 bits/2000 mV) of the osciloscope was to small, hence the scaling factor obtained from measurements at finer scale was used to scale down the noise afterwards (Fig. 6.4 a). Channel-to-channel noise variation was less than 10% of the average noise.

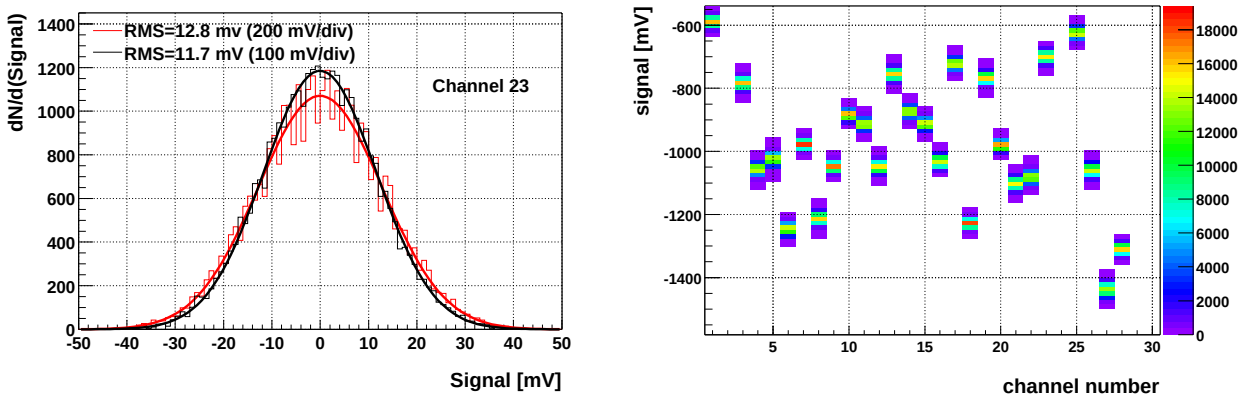

a.) b.)

Figure 6.4 : a.) A channel noise at two different scales of the osciloscope and b.) the pedestal plot together with the noise, i.e. distribution of $P_j^{\,i} - P_j^{cm}$ around the mean value $\overline{P^i}$, at $T = -11°$C for detector B02 irradiated to high fluence.

6.4.2 Signal

After the pedestals and noise were calculated the signal corresponding to the electron passage through the detector was determined as the cluster signal satisfying the following cuts:

- $S_j^{\,i}/\sigma_i > 4$ for the central strip-seed
- $S_j^{\,i}/\sigma_i > 2$ for the neighboring strips
- $(\sum_i^{N_{cl}} S_j^{\,i}/\sigma_i) = S/N > 5$ for the cluster signal

The distribution of the cluster signals represents the energy loss distribution of strontium electrons in the detector. Since the measured signal (S_j^i) is smeared by noise and electrons are not monoenergetic [50], as well as rather poorly collimated, the energy loss distribution is broader than Landau distribution with the same mean energy loss. The cluster signal distribution was therefore fitted with convolution of the Landau and Gaussian functions. An example of fits to the measured cluster signal-to-noise distribution is shown in Fig. 6.5. The position of the fitting function maximum was declared as the most probable event cluster signal-to-noise and the corresponding cluster signal as the most probable signal.

As discussed in the first chapter the signal from the preamplifier should be sampled at peak. The delay between the clock and the scintillator trigger (see Fig. 6.1) was chosen with the requirement of the largest measured most probable cluster signal-to-noise at different delays. The non-irradiated detector (B02) at 100 V and $T = 300$ K (see Fig. 6.6a) was used for that purpose. The spread of the delay between the clock and scintillator trigger is small (RMS=1.2 ns) as can be seen in Fig. 6.6b. The delay of ~ 28 ns was used for all measurements done with the strontium source.

[50] See Section 7.2.2 for the ^{90}Sr spectrum.

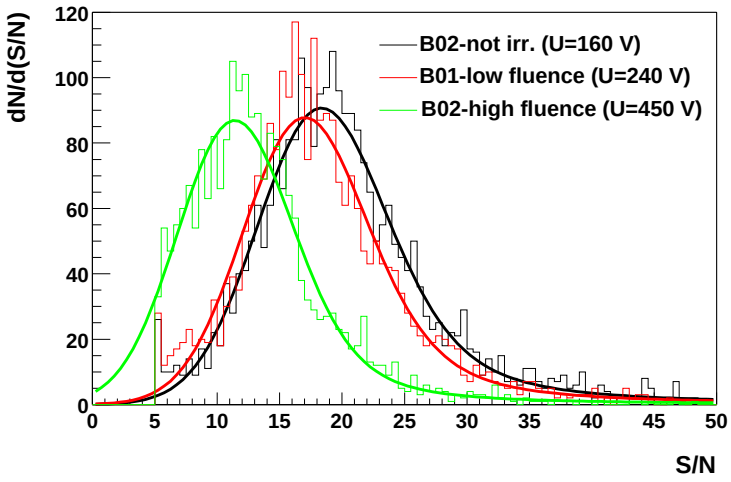

Figure 6.5 : Example of Landau and Gaussian functions convolution fit to the cluster signal-to-noise spectra for B01 and B02 detectors. Irradiated detectors were annealed for around 12 hours at 25°C.

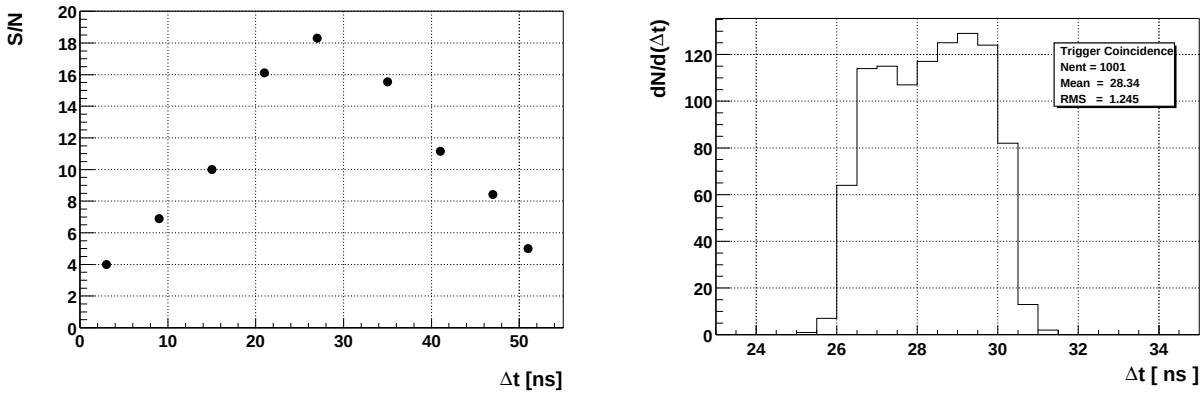

Figure 6.6 : a.) Most probable cluster signal-to-noise for a non-irradiated detector (B02) at 100 V and $T = 300$ K as a function of the delay between the photomultiplier pulse and clock pulse and b.) measured spread of the delay - coincidence curve.

6.4.3 Calibration signal

Each channel of the read-out chip is equipped with a calibration capacitor of 100 fF which results in approximately 22500 e_0 of charge when a calibration step voltage signal of 36mV is applied on input (Fig. 6.7b). The charge injection time from the HP 8112 pulse generator could be delayed with respect to the clock. Consequently the output from the preamplifier and shaping circuit could be sampled at different stages of the signal evolution. By scanning over the delays the pulse shape was measured and it is shown in Fig. 6.7a.

The height of the sampled signal at the peak was used to calibrate the signal scale in electrons. The conversion factor was 84 e_0/mV.

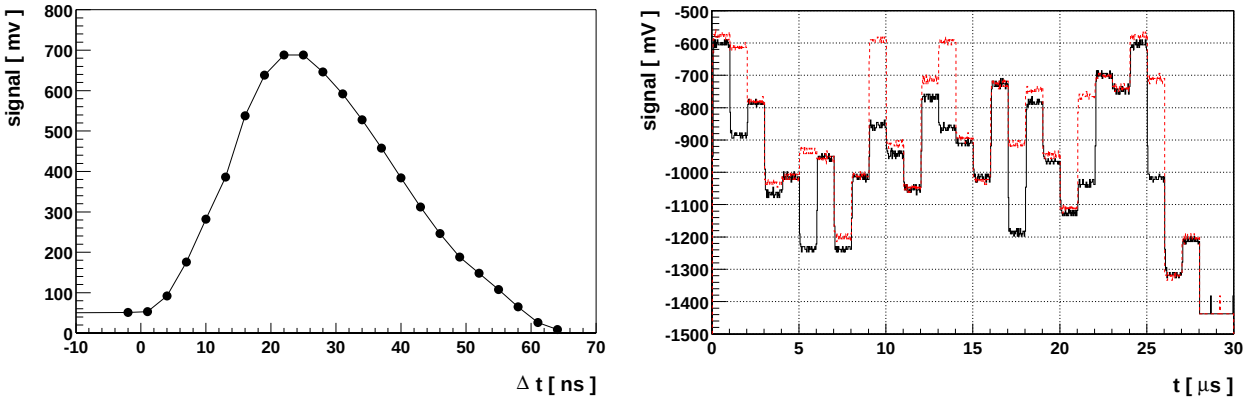

a.) b.)

Figure 6.7 : a.) Height of the sampled signal as a function of the delay between the charge injection time and clock pulse - preamplifier pulse shape a.). The injected charge was approximately three times larger than the charge deposited by a m.i.p.. b.) A view of the multiplexed signal after injection of a calibration pulse equivalent to charge deposited by m.i.p. b.). The black line represents the pedestals (see Fig. 6.4b) , while the red line represents the multiplexed signal after injection of the calibration pulse. Every fourth channel is connected to the same calibration line. The signals shown are inverted for easier reading.

6.5 Signal and noise performance

The most probable cluster signal to noise ratio, is the most important property for evaluating the detector performance. It affects the position resolution and, even more important at LHC conditions, the occupancy of the detector by noise. The S/N ratio is affected by irradiation due to signal degradation which is a consequence of charge trapping, and increase of noise.

In general, the increase of noise may be attributed partially to the increase of leakage current and partially to the increase of the interstrip capacitance after irradiation.

Detectors were kept at $T = 25°C$ for 12 hours before the first measurements were performed so most of the short term beneficial annealing of the effective dopant concentration already took place.

The S/N ratio measured at different bias voltages before and after irradiation may be seen in Fig. 6.8a. Its voltage dependence is mainly dominated by the charge collection efficiency, which is reflected in measurements of most probable cluster signals (Fig. 6.8b). The dependence of noise on voltage is quite weak (Fig. 6.8c), thus having only a small influence on the S/N behavior.

For irradiated detectors we define U_s as the voltage obtained by the intersection of two linear functions fitted to two different slopes of the most probable cluster signal vs. voltage plot (Fig. 6.8b). In this way the definition of U_s is equivalent to the definition of V_{FD} in the C/V method or to the definition of $V_{FD,TCT}$ by the TCT method. The full depletion voltage determined with the C/V method at 10 kHz ($T = -11°C$) before signal and noise measurements was approximately 45 V for detector irradiated to low fluence and about 220 V for the one irradiated to high fluence. This can be compared to

$U_s = 105$V and $U_s = 320$V, respectively.

It is obvious that at high fluence, additional overdepletion of the detector is required in order to obtain efficient charge collection. In addition the signal does not saturate for irradiated detectors at higher voltages due to trapping of the drifting charge. This is in agreement with measurements presented in the previous chapter. The signal increases with the slope $(5 \pm 1)\, e_0$/V for B01 and $(8 \pm 1)\, e_0$/V for B02.

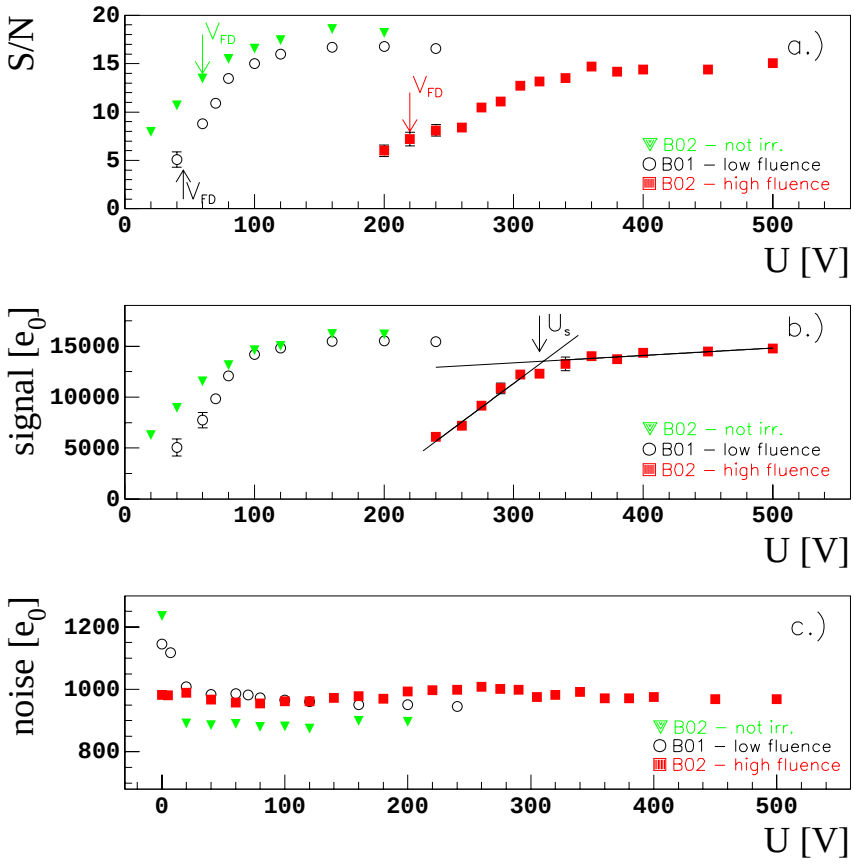

Figure 6.8 : Voltage scan of non-irradiated detector B02 ($T = 24°$C), low fluence irradiated B01 ($T = -11°$C) and high fluence irradiated B02 ($T = -11°$C).

The signal and the noise were also measured at different temperatures. No systematic temperature dependence of noise or signal may be observed in the temperature range from $T = -5°$C to $T = -27°$C (Fig. 6.9).

The noise of the irradiated detector may be estimated from the equation:

$$ENC_{irr} = \sqrt{((ENC_{nirr} + \Delta C\, \gamma)^2 + I_r\, \tau_p\, e_0)} \quad , \tag{6.5}$$

where ENC_{nirr} is the noise measured with the non-irradiated detector for which $I_r \sim 0$, ΔC is the increase of the strip capacitance after irradiation, for the SCT chip $\gamma \equiv 33\, e_0/\mathrm{pF}$ [Ang97], I_r is the leakage current per strip and $\tau_p = 25$ ns is the peaking time of the preamplifier. Leakage current as measured at $T = -11°\mathrm{C}$ and calculated from the total detector current (without guard ring) was 30 nA per strip (B01) and 98 nA per strip (B02) after irradiation, both corresponding to the leakage current damage constant $\alpha(20°\mathrm{C}) = 4.8 \cdot 10^{17}$ A/cm. The contribution of shot noise for B02 at this temperature is approximately 125 e_0 thus having a negligible contribution in Eq. 6.5. Therefore it is expected to have no significant temperature dependence of noise in this temperature region for detectors with similar strip areas irradiated to LHC fluences.

Lead by this conclusion we may explain the increase of the noise after irradiation (Fig. 6.8c) by the increase of strip capacitance caused by the ionizing radiation [HSi94] in the reactor. The measured radiation dose in SiO_2 for the irradiation with higher fluence is about 4 kGy (see also Appendix H). An increase of noise at low voltages, caused by the

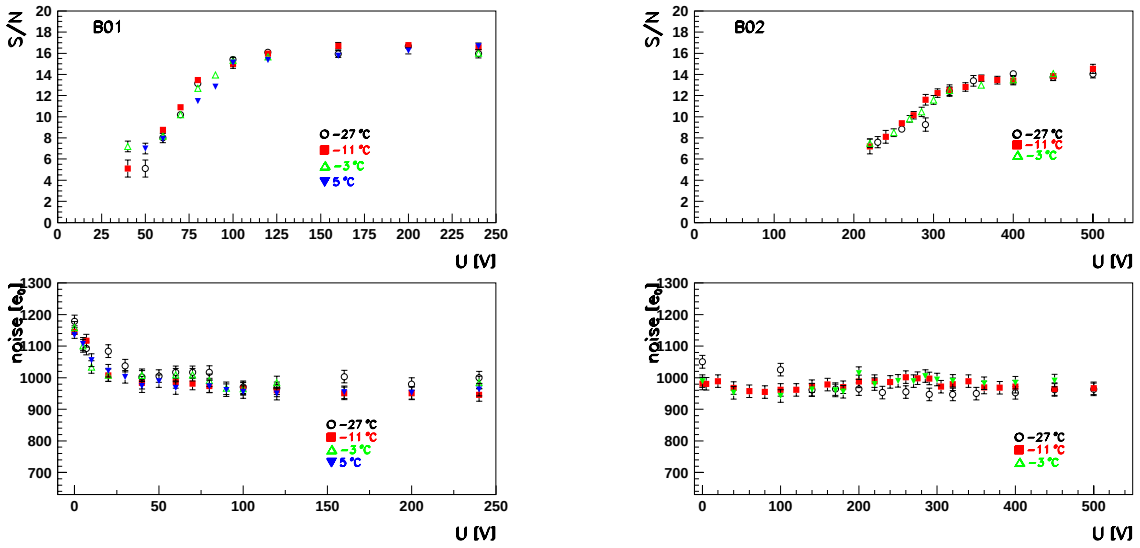

Figure 6.9 : Signal/Noise and noise vs. voltage at low fluence (left) and high fluence (right) at different temperatures.

increase of strip to backplane capacitance may not be observed for the highly irradiated detector. This is in agreement with the results of C/V measurement, where nearly no voltage dependence of capacitance at higher frequencies has been observed.

6.6 Fluence dependence of charge collection efficiency

Charge collection efficiency measured for non-irradiated and irradiated detectors is shown in Fig. 6.10. Here the CCE of the non-irradiated detector is defined to be equal to 1. This signal corresponds roughly to 17000 electrons if the scale is derived from calibration

signals. Simulation of charge generation in the 280 μm thick detector with the ^{90}Sr source and with same geometry predicts around 23300 electrons (Section 7.2.2). Around 15% lower signal than predicted is expected due to loss of charge induced on interpolation strips (see section 2.2.3). As will be shown in the next chapter, a not proper sampling delay is, besides the inaccurate calibration capacitors, the most likely explanation for the remaining difference. For the irradiated detector, CCE was determined with the ratio of irradiated detector signal at U_s and the saturated signal of the non-irradiated detector. Higher values of CCE can be obtained if the applied voltage is higher than U_s due to reduced trapping of the drifting charge.

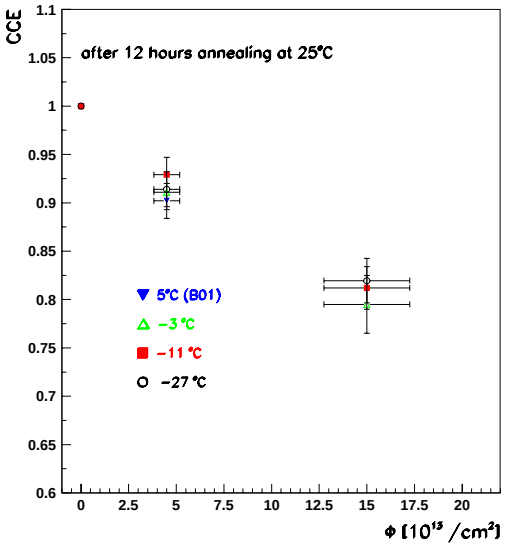

Figure 6.10 : Measured charge collection efficiency at two fluences and different temperatures.

6.7 Evolution of signal after irradiation

Since the effective dopant concentration changes after irradiation with time, it was checked if this behavior is reflected in the signal evolution as well.

Therefore the time dependence of the performance of detector B02 was followed in the laboratory. The first 22 days of annealing in the laboratory were done at room temperature ($T = 25°$C), after that reverse annealing was accelerated in the oven at $T = 60°$C. The detector was annealed without bias in steps. After each annealing step was completed, ^{90}Sr signals at different voltages were recorded at $T = -11°$ and a C/V measurement was performed. The results are shown in Fig. 6.11. Scaling of time at $T = 60°$C to the equivalent time at $T = 25°$C was done by using Eq. 3.14 with the activation energy of $E_a = 1.31$ eV [Lin99]. We may observe that U_s increases due to reverse annealing

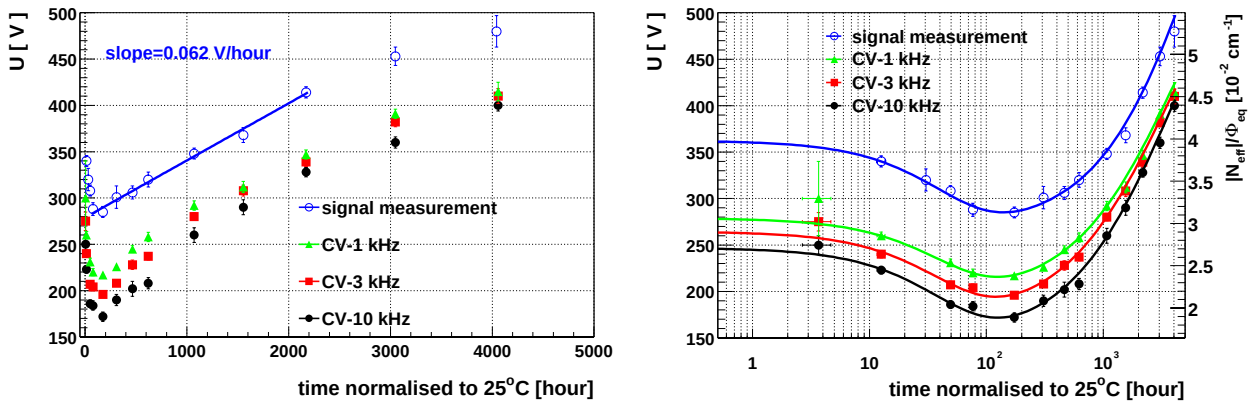

Figure 6.11 : a.) Evolution of U_s and V_{FD} with annealing in linear and b.) log scale. Measurements fitted with the Hamburg model are also shown.

in a similar way as V_{FD} determined from C/V measurements (Fig. 6.11). The slope of increase in the initial (linear) part of reverse annealing is ≈ 1.5 V/day.

	g_a [10^{-2} cm^{-1}]	τ_a [h]	g_c [10^{-2} cm^{-1}]	g_Y [10^{-2} cm^{-1}]	τ_{ra} [day]
signal	1.01 ± 0.13	93 ± 25	2.95 ± 0.09	6.7 ± 2.4	722 ± 378
1 kHz	0.89 ± 0.09	93 ± 19	2.16 ± 0.04	4.96 ± 0.68	422 ± 106
3 kHz	0.98 ± 0.08	91 ± 17	1.91 ± 0.05	4.94 ± 0.47	361 ± 70
10 kHz	1.05 ± 0.09	91 ± 19	1.66 ± 0.07	5.42 ± 0.6	399 ± 93

Table 6.2 : The results of the Eq. 6.6 fit to the measurements shown in Fig. 6.11b. The time constants are scaled to 20°C. According to Eq. 3.14 scaling factors 2.39 and 2.07 can be used to scale reverse and beneficial annealing time constants, respectively. Assumed activation energies are $E_a = 1.31$ eV for reverse annealing and $E_a = 1.09$ eV for beneficial anneling [Lin99].

To compare the results with previous work $|N_{eff}|$ was calculated from U_s and V_{FD} using Eq. 4.3. The evolution of $|N_{eff}(t)|/\Phi_{\rm eq}$ was fitted using the same ansatz as in the section describing TCT measurements of N_{eff} reverse annealing (Eq. 5.8), with an additional term describing defect annealing in time

$$\frac{N_{eff}(t)}{\Phi_{\rm eq}} = g_a \exp(\frac{-t}{\tau_a}) + g_c + g_Y \left[1 - \frac{1}{1 + t/\tau_{ra}}\right] \quad . \tag{6.6}$$

The results of the fits are listed in the Table 6.7. As can be seen the parameters of the fit at different frequencies with exception of g_c agree with each other and measurements referenced in [ROSE3]. Values around 400 days are obtained for $\tau_{ra}(20°\text{C})$, which is comparable to 480 days found in [ROSE3].

Around 30 hours longer time constant $\tau_a(20°\text{C})$ is obtained for beneficial annealing compared to [Lin99]. This could be an effect of time required by bonding and mounting,

where the precise temperature history is not known, as well as the time spent at 0°C at the reactor which was not taken into account.

Although the value of reverse annealing time constant τ_{ra} derived from signal measurements is compatible with C/V measurements the increase of U_s with reverse annealing tends to be slower than the increase of V_{FD} extracted from C/V measurements. A possible explanation would be that at higher full depletion voltages the average electric field in the detector is higher and less overdepletion is needed to reduce the carrier collection time and by that the amount of the charge being trapped.

The signal measurements at U_s and $U = 500$ V show a small degradation with time after irradiation (Fig. 6.12). If the voltage is fixed to $U = 500$ V the decrease of the most probable signal is a consequence of reduced overdepletion and increased effective hole trapping probability [51] with time in accordance with results of Section 5.2.4. On the other hand a smaller decrease of most probable signal measured at U_s, can be explained by the higher average field and faster hole drift which partially compensates the increase of effective hole trapping probability. The slope of the decrease of signal, measured at U_s, is ≈ 0.2 e_0/h at $T = 25°$ C. As the silicon detectors operated at LHC will be reverse annealed to about 10% of the reverse annealing amplitude the most probable signal will not be significantly affected.

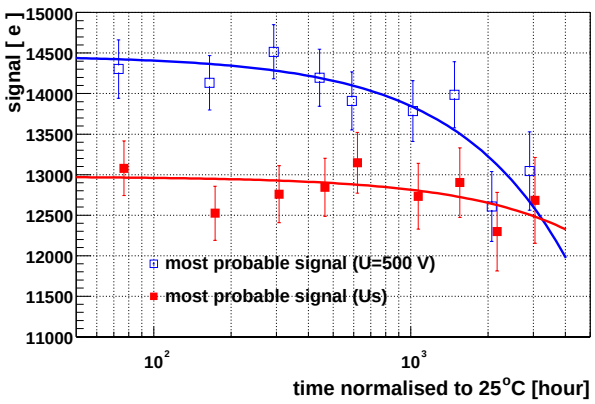

Figure 6.12 : Most probable signal measured at $U = 500$ V and U_s as a function of time after irradiation. Linear fit to the data is also shown.

6.8 Cluster width

The increase of the noise and trapping of the drifting charge reduce the mean cluster width with irradiation. Higher noise results in more signal required on the neighboring strips to be included in the cluster signal. The reduction of signal due to trapping has the

[51] The dominant part of the induced charge in a detector with p^+ strips comes from drift of holes (Chapter 7)

same effect. In addition the importance of diffusion becomes smaller, since some charge is trapped before reaching the neighboring strip [52].

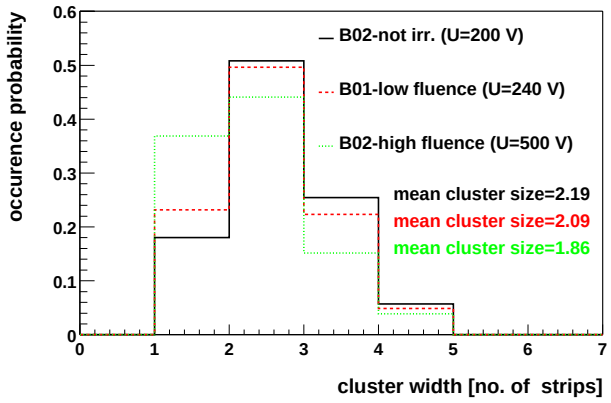

Figure 6.13 : The mean cluster width as measured after 15 hours of annealing at $T = 25°\mathrm{C}$.

The cluster width was found to follow the predictions. The measured event cluster width probability is shown in Fig. 6.13. It was measured after 15 hours annealing at $T = 25°\mathrm{C}$.

[52] In highly irradiated silicon detector some charge is always induced on the neighboring strips. The mechanism which effectively takes over the role of diffusion will be discussed in Section 7.5.

7

Simulation of silicon detectors

A simulation of silicon detectors is a powerful tool for designing silicon detectors and also for predicting their operation. Therefore it is not surprising that in the past results of several simulations were published. They were, however, focused on different aspects of operation.

Double sided detector performance was simulated by [Les93]. The drift of carriers generated by minimum ionizing particles in electric and magnetic fields was simulated in order to predict the resolution of the detector. A single detector geometry at fixed bias voltage and magnetic field was considered.

Similar but extended simulation for single sided detectors was used by [Dab95]. In addition the influence of CMOS and bipolar preamplifier design to noise and consequently the resolution of detectors with different geometries was investigated. Non-inverted detectors with with equal effective dopant concentration at fixed voltage and magnetic field were simulated. A more detailed analysis of performance of detectors with interpolation strips was later given in [Dab96]. A simple simulation which did not include an accurate calculation of the induced current was used by [Iwa98] to establish position dependent decrease of charge collection efficiency in such detectors.

The purpose of this simulation is to predict the behavior of irradiated silicon detectors in terms of signal formation and detection. A special emphasis is given to trapping of the drifting charge by using the effective trapping times measured in this thesis. The presented simulation consists of three parts: the calculation of the electric and weighting field, the simulation of the charge generation and the drift of the generated charge in the electric field, and the electronic processing of the signal followed by analysis. It was written in the C++ programming language using the following tools:

- ROOT [ROOT] for storage, manipulation and visualization of results
- GEANT [GEANT] for simulation of electron tracks
- Numerical recipes [NumRe] for numerical calculations.

7.1 Electric and Weighting Field Calculation

7.1.1 Electric field

The calculation of electric is a non trivial problem in strip detectors. Even for pad detectors an analytical solution of Eq. 2.4 is not possible for an arbitrary effective doping profile. Thus in both cases for pad and strip detectors the numerical solution of

$$\begin{aligned} \nabla^2 U(\vec{r}) &= -\frac{e_0\, N_{eff}(\vec{r})}{\epsilon_{Si}\epsilon_0} \\ \vec{E} &= -\nabla U(\vec{r}) \quad , \end{aligned} \tag{7.1}$$

was searched for the electric field. In general finding $N_{eff}(\vec{r})$ and the electric field profile requires solution of set of three differential equations, besides the Poisson equation also the continuity equation for holes and electrons

$$\begin{aligned} \frac{\partial n}{\partial t} &= \mu_e\, n\, \nabla\vec{E} + D_e\, \nabla^2 n + G_n - R_n \\ \frac{\partial p}{\partial t} &= -\mu_h\, p\, \nabla\vec{E} + D_h\, \nabla^2 p + G_p - R_p \\ N_{eff} &= p - n + N_D - N_A + \sum_{deep} Q_t \quad , \end{aligned} \tag{7.2}$$

where $D_{e,h}$ are diffusion constants of electrons and holes (see Section 7.2.1). However in the scope of this work only the case of abrupt junction approximation with constant N_{eff} will be considered. The reader is referred to [StudD] for an example of exact solution of Eqs. 7.1 and 7.2.

Obtaining the electric field profile for pad detectors is an one dimensional problem, with the voltage defining boundary conditions at the front and back contact. The solution of the Poisson equation is obtained by integration of Eq. 7.1 and familiar profiles of Fig. 2.6 are obtained.

In a strip detector the calculation of electric field requires solving the true partial differential equation. If the strips are much longer than the strip pitch, which is true in most applications, the problem of finding the electric field and the weighting field is two dimensional. This holds for single-sided $p^+ - n - n^+$ and $n^+ - n - p^+$ strip detectors simulated in this work.

Eq. 7.1 was solved on a two-dimensional discrete uniform mesh of size $\Delta x = \Delta y = 1\ \mu$m (see Fig. 7.1). The boundary conditions at the surface of the microstrip detector were

- $U = 0\ V$ ($p^+ - n - n^+$ detectors) or $U = U_{operation}$ ($n^+ - n - p^+$ detectors) at all strips.
- $U = U_{operation}$ ($p^+ - n - n^+$ detectors) or $U = 0\ V$ ($n^+ - n - p^+$ detectors) at the backplane.

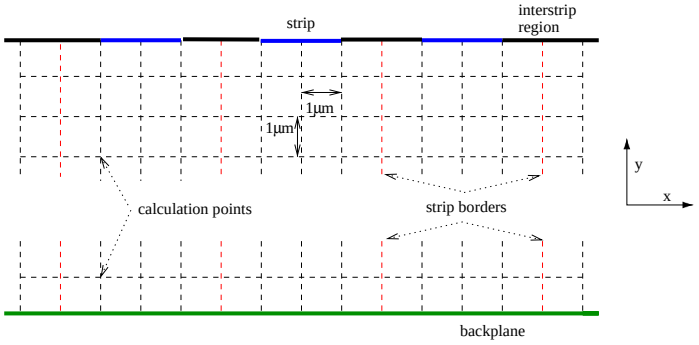

Figure 7.1 : Schematic view of the detector as used for electric and weighting field calculation.

- $\partial U(x,y)/\partial\, y \;=\; 0$ at the surface in the inter-strip region (no field normal to the detector).
- $\partial U(x,y)/\partial\, x \;=\; 0$ at the x edges ($\pm$ half strip pitch). This is required by detector symmetry (no field across detector cells).

The implants (p^+ or n^+ strips) were taken to be less than a micron thick, thus 1-D. Electric field between the calculation points was obtained by linear interpolation of the electric field at neighboring calculation points. An example of electric field profile in the case of positive and negative effective dopant concentration is shown in Fig. 7.2.

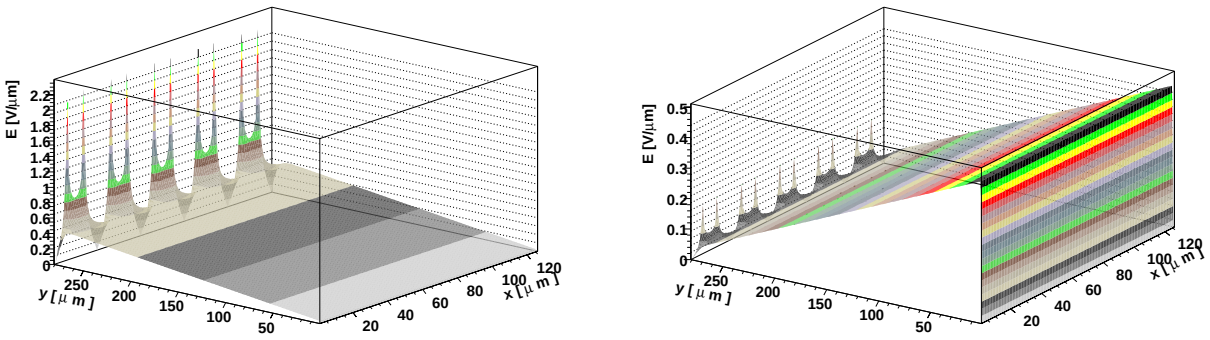

a.) b.)

Figure 7.2 : An example of calculated electric field for 280 μm thick detector with strip pitch of 25 μm and strip width of 10 μm operated at 70 V ($\approx V_{FD}$). The effective dopant concentration is: a.) 10^{12} cm^{-3} (non-inverted detector) and b.) -10^{12} cm^{-3} (inverted detector).

7.1.2 Weighting field

The weighting potential U_w and weighting field E_w are obtained as a solution of Eq. 7.1 with $N_{eff} = 0$. The boundary conditions are the following:

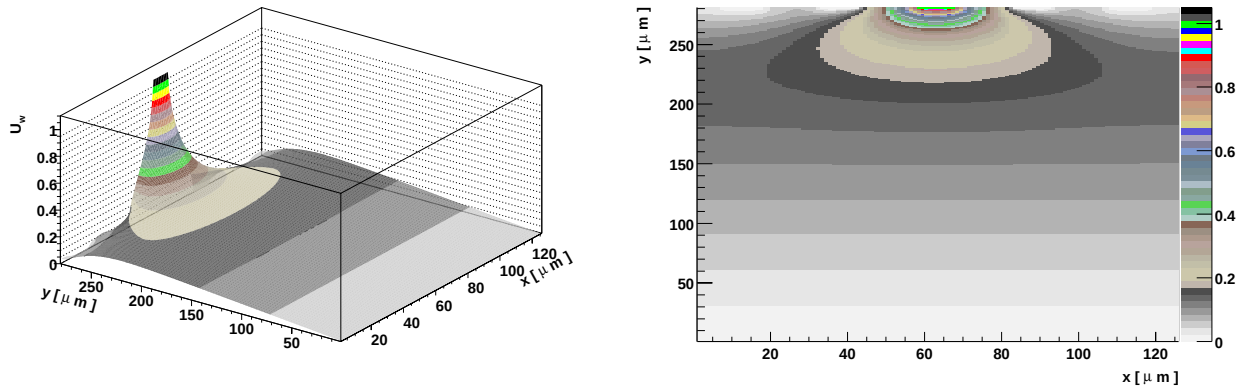

a.) b.)

Figure 7.3 : Calculated weighting potential for a 280 μm thick detector with strip pitch of 25 μm and strip width of 10 μm: a.) surface plot and b.) contour plot.

- $U_w = 1$ at the read-out strip
- $U_w = 0$ at all other strips and the backplane.
- $\partial U_w(x, y)/\partial y = 0$ at the surface in the inter-strip region.
- $\partial U_w(x, y)/\partial x = 0$ at the x edges of the 5 strip segment.

The weighting field was calculated for a group of five strips with the middle strip being the one for which the weighting field was calculated. In principle all strips should be included in the calculation of the weighting field, however that would require large amount of CPU time. The mapping was checked for different number of strips included in the calculation. The difference between the induced charge of electrons and holes for minimum ionizing particle track (see Section 7.2.3) if three, five or seven strips were included was below 3% for a detector with 80 μm strip pitch, 18 μm strip width and thickness of 280 μm. A similar difference was observed for the detector with geometry defined in Fig. 7.3, if five, seven or nine strips were included in calculation.

As in the case of electric field calculation the weighting field between the calculation points was obtained by linear interpolation of the weighting field at neighboring calculation points. The calculated weighting field for the detector geometry as used in the example of electric field calculation is shown in Fig. 7.3. A strong field in the region close to the strips can be observed.

According to Eq. 2.23 the product of mobility, electric field and weighting field gives a scalar field ($I(\vec{r})$) which determines in each point the induced current due to motion of drifting charge. It is very illustrative to use $I(\vec{r})$ since different detector regions can be identified in terms of the induced current. In Fig. 7.4 the difference between non-inverted (a.)) and inverted detector (b.)) can be seen. In both cases the largest current is induced by charge drifting close to the strip. However, in the inverted detector the charge drifting in regions away from the strip induces higher currents than in a non-inverted detector.

There are also regions in the detector where the induced current is negative. The mobility was left out of the product in order to use the same figure for electrons and holes [53].

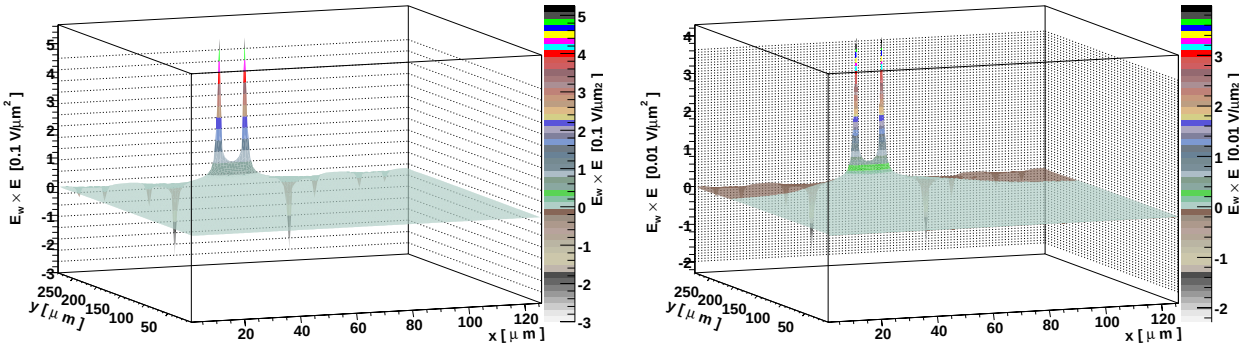

a.) b.)

Figure 7.4 : The product of the fields $\vec{E} \cdot \vec{E}_w$ shown in Figs. 7.2 and 7.3 for: a.) non-inverted detector and b.) inverted detector. Note that the color scales for both plots are different.

7.2 Simulation of drift

According to Ramo's theorem Eq. 2.23 the motion of charge q in the detector induces current at all contacts of the detector. An ionizing particle when traversing the detector leaves a track of continuously generated electron-hole pairs. In the simulation such

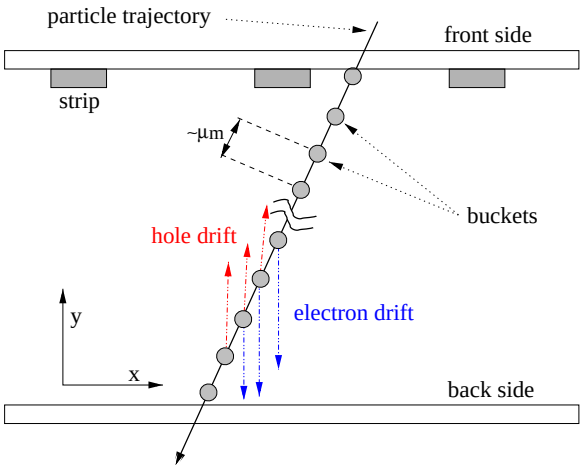

Figure 7.5 : Schematic view of the track drift simulation in a $p^+ - n - n^+$ detector.

[53] At the detector bias of 70 V the electric field in the detector is low enough to assume constant mobility.

continuous distribution of charge was cut into $N_{buckets}$ buckets, each corresponding to 1 μm of the track (see Fig 7.5). Each bucket consisted of an equal number of electrons and holes drifting in opposite directions. The total induced current was then calculated as

$$I(t) \;=\; \sum_{k=1}^{N_{buckets}} \; I_e^k(t) \;+\; I_h^k(t) \;=\; I_e(t) \;+\; I_h(t) \quad , \tag{7.3}$$

where k-th bucket contribution to the total current is denoted by $I_{e,h}^k(t)$.

Once the bucket was generated, its motion was simulated in micron steps until it reached the electrode. The differential equation of motion (Eq. 2.24) was approximated with [54]

$$\begin{aligned} |\vec{r}_{n+1} \;-\; \vec{r}_n| \;&=\; \Delta r_{drift} \;=\; 1\ \mu\mathrm{m} \\ \frac{\vec{r}_{n+1} \;-\; \vec{r}_n}{t_{n+1} - t_n} \;&=\; \mu\Big(E\big[\vec{r}_n + \frac{\vec{E}(\vec{r}_n)}{E(\vec{r}_n)}\,\frac{\Delta r_{drift}}{2}\big]\,,\,T\Big)\;\vec{E}(r_n) \\ Q_{n+1} \;-\; Q_n \;&=\; -q\,\vec{E}_w(r_n)\cdot(\vec{r}_{n+1} - \vec{r}_n) \quad , \end{aligned} \tag{7.4}$$

where Q_n denotes the total induced charge at t_n. After each step the new spatial coordinate ($\vec{r}_{n+1}$), time needed for the step ($t_{n+1} - t_n$) and induced charge in the step ($Q_{n+1} - Q_n$) were calculated. From here the induced current for each electron or hole bucket can be calculated as

$$I_{e,h}^k(t_{n+1}) = \frac{Q_{n+1} - Q_n}{t_{n+1} - t_n} \quad . \tag{7.5}$$

The mobility parameterization, used in Eq. 7.4, was proposed by [Sel90] and can be found in Appendix C.

7.2.1 Diffusion

The diffusion of the drifting carriers was also taken into account. The Einstein relation for a non-degenerate ($n \ll N_C$, $p \ll N_V$) semiconductor states

$$D_{e,h} \;=\; \big(\frac{k_B\,T}{e_0}\big)\,\mu_{e,h} \quad , \tag{7.6}$$

[54] If the magnetic field $\vec{B}(\vec{r})$ were present the second equation in Eq. 7.4 would be replaced by

$$\begin{aligned} \frac{\vec{r}_{n+1} \;-\; \vec{r}_n}{t_{n+1} - t_n} \;&=\; \mu\Big(F\big[\vec{r}_n + \frac{\vec{F}(r_n)}{F(r_n)}\,\frac{\Delta r_{drift}}{2}\big]\,,\,T\Big)\,F(\vec{r}_n)\,\vec{s} \\ \vec{s} \;=\; \frac{\vec{F}}{F} \quad &,\quad ,\vec{F} \;=\; \vec{E} \;+\; \mu_{H_{e,h}}\,\vec{E}\times\vec{B} \quad , \end{aligned}$$

with $\mu_{H_{e,h}}$ the Hall mobility of electrons and holes, respectively.

where $D_{e,h}$ is the carrier diffusion constant. The mobility is spatially dependent and thus also the diffusion constant.

When the diffusion was included in the simulation each bucket was split into smaller buckets ($\sim 10-100$) which were considered as point charges. The drift of the subbuckets was performed according to Eq. 7.4. At each point $\vec{r}_n$ of the subbucket drift path a random component to the drift velocity was added. The step $\vec{r}_{n+1} - \vec{r}_n$ in Eq. 7.4 is

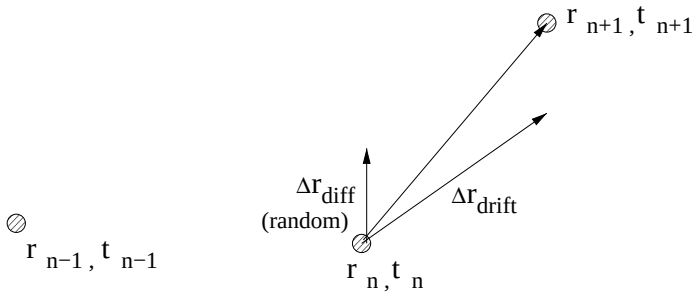

Figure 7.6 : The schematic view of the subbucket drift step when diffusion is included in the simulation.

therefore modified for an additional term $\Delta\vec{r}_{diff}$ (Fig. 7.6) that is distributed normally in all directions with the standard deviation defined as $\sigma_{D_{e,h}} = \sqrt{2\,D_{e,h}\,(t_{n+1} - t_n)}$

$$\vec{r}_{n+1} - \vec{r}_n = \Delta\vec{r}_{drift} + \Delta\vec{r}_{diff}(\sigma_{D_{e,h}}) \quad . \tag{7.7}$$

The induced current for each bucket was calculated as the sum of all subbuckets' current. An example of spatial distribution of the bucket charge after the drift through the diode with $N_{eff} = 10^{12}$ cm^{-3} is shown in Fig. 7.7. The obtained width of distribution

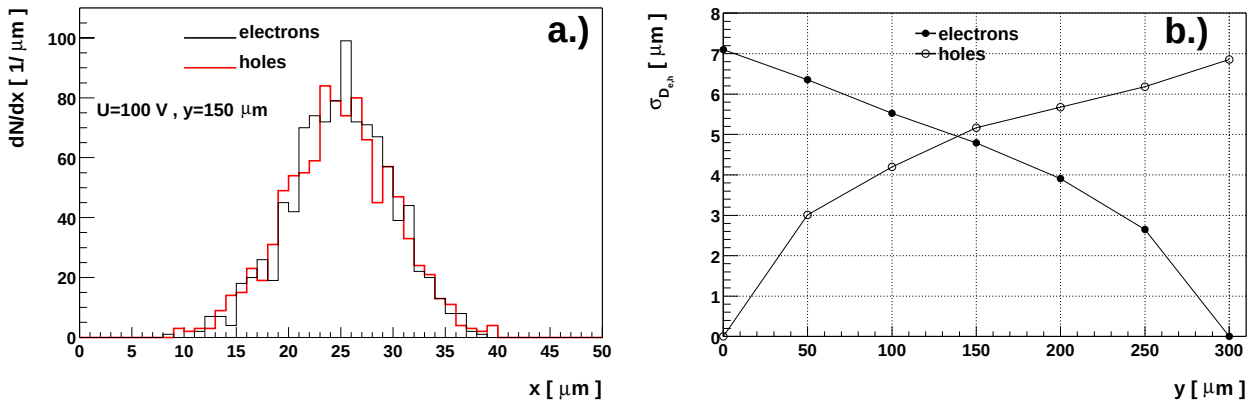

Figure 7.7 : a.) Spread of bucket charge generated at the surface at $x = 25$ μm after 150 μm of drift and b.) the standard deviation of the bucket charge distribution at different depths. The applied voltage was 100 V and temperature $T = 263$ K.

(5 μm) after 150 μm of drift, which is the average drift path of the charge generated by minimum ionizing particles, is in agreement with [Bel83].

The number of subbuckets required depends on the desired time resolution of the induced current curve and the charge collection time (see Fig. 5.19 for its definition). If the induced current is sampled (calculated) every 0.5 ns and the width of the induced current pulse was 10 ns already 10 subbuckets were sufficient to get a smooth induced current shape.

7.2.2 Electron-Hole pair generation

The simulation of the generated charge was done in two ways. If only a relative comparison between different pad or strip detectors was looked at, or different detector designs were considered, a particle track was taken as a strait line with selected end points and the most probable energy loss of 75 e-h pair/μm.

In simulation of measurements from previous chapter particle tracks were simulated using the GEANT package [GEANT] in which all the important processes such as multiple scattering energy loss straggling, production of knock-on electrons (E_δ) and bremstrahlung photons were considered.

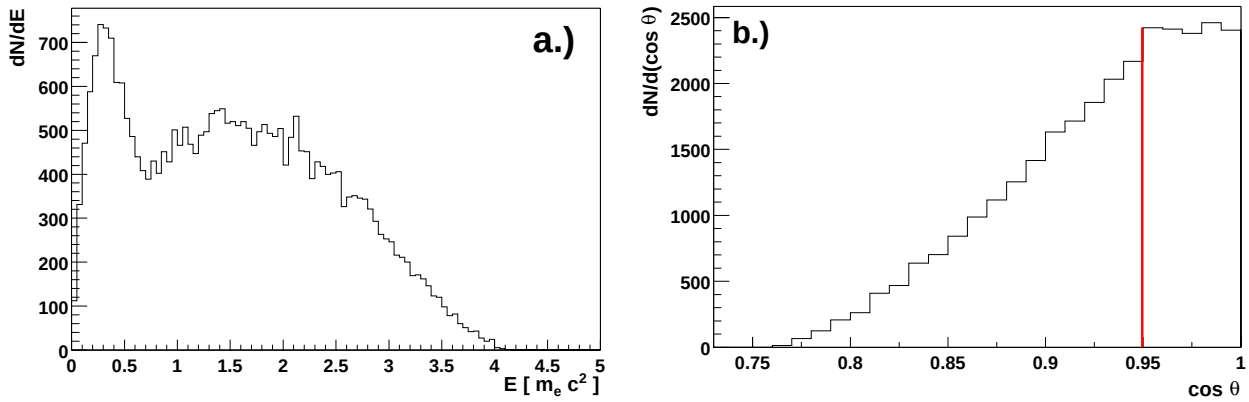

Figure 7.8 : a.) Simulated spectrum of electrons from ^{90}Sr source after they penetrated the housing and b.) the angular distribution of emitted electrons on the detector surface. The red line denotes the collimation angle used in the simulation.

Strontium electrons (Fig. 7.8) were generated and then tracked in steps through the simplified measurement setup shown in Fig. 7.9. The number of steps and their size depend on electron energy, material they traverse and its boundaries. The step size could be also limited by the user [55].

Secondary particles such as knock-on electrons and bremstrahlung photons were also tracked provided that their energy was above some threshold (E_δ = 100 keV $-$ 40μm range, E_γ = 50 keV). Below that threshold the energy loss of the primary electron was considered as continuous with the mean value calculated for each step from Berge-Salzer equation [GEANT]. Energy loss distribution around its mean value was calculated according to Landau distribution.

[55] Details about simulation of charge generation can be found in [KramD].

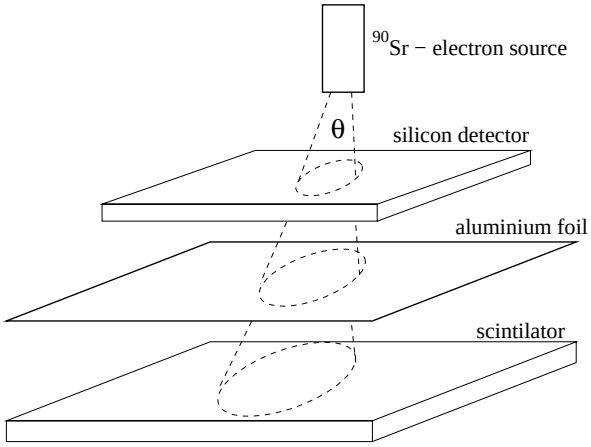

Figure 7.9 : Schematic view of the simulation setup. The thickness and positioning of the detector, aluminum foil and scintillator are the same as in Fig. 6.2. When simulating the induced current response to the strontium electrons traversing the diodes in the TCT setup the foil and scintillator were excluded from the simulation.

The energy lost in silicon was obtained from

$$\Delta E_{\mathrm{Si}} = \sum_{i=1}^{N} (\frac{dE}{dx})_i \Delta x_i \tag{7.8}$$

where the sum runs over all tracking steps in silicon, usually $N = 1$ to 4. From $(\frac{dE}{dx})_i$ the bucket charge for the i-th tracking step was calculated as

$$Q_i^{bucket} = \frac{1}{3.6 \text{ eV}} (\frac{dE}{dx})_i \ \Delta x_{bucket} \quad , \tag{7.9}$$

where Δx_{bucket} is distance between two neighboring buckets.

In order to simulate the measurements, only the strontium electrons penetrating the aluminum foil and reaching the scintillator were used in the analysis. Once the electron reached the scintillator it was considered energetic enough to produce a detectable signal in the scintillator and trigger the experiment.

The simulation used for calibration of the TCT setup was an exception. There also the electrons stopped in the silicon are detected and therefore all simulated strontium electrons were taken into account.

7.2.3 Processing of the induced current

An example of the induced current shape for a minimum ionizing particle track traversing the silicon microstrip detector is shown in Fig. 7.10. The induced current was used as an input to the preamplifier.

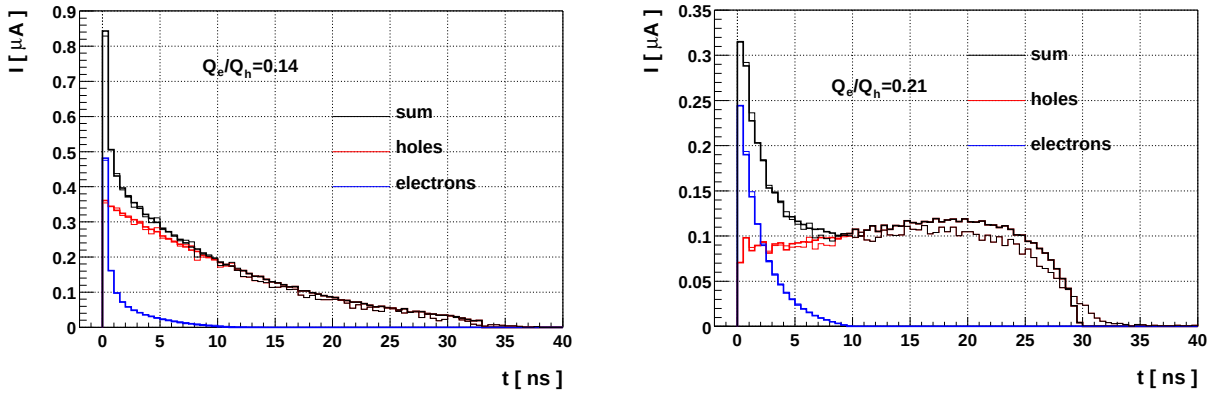

a.) b.)

Figure 7.10 : An example of induced current of a minimum ionizing particle track of normal incident angle in the middle of the strip: a.) a non-inverted detector and b.) an inverted detector operated at $T = 263$ K and $U = 70$ V ($\approx V_{FD}$) are considered. For the geometry of detectors and consequently the electric and weighting field profile see Figs. 7.2, 7.3. The separate carrier induced currents calculated with diffusion simulation (thin line) and without it (thick line) are shown. The effective trapping times used in simulation of the inverted detector were taken into account as the detector was irradiated to $\Phi_{\rm eq} = 5 \cdot 10^{13}$ n cm^{-2}. The ratio of electron and hole induced charges Q_e/Q_h is also given.

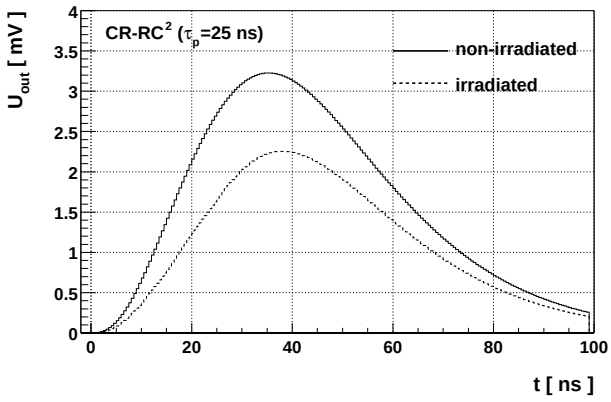

Figure 7.11 : Processed induced currents shown in Fig. 7.10. No amplification of the charge was assumed. A difference of ~30 % is a consequence of both charge trapping and ballistic deficit. Note that the operation voltage is close to V_{FD}.

The simulation of the preamplifier and shaping circuit exploits Eqs. 2.45, 2.49 and 2.53. Since the simulation was focused on signal formation the detector design features that influence mainly noise were neglected. In particular case of silicon strip detectors the interstip capacitance, resistance of the metal and implant strips were neglected. The detector equivalent circuit that allows the calculation of the contribution to the noise due to detector design is described in [Dab95].

Using the preamplifier ($C_C = 1$ pF, $R_C = 0.3$ MΩ) followed by a CR-RC^2 shaping

circuit with $\tau_p = 25$ ns, the induced current shown in Fig. 7.10 results in an output voltage as shown in Fig. 7.11.

7.3 Simulation of microstrip detectors

The main goal of the simulation of the measurement was to check the agreement between measured and simulated data and consequently the TCT measurements of effective trapping times. In addition, the simulation gave an opportunity to check how the operation of the detector is influenced by different detector geometries, front-end electronic schemes and the choice of the delay between sampling clock and time of particle arrival. The

strip pitch	strip width	$N_{k,k\pm1}$	$N_{k,k\pm3}$	motivation
25 μm	10 μm	0.351	0.063	measured detectors
56 μm	18 μm	0.329	0.060	ATLAS analog read-out
80 μm	18 μm	0.300	0.057	ATLAS binary read-out

Table 7.1 : Simulated detector geometries. Calculated fraction of charge induced on strip k if the charge q is placed on the interpolation strip i if every second strip is connected to the readout electronics. If every strip is connected to the read-out electronics the $N_{k,i} = 0$. All detectors were 280 μm thick and had strips of 4 cm length. Detectors designed for a binary read-out are without interpolation strips.

choice of the simulated detector geometries was governed by the proposed design for ATLAS silicon microstrip detectors and by the geometry of the measured detectors. The list of simulated geometries together with the charge sharing coefficients (see section 2.2.4) for one interpolation strip is given in Table 7.1. Pitches 56 and 80 μm correspond to the design of ATLAS analog[56] and binary module [ATLID, ATLTP], while 25 μm pitch was chosen in order to compare the results of the simulation with measurements.

The effective space charge density $e_0 N_{eff}$ used in the Poisson equation 7.1 was determined from measurements of V_{FD} using the C/V method at room temperature and 1 kHz frequency. The parameters are gathered in Table 7.2.

$\Phi_{\rm eq}$ /cm^2	not irradiated	$5 \cdot 10^{13}$	$15 \cdot 10^{13}$
V_{FD}	60V	50V (1kHz)	240V (1kHz)
N_{eff}	10^{12} cm^{-3}	$-0.9 \cdot 10^{12}$ cm^{-3}	$-4 \cdot 10^{12}$ cm^{-3}

Table 7.2 : Parameters used in simulation: $\Phi_{\rm eq}$, V_{FD} and N_{eff}. V_{FD} was obtained from C/V measurements at 1kHz. Irradiated detectors were annealed close to minimum in V_{FD}. The effective trapping times and their temperature dependence are listed in Table 5.2 and 5.3.

The effect of a thin positive space-charge layer at the strip side ("double junction")[57]

[56] The read-out pitch would be 112 μm.

[57] Spatially dependent N_{eff} was used in Eq. 7.1 in this case.

was investigated for irradiated detectors with its parameters taken from [LiZ92, Bea98]. Its influence on charge collection efficiency was negligible at any operating point above V_{FD}. Only $U > V_{FD}$ were simulated due to the simple fact that high noise and trapping of the drifting charge require fully depleted microstrip detectors for operation at LHC. The simulation was meant to give an answer to the question of the amount of overdepletion needed for successful operation. At $U > V_{FD}$ the influence of diffusion on induced charge becomes small (see Fig. 7.10). Since the diffusion simulation takes up to 100 times more CPU time, it was not considered in further Monte Carlo simulations.

read-out chip	shaping circuit	preamplifier	τ_p
Felix	CR-RC	$C_c = 1$ pF, $R_c = 1$ MΩ	$\tau_s = \tau_p = 75$ ns
APV	CR-RC	$C_c = 1$ pF, $R_c = 1$ MΩ	$\tau_s = \tau_p = 50$ ns
SCT, ABCD	CR-RC^2	$C_c = 1$ pF, $R_c = 0.3$ MΩ	$\tau_s = 1/2\,\tau_p = 12.5$ ns

Table 7.3 : Electronic schemes used in simulation.

Three different electronics schemes were considered. They are listed in Table 7.3. The CR-RC^2 shaping circuit with $\tau_p = 25$ ns is used in SCT read-out chip, while the APV chip uses CR-RC with $\tau_p = 50$ ns. Felix read-out chip has a CR-RC shaper and $\tau_p = 75$ ns.

7.3.1 Analysis procedure

The strip to which the generated charge drifts is determined by the electric field profile. Charge drift to any strip induces current also on the neighboring strips (Fig. 7.4). Provided that the charge drift is completed and time constant of the charge flow from the strip ($R_b \cdot C_d$) is much shorter than drift time the induced current integral vanishes hence no charge is induced on neighboring strips. If a part of the drifting charge is trapped the induced charge on neighboring strips stays finite. At simulated fluences the estimation of the induced current on neighboring strips gave signals that were way below the noise of the front-end electronics and hence ignored (see Section 7.5).

Drift of the charge to an interpolation strip results in an induced charge on neighboring read-out strips according to Eq. 2.38. Only two nearest read-out neighbors on each side of the interpolation strip were considered in the simulation (Table 7.1). The induced charge on other read-out strips was below the noise level of the electronics and therefore ignored.

It was not the purpose of this study to investigate details of noise influence on the measured signal. Equal noise was assumed for all three different types of simulated readout electronics. The noise used as the input for simulation was taken from the measurements shown in Fig. 6.8. Its value was 900 e_0 for non-irradiated and 1000 e_0 for irradiated detectors.

The strip signal height in units of elementary charge e_0 was obtained by simulating an injection of an instant charge pulse $I(t) = A \cdot \delta(0)$ corresponding to the most probable energy loss of electrons from a ^{90}Sr source. The resulting normalization signal height

corresponded to creation of 23300 electron-hole pairs in the detector volume. The most probable energy loss was determined by simulation. After the signal height was converted to units of elementary charge a Gaussian distributed noise was added to each strip signal.

Cluster signals were then calculated for every track as the sum of signals on strips satisfying the same criteria as in the analysis of detector measurements: at least one (central) strip should have signal to noise ratio $S/N > 4$ (S is signal and N noise of a strip) all neighboring strips with $S/N > 2$ are included in a cluster and the sum of S/N over a cluster should be at least 5. Due to cuts, the cluster signals may depend on noise, particularly for low S/N.

The most probable cluster signal was obtained by fitting a convolution of Landau and Gaussian functions to the histogramed cluster signals (Fig. 7.12).

The charge collection efficiency (CCE) was defined as the ratio of the most probable cluster height obtained when simulating detector response to beta source signals and the height of normalization signal.

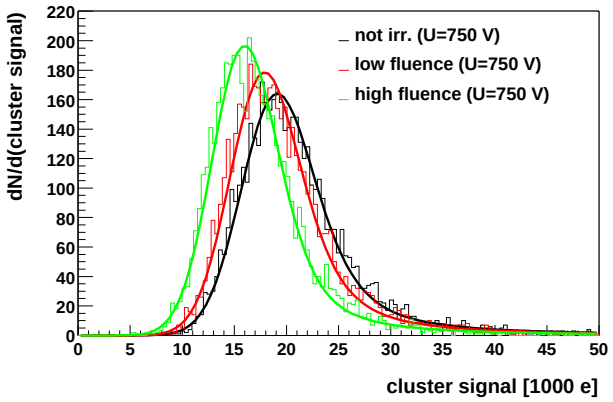

Figure 7.12 : An example of most probable signal determination for the detector with 25 μm pitch and every second strip read-out. The irradiated detectors were simulated at $T = 262$ K and the non-irradiated at $T = 300$ K.

7.3.2 Charge collection efficiency dependence on voltage

Simulated CCE as a function of bias voltage applied to the detector with 25 μm strip pitch is shown in Fig. 7.13. Since the trapping times before irradiation are long compared to the shaping times, the CCE voltage dependence (Fig. 7.13a) can be explained by the increase of drift velocity at higher bias voltages, and the consequent reduction of ballistic deficit. The latter is far more significant for short shaping times. About 100 V above V_{FD} is needed to reach the saturated value of CCE with a 25 ns shaping time, while nearly no over-depletion is needed for longer shaping times ($\tau_p \geq 50$ ns). Trapping of the charge becomes the dominant process reducing CCE above V_{FD} after irradiation. Since the detrapping time is long compared to all electronic integration times used, charge, once trapped, does not contribute to the signal. Therefore after irradiation the difference

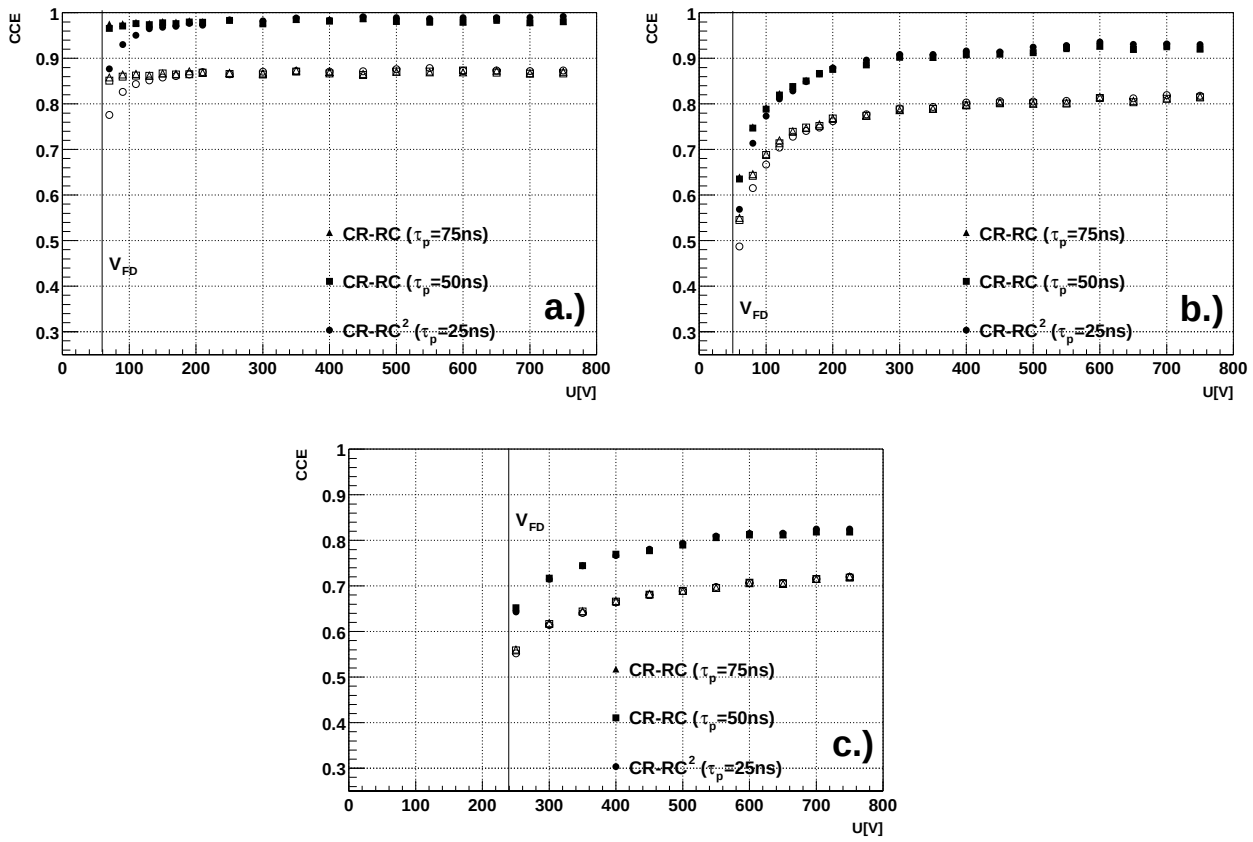

Figure 7.13 : Calculated CCE as a function of bias voltage at T=262 K for: a) non-irradiated detector, b) detector irradiated to $\Phi_{\rm eq} = 5{\cdot}10^{13}$ cm^{-2} and c) detector irradiated to $\Phi_{\rm eq} = 15{\cdot}10^{13}$ cm^{-2}. Open markers denote CCE if every second strip is being read out. Strip pitch is 25μm. Note the suppressed zero on the CCE scale.

between different electronic schemes can hardly be observed in Fig. 7.13b and definitely vanishes in Fig. 7.13c. The effect of trapping can be clearly seen slightly above V_{FD} where a substantial part of the charge is trapped due to the slow drift. At higher voltages the signal increases further due to the faster drift and reduced trapping. There is no clear saturation of CCE even at voltages a few hundred volts above V_{FD} explained by the fact that velocity saturation has not yet been reached along the whole drift path. Since the trapping probability is proportional to the fluence, this effect is more pronounced at the higher fluences.

If every second strip is read out, the most probable signal is reduced (open markers in Fig. 7.13) as expected from values of $N_{k,i}$ in Table 7.1.

7.3.3 CCE of different detectors

Results for the CCE with different strip pitches and fixed (25 ns CR-RC^2) shaping time are shown in Fig. 7.14. A few percent lower CCE of large pitch detectors with interpolation

strips is expected due to the smaller coupling to neighboring strips (see Table 7.1) [58]. This is true for the non-irradiated detector, where CCE of the 25 micron pitch detector is always at the same level or higher than of the 56 micron pitch detector.

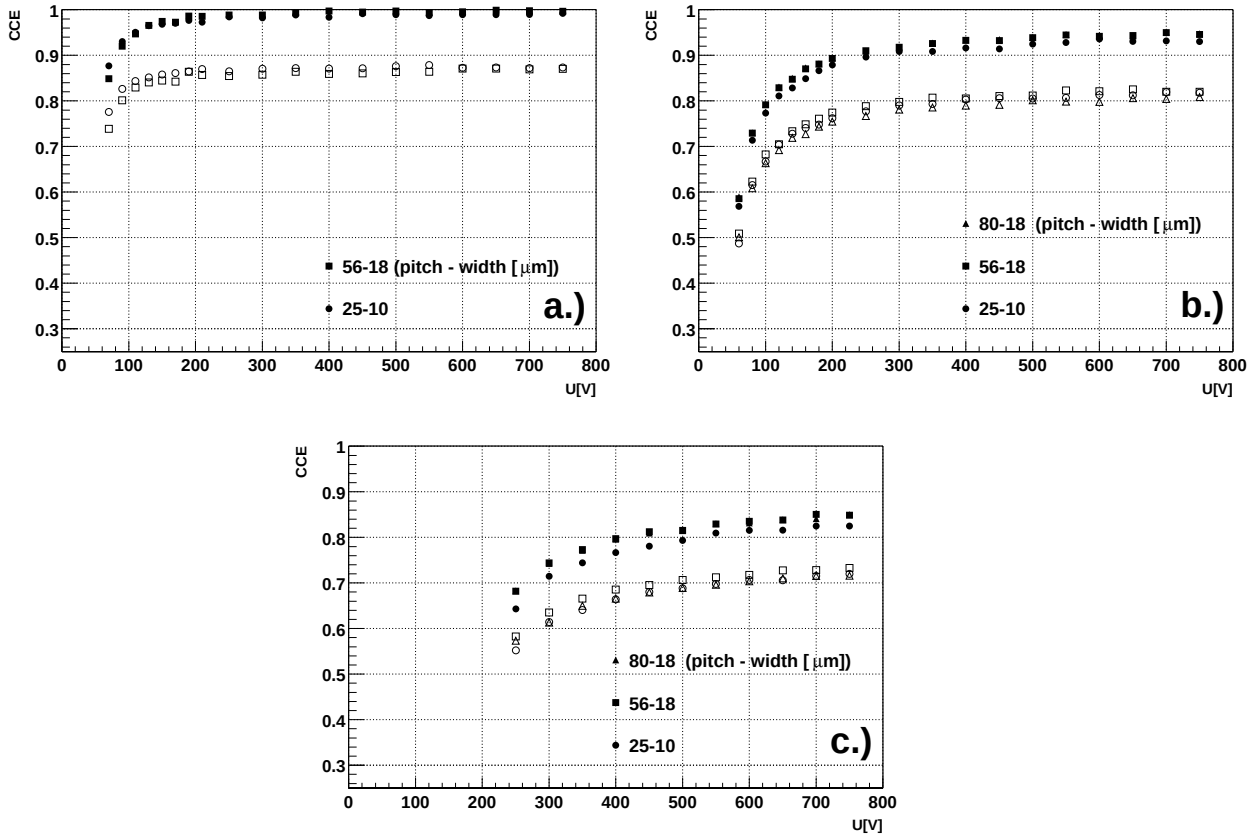

Figure 7.14 : Calculated CCE of detectors with different pitches as a function of applied voltage. Fast 25 ns (CR-RC^2) shaping was used at $T = 262$ K. a.) non-irradiated, b.) irradiated to low fluence, c.) irradiated to high fluence. Open markers denote detectors with every second strip read-out.

Charge trapping and higher noise in irradiated detector, make large pitch detectors more appropriate in terms of CCE in spite of somewhat longer drift time from some detector regions. Charge spread over many strips results in induced charge comparable with noise in each of them. If the strip S/N is smaller than required by cuts the strip is not included in the cluster and a part of the charge is lost for the measurement. In addition, contribution of holes to the total induced charge is larger for small pitch detector (see Section 7.4.1) and consequently charge trapping has larger influence. As can be seen in Fig. 7.14b and Fig. 7.14c a difference, although small, in CCE between large pitch and small pitch detectors can be seen.

The most appropriate pitch depends on particles' incident angle and consequent charge

[58] The noise of small pitch detector would be higher, due to larger interstrip capacitance.

spread. In this particular case a difference of around 4% is predicted between large and small pitch detectors at high fluence (Fig. 7.14c).

7.3.4 Temperature dependence of CCE

The temperature dependence of CCE was also studied by simulation. The temperature dependence of trapping times (Eq. 5.5) and the change of the mobility (see Appendix C) were taken into account, while weak temperature dependence of N_{eff} was ignored. Lower temperature increases the drift velocity but also the trapping probability. A difference is predicted at the lowest voltage in Fig. 7.15a,b, where the drift time reduction at lower temperature prevails over increased trapping probability, even at the highest fluence studied. At higher voltages there is almost no difference in CCE at different temperatures.

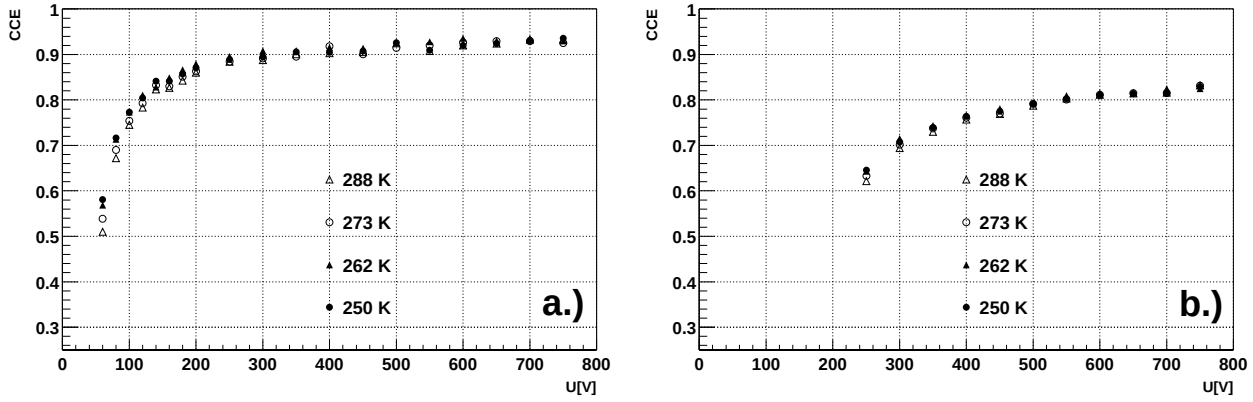

Figure 7.15 : Temperature dependence of the CCE with 25ns CR-RC^2 shaping at a.) low fluence; b.) high fluence; for detector with 25 μm read-out pitch.

The prediction of simulation agrees with measurements shown in Fig. 6.9, where also no difference in collected charge at different temperatures was observed.

7.3.5 Influence of timing

CCE for various delays in the range between 25 ns and 40 ns and different bias voltages on the detector is shown in Fig. 7.16. A detector with 50 μm read-out pitch having one interpolating strip has been used in this simulation. For a comparison measured values at a fixed delay ($\approx$28 ns) determined for an non-irradiated detector (Fig. 6.6) are also plotted. Voltage dependence of measured CCE is in good agreement with simulated values, which also confirms the measured effective trapping times. The slightly larger discrepancy for the non-irradiated detector could be caused by a too short delay.

Simulated values obtained with optimal timing (sampling in the peak of signal with different delay for each event) are also plotted. A fixed delay of 25 ns gives values close to the optimal if the voltage applied on the detector is sufficiently higher than V_{FD}.

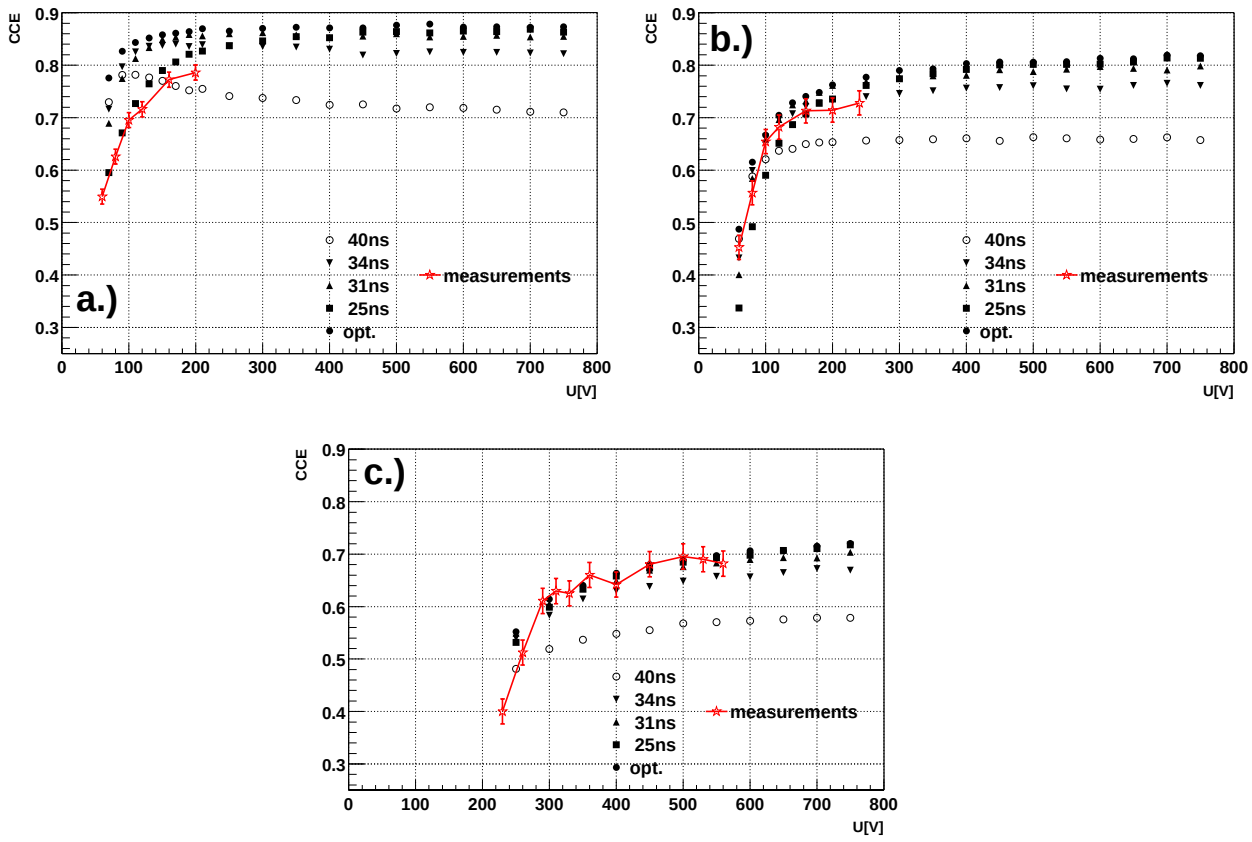

Figure 7.16 : Simulated CCE with different delays of signal sampling with respect to the passage of the particle for a.) non-irradiated detector, b.) irradiated to low fluence, c.) irradiated to high fluence. The measurement with a fixed 28 ns delay is shown for comparison. The measurement and simulation were performed with 25 ns CR-RC^2 shaping.

The best sampling time and the corresponding CCE as a function of applied voltage are shown in Fig. 7.17. As expected the best sampling time approaches the nominal peaking time as the voltage increases. On the other hand CCE increases with voltages well beyond the depletion voltage. The slope of this rise is around 2.3 e_0/V for the detector irradiated to a low fluence and 4.3 e_0/V for the detector irradiated to a high fluence. CCE at different voltages and sampling times can be extracted from Fig. 7.18.

7.3.6 Cluster width

The simulated mean cluster width (Fig. 7.19) was compared with the measured ones (Fig. 6.13). A good agreement was found. A slightly smaller simulated mean cluster width than the measured was found for non-irradiated and low-fluence irradiated detector. This can be an effect of diffusion which increases the mean cluster width and was not taken into account in the simulation. The effect of diffusion is less important at higher fluences, hence the agreement of simulated and measured mean cluster widths is better.

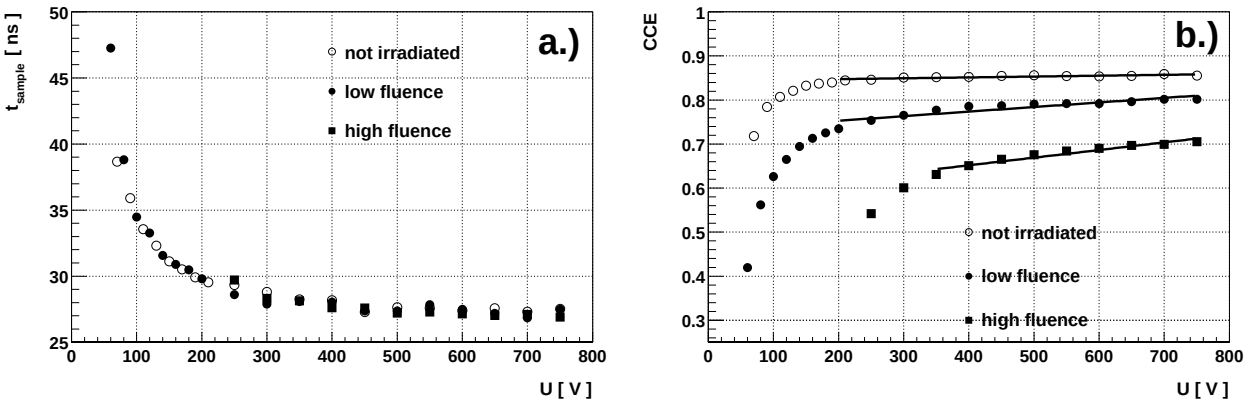

Figure 7.17 : a.) The best sampling time for detector of 50 μm read-out pitch and one interpolation strip with a 25 ns CR-RC^2 shaping circuit. b.) CCE at best sampling time. Particle hits detector at t=0.

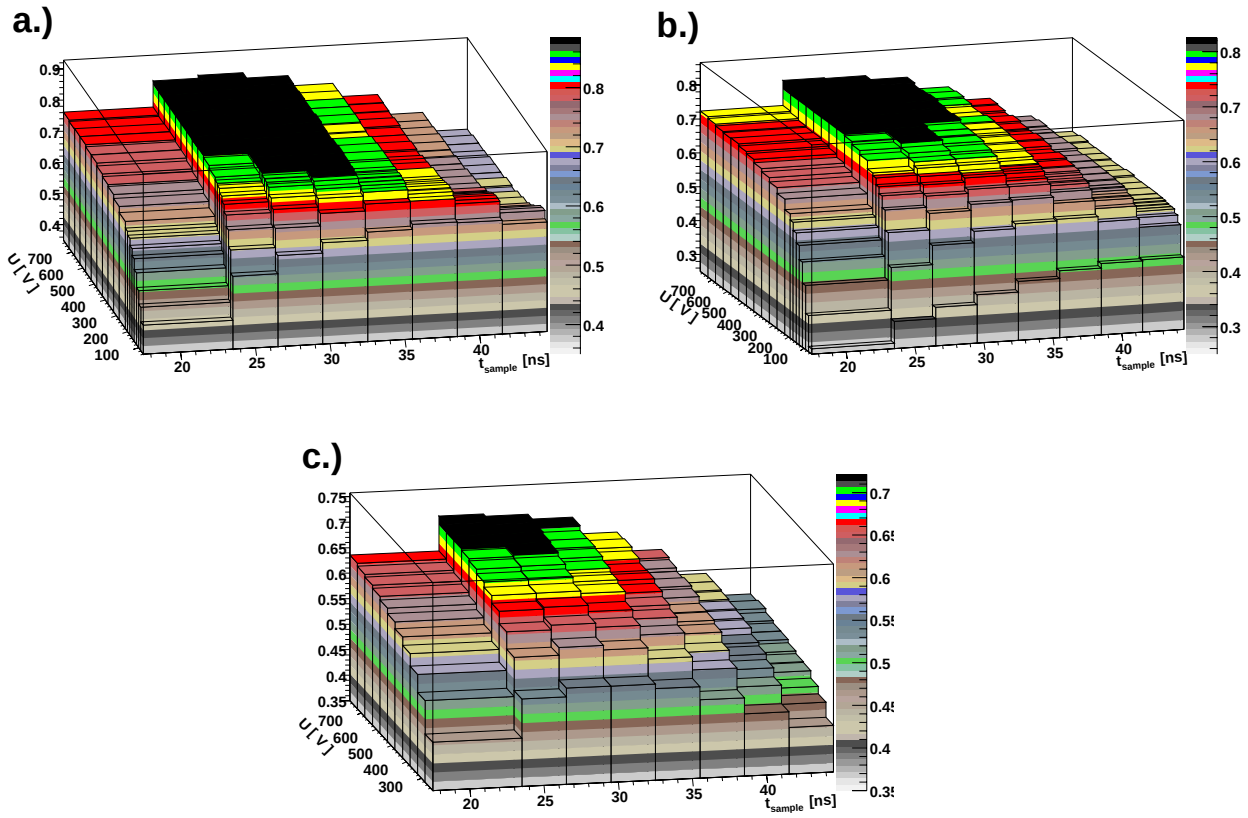

Figure 7.18 : Simulated CCE dependence on voltage and sampling time for: a.) non irradiated detector, b.) detector irradiated to low fluence and c.) detector irradiated to high fluence. A 25 micron pitch detector with an interpolation strip connected to 25 ns CR-RC^2 shaping is considered.

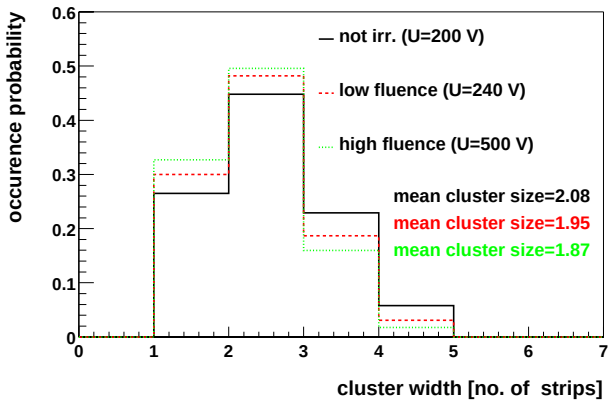

Figure 7.19 : Simulated mean cluster width.

7.4 Detector design

Effective trapping times significantly influence the design of the detector. The spatial resolution of the detector is determined by the read-out pitch and the signal-to-noise ratio. Operation of silicon detectors irradiated to high fluences requires all the signal available in order to achieve a good signal-to-noise ratio and therefore the detectors using interpolation strips are less appropriate.

At a given read-out pitch, which in coarse terms determines the position resolution, some design parameters can be tuned to give the best performance in terms of signal and also operation voltage. These parameters are: strip type (p^+,n^+), strip pitch/width ratio and detector thickness.

The simulation of different detector designs was done under the following considerations:

- A strip detector of 80 μm strip pitch was investigated, which gives at least 23μm position resolution required by ATLAS-SCT.
- The temperature of operation was set to $T = 263$ K which is close to the operation temperature of both LHC detectors ATLAS and CMS.
- Only the tracks traversing the detector perpendicularly to the surface were considered. The generated charge of 75 electron-hole pairs/μm corresponded to the most probable energy loss of a minimum ionizing particle.
- Diffusion was included in the simulation.
- Induced charge was calculated as integral of the induced current in time window of 60 ns.
- Hadron fluences in the range of $\Phi_{\mathrm{eq}} = 5 - 50 \cdot 10^{13}$ cm^{-2} with $N_{eff} = -g_c\,\Phi_{\mathrm{eq}}$ and $g_c = 0.02$ cm^{-1}.

7.4.1 Choice of the strip type: $p^+ - n - n^+$ vs. $n^+ - n - p^+$ detector

As shown in Fig. 7.4 the scalar product of weighting and electric fields is highest at the strip for both, non-irradiated and irradiated detectors. If the strips are of p^+-type silicon the larger part of the induced charge for a minimum ionizing particle comes from holes which drift to the strip and a smaller part from electrons drifting to the backplane (see Table 7.4).

thickness	strip pitch	strip width	$Q_h/(Q_e+Q_h)$
280 μm	80 μm	8 μm	0.83
280 μm	80 μm	18 μm	0.81
280 μm	80 μm	40 μm	0.78
220 μm	80 μm	18 μm	0.78
340 μm	80 μm	18 μm	0.83
280 μm	56 μm	18 μm	0.83
280 μm	25 μm	10 μm	0.88

Table 7.4 : Contribution of holes to the total induced charge in a $p^+ - n - n^+$ detector for a minimum ionizing particle track through the centre of the strip. In absence of charge trapping $Q_h/(Q_e+Q_h)$ depends on weighting potential only. The charge trapping reduces $Q_h/(Q_e+Q_h)$ ratio as a larger amount of holes is trapped compared to electrons. The role of holes and electrons is reversed in a $n^+ - n - p^+$ detector of the same geometry.

The picture is inverted if the strips are of n^+-type silicon, where electrons drift to the strips and holes to the back plane. After the irradiation beyond the type inversion point the junction grows from the strip side. The electric field established in such a detector has a similar profile as the electric field in a non-irradiated $p^+ - n - n^+$ detector. As a result the product of weighting and electric field is relatively large also for $U < V_{FD}$. One of advantages of such detectors is therefore the ability of operating them partially depleted.

A 280 μm thick detector with 18 μm strip width was simulated [59]. In the simulation of the $n^+ - n - p^+$ detector p-stop or p-spray technique (see Section 2.1.2) for n^+ strip isolation was not taken into account. Effectively n^+ strip detectors were considered as to be p^+ strip detectors with changed polarity of the applied voltage with respect to the strips.

In Fig. 7.20 the results of the simulation for minimum ionizing particle tracks crossing the strip centre perpendicular to the detector are shown. It is evident that less overdepletion is needed for a $n^+ - n - p^+$ compared to the $p^+ - n - n^+$ detector. The higher mobility of electrons compared to holes results in a shorter drift time thus less charge is trapped. In addition, the effective trapping times of electrons are longer than those of holes. As a result, higher CCE can be reached in an irradiated $n^+ - n - p^+$ detector

[59] Design specification of an ATLAS silicon microstrip detector.

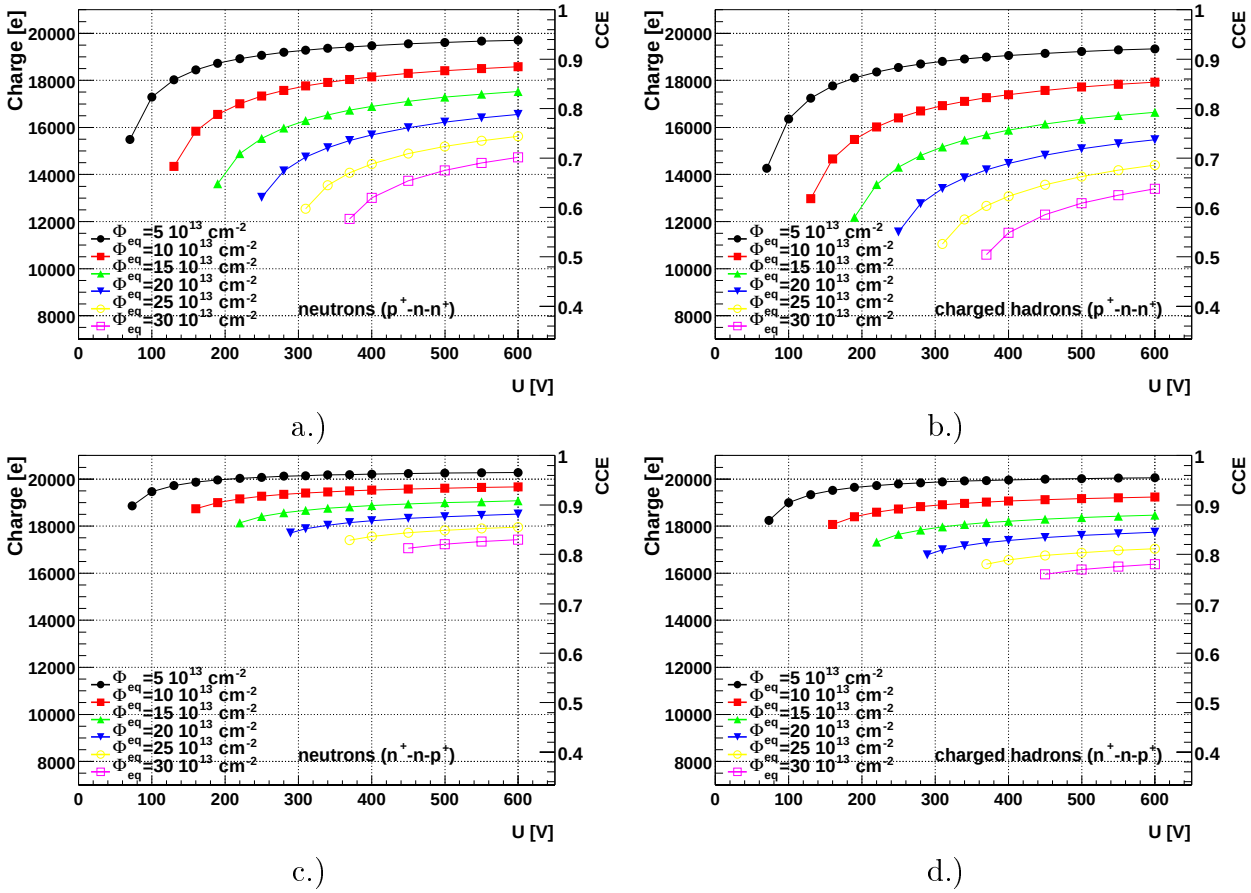

Figure 7.20 : Calculated charge and CCE at different fluences for: a.) p^+-n-n^+ detector irradiated with neutrons, b.) p^+-n-n^+ detector irradiated with charged hadrons (pions,protons), c.) n^+-n-p^+ detector irradiated with neutrons and d.) n^+-n-p^+ detector irradiated with charged hadrons. The minimum ionizing particle track is perpendicular to the strip and hits the detector at the strip center. Note suppressed zero on y-axis.

compared to a p^+-n-n^+ detector. A significant difference remains even at 600 V [60]. This is in agreement with measurements found in [Nak00]. Here the CCE is defined as the ratio of the induced charge and the charge deposited by a minimum ionizing particle in the detector bulk ($e_0\, N_{e-h}$).

The voltage required to establish electric field in the entire detector was found up to 50 V higher for an irradiated n^+-n-p^+ detector compared to p^+-n-n^+ detector at equal negative N_{eff}. The reason is much stronger potential drop in the interstrip region

[60] The difference can disappear in the signal-to-noise ratio. Detectors with n^+ strips can have larger interstrip capacitance, since the positive charge accumulated in the oxide between two strips effectively increases the width of the n^+ strip and by that the interstrip capacitance. Careful design with p-stop or p-spray structures covering as much of the interstrip region as possible is required. Capacitances of around 2 pF/cm were reported by [MaJ95], but it is decreasing with the bias voltage. Double sided detectors used by the CDF collaboration, on the other hand, have similar interstrip capacitances on both sides [Har99].

leading to higher electric field near the strip edge and fringing fields [And96, Har99].

In the case of tracks passing the detector perpendicularly to the strips, but away from the strip center (up to ± pitch/2), the charge collection efficiency is worse. The simulation of both detector types irradiated to $\Phi_{eq} = 20 \cdot 10^{13}$ cm^{-2} with neutrons and charged hadrons is shown in Fig. 7.21. Longer drift of the charge and its start in the

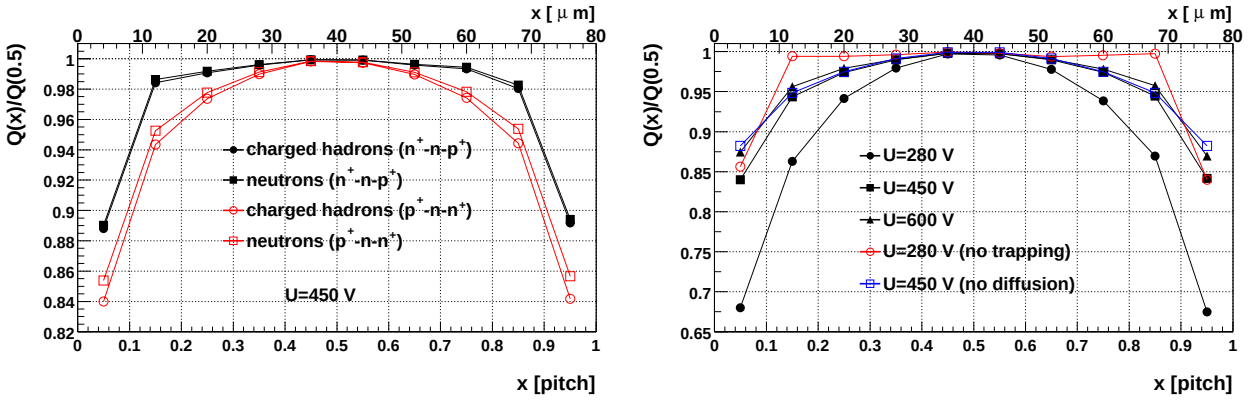

Figure 7.21 : The induced charge for tracks away from the strip centre ($x = 40$ μm) : a.) for different detector types and irradiation particles at $U = 450$ V and b.) for the $p^+ - n - n^+$ detector irradiated with charged hadrons at different voltages. The influence of charge trapping and diffusion is also shown. Q denotes the induced charge. Note suppressed zero and different scale on y-axis for both graphs.

low weighting field region results in a larger amount of charge trapped and consequently reduced CCE. In addition, charge diffusing to the neighboring strip also reduces the CCE[61]. Again the $n^+ - n - p^+$ detector is predicted to perform better (Fig. 7.21a). Around 30% less charge is induced for the track close to the strip border compared to the track hitting the strip centre for the $p^+ - n - n^+$ detector at 280 V (Fig. 7.21b). At higher voltages the difference between tracks becomes smaller, however around 10% difference still remains at 600 V. It can be also concluded that the CCE reduction is dominated by charge trapping as there is very little difference between simulated CCE with and without diffusion at 450 V [62].

No difference in CCE between irradiated $p^+ - n - n^+$ and $n^+ - n - p^+$ pad detectors or pixel detectors, if pixel dimensions are much larger than detector thickness, is predicted. The constant weighting field results in equal contribution to the induced current from electrons and holes. The CCE of the silicon pad detector at a given fluence and voltage is between CCE of the $n^+ - n - p^+$ and $p^+ - n - n^+$ strip detector (Fig 7.22). The simulated CCE of pad detectors is in agreement with measurements reported in [Ler97, Bor98].

[61] One also has to keep in mind that charge diffusion to the neighboring strip can give rise to a detectable signal (see section 7.3.3)

[62] Maximal voltage that will be applied to detectors at ATLAS experiment.

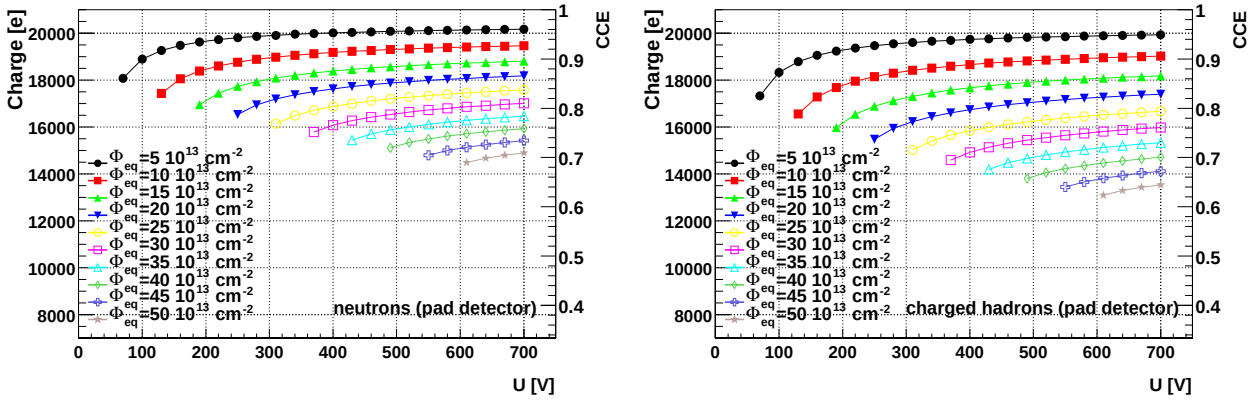

a.) b.)

Figure 7.22 : Simulated CCE in 280 μm thick silicon pad detector at different fluences of: a.) neutrons and b.) charged hadrons. Note suppressed zero on y-axis.

7.4.2 Strip width optimization

The strip width influences both electric and weighting field. The dependence of CCE on the strip width for a $p^+ - n - n^+$ detector irradiated with charged hadrons can be seen in Fig. 7.23. For the central track an additional 400 electrons can be obtained if the strip width is 78 μm instead of 18 μm (Fig. 7.23a). The interstrip capacitance is larger for wider strips and by that also the noise. As a consequence signal to noise ratio for detectors with wide strips can be smaller.

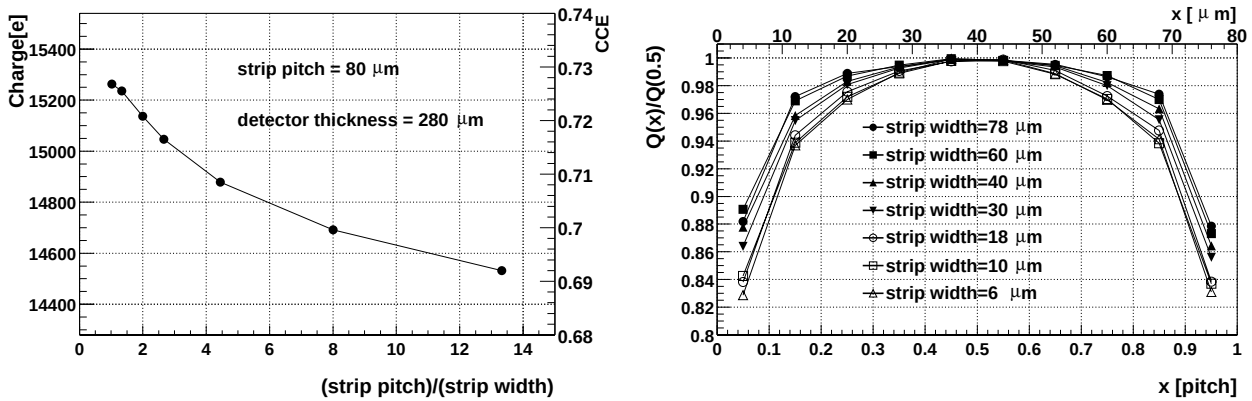

a.) b.)

Figure 7.23 : CCE of $p^+ - n - n^+$ strip detector of different strip pitch/width ratios for: a.) central track and b.) tracks away from the strip centre. The simulated charged hadron fluence was $\Phi_{eq} = 20 \cdot 10^{13}$ cm^{-2}. A bias of 450 V was applied. Note suppressed zero on y-axis.

Only a minor improvement in CCE is predicted with increasing strip width also for tracks away from the strip center (Fig. 7.23b). The electric field in detectors with very wide strips becomes similar to that of the pad detectors. Although one would therefore

expect little difference in CCE between different tracks, it is observed. It is mainly a consequence of charge diffusion to the neighboring strips.

A small difference between detectors with wide and narrow strips could be explained by cancellation of two effects. Less charge trapped due to shorter drift paths for tracks tracks close the strip border in detectors with wide strips is canceled by more charge diffusing to neighboring strips.

7.4.3 Detector thickness optimization

Although the $n^+ - n - p^+$ strip detectors perform better in terms of CCE after irradiation, $p^+ - n - n^+$ strip detectors were chosen by both experiments, ATLAS and CMS, due to the lower cost. As shown in Fig. 7.10 the bulk of induced charge comes from the drift of holes. This poses a question of the ideal thickness of the strip detector.

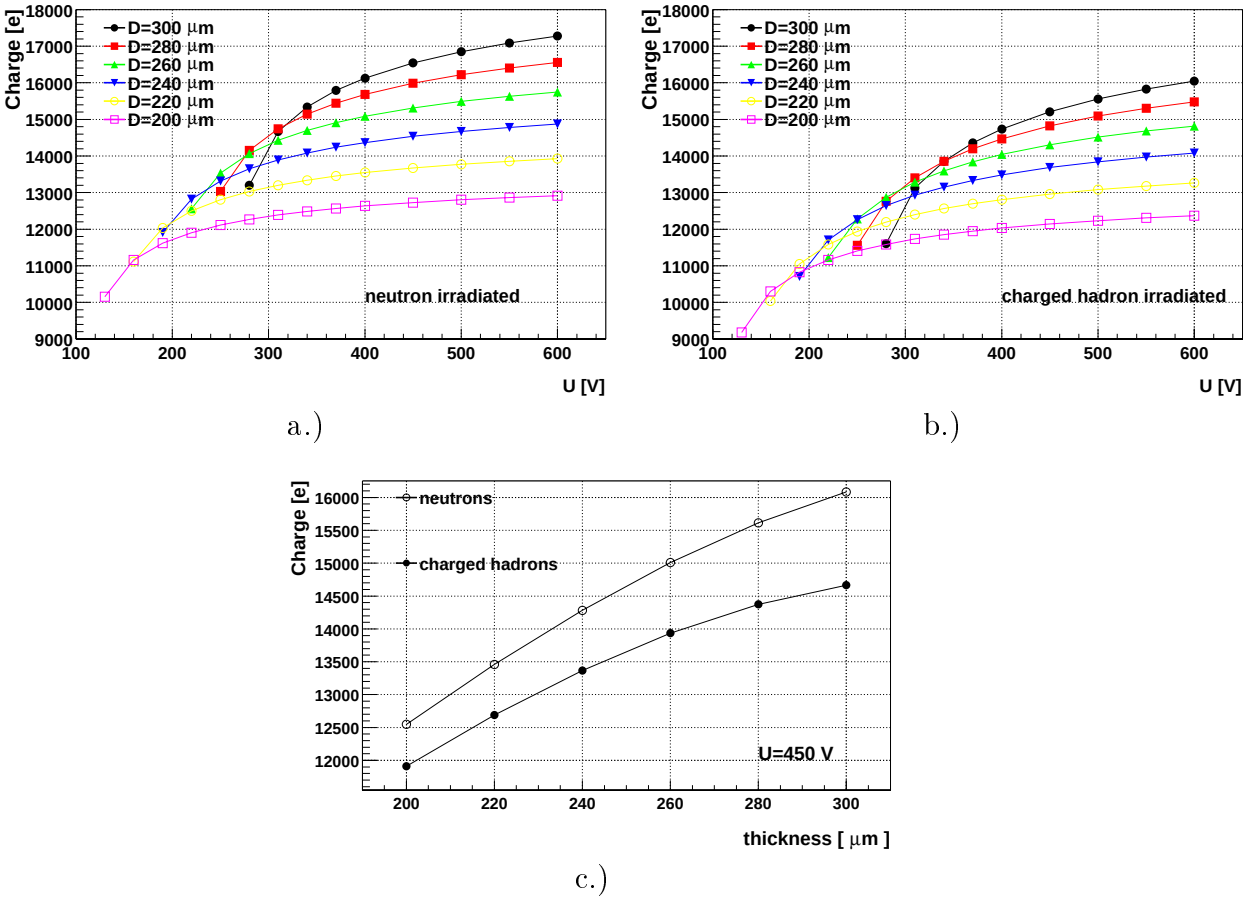

Figure 7.24 : Induced charge for the central track as a function of voltage at different detector thicknesses: a.) detector irradiated with neutrons and b.) detector irradiated with charged hadrons both to equivalent fluence of $\Phi_{eq} = 20 \cdot 10^{13}$ cm^{-2}. c.) Induced charge at $U = 450$ V averaged over the tracks between both strip borders. Note suppressed zero on y-axis.

For a non-irradiated detector connected to electronics with sufficiently long shaping

time ($\sim$ 1 μs) the induced charge is proportional to the detector thickness D. Increase of N_{eff} with fluence in an irradiated detector inevitably leads to a limitation of detector thickness since $V_{FD} \propto N_{eff} D^2$. In addition overdepletion is needed to reduce the drift time and by that the amount of trapped charge.

If holes are trapped before they reach the high weighting field region their contribution to the induced current is small. This effect is more pronounced in thicker detectors where the drift time is longer. As a result of that, at a given voltage limit [63], it may be better to operate a thinner detector. The smaller amount of charge generated by charged particle in a thinner detector can be compensated by less charge trapped and by that a larger portion of charge reaching the high weighting field region.

In Fig. 7.24 results of the simulation for silicon detectors with 18 μm strip width and different thicknesses are shown for the central track. The simulated fluence was $\Phi_{\rm eq} = 20 \cdot 10^{13}$ cm^{-2}. Provided that more than 350 V can be applied to the detector the 300 μm thick detector provides the best solution. However if the voltage is limited to 300 V already a 260 μm thick detector represents a better choice. Even at 600 V the difference in induced charge between 200 and 300 μm thick detectors is only 25 % instead of the expected 33 % from the thickness difference.

The induced charge at $U = 450$ V averaged over the tracks between both strip borders increases with the detector thickness as well (Fig. 7.24c). A few percent less induced charge is predicted for the track average as compared to the charge induced by the central track.

7.5 Trapping as a charge sharing mechanism

In absence of charge trapping, the drift of the charge to strip k induces no charge on neighboring strips $k \pm 1$ if the current integration time is longer than the drift time. The induced current on strip $k \pm 1$ has a bipolar shape (Fig. 7.25). Charge trapping reduces the induced current more at late stages of the drift. As a result the induced charge does not cancel out. The induced charge on the neighboring strips depends on: the effective trapping probability, applied voltage, detector geometry and particle track position. To determine the significance of the effect the parameter $\xi_n(x) = Q_{k\pm n}(x)/Q_k$ is introduced. The induced charge Q_k is determined for the central track on strip k, while $Q_{k\pm n}(x)$ is the charge induced on strip k by the drift of the charge to the strip $k \pm n$. x is the distance of the track from the strip border, with $x = 0.5$ being the strip center.

The dependence of $\xi_1(0.5)$ on voltage for 280 μm thick detectors (strip pitch of 80 μm, strip width of 18 μm) irradiated to different fluences in shown in Fig. 7.26. The effect is more pronounced for $p^+ - n - n^+$ detectors, due to the longer hole collection time, where up to 15% of Q_k is induced on the neighboring strip for a detector irradiated with charged hadrons to $\Phi_{\rm eq} = 3 \cdot 10^{14}$ cm^{-2}. This can result in enhanced mean cluster width and also larger measured cluster signal. Operation of detector irradiated to $\Phi_{\rm eq} = 3 \cdot 10^{14}$ cm^{-2} at 450 V results in around 1200 e on both closest neighboring strips, which is comparable to typical strip noise.

[63] Posed, for example, by the maximal allowed power consumption.

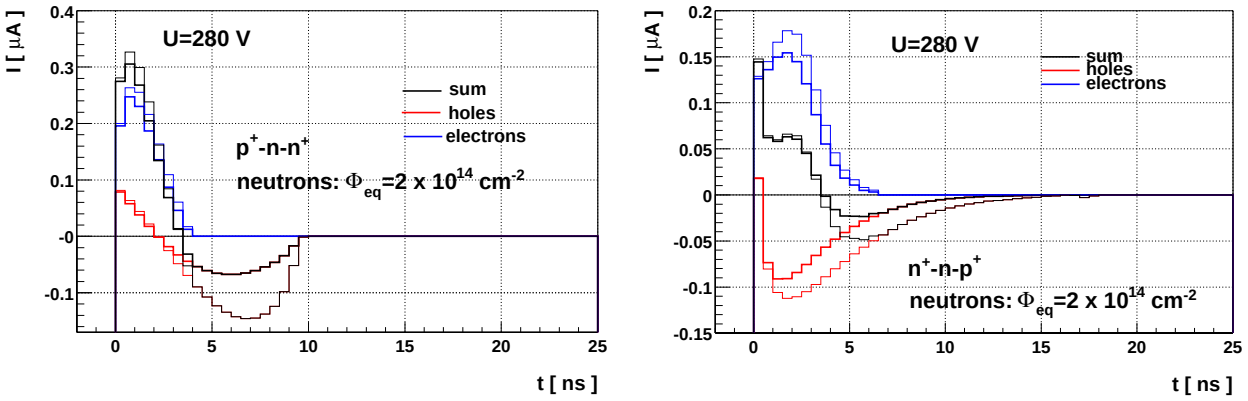

Figure 7.25 : An example of current shape induced on strip k, due to drift of the charge to the strip $k \pm 1$. The case of a track perpendicular to the detector surface passing through the neighboring strip centre is shown. A 280 μm silicon detector with a strip pitch of 80 and width of 18 μm is considered. The simulated neutron fluence was $\Phi_{\rm eq} = 2 \cdot 10^{14}$ cm^{-2}. The simulated current responses for: a.) $p^+ - n - n^+$ detector and b.) $n^+ - n - p^+$ detector biased to 280 V, are presented. The temperature is 263 K. The thin line denotes the hypothetical case of no charge trapping where the integral of the induced current cancels out. The realistic case is denoted with the thick line.

Up to an order of magnitude smaller $\xi_1(0.5)$ is predicted for $n^+ - n - n^+$ detectors (Fig. 7.26c,d). In addition the polarity of the induced charge on strips $k \pm n$ is reversed with respect to the polarity of Q_k.

The induced charge $Q_{k\pm n}$ depends strongly on the track position. The larger the distance of the track from strip k the less charge is induced on strip k. The strip width influence on ξ was also checked and was found to be of minor importance. An example of the $\xi_n(x)$ for different strip widths (strip pitch=80 μm) is shown in Fig. 7.27 for different detectors irradiated with charged hadrons to $\Phi_{\rm eq} = 2 \cdot 10^{14}$ cm^{-2} and operated at 450 V. If the strip width is much smaller than the pitch, the induced charge is not minimal for the most distant track. The longer drift and the related trapped charge prevail over the smaller weighting field. The induced charge on second closest neighbors was found to be smaller, as can be seen in Fig. 7.27b.

The trapping-induced " charge sharing" can play an important role in heavily irradiated silicon detectors, where the diffusion is less important. It seems to be the dominant mechanism in diamond detectors where trapping times even for non-irradiated detectors are very short (< 2 ns). Therefore the diffusion spread of the drifting charge is negligible. An enhanced content of two-strip hits was observed at measurements of diamond detectors in the test beam [Bor94], without a clear explanation for it.

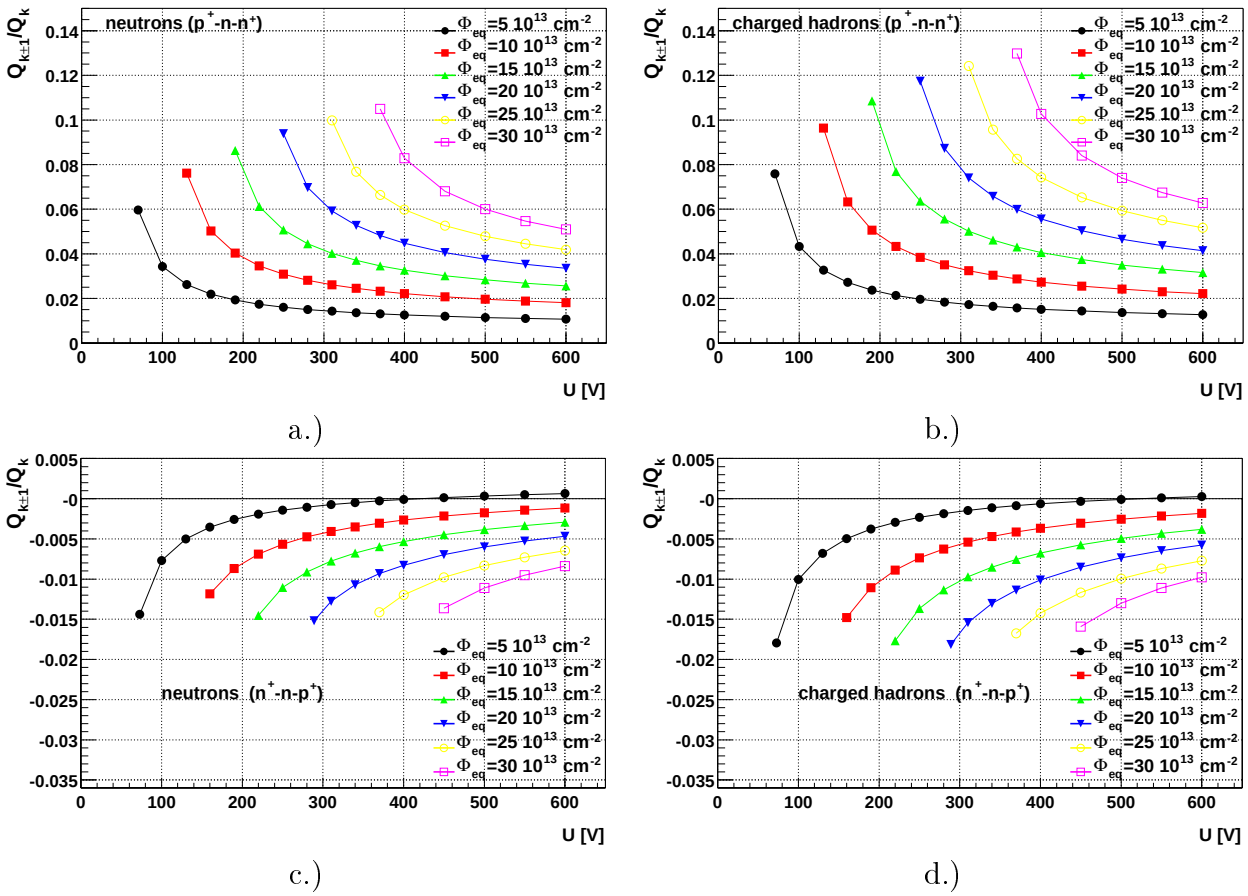

Figure 7.26 : $\xi_1(0.5) = Q_{k\pm1}/Q_k$ as a function of voltage for: a.) $p^+ - n - n^+$ detectors irradiated to different fluences with neutrons, b.) $p^+ - n - n^+$ detectors irradiated to different fluences with charge hadrons. c.) and d.) are same as a.) and b.) for the $n^+ - n - n^+$ detectors. The operation temperature was $T = 263$ K. Note different scales of a,b and c,d.

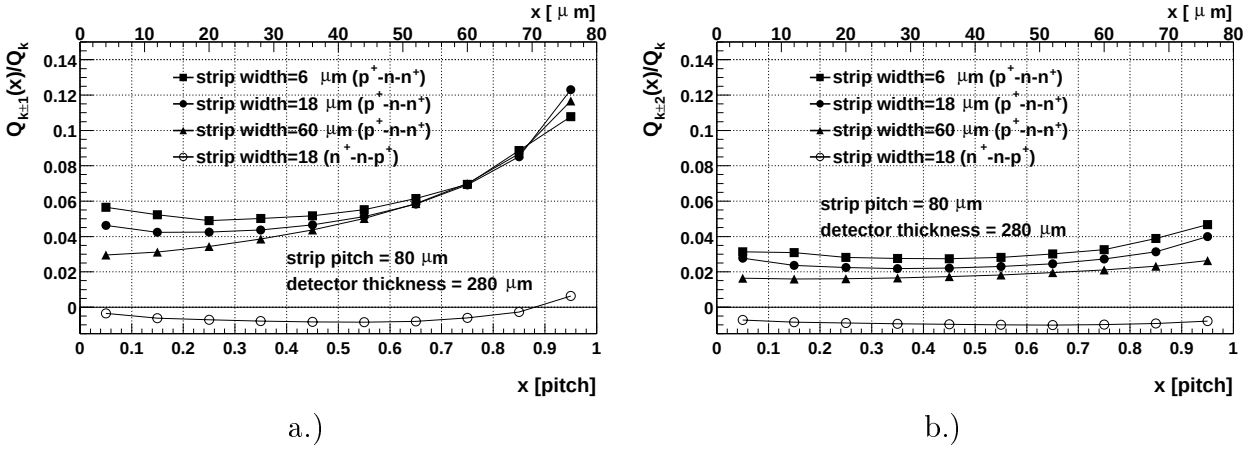

Figure 7.27 : a.) $\xi_1(x)$ and b.) $\xi_2(x)$ for different strip widths for detectors irradiated with charged hadrons to $\Phi_{\rm eq} = 2 \cdot 10^{14}$ cm^{-2}. The simulated detectors were biased to $U = 450$ V and operated at $T = 263$ K.

7.6 Comparison with results using previously measured trapping times

Previous measurements of effective trapping times are scarce. Using an extrapolation of effective trapping times found in [Kra93] the values of $\beta_e = 6.5 \cdot 10^{-16}$ cm^2/ns and $\beta_h = 2.8 \cdot 10^{-16}$ cm^2/ns are obtained for neutron irradiated silicon at $T = 263$ K.

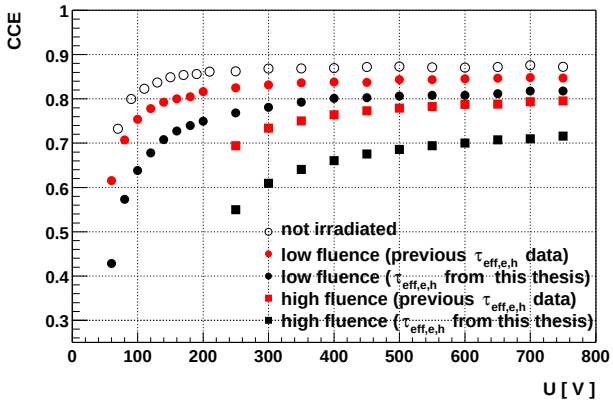

Figure 7.28 : Same as Fig. 7.17b. using different $\beta_{e,h}$.

Since the temperature dependence was not given only a scaling $\sqrt{T/300\ \text{K}}$ of trapping probability due to thermal velocity was assumed. A simulation of the microstrip detectors, used in our measurements (280 μm thick, 25 μm strip pitch with every second strip readout), with different effective trapping times can be seen in Fig. 7.28. CCE depends substantially on the choice of effective trapping times. The main reason is in the around three times lower effective trapping probability of holes found in previous data.

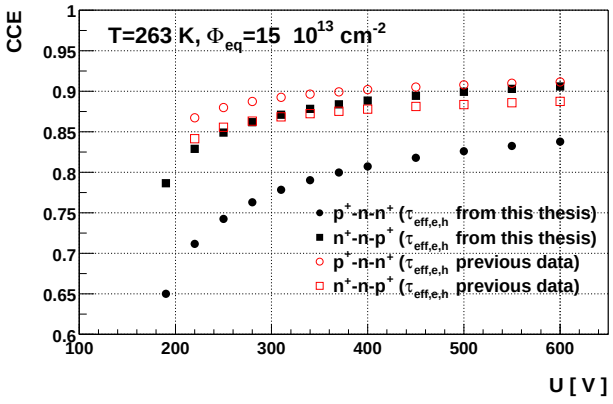

Figure 7.29 : Simulation of CCE for the central track using different detector types and effective trapping probabilities $\beta_{e,h}$. The 280 μm thick detector with strip pitch of 80 μm and strip width of 18 μm was used (same as in Fig. 7.20).

Longer effective trapping times of holes than of electrons reflect also in better simulated performance of $p^+ - n - n^+$ detectors compared to $n^+ - n - p^+$ detectors (see Fig. 7.29), so that the difference is small. A large difference in simulated performance of $p^+ - n - n^+$ detectors can be observed if the effective trapping times found in this thesis are used. The measurement results [Nak00, Gar00] confirm the larger effective trapping probability of holes, by finding a better CCE of $n^+ - n - p^+$ detectors compared to equal $p^+ - n - n^+$ detectors, while the measurements [Gar00, Bro00] confirm also the values of $\beta_{e,h}$.

8

Bistable damage

Recent work has revealed that defect evolution in time depends on bias voltage [Ci00B]. It was concluded that the difference between biased samples during and after irradiation and unbiased samples does not come from different creation rates for the defects, but from different annealing of the defects with and without bias applied to the detector. This may be best illustrated in Fig. 8.1. Two pad detectors were irradiated in pair to the same neutron fluence ($\Phi_{\text{eq}} = 4.5 \cdot 10^{13}$ cm^{-2}) had the same temperature history. The only difference between them was that S3B had been irradiated under bias and kept biased after irradiation while S3B was unbiased all the time. The difference in the minimum of V_{FD} is a factor of two in $|N_{eff}|$. This would present a disaster to the silicon detectors operating at LHC especially pixel detectors, which will be receiving up to an order of magnitude higher fluxes than the microstrip detectors.

Fortunately the difference in effective space charge between biased and unbiased diodes diminishes after the bias is switched off. The annealing of the bias induced difference in effective space charge is modeled with three different defects decaying exponentially with time. Eventually, there is no difference in effective dopant concentration between both diodes. However, applying the bias, a part of the difference reappears. And again, by switching off the bias, the difference disappears. Hence this part of the damage is bistable upon bias application. Moreover, the diode that was never biased before also exhibits the same behavior.

All the measurements of the bistable damage were done using the C/V method for determination of N_{eff}. To check the influence of bias also directly on CCE, TCT measurements were performed. The increase of N_{eff} should alter the electric field what must reflect in the measured signal.

8.1 C/V measurement

To study the bistable damage a pad detector produced on standard silicon material by ITE with initial resistivity around 5 kΩcm ($V_{FD} = 60$ V) was used. It was designed for TCT measurements.

After irradiation with neutrons to $\Phi_{\text{eq}} = 5 \cdot 10^{13}$ cm^{-2} it was kept 10 months at

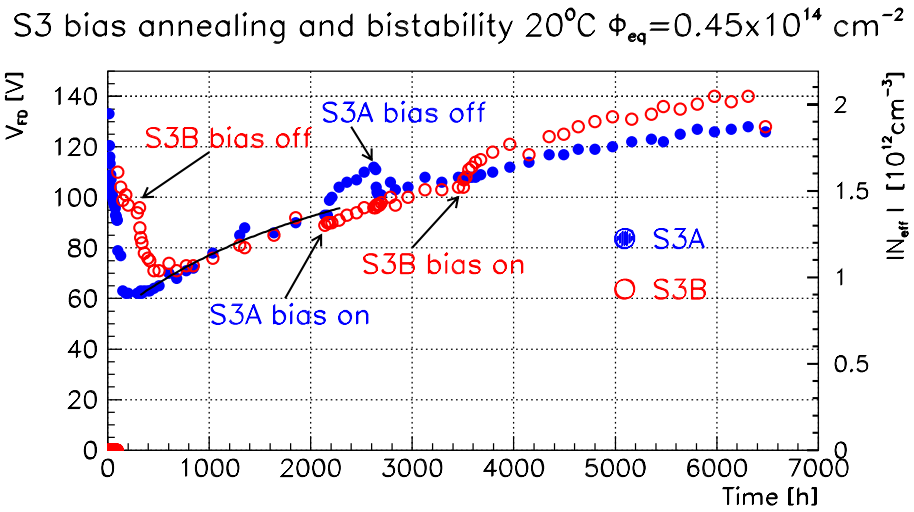

Figure 8.1 : V_{FD} time development of the S3A/S3B pair. After 400 hours of annealing, voltage on the previously biased sample S3B was switched off and 3100 hours later switched back on. After 2200 hours of annealing bias on the previously unbiased sample S3A was switched on. From reference [ZontT].

$T = 20° \pm 1$ C. Around 40% of reverse annealing in N_{eff} took place. During and after irradiation no bias was applied to the diode.

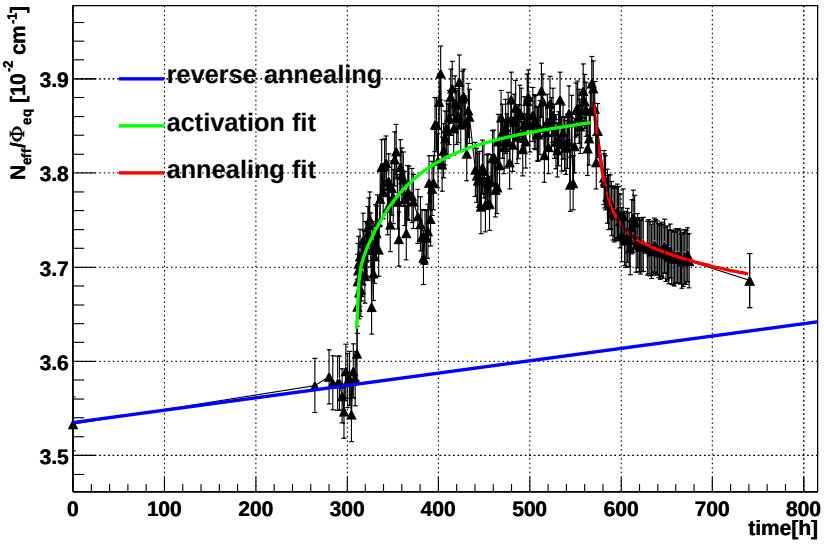

Figure 8.2 : Activation and annealing of bistable damage as measured with the C/V method at $T = 20°$C. The fits of Eqs. 8.1, 8.2 to the measurements are also shown.

The evolution of the bistable damage at $T = 20°$ C was measured first with the C/V method. This measurement served as a reference for comparison with the TCT

measurements.

Before the bias was switched on, regular measurements were performed to determine the slope of the reverse annealing. After that the diode was connected to bias high enough (200 V) to fully deplete it. V_{FD} of the diode was around 125 V. With the bias switched on, C/V characteristics were measured only at voltages high enough to deplete more than 3/4 of detector. In this way a possible effect of annealing the bistable damage during the measurement at low voltages was reduced. The bias was switched off after 11 days. C/V characteristics were again measured regularly, now however, starting at zero voltage.

In order to quantify the activation of the bistable damage $|N_{eff}|/\Phi_{\text{eq}}$ after application of bias at $t = t_{on}$ was fitted with:

$$\frac{|N_{eff}(t)|}{\Phi_{\text{eq}}} = g_o + k \cdot t + g_{acf} \cdot (1 - e^{-\frac{t-t_{on}}{\tau_{acf}}}) + g_{acs} \cdot (1 - e^{-\frac{t-t_{on}}{\tau_{acs}}}) \tag{8.1}$$

where g_o represents the damage stable in time, k the slope of reverse annealing approximated with a linear function[64], g_{acf} and g_{acs} are amplitudes of two exponential functions having time constants τ_{acf} and τ_{acs}, respectively.

Similarly, the annealing of the bistable damage, after switching off the bias at t_{off}, was parametrized:

$$\frac{|N_{eff}(t)|}{\Phi_{\text{eq}}} = g_o + k \cdot t + g_{anf} \cdot e^{-\frac{t-t_{off}}{\tau_{anf}}} + g_{ans} \cdot e^{-\frac{t-t_{off}}{\tau_{ans}}} \tag{8.2}$$

The data (Fig. 8.2) shows that bistable damage activation and annealing have a fast (τ_{acf}, τ_{anf}) and a slow (τ_{acs}, τ_{ans}) component, with characteristic times of a few and about 100 hours, respectively. The fast and slow component have the amplitudes of around $g_{acs} \approx g_{anf} \approx 1.5 \cdot 10^{-3}$ cm^{-1} and $g_{acf} \approx g_{ans} \approx 1 \cdot 10^{-3}$ cm^{-1}. This measurement is in agreement with [Cin00].

8.2 TCT study of the bistable damage

The increase of V_{FD} due to activation of the bistable damage should manifests itself also in a change of the electric field. As a consequence of that charge collection efficiency for minimum ionizing particles should change as well. How much it changes is the most relevant information for detector operation. Usage of two different laser wavelengths offered two different examination tools of detector operation. The infra red light (1060 nm) laser with a long absorption length in silicon produced electron-hole pairs uniformly along the light beam, thus generating electron hole pairs in the same way as the charged particles. The red laser on the other hand with short absorption length, resulting in close-to-surface generated electron hole pairs, is a better tool to examine the electric field in the detector.

[64] Reverse annealing time constant of 480 days at $T = 20°$C, is much larger than the interval of the fit.

8.2.1 Observation of the change in electric field

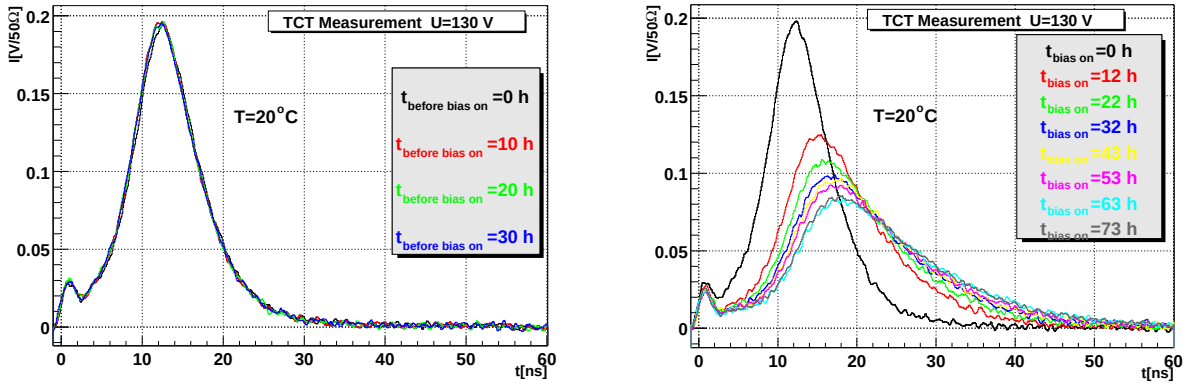

a.) b.)

Figure 8.3 : a.) Measurements at different times before the biased was switched on and b.) evolution of the induced current shape after the biased was switched on. The temperature was kept at 20°C before and after the bias was on.

The change in electric field due to activation of the bistable damage and related increase of $|N_{eff}|$ can be observed in the induced current shape. Since the detector underwent bulk inversion from n type to p type, the red laser illumination of the p^+ side injects the electrons in the low field region. If the bias voltage is close to V_{FD} before the onset of bistable damage the induced current shape is very sensitive to any change in V_{FD}. Once the bias voltage at some point becomes lower than V_{FD} the electrons must overcome a certain undepleted region in the detector by diffusion. A consequence of that is a much longer duration of the induced current pulse.

In Fig. 8.3b the evolution of the induced current at 130 V and $T = 20°C$ is shown after switching on the bias (200V). It can be seen clearly that the tail of the induced current becomes longer with time as the 130 V becomes insufficient to deplete the detector. No such effect is observed before the bias was switched on as can be seen in Fig. 8.3a.

8.2.2 Charge Collection

The change in the electric field affects also the induced charge. This can be observed by illumination of the diode with both lasers. The voltage dependence of the induced charge however depends on the wavelength.

In case of electron injection a steep increase in charge collection can be observed as the operational voltage approaches V_{FD} [65](Fig. 8.4a). A clear difference can be observed after 75 h with detector under bias. Approximately 15 V more is needed to reach the same charge collection efficiency as before the bias was applied.

The same difference of $\approx$ 15 V can also be observed if the infra-red laser pluses are used instead of red (Fig. 8.4b). The dependence of the induced charge on voltage is different,

[65]See section 5.2.4 for explanation.

but as predicted. The linear increase of collected charge with voltage is a consequence of two terms. As only electron-hole pairs generated in the depleted region contribute to the induced current, the induced charge grows linearly with the thickness of depleted region which in turn increases as $\sqrt{U}$. Since only the carriers drifting in the depleted region contribute to the induced charge in 60 ns window, another factor of $\sqrt{U}$ is obtained. The result is a linear rise ($Q \propto \sqrt{U} \cdot \sqrt{U}$) of the observed charge with voltage until V_{FD} is reached.

The intersection point of two lines as indicated in Fig. 8.4a,b was proclaimed as $V_{FD,TCT}$ determined from TCT measurements using the IR light. $V_{FD,TCT}$ determined with both red and IR laser was found to be equal.

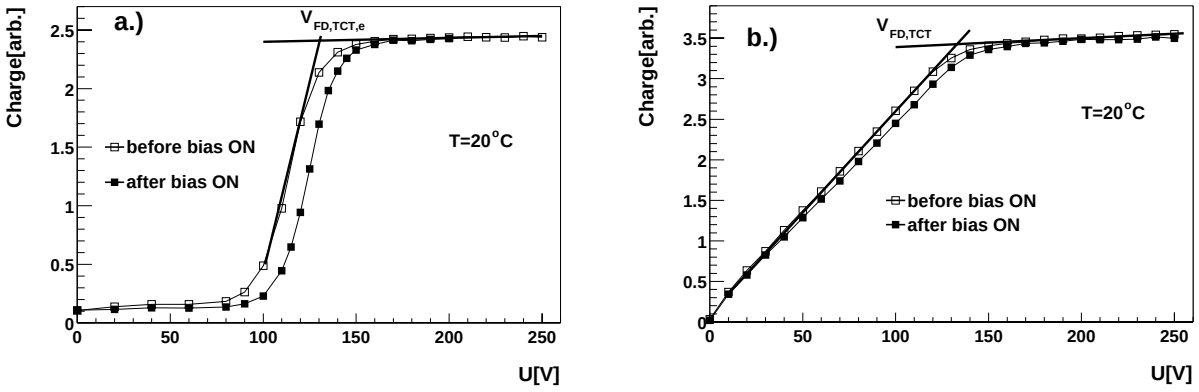

Figure 8.4 : The difference in the charge collection efficiency before the bias on and after 75h with bias applied to the diode for: a.) red laser and b.) infrared laser. The temperature was kept at 20°C before and after the bias was on.

8.2.3 Activation and annealing of the bistable damage

The temperature range of the Peltier cooler was exploited for measurements of $V_{FD,TCT}$ evolution at different temperatures. The temperature was monitored with a Pt-100 sensor and was found to be stable within 0.5°C. The choice of the infrared laser used for this study was governed by a more reliable determination of $V_{FD,TCT}$ and the fact that the diode response to the infrared pulse and to a minimum ionizing particle is similar.

The measurements at different temperatures were performed one after another with increasing temperatures. $V_{FD,TCT}$ evolutions at different temperatures are shown in Fig. 8.5. There was a problem at $T = 14°$ C where the reverse current reached the compliance level and the bias voltage dropped. Although the determination of $V_{FD,TCT}$ was not possible it was always above V_{FD}. The reason for the problem is not known, but it was probably due to some shortcut over the guard ring. This effect was not observed at other temperatures. It is worth mentioning that the measurements were also performed at the same temperature at which the diode was held.

The behavior of the effective dopant concentration normalized to fluence was again modeled with two different defects resulting in the same ansatz (Eqs. 8.1, 8.2) as used in

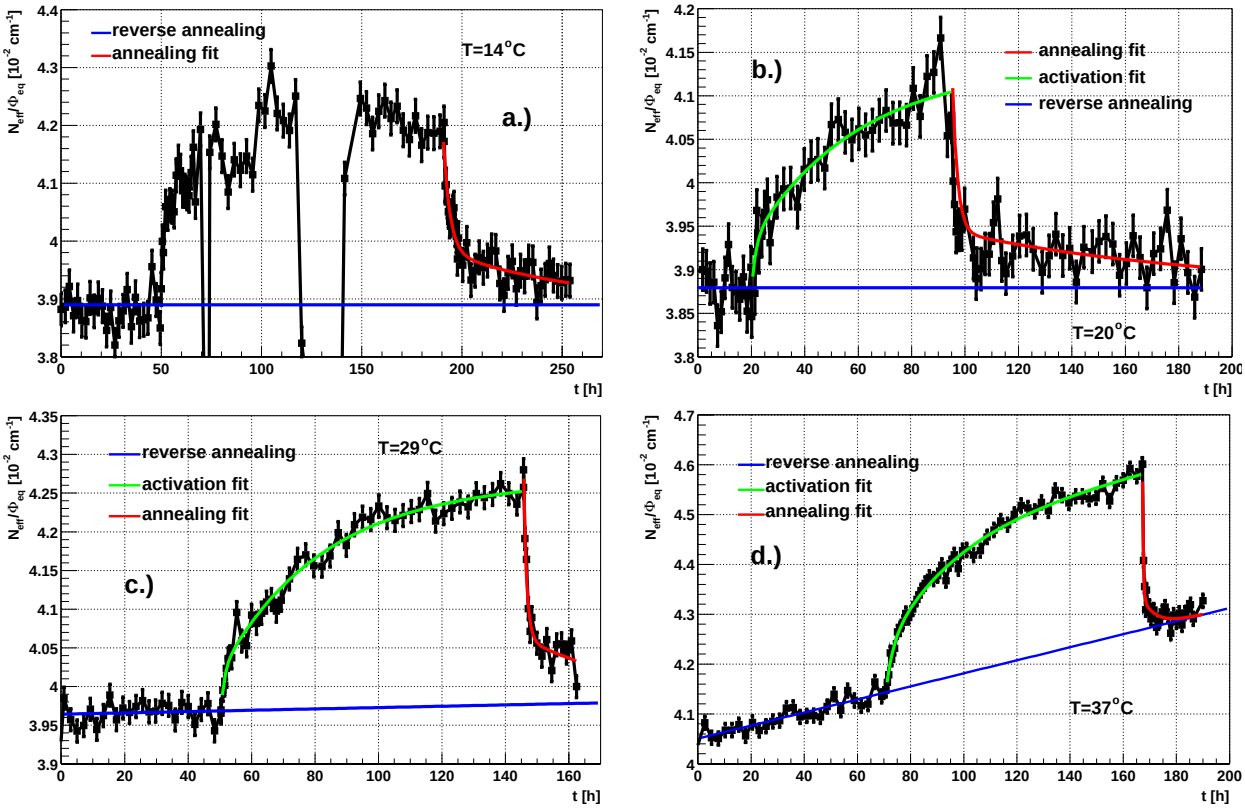

Figure 8.5 : The $|N_{eff}|/\Phi_{\mathrm{eq}}$ evolution at different temperatures before the bias was switched on, during the period with bias switched on and after the bias was switched off again. Due to the problem with the reverse current only the annealing of the bistable damage was studied at $T = 14°$ C.

the case of C/V measurement. The measurement procedure was also the same with one exception. The voltage scan always started at 0 V and needed around 1 minute to reach $V_{FD,TCT}$.

The amplitudes and time constants were determined from the fit of Eq. 8.1 and Eq. 8.2 to the measured data.

8.2.4 Time constants and activation energy

The time constants and amplitudes are gathered in Table 8.1. Those are however only very preliminary results obtained from the measurements of only one diode. Certainly more statistics is needed to claim more precise results.

To determine activation energies for both processes, the Arrhenius relation (see Eq. 3.14)

$$\tau(T) = \tau_0 e^{\frac{E_a}{k_B T}} \tag{8.3}$$

T[°C]	g_{acf}	τ_{acf}	g_{acs}	τ_{acs}	g_{anf}	τ_{anf}	g_{acs}	τ_{ans}
14	-	-	-	-	0.18±0.03	3.18±1.3	0.1±0.03	70±40
20	0.065±0.025	1.46±1.3	0.2±0.03	40±8	0.2±0.02	1.9±0.8	0.065±0.025	93±25
29	0.05±0.01	1.1±0.6	0.235±0.01	31.6±4	0.21±0.02	1.±0.2	0.09±0.02	37±25
37	0.09±0.02	2.6±1	0.227±0.02	26.4±4	0.26±0.025	0.33 ± 0.07	0.06±0.02	5.2 ± 2.5

Table 8.1 : The amplitudes and time constants of the activation and annealing of the bistable damage. The amplitudes are given in $10^{-2}\mathrm{cm}^{-1}$. All time constants are in hours at the given temperature.

or

$$\ln \tau(T) = \ln \tau_0 + \frac{1}{k_B T} E_a \tag{8.4}$$

is used. If one plots $\ln(\tau(T))$ versus $1/k_BT$ (Arrhenius plot), the activation energy can be determined from the slope of the linear function fit to the data (Fig. 8.6).

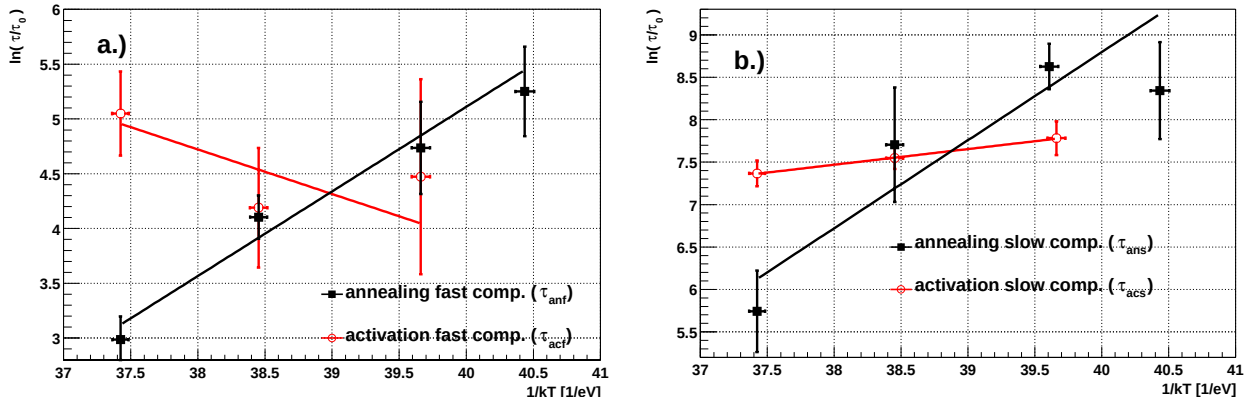

Figure 8.6 : Arhenious plots for: a.) fast components of activation and annealing of the bistable damage and b.) for the slow component for both processes.

The fit gives a negative activation energy for the fast component of bistable damage activation (E_{acf}). This could be an artifact of large correlation in fit between fast and slow component. The unbiased period during the measurements can be also important, especially at higher temperatures.

A more reasonable value of $E_{acs} = 0.47 \pm 0.13\,\mathrm{eV}$ was obtained for the slow component The activation energies for the annealing of the bistable damage are larger. $E_{anf} = 0.63 \pm 0.11\,\mathrm{eV}$ was found for the fast component and $E_{ans} = 0.8 \pm 0.13\,\mathrm{eV}$ for the slow one.

The amplitudes for the activation and annealing process are shown in Fig. 8.7. It seems that the amplitudes g_{acs} and g_{anf} could be equal $g_{acs} \sim g_{anf} \sim 0.2 \cdot 10^{-2}$ cm^{-1} and also $g_{ans} \sim g_{acf} \sim 0.08 \cdot 10^{-2}$ cm^{-1}. This could indicate that the defect which is activated fast anneals slowly and vice versa. According to the measurements the activated bistable damage anneals completely.

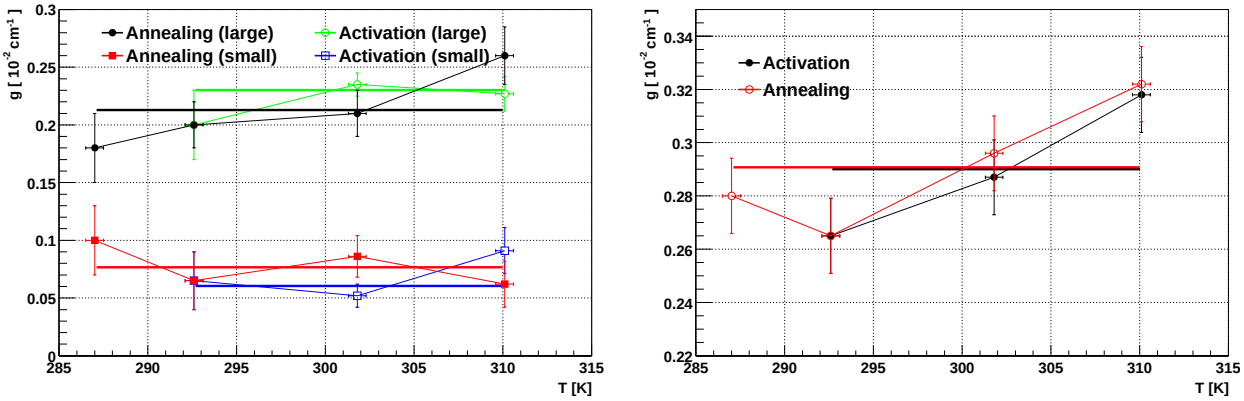

Figure 8.7 : a.) Activation and annealing amplitudes of the bistable damage and b.) the sum of both fast and slow amplitudes for both processes.

8.3 Predictions for ATLAS-SCT

It is interesting to predict the extent of the additional bias-related radiation damage influence on operation of the ATLAS-SCT microstrip detectors.

At inner radii, detectors will receive an equivalent fluence of $2 \cdot 10^{12}$ cm^{-2} per low-luminosity and $2 \cdot 10^{13}$ cm^{-2} per high-luminosity year. The standard LHC scenario of 3 low and 7 high-luminosity years was considered. When comparing with conventional damage projections, one should care, that damage estimates usually include a safety factor of 1.5, which was not applied in this estimate.

The standard ATLAS yearly temperature and biasing scenario was applied implying 100 days operation under bias at $-7°$C. Then the bias is switched off first for 100 days still at $-7°$C, followed by a 2 plus 14 days maintenance at 20 and 17°C, respectively. The remaining 150 days are spent again unbiased at the operational temperature of $-7°$C.

Since the measurements of TCT signals gave compatible results with C/V technique, it is reasonable to take more precise bias-induced damage parameters from the C/V measurements [Mik00]. The annealing times of the bistable damage were scaled with the respective activation energies according to Eq. 8.3. The bistable damage introduction rates were set to $0.45 \cdot 10^{-2}$ cm^{-1} [Cin00] since the amplitude of bistable damage was measured to be larger at earlier anneling times. [66] Defects available for activation were the ones created by irradiation in previous years and annealed out in the idle period. The activation time under bias at $-7°$C is 100 days, so about 60 % of this damage are re-activated. On the basis of the measurements in this work, a complete annealing of the bistable part could be assumed during each year's high temperature period.

The prediction for additional acceptor density and additional voltage, needed to fully deplete ATLAS SCT detectors, resulting from bias-induced damage is shown in Fig. 8.8. Additional damage, corresponding to an additional 25 V of bias, is created during irradiation in each high-luminosity year. The relatively short time constants (τ_1) of the

[66] Detectors will be operated close to the minimum in V_{FD} and will reach around 10% of the reverse annealing at the end of the operation.

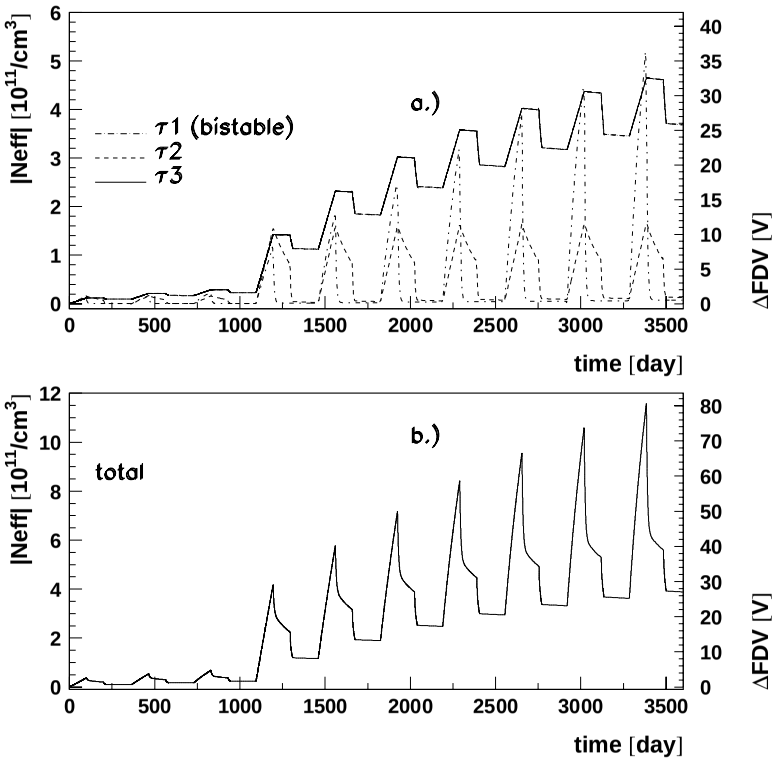

Figure 8.8 : Prediction of the influence of bias-related damage to ATLAS SCT detectors in 10 years of LHC operation: a) each of the components considered separately and b) the total of the bias-related damage. For fluences and temperature scenarios applied see text. ΔFDV denotes additional contribution to the V_{FD}.

non-bistable bias induced damage annealing allow for a complete annealing of the respective damage during idle time. The longest annealing component (τ_2) exhibits a saturation leading to an additional 30 V at end of operation, where re-activation of previous years' bistable damage contributes another 30 V. All added up, additional 80 V are predicted to be needed to fully deplete ATLAS SCT detectors near the end of operation. This is about half the expected contribution from the introduction of stable acceptors by irradiation.

9

Conclusions

Position sensitive silicon detectors, undoubtedly represent the most often used solution for vertex detectors. Although they were used in a large number of experiments in the last decade, the experiments at the new Large Hadron Collider (LHC) require another step forward in development of position sensitive silicon detectors. The large fluxes of hadrons traversing detectors in these experiments will cause changes in operation of the detectors. The changes in behavior of irradiated silicon detectors have been extensively studied in the last decade and are still not completely resolved. This work represents an additional contribution to a better understanding of silicon as the base material of a position sensitive detector for ionizing radiation. It is focused to the changes in formation of the signal in irradiated silicon detectors.

The core of this study represent the TCT (transient current technique) measurements performed with a large number of irradiated silicon pad detectors made from different silicon materials. The detectors were irradiated with 24 GeV protons at CERN-PS, 200 MeV pions at PSI (Villigen) and reactor neutrons from the TRIGA research reactor near Ljubljana. The reactor neutrons were also used for irradiation of silicon strip detectors. During and after irradiation the detectors were always kept at well defined conditions. The results obtained from these measurements served as input to the simulation of silicon detector operation.

In the scope of this work, the first systematic study of effective carrier trapping time dependence on silicon materials, fluence, irradiation particle type, temperature and time after irradiation has been performed. For that purpose a new method based on detector response to a short transient light pulse has been proposed. Another interesting topic is the investigation of silicon detectors operated in presence of enhanced hole concentration in the silicon bulk. The charge collection efficiency of silicon strip detectors connected to LHC design electronics was also investigated. The measured effective carrier trapping times are expected to have a major impact on detector design. This fact was confirmed by the simulation. Its predictions are in agreement with some, previously not fully understood measurements.

The results of the work can be summarized in the following outline:

Charge correction method - determination of effective trapping times
The charge correction method for the determination of the effective trapping time is based on the assumption that the decrease of charge due to trapping is exponential with time, as the charge drifts through the detector. Therefore the integral of the induced current (induced charge) does not saturate in an irradiated detector but exhibits a rise also at voltages above the full depletion voltage (V_{FD}). At higher voltages the drift time is reduced due to the higher electric field and thus less charge gets trapped. To determine the effective trapping time (τ_{eff}), the measured induced currents ($I_m(t)$) are corrected with an exponential $\exp(t/\tau_{eff})$ so that the integral of the corrected currents give equal charges for all voltages above V_{FD}.

Effective trapping times of electrons and holes
Several sets of diodes of different resistivities and oxygen content were irradiated with neutrons, pions and protons up to $\Phi_{\rm eq} = 2.4 \cdot 10^{14}$ cm^{-2}. TCT measurements were performed after the irradiated pad detectors were annealed to the minimum in V_{FD} at room temperature. Using the charge correction method the electron and hole effective trapping probabilities were determined for all diodes in the temperature range between 223 K and 293K.

The effective trapping probability was found to scale linearly with equivalent fluence ($1/\tau_{eff_{e,h}} = \beta_{e,h}\ \Phi_{\rm eq}$) and not to depend on oxygenation level and resistivity. Holes were observed to have higher trapping probability ($\beta_h = 6 \cdot 10^{-16}$ cm^2/ns) than electrons ($\beta_e = 4 \cdot 10^{-16}$ cm^2/ns) in the minimum of V_{FD} after neutron irradiation. Charge trapping is seen not to scale according to the NIEL hypothesis since charged hadrons induce 30-40 % more trapping than neutrons at the same NIEL equivalent fluence.

For both electrons and holes the effective trapping probability decreases with temperature by 20-30 % over the investigated -50 to $+20$°C temperature range. A power scaling law, universal in terms of particle type, was found to parameterize the data well.

Distinct annealing behavior of effective trapping probability for electrons and holes was observed. The electron effective trapping probability at $T = 283$ K decreases by $\sim 35\%$ while the hole effective trapping probability increases by $\sim 30\%$. Time constants for these changes are of the order of 10 hours at 60°C.

N_{eff} reverse annealing study using TCT
The reverse annealing amplitude and time constant were found to coincide with the ones measured with the C/V method for the high-resistivity neutron-irradiated detectors. At each measurement point in time the electric field profile was checked. The proportionality between depletion depth and the bias voltage ($w \propto \sqrt{U}$) could be confirmed for detectors (15 kΩcm) irradiated with neutrons which implies that the effective dopant concentration N_{eff} remains constant over the detector volume during the reverse annealing.

Influence of continuous carrier injection to detector operation
The operation of highly irradiated silicon detectors in the presence of enhanced electron or hole concentration in the bulk was investigated. This mode of operation was theoretically

proposed before, however was left experimentally only partially investigated. In this work electrons and holes were continuously injected by means of a red laser. The electron injection was found to increase the voltage required for successful operation while the hole injection decreased it. The deep levels responsible for space charge inversion (n-type $\rightarrow$ effectively p-type) are in this mode of operation less occupied as compared to normal operation and, as a consequence $|N_{eff}|$, decreases. A deep donor is required, in addition to deep acceptor, to explain the space charge re-inversion once the concentration of holes in the bulk becomes sufficiently high.

As the result at given a voltage and temperature the continuous hole injection can be set to a value where the $N_{eff} \sim 0$. This point of operation, called also the optimal point, is fluence independent provided that the remaining initial dopant concentration can be ignored. Although the optimal point can be set as low as few volts, the trapping of the drifting charge and long charge collection time limit the useful voltages to few ten volts. Contrary to the effective space charge, the effective trapping times do not seem to be influenced significantly by the enhanced hole concentration.

The reduction of operational voltage compensates for the increase of the leakage current resulting in comparable and even lower power dissipation. Relatively high leakage current has for a consequence an increase in shot noise, particularly for strip detectors where the active surface is large. However, the increase of noise could be compensated in the signal to noise ratio by using a thicker detector, hence obtaining larger signal.

The dominant trap position

Assuming that a single dominant trap is responsible for both the trapping of drifting charge in a fully depleted detector and also for the change in the effective space charge, when the detector is operated in the presence of high free carrier concentration, the position of such a trap can be determined. The main hole trap was determined to be at $E_t = E_V + 0.34$ eV and the main electron trap at $E_t = E_C - 0.48$ eV.

Silicon micro-strip detector measurements

Measurements with single sided silicon strip detectors showed that substantially higher voltage of around 100-150 V above V_{FD} is required at any point in time for reaching a high charge collection efficiency. Even for a non-irradiated detector an overdepletion of the same order is required to minimize the ballistic deficit. CCE was found to be almost independent on temperature in the temperature range between $-30°$C and $5°$C.

CCE decreases with time after irradiation, which is in agreement with measurements of effective trapping times, since the dominant contribution to the induced charge in the detector with p^+ strips comes from holes.

Silicon microstrip detector simulation

A simulation of silicon strip detectors confirmed the results of measurements. In general it can be concluded that for irradiated detectors charge trapping is dominating the loss of signal and the CCE becomes nearly independent of shaping time. The signal does not saturate even at voltages a few hundred volts above the V_{FD}.

The choice of detector type and design was found to play an important role in signal detection:

- Around 10% higher charge collection efficiency can be expected for detectors with n^+ strips compared to those with p^+ strips after irradiation with charge hadrons to $\Phi_{\text{eq}} = 2 \cdot 10^{14}$ cm^{-2}. Both, the larger hole trapping probability and longer drift time of holes compared to those of electrons, are the reasons.
- The strip width does not significantly affect the CCE.
- Although higher CCE can be reached for thinner detectors (< 300 μm) the induced charge at 450 V is largest for a 300 μm thick detector.
- In an irradiated position sensitive silicon detector a significant amount of charge can be induced also in the case of charge drifting to the neighboring strips. That can be explained by a non-vanishing induced current integral due to charge trapping. The effect is more pronounced for detectors with p^+ strips.

Bistable damage

The increase of N_{eff} after application of bias to a previously unbiased sample and the decrease of N_{eff} after switching the bias off was also observed in measurements of the induced current. Amplitudes and time constants measured in this way agree with those measured with the C/V method.

Appendix A

FoxFET biased detectors

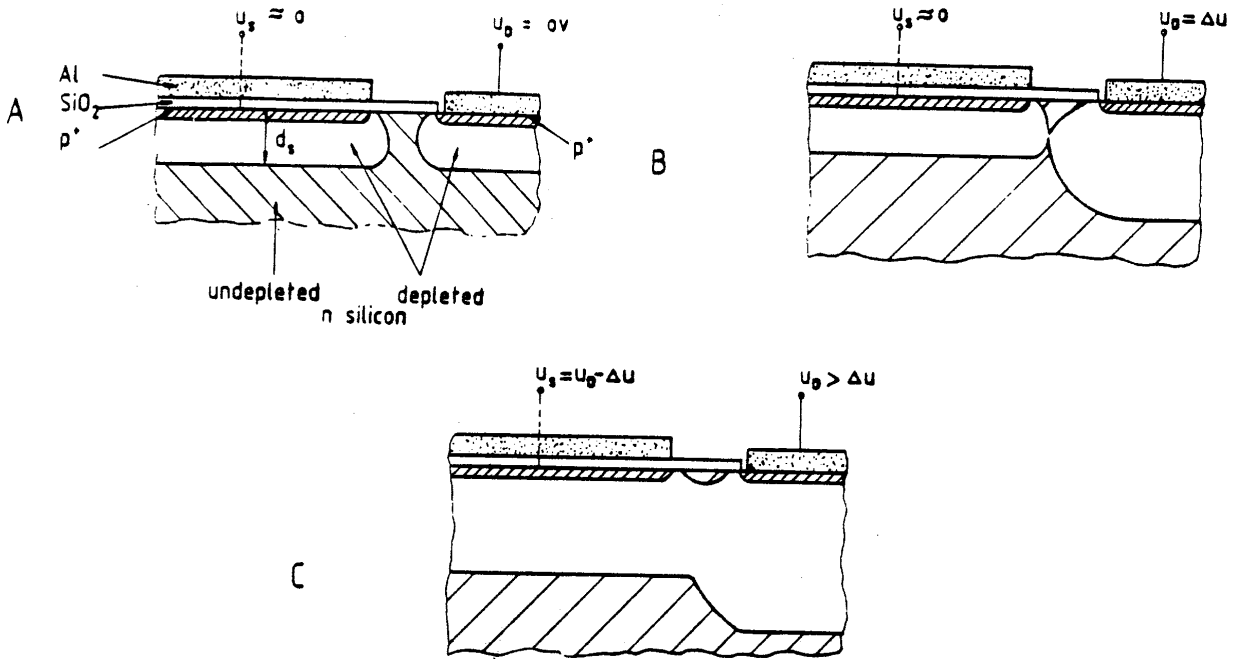

Figure A.1 : Schematic sequence of biasing. A: No bias voltage is applied. B: The Voltage ΔU is just sufficient to cause the depletion zone around the right p^+ strips. C: For still higher bias the voltage at p^+ strips follows the bias voltage at almost constant difference of ΔU (taken from [Dij89]).

An alternative method for providing the bias voltage to the p^+ strips in AC-coupled detectors is through a so called punch through effect [Dij89, Ell90]. In Fig. A.1 the principle of this method is illustrated. In absence of a bias voltage there is a thin layer of space charge around the junction (Fig. A.1a). Applying an increasing potential, U_D to the right hand strip increases the width of the depletion zone around it until it reaches the the left hand zone. It happens when U_D reaches the threshold value, ΔU (Fig. A.1b). A

hole current flows between the strips until a state of equilibrium is attained. The potential of the floating strip is equal to $U_D - \Delta U$. For still higher voltages the floating strip follows the bias voltage with an almost constant difference ΔU (Fig. A.1c).

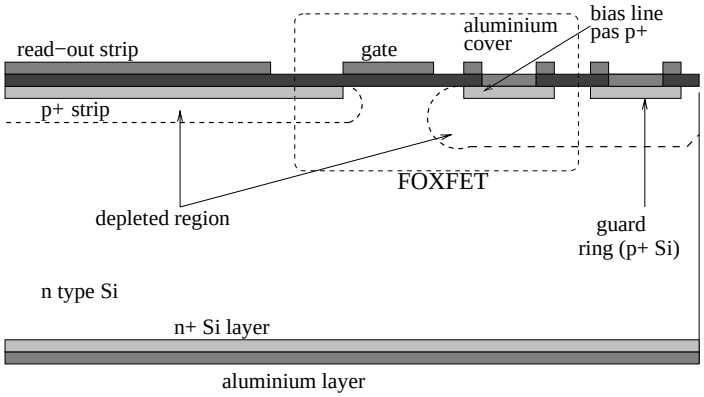

Figure A.2 : Schematic view of a FOXFET biased detector. A gate electrode is placed on top of the oxide in the region between p^+ strip and bias line.

A similar biasing scheme (Fig. A.2) is achieved by introducing a gate electrode, which is placed on top of the oxide in the strip - bias line channel (typically 5-10 μm long). In this way the circuit is equivalent to a FET transistor where the source electrode is the strip and drain electrode is the bias line. The whole detector can be seen as a multi-source transistor with common drain and gate electrode. The advantage of such a circuit is that by using the proper negative gate voltage the potential difference between p^+ strips and the bias line can be controlled.

The radiation influences the FOXFET structure mainly in two ways. The charge built up in the oxide and at the Si-SiO_2 interface increases the punch through voltage [Laa93]. Increase of leakage current flowing through the FOXFET structure decreases the dynamic resistance defined as $R_d = \delta V_{strip}/\delta I_s$, where V_{strip} is a strip potential and I_s current flowing from the strip to the drain. The dynamic resistance is inversely proportional to the leakage current $R_d \propto 1/I_s$ [Laa93], as long there is some potential difference between bias line and strips and exhibit an abrupt decrease, if there is in none. This inevitably leads to reduction of bias resistance with irradiation and according to Eq. 2.56 the increase of parallel noise. There is also a potential danger of losing signal, due to short time constant of charge flow from the strip to the drain [67]. Although the increase of noise seems to be understood in γ irradiations [Laa93], the measurements of the detector performance after hadron irradiation exhibit an unexpected excess of noise. This was first reported from CDF collaboration [Azz96] and confirmed by CMS [Ham98] collaboration. It was shown that the noise can be brought to acceptable level by cooling detector to $T < -30°$C, which is however impractical and often not possible.

[67] $\tau_{sd} = R_d\, C_d$, where C_d is a strip to backplane capacitance.

Appendix B

Reciprocity theorem

Consider a system of conducting electrodes, which are either at some fixed potential or there is some charge on them. If V is the potential of electrostatic field in the region between electrodes then it holds $\nabla^2 V = 0$.

Let us imagine a tiny sphere around the charged electrodes and call V_i the potential of the i-th sphere. It is required by the Gauss' law that

$$-\int_{sphere's\ surface} \nabla V d\vec{S} = Q_i \quad , \tag{B.1}$$

In a another possible electrostatical case where different electrodes can be charged or at fixed potential, a new electrostatic field is established with potential $\grave{V}$, so that again $\nabla^2 \grave{V} = 0$ between the electrodes. Since ∇^2 is a self adjoin linear operator it holds $< \nabla^2 V | \grave{V} > = < V | \nabla^2 \grave{V} >$[68] and from Green's theorem it follows

$$\int_{volume\ between\ boundaries} [\grave{V}\nabla^2 V - V\nabla^2 \grave{V}]\, dV = -\int_{boundary\ surfaces} [\grave{V}\nabla V - V\nabla \grave{V}]\, d\vec{S}\ . \tag{B.2}$$

By choosing the volume to be that bounded by the electrodes at fixed potential and tiny spheres, the left hand side of Eq. B.2 is zero, since $\nabla^2 V = \nabla^2 \grave{V} = 0$. The right-hand side can be rewritten into

$$0 = \grave{V} \int_{boundary\ surfaces} \nabla V d\vec{S} - V \int_{boundary\ surfaces} \nabla \grave{V} d\vec{S} \quad , \tag{B.3}$$

where the integral runs over all electrodes and tiny spheres in the system. Using Eq. B.1 in Eq. B.3 the reciprocity theorem states

$$\sum_{electrodes} \grave{V}_i Q_i = \sum_{electrodes} V_i \grave{Q}_i \quad , \tag{B.4}$$

where the sum runs over all electrodes. The Eq. B.4 relates the potentials and charges of electrodes in two different electrostatically possible states.

[68] The $< f|g >$ denotes the scalar product of two functions defined as $\int f(\vec{r})\, g(\vec{r}) d^3\vec{r}$.

Appendix C

Mobility parameterization

The mobility parameterization is taken from [Sel90]. The temperature dependence of mobility in intrinsic silicon crystal is modeled by simple power laws

$$\mu_e^L = 1430 \frac{\mathrm{cm}^2}{\mathrm{V\,s}} \cdot \left(\frac{T}{300\ \mathrm{K}}\right)^{-2} \tag{C.1}$$

$$\mu_h^L = 460 \frac{\mathrm{cm}^2}{\mathrm{V\,s}} \cdot \left(\frac{T}{300\ \mathrm{K}}\right)^{-2.18} \quad . \tag{C.2}$$

To account for mobility reduction due to ionized dopant scattering the formulae of Caughey and Thomas [Cau67] is used in conjunction with temperature dependent coefficients

$$\begin{aligned}
\mu_{e,h}^{LI} &= \mu_{e,h}^{min} + \frac{\mu_{n,p}^L - \mu_{e,h}^{min}}{1 + \left(\frac{N_{eff}}{C_{e,h}^{ref}}\right)^{\alpha_{e,h}}} \\
\mu_{e,h}^{min} &= K_{e,h} \cdot (\frac{T}{300\ \mathrm{K}})^{-0.45} \quad , \quad T > 200\ \mathrm{K} \quad , \quad K_e = 85\frac{\mathrm{cm}^2}{\mathrm{V\,s}}, \quad K_e = 45\frac{\mathrm{cm}^2}{\mathrm{V\,s}} \\
\mu_e^{min} &= K_{e,h} \cdot (\frac{200\ \mathrm{K}}{300\ \mathrm{K}})^{-0.45} \cdot (\frac{T}{300\ \mathrm{K}})^{-0.15} \quad , \quad T < 200\ \mathrm{K} \\
C_{e,h}^{ref} &= S_{e,h} \cdot (\frac{T}{300\ \mathrm{K}})^{3.2} \quad , \quad S_e = 1.12 \cdot 10^{17}\ \mathrm{cm}^{-3}, S_h = 2.23 \cdot 10^{17}\ \mathrm{cm}^{-3} \\
\alpha_{e,h} &= 0.72 \cdot (\frac{T}{300\ \mathrm{K}})^{0.065} \quad .
\end{aligned} \tag{C.3}$$

Deviations from the ohmic low-field mobility are given for both electrons and holes by

$$\begin{aligned} \mu_{e,h} = \mu_{e,h}^{LIF} &= \frac{2 \cdot \mu_{e,h}^{LI}}{1 + \left(1 + \left(\frac{2\,\mu_{e,h}^{LI}\,E}{v_{n,p}^{sat}}\right)^{\zeta_{e,h}}\right)^{\zeta_{e,h}^{-1}}} \quad , \quad \zeta_e = 2 \quad , \quad \zeta_h = 1 \\ v_e^{sat} &= 1.45 \cdot 10^7 \text{ cm/s} \cdot \sqrt{\tanh(\frac{155 \text{ K}}{T})} \\ v_h^{sat} &= 1.45 \cdot 10^7 \text{ cm/s} \cdot \sqrt{\tanh(\frac{312 \text{ K}}{T})} \end{aligned} \tag{C.4}$$

The saturation drift velocity is denoted by $v_{e,h}^{sat}$. The effect of effective dopant concentration is very small at typical concentrations obtained by irradiation. The drift velocity as a function of electric field and temperature for both electrons and holes is given in Fig. C.1.

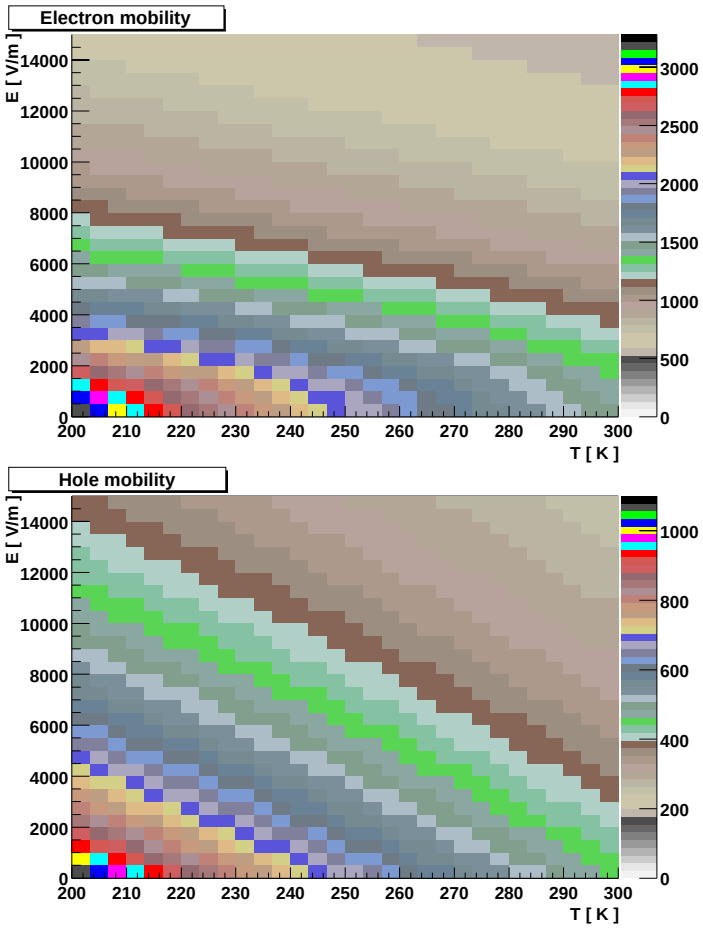

Figure C.1 : Mobility of electrons and holes as a function of temperature and electric field. The effective dopant concentration is $N_{eff} = 0$.

Appendix D

Damage parameters

Initial dopant removal

There were different proposals in the past, how irradiation influences the initial dopant concentration:

- Both, concentration of initial donors (N_D) and acceptors (N_A) change according to the equation: $-dN_{D,A} = c_{D,A}\, N_{D,A}\, d\Phi_{\text{eq}}$, thus resulting in exponential decrease of $N_{D,A}$ with fluence $N_{D,A} = N_{D_0,A_0}\, \exp(-c_{D,A}\, \Phi_{\text{eq}})$. Such model was proposed in [Wun96] with $c_D \approx 2.5 \cdot 10^{-13}$ cm^2 and $c_A \approx 2 \cdot 10^{-13}$ cm^2.

- No donors or acceptors are removed in calculations found in [Mat95] and measurements in [Dez98]. It is claimed that compensation of shallow donors by deep acceptors is sufficient to successfully explain the fluence dependence of N_{eff}.

- In [FeicT] only initial donor removal is proposed. However, not all initial donors are removed. In the latest ROSE collaboration report [ROSE3] incomplete donor removal in neutron irradiated samples and complete removal in charged hadron irradiated samples is reported.

Hamburg Model

In projections of N_{eff} evolution with time, Eq. 3.39 is most often used with only one anneling and one reverse annealing defect. The removal of initial donor is proposed, while the initial acceptor removal is neglected due to much lower initial concentration. The Eq. 3.39 can be rewritten as

$$\frac{\Delta N_{eff}}{\Phi_{\text{eq}}} = g_a \exp\left[-\frac{t}{\tau_a}\right] + g_c + g_Y \left[1 - \frac{1}{1+\frac{t}{\tau_{ra}}}\right] + N_{C0}\, \frac{(1-\exp(-c\cdot\Phi_{\text{eq}}))}{\Phi_{\text{eq}}} \quad , \quad \text{(D.1)}$$

where $N_{C0}/N_{eff,0}$ is the ratio of the initial donors removed and c the donor removal rate.

Due to better agreement of the function describing the second order process with the measured data, particularly at late stages of N_{eff} time evolution, reverse annealing was attributed to to the reaction between two identical electrically neutral defects forming

a new electrically active defect. However, a linear dependence of the reverse annealing initial slope on fluence clearly reveals a first order process to be responsible. In fact the a model with two defects which dynamics is described by first order process also fits well the measurements at late stages of reverse annealing, but more free parameters are required. Therefore a second order model is used with reaction constant inversely proportional to the fluence ${k_2}^Y \rightarrow {k_2}^Y/\Phi_{\mathrm{eq}}$. Although physically unjustified this model gives good fits, requiring the smallest number of free parameters.

The parameters of the model for different irradiation particle types and silicon materials are given in the Tables D.1, D.2, D.3 and D.4. The evolution of the defects is influenced by bias voltage [Ci00B]. So far available data for parameters of annealing and reverse annealing under bias are also given.

	g_c [10^{-2} cm^{-1}] (S)	g_c [10^{-2} cm^{-1}] (O)
neutrons	1.5	2.0
protons	1.9	0.53
neutrons (biased)	4.1	$\approx$4
pions (biased)	≈ 4	-

Table D.1 : Contribution of deep defects to stable damage. The measurements under bias were taken from [Ci00B, KolaD].

	N_{C0}/N_{eff0} (S)	N_{C0}/N_{eff0} (O)	c (S)	c (O)
neutrons	0.7	0.45	-	$0.8 \cdot 10^{-13}$ cm^2
protons	-	1	-	-

Table D.2 : The parameters used in calculation of donor removal. N_{C0}/N_{eff0} denotes the fraction of removed donors.

	τ_a(20°C) (S)	τ_a(20°C) (O)	g_a [10^{-2} cm^{-1}] (S)	g_a [10^{-2} cm^{-1}] (O)
neutrons	55 h	70 h	1.8	1.4
protons	-	-	-	-
neutrons (biased)	-	-	-	-
protons (biased)	-	-	-	-

Table D.3 : Annealing data for standard (S) and oxygen enriched (O) silicon detectors. Measurements of annealing of defects with time constants shorter than few hours is not precisely known. Some measurements of beneficial anneling under bias can be found in [ZontT, KolaD].

	$\tau_{ra}(20°C)$ (S)	$\tau_{ra}(20°C)$ (O)	g_Y [10^{-2} cm^{-1}] (S)	g_Y [10^{-2} cm^{-1}] (O)
neutrons (unbiased)	480 days	800 days	5.2	4.8
protons (unbiased)	-	950 days	6.6	2.3
neutrons (biased)	1120 days	-	5.4	-
protons (biased)	-	-	-	-

Table D.4 : Reverse annealing time constants and amplitudes for oxygenated and standard material at $T = 20°C$. The bias voltage was always larger than V_{FD} when measuring the reverse annealing parameters under bias.

Leakage current

The parameters of leakage current evolution with time after irradiation (see Eq. 3.44) are given in the Table D.5.

α_0 [10^{-17} A/cm]	α_1 [10^{-17} A/cm]	α_2 [10^{-18} A/cm]	$\tau_\alpha[min]$	t_{norm} [min]
1.01±0.38	93 ± 24	5.03 ± 0.09	3.34 ± 0.26	1

Table D.5 : Parameters used to model the leakage current evolution with time. The annealing takes place at $T = 60°C$, while the current is measured at $T = 20°C$. The activation energy of 1.11 eV [ZontT, MollT] can be used to scale the annealing times to different temperatures.

Appendix E

The setup for strip detector read-out

Pulse contractor

The width of a logical signal obtained from most of discriminators on the market is longer that 10 ns. The corresponding coincident curve of two such signals has therefore a minimum width of around 20 ns. This value can be significantly reduced with the circuit shown in Fig. E.1. By using this circuit the width of a logical signal is reduced from 10 ns to 2-3 ns. The resulting coincident curve of two such signals is less than 5 ns wide.

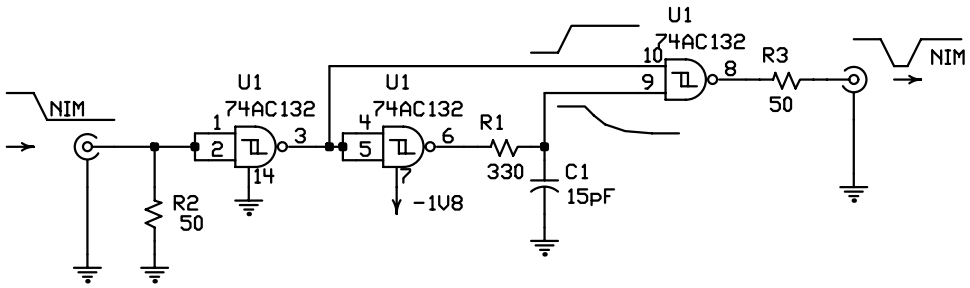

Figure E.1 : The pulse contractor circuit.

Setup scheme

A detailed setup scheme is shown in Fig. E.2. All the components of the setup are shown although some are used for calibration of the chips and some for the measurements of signals resulting from passage of beta source electrons through silicon strip detectors.

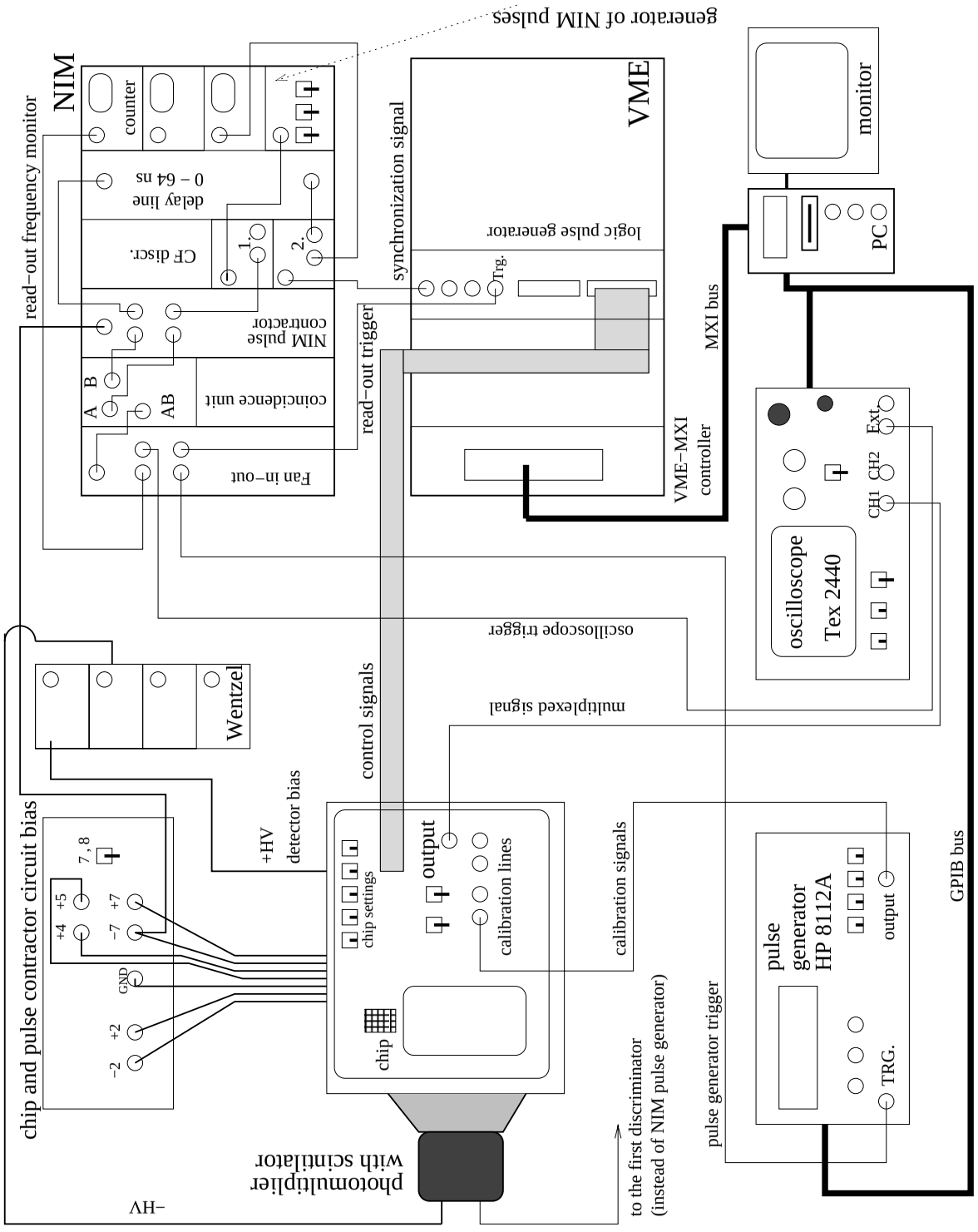

Figure E.2 : The detailed scheme of the strip detector read-out setup.

Appendix F

Silicon material properties

atomic number	14
atomic mass	28.09
distance between lattice atoms	5.34 10^{-10} cm
ε	11.9
density	2.328 g/cm^{-3}
density (SiO_2)	2.33 g/cm^{-3}
density of atoms	$5.0 \cdot 10^{22}$ cm^{-3}
intrinsic carrier concentration at $T = 300$ K (n_i)	$1.45 \cdot 10^{10}$ cm^{-3}
effective density of states ($T = 300$ K): in conduction band (N_c) in valence band(P_v)	 $2.80 \cdot 10^{19}$ cm^{-3} $1.04 \cdot 10^{19}$ cm^{-3}
energy gap ($T = 300$ K) (E_g)	1.12 eV
average minimum ionizing particle energy loss (dE/d(ρx))	166 keV kg^{-1} m^2
electron mobility $\mu_{0,e}$ hole mobility $\mu_{0,h}$	1380 cm^2/Vs 480 cm^2/Vs
$m_e{}^*$ (at bottom of conduction band) $m_h{}^*$ (at top of valence band)	0.558 m_e 1.08 m_e
$v_{th,e}$ (at $T = 300$ K) $v_{th,h}$ (at $T = 300$ K)	$2.3 \cdot 10^7$ cm/s $1.65 \cdot 10^7$ cm/s

Table F.1 : Some important silicon properties.

Light absorption

Light absorption in silicon depends on temperature and wavelength. In silicon absorption takes place by indirect inter-band transitions, where the lattice phonon is incorporated

in order to conserve lattice momentum. The penetration depth depends on temperature through the temperature dependence of phonon spectra and band gap. It can be parametrized as $\alpha_{abs}^{-1} = a \cdot T + b$, provided that the photon energy is sufficient ($E_\gamma > E_g$) to generate electron-hole pairs (Fig. F.1a). The values of a and b for light of different wavelengths can be found in the Table F.2.

source	λ [nm]	hc/λ eV	$\alpha_{abs}(77K)$ [μm]	$\alpha_{abs}(300K)$ [μm]	a [cm^{-1} K^{-1}]	b [cm^{-1} K^{-1}]
[Das55]	670	1.85	7.7	3.3	7.6	720
[Das55]	830	1.49	32	13	2.15	145
[Das55]	980	1.27	290	63	0.56	-8.1
[Mac58]	1060	1.17	$24 \cdot 10^4$	1040	0.24	-59.4

Table F.2 : Optical absorption data for different wavelengths.

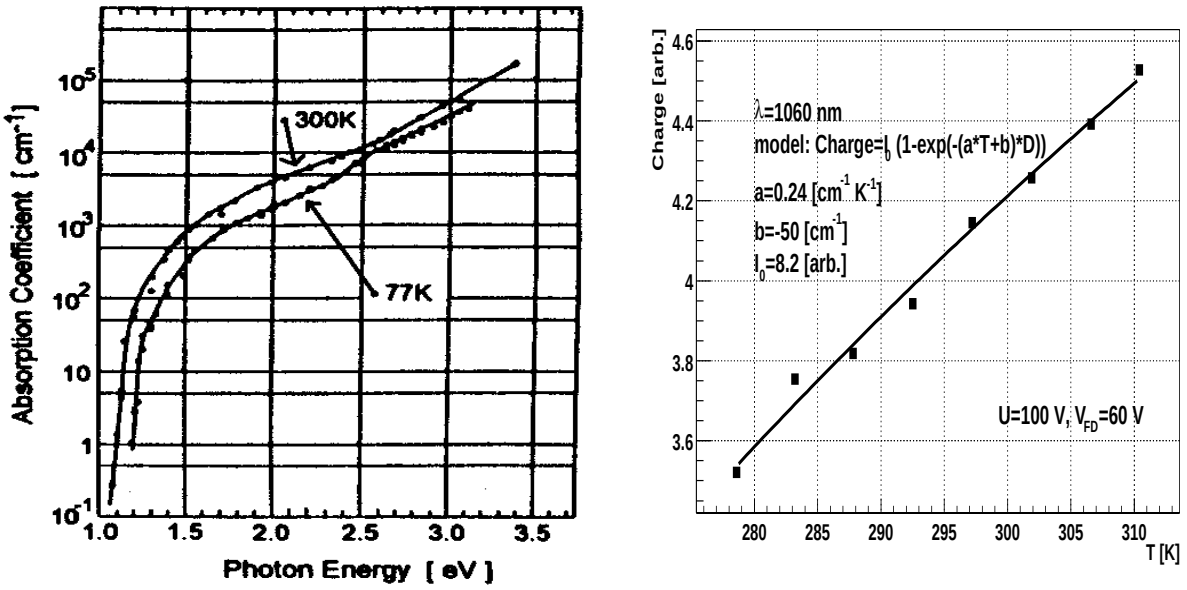

Figure F.1 : a.) Optical absorption constant in intrinsic silicon at 77 K and 300 K as a function of photon energy, from [Das55]. b.) Measurements of the absorption constant temperature dependence with a 1060 nm laser.

The measurements of absorption constant of 1060 nm light in silicon were performed at different temperatures (Fig. F.1b). An non-irradiated diode produced by ITE (300 μm thick, $V_{FD} = 60V$) was used for that purpose. Instead of measuring the transmittance as in [Mac58] the absorption was measured directly. The ansatz $Q = I_0\,(1-\exp(-(a\,T+b)D))$ (see Fig. F.1) was fitted to the measurements. Q denotes the measured charge, I_0 the intensity of light and D the detector thickness. Slightly different values of a and b as those found in [Mac58] can be attributed to non-collimated laser.

In a similar way red laser absorption constant could be measured. Instead of using a fully depleted detector, a low resistivity (1 kΩcm) detector at built-in voltage should be operated, so that the depleted region and effectively the detector thickness is only a few microns thick.

Appendix G

Transient time method

The use of transient time constant method requires known electric field in the silicon bulk. If it is linear the method is based on Eq. 2.35. The effective trapping time can be determined from the fit of $I_{e,h}(t)$ (Eq. 2.35) to the measured induced current pulse shape in the transient region.

The unknown parameters of the fit are the amplitude of the current and the effective trapping time, while $\tau_{e,h}$ is determined from the effective dopant concentration.

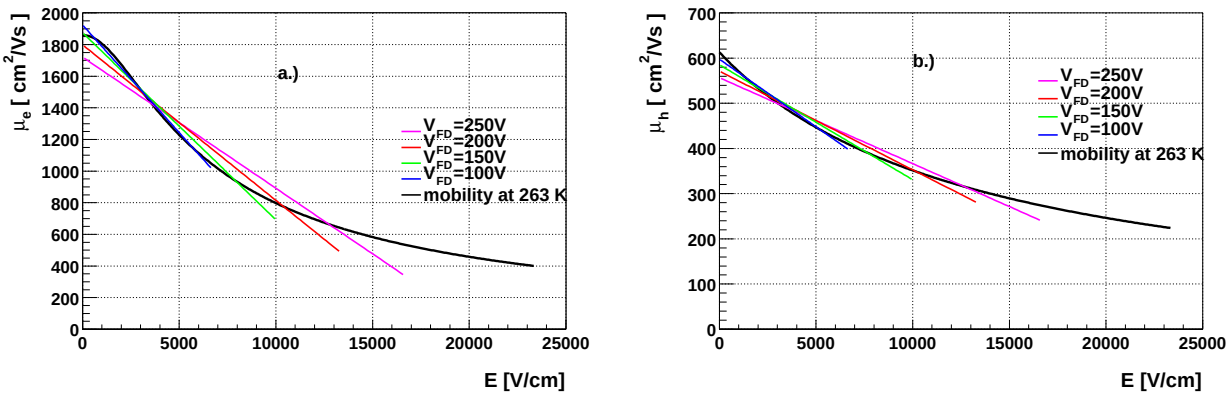

Figure G.1 : Linear approximation to more complex mobility parameterization (black line) for the electric field intervals ranging from 0 to $2 \cdot V_{FD}/D$: a.) electrons and b.) holes.

Eq. 2.35 is derived with an assumption of a constant mobility. If the latter is replaced with $\mu_{e,h} = \mu_{0_{e,h}} (1 - a\,E)$ the solution of equation of motion (Eq. 2.31) inserted in Eq. 2.29 gives for the induced current

$$I_{e,h}(t) = \frac{e_0\,\mu_{0_{e,h}}\,N(0)}{D}\left(\frac{U + kV_{FD}}{D} - a\right)\frac{\exp(-t(\frac{k}{\tau_{e,h}} + \frac{1}{\tau_{eff_{e,h}}}) - 1}{(a\,(\exp(-\frac{k\,t}{\tau_{e,h}}) - 1) + \frac{D}{U + k\,V_{FD}})^2} \quad . \qquad \text{(G.1)}$$

Parameters $\mu_{0_{e,h}}$ and a are obtained by fitting more complex relation (see Appendix C) with a linear function in the electric field interval ranging from $(U - V_{FD})/D$ to $(U + V_{FD})/D$ (see Fig. G.1).

The dependence of the $\tau_{eff_{e,h}}$ on two terms: N_{eff} and mobility parameterization, results in less accurate determination of $\tau_{eff_{e,h}}$ compared to charge correction method. In addition the electric field in an irradiated detector may deviate from linear.

The same consideration about the interval of the $I_{e,h}(t)$ (Eq. G.1) fit to the measured induced current shapes as in Section 5.4.5 are made.

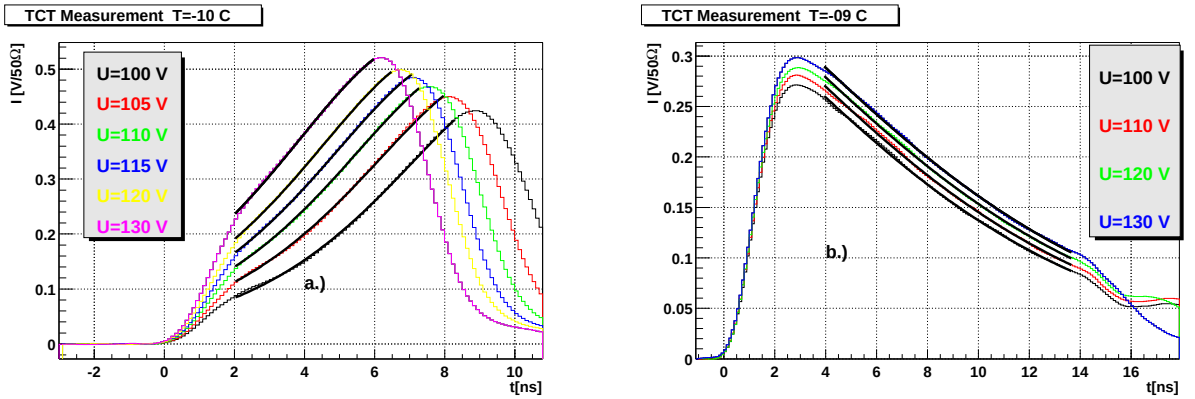

Figure G.2 : $I_{e,h}(t)$ (Eq. G.1) fit to the measured induced current pulse shapes for injection of: a.) electrons and b.) holes.

An example of effective trapping time determination for diode from wafer W339 (standard high resistivity silicon) irradiated with neutrons to $\Phi_{\text{eq}} = 5 \cdot 10^{13}$ cm^{-2} is shown in the Fig. G.2. Effective trapping times were determined at each voltage. The measurements at many voltages thus give an average value. For both electrons and holes the trapping times: $\beta_e = 4 \cdot 10^{-16}$ cm^2/ns and $\beta_h = 5.8 \cdot 10^{-16}$ cm^2/ns agree with those measured using charge correction method. A value of $V_{FD} = 83$ V obtained as an average of C/V (≈ 70 V) and $V_{FD,TCT}$ (≈ 95 V) measurements was used. The measurement of $1/\tau_{eff_{e,h}}$ served as a cross-check for charge correction method. However, variation of V_{FD} for ± 15 V and by that N_{eff} gives around 40% different effective trapping probabilities.

Appendix H

Interstrip capacitance

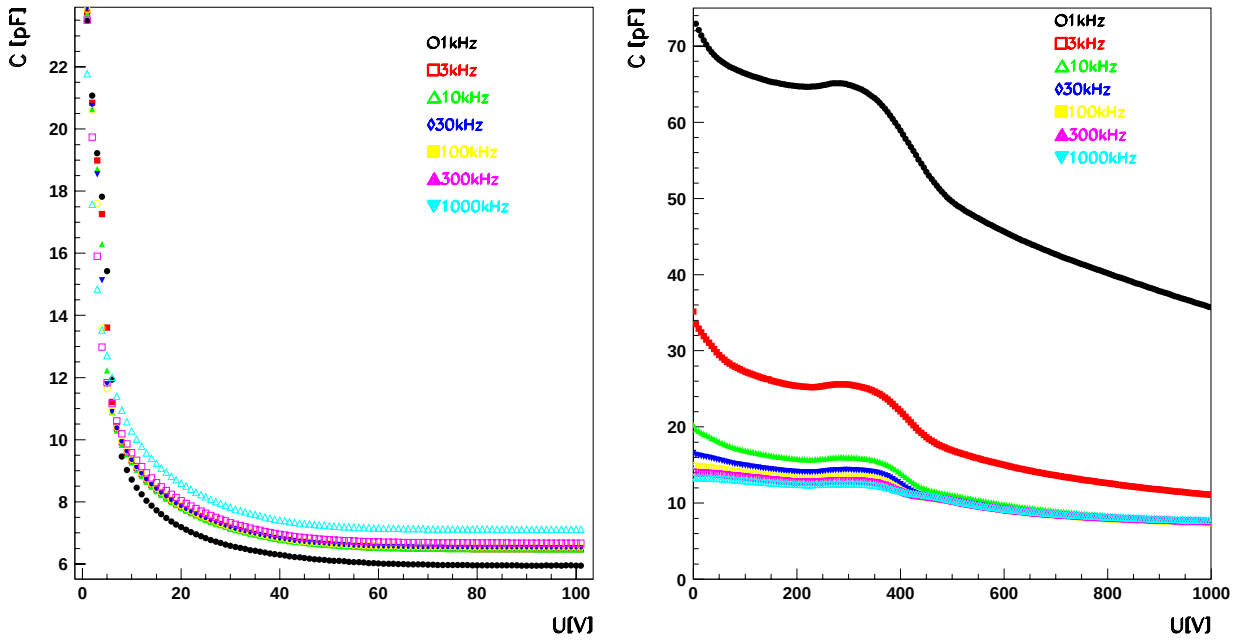

Figure H.1 : Strip capacitance to all neighbors measured for ATLAS-SCT prototype detector: a.) before ($V_{FD} = 55$ V) and b.) after irradiation ($V_{FD} = 300$ V) with neutrons to $\Phi_{\text{eq}} = 2 \cdot 10^{14}$ cm^{-2}. Note different scale on y-axis for both plots.

The load capacitance on the input of the preamplifier increases noise (Eq. 2.54). After the irradiation the interstrip capacitance increases, mainly because of the charge accumulated in the oxide and at the oxide silicon interface. The increase of interstrip capacitance dominates the increase of noise after irradiation providing the shot noise contribution is negligible because of short integration time (25 ns) and appropriate cooling at LHC experiments.

To evaluate the interstrip capacitance a barrel ATLAS-SCT detector produced by

CSEM (Neuchatel,Switzerland) was used. It was 300 μm thick and had 6 cm strips with pitch of 80 μm and width of 18 μm. A multi guard ring structure was implemented to reduce the surface currents. The V_{FD} before irradiation was 55 V. It was irradiated with neutrons to $\Phi_{\text{eq}} = 2 \cdot 10^{14}$ cm^{-2}. The accompanied ionizing dose coming mainly from gamma radiation was estimated to around 4 kGy. At this level of ionizing dose the saturation of interstrip capacitance is expected [HSi94]. The measurements of strip capacitance to all neighbors before irradiation and in the minimum of V_{FD} after irradiation are shown in Fig. H.1. A clear difference can be observed in the voltage dependence of interstrip capacitance. While the interstrip capacitance is flat for $U > V_{FD}$ in a non-irradiated detector it decreases for $U > V_{FD}$ in an irradiated detector. The influence of measurement frequency diminishes at high frequencies which are the only ones relevant for the noise behavior of the detectors connected to read-out electronics. This is in agreement with results found in [Cas99].

It was reported by [Fel98, Rad00] that the interstrip capacitance may depend on crystal orientation. Those results claim lower interstrip capacitance after irradiation of detectors made from silicon crystal cut along $< 100 >$ plane compared to detectors cut along $< 111 >$ plane. Theoretical explanation of that effect was investigated and simulated by [Pas00]. However, the measurements performed in [Cas99] show no difference between different crystal orientation at high bias voltages, moreover, the measurements of noise with a fast (25 ns) front-end electronics did also not reveal any difference.

Appendix I

Emission times

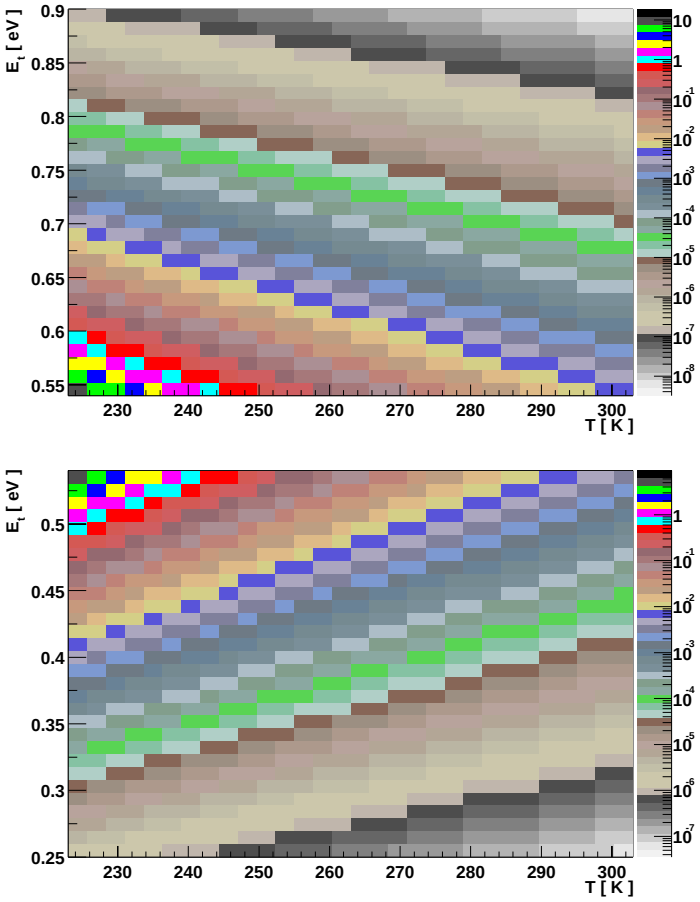

Figure I.1 : Emission time of electrons (up) and holes (down) as function of trap position and temperature.

Emission times of holes and electrons calculated from Eqs. 3.27 and 3.28, with $\sigma_{t_{e,h}} = 10^{-15}$ cm^2 taken for electron and hole cross-section. The intrinsic carrier density is given by

$$n_i(T) \;=\; 1.45 \cdot 10^{10}\ \mathrm{cm}^{-3}\ \exp\!\left(\frac{E_g}{2\,k_B}\left[\frac{1}{300\ \mathrm{K}} - \frac{1}{T}\right]\right) \quad . \tag{I.1}$$

References

[Aar95] P.A. Aarnio et al., Nucl. Instr. Meth. A360 (1995) 521,

[Aba78] V.N. Abakumov et al., Sov. Phys. Semicond., 12, 1 (1978).

[And96] L. Andricek, *Irradiation results of double sided analog readout detectors and design of single sided $p^+ - n$ binary readout detectors for the ATLAS silicon tracker*, ATLAS Internal Note INDENT-NO-190 (1997).

[Ang97] F. Anghinolfi et al., IEEE T. NUCL. SCI. Vol. 44 (1997) 298.

[ATLID] *ATLAS Inner Detector Technical Design Report*, CERN/LHCC/97-16, ATLAS TDR 4 (1997).

[ATLTP] *ATLAS Technical Proposal for a General Purpose pp Experiment at the Large Hadron Collider at CERN*, CERN/LHCC/94-43,LHCC/P2 (1994).

[Azz96] P. Azzi et al., Nucl. Instr. Meth. A383 (1996) 155.

[Bat95] S.J. Bates et al., *Pion-induced damage in silicon detectors*, CERN-ECP/95-26 (1995).

[Bea98] L. J. Beattie et. al., Nuclear Instr. and Meth. A418 (1998) 314.

[Bec00] C. Becker et al., Nucl. Instr. Meth. A444 (2000) 605.

[Bel83] E. Belau et al., Nucl. Instr. Meth. A214 (1983) 253.

[Bin93] N. Bingefors et al., Nucl. Instr. Meth. A326 (1993) 112.

[Bor94] F. Borcheld et al., Nucl. Instr. Meth. A354 (1994) 318.

[Bor98] F. Borchi et al., IEEE T. NUCL. SCI. Vol. 45 (1998) 141.

[Bre94] R. Brenner et al., Nucl. Instr. Meth. A339 (1994) 564.

[Bro00] T.J. Brodbeck et al., Nucl. Instr. and Meth. A455 (2000) 645.

[Cas99] G. Casee et al., NUOVO CIMENTO A 112:(11) (1999) 1253.

[Cau67] D.M. Caughey and R.E. Thomas, *Carrier Mobilities in Silicon Empirically Related to Doping and Field.*, Proc.IEEE Vol 52. (1967) 2192.

[Cav63] G. Cavalleri et al., Nuclear Instr. and Meth. 21 (1963) 177.

[Cav71] G. Cavalleri et al., Nuclear Instr. and Meth. 92 (1971) 137.

[CMSTP] CMS collaboration, *CMS Technical Proposal*, CERN/LHCC/94-38,LHCC/P1 (1994).

[Chi95] A. Chilingarov et al., Nucl. Instr. Meth. A360 (1995) 432.

[Chi00] A. Chilingarov et al., *Recommendations for the corrections of the depletion voltage values extracted from the C/V measurements* , ROSE/TN/2000-10.

[Cin00] V. Cindro et al., *Bistable Damage in Neutron Irradiated Silicon Diodes* , presented at The 3^{rd} International Conference on Radiation Effects on Semiconductor Materials Detectors and Devices, Firenze, June 28-30 2000, to appear in Nucl. Instr. and Meth. A

[Ci00E] V. Cindro et al., Nuclear Instr. and Meth. A439 (2000) 337.

[Ci00B] V. Cindro et al., Nucl. Inst. and Meth. A333 (2000) 333.

[D1MeV] Annual Book of ASTM Standards, Vol 12.02, chapter ASTM

[Dab95] W. Dabrowski et al., Nucl. Instr. Meth. A356 (1995) 241.

[Dab96] W. Dabrowski et al., Nucl. Instr. Meth. A383 (1996) 137.

[Dab99] W. Dabrowski et al., Nucl. Instr. Meth. A421 (1999) 303.

[Das55] W. Dash and R. Newman, Phys. Rev. 99 (1955) 1151.

[Dav00] C. Da Via and S. Watts, *Studies of charge trapping versus temeprature: evidence of double junction formation in heavily irradiated samples operrated at cryogenic T*, presented at 6^{th} ROSE Workshop on Radiation Hardening of Silicon Detectors, CERN 23-24 October 2000, CERN/LEB 2000-006 (92).

[Den93] M. Dentan et al. IEEE T. NUCL. SCI. Vol. 40 (1993) 1555.

[Dez98] B. Dezillie et al., *Defect analysis of ROSE detectors made of different materials*, presented at 3^{rd} ROSE Workshop on Radiaton Hardening of Silicon Detectors, Hamburg, February 12-14 1998, DESY-PROCEEDINGS-1998-02.

[Dez99] B. Dezillie et al., IEEE T. NUCL. SCI. Vol. 46 (1999) 221.

[Dij89] H. Dijkstra et al., IEEE T. NUCL. SCI. Vol. 36 (1989) 591.

[Ell90] J. Ellison et al., IEEE T. NUCL. SCI. 36 (1989) 267.

[Eng81] J.B.A. England et al., Nucl. Instr. Meth. 185 (1981) 43.

[Ere95] V. Eremin et al., Nucl. Instr. Meth. A360 (1995) 458.

[Ere99] V. Eremin and E. Verbitskaya, *Analytical Simulation of Electric Field Manipulation and Reduction of Full Depletion Voltage by Non-Equilibrium Carrier Injection*, presented at The RD-39 Workshop.

[Ere00] V. Eremin et al.: *Charge Collection and Charge Pulse Formation in Highly Irradiated Silicon Planar Detectors*, presented at 3^{rd} International Conference on Radiation Effects in Semiconductor Materials, Detectors and Devices, Firenze, June 28-30 2000, to appear in Nucl. Instr. and Meth. A.

[FBG] P.Fischer et al., ATLAS Internal Note INDET-NO-086 (1994),
A. Brandl et al., CDF Internal Note CDF/DOC/SEC-VXT/PUBLIC/3512,
G. Gorfine et al., ATLAS Internal Note, INDET-No-139 (1996).

[FeicT] H. Feick, *Radiation Tolerance of Silicon Particle Detectors for High-Energy Physics Experiment*, Ph.D. Thesis, Hamburg, DESY F35D-97-08 (1997).

[Fel98] L. Feld et. al., *Radiation induced changes in the Interstrip Capacitance of Silicon Microstrip detectors, presented at* 4^{th} *ROSE Workshop on Radiation Hardening of Silicon Detectors, CERN 2-4 December 1998*, CERN/LEB 98-11 (697).

[Fre99] E. Fretwurst et al.,*Relation between microscopic defects and macroscopic changes in silicon detector properties after hadron irradiation*, Report given at 1st International Workshop on Defect Engineering of Advanced Semiconductor Devices Santorini, Greece, 21-22 April 1999.

[Fre00] E. Fretwurst et. al., *TCT Measurements on Oxygenated Detectors*, presented at 5^{th} ROSE Workshop on Radiation Hardening of Silicon Detectors, CERN, March 16-17 2000, CERN/LEB 2000-005 (315).

[Gad92] S. Gadomski et al., Nucl. Instr. Meth. A320 (1992) 217.

[Gar00] S. Martí i García et al.: *A model of charge collection for irradiated* p^+n *detectors*, presented at 9^{th} International Workshop on Vertex Detectors, Sleeping Bear Dunes National Lakeshore, Michigan, USA, September 10-15 2000, to appear in Nucl. Instr. and Meth. A.

[Gat82] E. Gatti et al., Nucl. Instr and Meth. 193 (1982) 651.

[GEANT] *GEANT 3.21 Detector description and simulation tool*,
http://consult.cern.ch/writeup/geant/

[CluMo] B.R. Gossick, Journal of Applied Physics 30 (1959) 6.
L.S. Smirnov *A Survey of Semiconductor Radiation Techniques*, Mir Publishers, Moscow, 1983.

[Gos99] C. Gossling et al., NUOVO CIMENTO A 112:(11) (1999) 1369-1376.

[Gri90] P. Griffin (SANDIA), data from ENDF/B-VI, unpublished.

[Ham98] R. Hammarstrom et al., Nucl. Instr. Meth. A418 (1998) 128.

[Hal95] G. Hall et al., Nucl. Instr. Meth. A360 (1995) 162.

[Hal96] A. Hallén et al., J. Appl. Phys. 79 (1996) 3906.

[Har99] K. Hara et al., Nucl. Instr. Meth. A435 (1999) 437.

[Hol89] P. Holl et al., IEEE T. NUCL. SCI. Vol. 36 (1989) 251.

[HSi94] A.Holmes-Siedle et al., Nuclear Instr. and Meth. A 339 (1994) 511

[Iwa98] Y. Iwata and M. Asai, *Signal simulation for silicon mictrostrip detectors*, presented at 8^{th} European Symposium on Semiconductor Detectors, June 14-17 1998.

[Kem80] J. Kemmer, Nucl. Instr. Meth. A169 (1980) 499.

[Kem84] J. Kemmer, Nucl. Instr. Meth. A226 (1984) 86.

[Kem88] J. Kemmer and G. Lutz, Nucl. Instr. Meth. A273 (1988) 588.

[Kin59] G. Kinchin et al., Rep. Prog. Phys. Vol. 18. (1959).

[KolaD] J. Kolar, *Meritve popuščanja sevalnih poškodb v silicijevih detektorjih*, Diploma Thesis, Ljubljana (2000).

[Kot85] U. Kötz et al., Nucl. Instr. Meth. A235 (1985) 481.

[Kra93] H.W. Kraner et al., Nuclear Instr. and Meth. A326 (1993) 350.

[Kra00] G. Kramberger et al., *Determination of effective trapping time of electrons and holes in irradiated silicon*, presented at 3^{rd} International Conference on Radiation Effects in Semiconductor Materials, Detectors and Devices, Firenze, June 28-30 2000, (ATL-INDET-2000-017) accepted for publication in Nucl. Instr. and Meth. A.

[Kri98] E.S. Krištof: *Characterization of Neutron Flux in the Exposure Channel F19 of the TRIGA Mark II Reactor in Ljubljana*, Proceedings of Nuclear Energy in Central Europe '98, Terme Čatež, Slovenia, September 7-10, (1998) 43.

[KramD] G. Kramberger, *Meritve in simulacija signalov izvora* ^{90}Sr *v pozicijsko občutljivem silicijevem detektorju*, Diploma Thesis, Ljubljana (1995).

[Laa93] M. Laakso et al., Nucl. Instr. Meth. A365 (1993) 214.

[Laz87] M.S. Lazo et al., *Silicon and silicon dioxide neutron damage functions*

[Lem94] F. Lemeilleur et al., CERN-ECP/94-8 (1994).

[Ler99] C. Leroy et. al., Nucl. Instr. Meth. A426 (1999) 99.

[Ler97] C. Leroy et. al., Nucl. Instr. Meth. A388 (1997) 289.

[Les93] J. Leslie et al., IEEE T. NUCL. SCI. Vol.40 (1993) 557.

[LHCDR] *The LHC Conceptual Design Report - The Yellow Book*, CERN/AC/95-05 (LHC) (1995).

[Lin99] G. Lindströom. M. Moll, E. Fretwurst, Nucl. Instr. Meth. A426 (1999) 1.

[Lin00] RD48 Collaboration: G.Lindström et al., *Radiation Hard Silicon Detectors - Developments by the RD48 (ROSE) Collaboration*, presented at 4$^{\text{th}}$ STD Hiroshima Conference, Hiroshima, Japan, March 23-25, 2000, ROSE/TN/2000-03, accepted for publication in Nucl. Instr. and Meth. A.

[LiZ92] Z. Li and H. Kraner, Journal of Electronic Material 21 (1992) 701.

[LiZ95] V. Eremin and Z. Li, Nucl. Instr. Meth. A362 (1995) 338.

[Lut96] G. Lutz, Nuclear Instr. and Meth. A377 (1996) 234.

[Mac58] G. Macfarlane et al., Phys. Rev. 111 (1958) 1245.

[Man00] I. Mandić et al., *TCT measurements at cryogenic temperatures*, presented at 6^{th} ROSE Workshop on Radiation Hardening of Silicon Detectors, CERN 23-24 October 2000, CERN/LEB 2000-006 (307).

[Mat95] J. Matheson et al., RD 20 Techincal Report RD20/TN/36 (1995).

[MaJ95] J. Matheson et al., Nucl. Instr. Meth. A362 (1995) 297.

[MauPC] M. Maučec, private communication

[Men99] D. Menichelli et. al., Nucl. Instr. Meth. A426 (1999) 135.

[Mes00] M. Meschini et al., Nucl. Instr. Meth. A447 (2000) 133.

[Mik99] M. Mikuž et al., NUOVO CIMENTO A 112:(11) (1999) 1391.

[Mik00] M.Mikuž et al., *Bias Dependence and Bistability of Radiation Defects*, presented at 4$^{\text{th}}$ STD Hiroshima Conference, Hiroshima, Japan, March 23-25 2000, accepted for publication in Nucl. Instr. and Meth. A.

[MollT] Michael Moll, *Radiation Damage in Silicon Particle Detectors-microscopic defects and macroscopic properties*, Ph.D. Thesis, Hamburg, DESY-THESIS-1999-040 (1999).

[Nak00] T. Nakayama et al., IEEE T. NUCL. SCI. Vol. 47 (2000) 1434.

[NumRe] V.H. Press et al., *Numerical Recipes in C*, Cambridge University Press (1992).

[Oug90] A.M. Ougang et al., IEEE T. NUCL. SCI. Vol.37 (1990) 2219.

[Pal98] V.G. Palmieri et al., Nucl. Instr. Meth. A413 (1998) 475.

[Pas00] D. Passeri et at., *Parasitic Capacitances in Thick Substrate Silicon Microstrip Detectors*, presented at 3^{rd} International Conference on Radiation Effects on Semiconductor Materials Detectors and Devices, Firenze, June 28-30 2000, to appear in Nucl. Instr. and Meth. A.

[Pei92] A. Peisert, *Silicon Microstrip Detectors*, 1992.

[PIrS] M. Glaser, Irradiation site information on WWW, http://irradiation.web.cern.ch/irradiation/Flux-3.htm.

[piE1] http://www1.psi.ch/users/FEREYDOUN/beam_pie1.html .

[PoSCD] S.M. Sze, *Physics of Semiconductor Devices*, John Wiley & Sons (1981).

[Rad88] V. Radeka, Ann. Rev. Nucl. Part. Sci. 38 (1988) 217.

[Rad00] V. Radicci et al., *A Comparison on Radiation Tolerance of* $< 100 >$ *and* $< 111 >$ *Silicon Substrates of Microstrip Detectors*, presented at 3^{rd} International Conference on Radiation Effects on Semiconductor Materials Detectors and Devices, Firenze June 28-30, 2000, to appear in Nucl. Instr. and Meth. A.

[Ram39] S. Ramo, Proc. IRE 27 (1939) 584.

[Rih96] R. H. Richter et al., Nucl. Instr. Meth. A377 (1996) 412.

[Roe96] S. Roe, *The FElix users guide*, 1996.

[ROOT] *ROOT - An Object-Oriented Data Analysis Framework*, http://root.cern.ch/

[ROSE1] LEB Status Report/RD48, CERN/LHCC 97-39, June 1997.

[ROSE2] LEB Status Report/RD48, CERN/LHCC 98-39, October 1998.

[ROSE3] LEB Status Report/RD48, CERN/LHCC 2000-09, December 1999.

[Ruz00] A. Ruzin, Nucl. Instr. and Meth. A447 (2000) 116.

[Sel90] S. Selberherr et al., Solid-State Electron. 33(11) (1990) 1425.

[SchuT] T. Schulz, *Investigation on the Long term Behaviour of Damage Effects and Corresponding Defects in Detector Grade Silifon after Neutron Irradiation*, Ph.D. Thesis, Hamburg, DESY 96-027 (1995).

[StudD] A. Studen, *Elektirčno polje v sevalno poškodovani silicijevi $p^+ - n - n^+$ diodi*, Diploma thesis, Ljubljana, Ljubljana (2000).

[Tay93] G. Gorfine et al., ATLAS Internal Note INDET-NO-030, UM-P-93/103 (1993).

[Thu75] C.D. Thurmond, J. Electrochem. Soc. Vol. 122 (1975) 1133.

[Ver00] E. Verbitskaya et. al., *N_{eff} evaluation in oxygen-rich irradiated Si detectors by TCT and its relationship with detector operational bias*, presented at 6^{th} ROSE Workshop on Radiation Hardening of Silicon Detectors, CERN 23-24 October 2000, CERN/LEB 2000-006 (56).

[Ve00L] E. Verbitskaya et al., *Optimization of electric field distribution by free carrier injection in silicon detectors operated at low temperatures*, presented at IEEE Nuclear Science Symposium, Lyon, October 2000, to be published in IEEE Trans. on Nucl. Sci.

[Wat99] S. Watts et al., *Radiation Effects in Silicon Detectors*, Report given at 1st Intenational Workshop on Defect Engineering of Advanced Semiconductor Devices Santorini, Greece, April 21-22 1999.

[WunsT] R. Wunsdorf, *Systematische Untersuchungen zur Strahelenresitenz von Silizium-Detektoren für die Verwendung in Hochenergiephysik-Experimenten*, Ph.D. Thesis, DESY FHIK-92-01 (1992).

[Wun96] R. Wunstorf et al., Nucl. Instr. Meth. A377 (1996) 228.

[ZontM] D. Žontar, *Razvoj pozicijsko občutljivih silicijevih detektorjev za spektrometer DEPLHI* , M.Sc. Thesis, Ljubljana (1995).

[ZontT] D. Žontar, *Study of radiation damage in silicon detectors for high luminosity experiments at LHC*, Ph.D. Thesis, Ljubljana (1998).